frontiers | Research Topics

Multi-parametric perfusion MRI by arterial spin labeling

Edited by
Long-Biao Cui, Guolin Ma and Danny J. J. Wang

Published in
Frontiers in Neuroscience

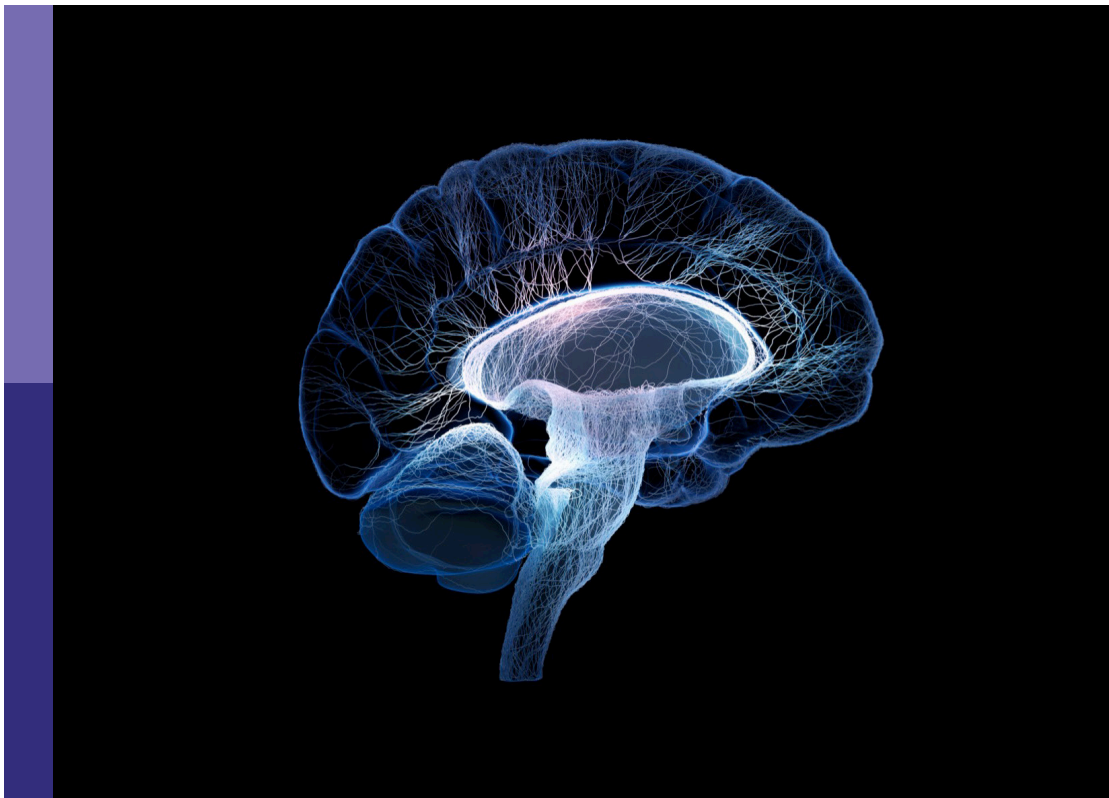

FRONTIERS EBOOK COPYRIGHT STATEMENT

The copyright in the text of individual articles in this ebook is the property of their respective authors or their respective institutions or funders. The copyright in graphics and images within each article may be subject to copyright of other parties. In both cases this is subject to a license granted to Frontiers.

The compilation of articles constituting this ebook is the property of Frontiers.

Each article within this ebook, and the ebook itself, are published under the most recent version of the Creative Commons CC-BY licence. The version current at the date of publication of this ebook is CC-BY 4.0. If the CC-BY licence is updated, the licence granted by Frontiers is automatically updated to the new version.

When exercising any right under the CC-BY licence, Frontiers must be attributed as the original publisher of the article or ebook, as applicable.

Authors have the responsibility of ensuring that any graphics or other materials which are the property of others may be included in the CC-BY licence, but this should be checked before relying on the CC-BY licence to reproduce those materials. Any copyright notices relating to those materials must be complied with.

Copyright and source acknowledgement notices may not be removed and must be displayed in any copy, derivative work or partial copy which includes the elements in question.

All copyright, and all rights therein, are protected by national and international copyright laws. The above represents a summary only. For further information please read Frontiers' Conditions for Website Use and Copyright Statement, and the applicable CC-BY licence.

ISSN 1664-8714
ISBN 978-2-83251-450-4
DOI 10.3389/978-2-83251-450-4

About Frontiers

Frontiers is more than just an open access publisher of scholarly articles: it is a pioneering approach to the world of academia, radically improving the way scholarly research is managed. The grand vision of Frontiers is a world where all people have an equal opportunity to seek, share and generate knowledge. Frontiers provides immediate and permanent online open access to all its publications, but this alone is not enough to realize our grand goals.

Frontiers journal series

The Frontiers journal series is a multi-tier and interdisciplinary set of open-access, online journals, promising a paradigm shift from the current review, selection and dissemination processes in academic publishing. All Frontiers journals are driven by researchers for researchers; therefore, they constitute a service to the scholarly community. At the same time, the *Frontiers journal series* operates on a revolutionary invention, the tiered publishing system, initially addressing specific communities of scholars, and gradually climbing up to broader public understanding, thus serving the interests of the lay society, too.

Dedication to quality

Each Frontiers article is a landmark of the highest quality, thanks to genuinely collaborative interactions between authors and review editors, who include some of the world's best academicians. Research must be certified by peers before entering a stream of knowledge that may eventually reach the public - and shape society; therefore, Frontiers only applies the most rigorous and unbiased reviews. Frontiers revolutionizes research publishing by freely delivering the most outstanding research, evaluated with no bias from both the academic and social point of view. By applying the most advanced information technologies, Frontiers is catapulting scholarly publishing into a new generation.

What are Frontiers Research Topics?

Frontiers Research Topics are very popular trademarks of the *Frontiers journals series*: they are collections of at least ten articles, all centered on a particular subject. With their unique mix of varied contributions from Original Research to Review Articles, Frontiers Research Topics unify the most influential researchers, the latest key findings and historical advances in a hot research area.

Find out more on how to host your own Frontiers Research Topic or contribute to one as an author by contacting the Frontiers editorial office: frontiersin.org/about/contact

Multi-parametric perfusion MRI by arterial spin labeling

Topic editors

Long-Biao Cui — Air Force Medical University, China

Guolin Ma — China-Japan Friendship Hospital, China

Danny J. J. Wang — University of Southern California, United States

Citation

Cui, L.-B., Ma, G., Wang, D. J. J., eds. (2023). *Multi-parametric perfusion MRI by arterial spin labeling*. Lausanne: Frontiers Media SA.

doi: 10.3389/978-2-83251-450-4

Table of contents

frontiers | Frontiers in Neuroscience

TYPE Editorial
PUBLISHED 11 January 2023
DOI 10.3389/fnins.2022.1132835

Check for updates

OPEN ACCESS

EDITED AND REVIEWED BY
Vince D. Calhoun,
Georgia State University, United States

*CORRESPONDENCE
Guolin Ma
✉ maguolin1007@qq.com

SPECIALTY SECTION
This article was submitted to Brain Imaging Methods, a section of the journal Frontiers in Neuroscience

RECEIVED 28 December 2022
ACCEPTED 30 December 2022
PUBLISHED 11 January 2023

CITATION
Cui L-B, Wang DJJ and Ma G (2023) Editorial: Multi-parametric perfusion MRI by arterial spin labeling. *Front. Neurosci.* 16:1132835. doi: 10.3389/fnins.2022.1132835

COPYRIGHT
© 2023 Cui, Wang and Ma. This is an open-access article distributed under the terms of the Creative Commons Attribution License (CC BY). The use, distribution or reproduction in other forums is permitted, provided the original author(s) and the copyright owner(s) are credited and that the original publication in this journal is cited, in accordance with accepted academic practice. No use, distribution or reproduction is permitted which does not comply with these terms.

Editorial: Multi-parametric perfusion MRI by arterial spin labeling

Long-Biao Cui[1], Danny J. J. Wang[2] and Guolin Ma[3]*

[1]Schizophrenia Imaging Lab, Fourth Military Medical University, Xi'an, China, [2]Laboratory of FMRI Technology (LOFT), Stevens Neuroimaging and Informatics Institute, University of Southern California, Los Angeles, CA, United States, [3]Department of Radiology, China-Japan Friendship Hospital, Beijing, China

KEYWORDS

perfusion-weighted imaging, cerebral blood flow, arterial spin labeling, blood-brain barrier, biomarker

Editorial on the Research Topic
Multi-parametric perfusion MRI by arterial spin labeling

In a wide range of psychiatric and neurological disorders, changes in cerebral blood flow (CBF) patterns may be potential indicators of altered brain metabolism and function that may contribute to understanding the underlying mechanisms of disease (Cui et al., 2017a,b; Kisler et al., 2017; Zhuo et al., 2017). Magnetic resonance imaging (MRI) with perfusion-weighted imaging (PWI) provides information about lesion-related changes in CBF in the brain, including dynamic susceptibility contrast (DSC) and arterial spin labeling (ASL) sequences. In contrast with DSC-PWI, ASL is a MRI technique to non-invasively assess CBF by magnetic labeling of inflowing arterial blood water both at rest and during hemodynamic challenges, such as CO_2 breathing or task activation (Haller et al., 2016). Depending on the labeling methods, ASL techniques are divided into different types, such as continuous ASL (CASL), pulsed ASL (PASL), and pseudo-continuous ASL (pCASL), with pCASL being the most commonly used method. In addition, several new ASL techniques have emerged in recent years, such as velocity-selective ASL (VS ASL), 4D-ASL-MRA, and territorial ASL (t-ASL).

The present Frontiers Research Topic entitled "*Multi-parametric perfusion MRI by arterial spin labeling*" set out to present the recent methodological developments in multi-parametric ASL technology and its applications in the study of brain hemodynamic function in health and disease, and how multi-parametric ASL could facilitate pathophysiological interpretation and clinical intervention in these diseases. The submissions in this Frontiers Research Topic clearly reflect the state-of-the-art research in the field by encompassing investigations including the differentiation of neoplastic and non-neoplastic tissues, the observation of changed CBF and/or arterial transit time (ATT) pattern, and the improvement of diagnostic efficacy.

Hu et al. enrolled 35 patients with high grade gliomas (HGG), 12 patients with brain metastasis, and 15 non-neoplastic patients to distinguish intracranial non-neoplastic from neoplastic lesions using three-dimensional pCASL (3D-pCASL). Compared with the patients with neoplasm, the relative CBF values of lesions and perilesional edema were significantly decreased in patients with no-neoplasm. The area under the receiver operating characteristic curve (AUC) further demonstrated that the relative CBF of lesions (0.994) and perilesional edema (0.846) exhibit excellent diagnostic ability in discriminating non-neoplastic from neoplastic lesions. Those results provide evidence about the utility of parameters based on ASL perfusion MRI for the differentiation of intracranial neoplastic and non-neoplastic lesions.

The underlying neuronal events and neuronal activity can be directly reflected by hemodynamics or metabolism. CBF, as the most important cerebral perfusion parameter, plays a critical role in the early diagnosis, mechanism exploration, and disease classification of psychiatric and neurological disorders. Chen et al. collected CBF images based on 3D-pCASL from 36 patients with unilateral Sudden Sensorineural Hearing Loss (SSNHL) and 36 healthy controls to explore the differences in the CBF between unilateral SSNHL and healthy controls and the relationships between changed CBF and clinical characteristics in patients with unilateral SSNHL, which furthers the understanding of the neuropathological mechanisms underlying the clinical symptoms of unilateral SSNHL. In another study, Wang X.-H. et al. explored the CBF changes associated with anxiety in patients with pulmonary nodules based on ASL, aiming to characterize the relationships between the cerebral perfusion pattern of anxiety associated with pulmonary nodules, blood perfusion status, and mode of pulmonary nodule induced anxiety state. The decreased CBF in the right insula/Heschl's cortex and increased CBF in the right postcentral gyrus can potentially be used as a biomarker to distinguish the patients with pulmonary nodules under the anxiety state from the non-anxiety patients. Xiao et al. investigated the abnormal blood perfusion metabolism in patients with obstructive sleep apnea (OSA) compared with healthy controls and the relationships between changed CBF and abnormal behavior, psychology, and cognitive function in patients with OSA, deepening the understanding of the pathophysiological mechanism of OSA. By measuring CBF using pCASL in patients with subjective cognitive decline, Li et al. found that increased CBF within the left parahippocampal gyrus as the risk factor associated with patients with spinocerebellar degeneration (SCD) independently and may serve as markers facilitating earlier identification of SCD. In another study, the CBF of cerebellum and the midbrain of brainstem were decreased in patients with SCD compared with healthy controls and further correlated with disease severity and depression status, suggesting the possibility of changed CBF value as neuroimaging biomarker to reflect the progression of SCD and the psychological states (Liu et al.). In the discrimination of mild cognitive impairment, the early stage of Alzheimer's disease, the combination of CBF and ATT with 7-delay ASL demonstrated higher accuracy than CBF of 1-delay (Sun et al.). In drug-naïve adolescents with first-episode major depressive disorder, the lower regional CBF in the left triangular part of the inferior frontal gyrus compared with healthy controls was negatively correlated with Hamilton depression scale scores (Xiong et al.).

Cerebral perfusion parameters based on ASL image can directly reflect microvascular blood flow, and are a powerful tool for non-invasive assessment of hemodynamics. Yu et al. evaluated the difference of mean CBF and ATT through enhanced ASL imaging between patients with intracranial atherosclerotic stenosis (ICAS) and healthy controls, and the correlation between mean CBF and ATT in patients and controls, respectively to directly observe the impact of the blood flow velocity of the extracranial carotid/vertebral arteries on mean CBF. Results suggested that mean CBF and ATT demonstrated significant correlation in patients with ICAS, providing further evidence about the influence of extracranial blood flow on intracranial hemodynamics in the posterior circulation. The preoperative collateral score based on brain perfusion parameters such as relative CBF has the promise to serve as an indicator for surgical collaterals in patients with moyamoya angiopathy after combined bypass surgery (Wang M. et al.). In patients with moyamoya disease, cerebral blood perfusion assessed by 3D pCASL demonstrated higher accuracy both before and after revascularization in comparison with CBF measured from DSC PWI (Zhang et al.).

In brief, this Research Topic highlights the present and recent methodological developments in ASL technology and its applications in the study of psychiatric and neurological disorders. However, more research is still needed to further broaden the application of ASL in disease diagnosis, classification, treatment, and follow-up, and mechanism exploration of psychiatric and neurological disorders.

Author contributions

L-BC, DW, and GM drafted and revised the manuscript. All authors contributed to the article and approved the submitted version.

Funding

This work was supported by the National Key Research and Development Program of China (No. 2020YFC2003903) and the grants from National Natural Science Foundation of China (Nos. 81971585, 82271953, and 82271949).

Acknowledgments

We thank Dr. Zeshan Yao and Ms. Shu-Wan Zhao for comments on this editorial. We thank all authors for their contribution to our Research Topic.

Conflict of interest

DW is a shareholder of Translational MRI, LLC and Hura Imaging, Inc., that developed CereFlow software for processing ASL data.

The remaining authors declare that the research was conducted in the absence of any commercial or financial relationships that could be construed as a potential conflict of interest.

Publisher's note

All claims expressed in this article are solely those of the authors and do not necessarily represent those of their affiliated organizations, or those of the publisher, the editors and the reviewers. Any product that may be evaluated in this article, or claim that may be made by its manufacturer, is not guaranteed or endorsed by the publisher.

References

Cui, L.-B., Chen, G., Xu, Z.-L., Liu, L., Wang, H.-N., Guo, L., et al. (2017a). Cerebral blood flow and its connectivity features of auditory verbal hallucinations in schizophrenia: a perfusion study. *Psychiatry Res. Neuroimaging* 260, 53–61. doi: 10.1016/j.pscychresns.2016.12.006

Cui, L.-B., Wang, L.-X., Tian, P., Wang, H.-N., Cai, M., Guo, F., et al. (2017b). Aberrant perfusion and its connectivity within default mode network of first-episode drug-naïve schizophrenia patients and their unaffected first-degree relatives. *Sci. Rep.* 7, 16201. doi: 10.1038/s41598-017-14343-7

Haller, S., Zaharchuk, G., Thomas, D. L., Lovblad, K.-O., Barkhof, F., and Golay, X. (2016). Arterial Spin Labeling Perfusion of the Brain: Emerging Clinical Applications. *Radiology* 281, 337–356. doi: 10.1148/radiol.2016150789

Kisler, K., Nelson, A. R., Montagne, A., and Zlokovic, B. V. (2017). Cerebral blood flow regulation and neurovascular dysfunction in Alzheimer disease. *Nat. Rev. Neurosci.* 18, 419–434. doi: 10.1038/nrn.2017.48

Zhuo, C., Zhu, J., Qin, W., Qu, H., Ma, X., and Yu, C. (2017). Cerebral blood flow alterations specific to auditory verbal hallucinations in schizophrenia. *Br. J. Psychiatry* 210, 209–215. doi: 10.1192/bjp.bp.115.174961

frontiers in Neuroscience

ORIGINAL RESEARCH
published: 17 February 2022
doi: 10.3389/fnins.2021.823876

Enhanced Arterial Spin Labeling Magnetic Resonance Imaging of Cerebral Blood Flow of the Anterior and Posterior Circulations in Patients With Intracranial Atherosclerotic Stenosis

*Hongwei Yu[1,2], Yangchen Li[1], Yibo Feng[3], Linwei Zhang[4], Zeshan Yao[5], Zunjing Liu[4], Wenwen Gao[1], Yue Chen[1] and Sheng Xie[1,2]**

[1] Department of Radiology, China-Japan Friendship Hospital, Beijing, China, [2] Graduate School of Peking Union Medical College, Chinese Academy of Medical Sciences and Peking Union Medical College, Beijing, China, [3] Department of Ultrasound Medicine, China-Japan Friendship Hospital, Beijing, China, [4] Department of Neurology, China-Japan Friendship Hospital, Beijing, China, [5] AnImageTech, Beijing Co., Ltd, Beijing, China

OPEN ACCESS

Edited by:
Long-Biao Cui, Fourth Military Medical University, China

Reviewed by:
Han Lv, Capital Medical University, China
Chang-Yang Xing, Fourth Military Medical University, China

***Correspondence:**
Sheng Xie
xs_mri@126.com

Specialty section:
This article was submitted to Brain Imaging Methods, a section of the journal Frontiers in Neuroscience

Received: *28 November 2021*
Accepted: *24 December 2021*
Published: *17 February 2022*

Citation:
Yu H, Li Y, Feng Y, Zhang L, Yao Z, Liu Z, Gao W, Chen Y and Xie S (2022) Enhanced Arterial Spin Labeling Magnetic Resonance Imaging of Cerebral Blood Flow of the Anterior and Posterior Circulations in Patients With Intracranial Atherosclerotic Stenosis. Front. Neurosci. 15:823876. doi: 10.3389/fnins.2021.823876

Objectives: This study analyzed differences in the mean cerebral blood flow (mCBF) and arterial transit time (ATT) of the anterior and posterior circulations between patients with intracranial atherosclerotic stenosis (ICAS) and control subjects. We also investigated the correlation between ATT and mCBF in the two groups, and evaluated whether the blood flow velocity of the extracranial carotid/vertebral arteries can influence mCBF.

Methods: A total of 32 patients with ICAS were prospectively enrolled at the Radiology Department of the China-Japan Friendship Hospital between November 2020 and September 2021. All patients had extensive arterial stenosis, with 17 having cerebral arterial stenosis in the anterior circulation and 15 in the posterior circulation. Thirty-two healthy subjects were enrolled as a control group. Enhanced arterial spin labeling (eASL) imaging was performed using a 3.0-T GE magnetic resonance imaging scanner, and all patients underwent carotid and vertebral Doppler ultrasound examinations. CereFlow software was used for post-processing of the eASL data, to obtain cerebral perfusion parameters such as mCBF and ATT. Independent samples *t*-tests were used to analyze and compare mCBF and ATT of the anterior circulation (frontal lobe, parietal lobe, and insula) and posterior circulation (occipital lobe, cerebellum) between the patient and control groups. The relationships of ATT and mCBF in the two groups were evaluated with Pearson's correlation. The blood flow velocity of the extracranial internal carotid/vertebral arteries, including the peak systolic velocity (PSV), end diastolic velocity (EDV), mean PSV (mPSV), and mean EDV (mEDV), was compared between the control and study groups using *t*-tests. Multiple linear regression analysis was then applied to determine the factors associated with mCBF in the two groups.

Results: The mCBFs of the anterior and posterior circulations in the patient group were lower than those of the control group. The ATTs in the patient group were all significantly longer than those of the control group ($p < 0.05$). Except for the insula in the control group, significant correlations were found between ATT and mCBF in all other investigated locations in the two groups ($p < 0.05$). The blood flow velocity of the extracranial internal carotid/vertebral arteries differed significantly between the control and patient groups ($p < 0.05$). The multiple linear regression analysis revealed that in patients with ICAS, mPSV of the vertebral arteries and local ATT correlated with mCBF of the occipital lobes and the cerebellum, respectively ($p < 0.05$). In contrast, there was no significant correlation within the anterior circulation (frontal lobes, parietal lobes, and insula).

Conclusion: There was a significant relationship between ATT and mCBF in patients with ICAS. Extracranial blood flow may influence intracranial hemodynamics in the posterior circulation in patients with ICAS. The maintenance of extracranial blood flow is of great significance in the preservation of intracranial hemodynamics.

Keywords: arterial spin labeling, intracranial atherosclerotic stenosis, magnetic resonance imaging, ultrasonography, hemodynamics

INTRODUCTION

Intracranial atherosclerotic stenosis (ICAS) is a major cause of ischemic stroke in the Chinese population, accounting for 30–50% of ischemic stroke (Wang Y. et al., 2014). The risk of hypoperfusion in patients with ICAS is an important consideration in prognosis and the development of treatment strategies. At present, the commonly used methods for perfusion evaluation are CT perfusion (CTP) imaging using an exogenous contrast agent, and magnetic resonance dynamic susceptibility contrast perfusion-weighted imaging. CTP is routinely used to evaluate cerebral hemodynamics because it provides relatively accurate perfusion quantification, including cerebral blood flow (CBF), cerebral blood volume, and mean transit time (MTT; Kang et al., 2008). However, the administration of exogenous contrast agents is invasive and presents risks from contrast agent allergy and renal interstitial fibrosis (Zaharchuk, 2007). Furthermore, the perfusion results obtained from patients with severe ICAS may present with errors because of changes in the blood–brain barrier (Leng et al., 2019). The three-dimensional pseudo-continuous arterial spin labeling (3D-pCASL) technique does not require administration of exogenous contrast agents, instead using magnetically labeled hydrogen protons in the blood as a freely diffusible contrast agent to measure CBF. It is advantageous as it is non-invasive, is repeatable, and does not require vascular injection of a contrast agent for the evaluation of cerebral blood perfusion. A previous study showed a significant correlation between perfusion data from ASL and (CTP) imaging in patients with moyamoya disease (Wang R. et al., 2014). However, the quantification of CBF by 3D-pCASL is affected by the arterial transit time (ATT). The delay in the time the hydrogen protons in the arterial blood take to flow through the labeled area to the acquisition area is likely to result in the loss of labeled signals and errors, leading to reduced CBF signals (Cheng et al., 2012; Ferré et al., 2013). Therefore, uncertainty in the ATT weakens the potential advantages of 3D-pCASL for the accurate and quantitative measurement of CBF. In contrast, the enhanced arterial spin labeling (eASL) imaging technique uses multiple post-labeling delay (PLD) times to calculate ATT (Detre and Alsop, 1999). Compared with a single PLD or three PLDs, eASL can better quantify blood perfusion and ATT, reduce physiological background noise, and improve the accuracy of mean CBF (mCBF) measurement (Wells et al., 2010; Wang et al., 2013).

Patients with ICAS usually have hemodynamic disorders, resulting in abnormal cerebral blood flow and elongation of ATT. ATT is a physiological parameter that reflects the time required for labeled spins to reach the region of interest in the brain (Wang et al., 2003). A previous study demonstrated significant correlations between ASL, ATT, and CTP MTT in moyamoya disease (Ravindra et al., 2020). In hemispheric transient ischemic attack patients, both perfusion-weighted imaging and ASL findings were more common in the symptomatic hemisphere. Agreement between neuroradiologists regarding abnormal studies was good for ASL and perfusion-weighted imaging (Zaharchuk et al., 2012). However, most studies focused on investigation of the hemodynamic changes in the anterior circulation. The posterior circulation, which is supplied by the basilar artery formed by the confluence of bilateral vertebral arteries at the level of the brainstem, has not been widely studied using ASL. The relationship between the ATT and CBF in the posterior circulation may not be as consistent as that in the anterior circulation. The upstream blood flow from the extracranial carotid and vertebral arteries may exert an effect on the blood flow downstream. If so, the blood flow velocity of the extracranial carotid/vertebral arteries should affect the intracranial hemodynamics. In this study, we aimed to investigate the relationship between ATT and CBF in both the

anterior and posterior circulation, determining the influence of extracranial flow on the intracranial hemodynamics.

MATERIALS AND METHODS

Subjects

A total of 32 patients [15 men and 17 women, mean age (standard deviation) 66.5 ± 9.8 years] with ICAS were prospectively enrolled at the Radiology Department of the China-Japan Friendship Hospital between November 2020 and September 2021. All patients had extensive arterial stenosis, with 17 having severe cerebral arterial stenosis in the anterior circulation and 15 in the posterior circulation. The inclusion criteria were as follows: patients were diagnosed with intracranial artery stenosis by CT angiography (CTA) and magnetic resonance angiography (MRA) of the head and neck; CTA of the head and neck and carotid Doppler ultrasound (CDU) showed no severe stenosis (stenosis >50% of the normal vessel diameter) or occlusion of the extracranial carotid and vertebral arteries; and the intervals between CTA, MRA, and CDU examinations were less than 72 h. The exclusion criteria were as follows: other diseases that could affect the hemodynamics, such as intracranial space-occupying lesions, arteriovenous fistula, moyamoya disease, cerebral edema, and massive cerebral infarction; systemic diseases that could affect cerebral blood flow, such as heart failure, serious cardiovascular disease, severe anemia, and hypovolemia; and intake of medications that could markedly affect the brain blood flow. Additionally, thirty-two healthy volunteers [16 men and 16 women; mean age (standard deviation) 64 ± 1.78 years] were enrolled as the control group. The study protocol was approved by the Institutional Review Boards of the China-Japan Friendship Hospital (approval number: 2015-23). Informed consent was obtained from each subject.

MRI Data Acquisition and Processing

A 3.0-T magnetic resonance imaging scanner (Discovery MR750, GE Healthcare, Waukesha, WI, United States) with an 8-channel head coil was used for imaging. The MRI sequences included T1-weighted imaging, T2-weighted imaging, diffusion-weighted imaging, three-dimensional time-of-flight MRA, and the eASL sequence. The perfusion-weighted images were acquired at seven consecutive pulsed pCASL labeling durations of 0.22, 0.26, 0.30, 0.37, 0.48, 0.68, and 1.18 s, with PLDs of 1.00, 1.22, 1.48, 1.78, 2.15, 2.62, and 3.32 s in the eASL sequence. The scan parameters included a 512 × 512 matrix, a 22 cm × 22 cm field of view, a 62.5-kHz bandwidth, 4-mm slice thickness, 36 slices, an echo time of 10.5 ms, and a repetition time of 5,936 ms. IDL-based RWCON code was used to reconstruct images, which were stored in the database as DICOM images.

CereFlow software (Translational MRI, LLC, Los Angeles, CA, United States) was used to process the eASL data according to the following steps (van der Thiel et al., 2018): (1) The eASL raw data and CBF data were converted into parametric cerebral perfusion maps to obtain mCBF and ATT. (2) The parametric cerebral perfusion maps were normalized into the standard brain space of the Montreal Neurological Institute (MNI), resampled after normalization, and spatially smoothed. (3) The atlas of arterial blood supply territories, ASPECTS brain atlas, and the automated anatomical labeling atlas were overlaid. (4) The mean perfusion values of each territory volume were obtained.

The perfusion regions of interest (ROIs) of the anterior circulation included the frontal lobe, parietal lobe, and insula, while the perfusion ROIs of the posterior circulation included the occipital lobe and cerebellum. Because the temporal lobe is supplied by both the anterior and posterior circulations, it was excluded from the measurements to avoid confusion.

CT Angiography Examination

A Gemstone Spectral Imaging CT scanner (Discovery CT750 HD, GE Healthcare, United States) was used to perform CTA of the head and neck. A 50-ml dose of non-ionic contrast agent was injected into the median cubital vein in the forearm of the patient using a high-pressure syringe at a rate of 4 ml/s. The scanning was performed in the caudocranial direction, from the aortic arch to the top of the skull.

Carotid Doppler Ultrasound Examination

A GE Logic E9 ultrasound machine (GE Healthcare, United States) with a 9L linear array probe at a frequency of 8–9 MHz was used for the CDU examinations. Bilateral common carotid, internal carotid, external carotid, and vertebral and subclavian arteries were measured conventionally by one experienced doctor who was blind to the clinical status of the subjects. The measurements of extracranial artery flow velocity were performed at the same location for each subject. The inner diameter, peak systolic velocity (PSV), end diastolic velocity (EDV), and vascular resistive index of the extracranial internal carotid and vertebral arteries were measured twice and average values were recorded.

Evaluation of Intracranial Perfusion

The raw eASL data were post-processed using CereFlow software to generate ATT and mCBF maps of the whole brain. Based on a vessel territory atlas, the ATT and mCBF maps of the bilateral frontal lobes, parietal lobes, insula, occipital lobes, and cerebellum were generated automatically for statistical analysis.

Statistical Analysis

Statistical analysis was performed using SPSS 25.0 software. A p-value < 0.05 was considered statistically significant. The continuous variables in this study followed a normal distribution and homogeneity of variance. The independent samples t-test was used to analyze and compare the mCBF and ATT of the anterior circulation (bilateral frontal lobes, parietal lobes, and insula) and posterior circulation (occipital lobes and cerebellum) between the patient and control groups. Pearson correlation analysis was used to evaluate the relationship between ATT and mCBF in the two groups. Differences in the blood flow velocity of the extracranial internal carotid/vertebral arteries between the two groups were compared using independent samples t-tests. Using PSV, EDV, and ATT as independent

factors, multiple linear regression analysis was then applied to analyze the factors affecting the mCBF of the ROIs in the two groups. Because the posterior circulation is supplied by the basilar artery formed by the confluence of the bilateral vertebral arteries, the bilateral PSV, EDV, ATT, and mCBF values of the occipital lobes and cerebellum were averaged for the regression analysis.

RESULTS

Comparison of Cerebral Perfusion Parameters Between the Study and Control Groups

Compared with those in the control group, the mCBF measurements in the anterior circulation (bilateral frontal lobes, parietal lobes, and insula) and posterior circulation (bilateral occipital lobes and cerebellum) were all significantly lower in the patient group. The ATTs of the ROIs were significantly longer in the patient group than in the control group (**Table 1** and **Figures 1–3**). There were also statistically significant differences in the blood flow velocity of the extracranial internal carotid/vertebral arteries between the control and patient groups ($p < 0.05$) (**Table 2**).

Correlation of Arterial Transit Time and Mean Cerebral Blood Flow

Taking the bilateral perfusion data as a whole, significant negative correlations between ATT and mCBF were found in the frontal lobes, parietal lobes, insula, occipital lobes, and cerebellum in the patient group ($r = -0.386$, $p = 0.002$; $r = -0.386$, $p = 0.002$; $r = -0.267$, $p = 0.033$; $r = -0.573$, $p < 0.001$; $r = -0.489$, $p < 0.001$, respectively).

Significant correlations between ATT and mCBF were also demonstrated in the control group, except for the insula, where the correlation did not quite reach significance ($r = -0.239$, $p = 0.057$).

Results of the Multiple Linear Regression Analysis

There was a relationship between ATT and mCBF in the ROIs of the frontal lobes and parietal lobes in the controls, and a significant but weak effect of PSV on mCBF in the insula ($\beta = 0.093$, $p = 0.013$), but no effect of extracranial flow velocity was observed in the posterior circulation (**Table 3**). No significant correlations with factors that could possibly affect mCBF in the ROIs of the anterior circulation (frontal lobes, parietal lobes, and insula) were found in the patients with ICAS ($p > 0.05$) (**Table 4**). For the posterior circulation, the mean PSV of the vertebral arteries and ATT of the cerebellum showed a relationship with mCBF of the cerebellum ($\beta = 0.397$, $p = 0.042$; $\beta = -0.528$, $p = 0.002$, respectively). In addition, the mCBF of the occipital lobes correlated with ATT and mean PSV of the vertebral arteries ($\beta = 0.468$, $p = 0.014$; $\beta = -0.632$, $p < 0.001$, respectively) (**Table 4**).

TABLE 1 | Comparison of the mCBF and ATT of all parts between the study and control groups.

Variables	Study group ($n = 32$)	Control group ($n = 32$)	p-value
Left frontal lobe mCBF (ml/100 g/min)	29.7775 ± 8.2272	40.2331 ± 5.6562	<0.001
Right frontal lobe mCBF (ml/100 g/min)	29.8481 ± 7.6619	39.0094 ± 5.6092	<0.001
Left parietal lobe mCBF (ml/100 g/min)	27.9381 ± 9.1233	39.7225 ± 5.8357	<0.001
Right parietal lobe mCBF (ml/100 g/min)	27.3203 ± 7.7837	37.7647 ± 5.8109	<0.001
Left insula mCBF (ml/100 g/min)	31.6787 ± 9.9949	39.2906 ± 4.9793	<0.001
Right insula mCBF (ml/100 g/min)	30.8713 ± 8.9645	39.9406 ± 5.8151	<0.001
Left occipital lobe mCBF (ml/100 g/min)	29.2641 ± 10.1001	39.9081 ± 7.8628	<0.001
Right occipital lobe mCBF (ml/100 g/min)	27.9938 ± 8.5938	39.0856 ± 6.5587	<0.001
Left cerebellum mCBF (ml/100 g/min)	27.4838 ± 8.8289	36.3209 ± 7.9350	<0.001
Right cerebellum mCBF (ml/100 g/min)	27.2756 ± 8.8254	36.2350 ± 7.4646	<0.001
Left frontal lobe ATT (s)	1.7400 ± 0.1471	1.6328 ± 0.0927	<0.001
Right frontal lobe ATT (s)	1.7747 ± 0.1438	1.6247 ± 0.1080	<0.001
Left parietal lobe ATT (s)	1.8112 ± 0.1596	1.6731 ± 0.1068	<0.001
Right parietal lobe ATT (s)	1.8000 ± 0.1717	1.6763 ± 0.1318	<0.001
Left insula ATT (s)	1.6700 ± 0.1204	1.5906 ± 0.1016	<0.001
Right insula ATT (s)	1.6650 ± 0.1429	1.5794 ± 0.0583	<0.001
Left occipital lobe ATT (s)	1.8569 ± 0.1391	1.6850 ± 0.1529	<0.001
Right occipital lobe ATT (s)	1.8509 ± 0.1477	1.6888 ± 0.1311	<0.001
Left cerebellum ATT (s)	1.7966 ± 0.1311	1.6591 ± 0.1471	<0.001
Right cerebellum ATT (s)	1.8278 ± 0.1267	1.6906 ± 0.1325	<0.001

ATT, arterial transit time; mCBF, mean cerebral blood flow; s, seconds.

DISCUSSION

In this study, we used eASL imaging technology to analyze the perfusion state of the anterior and posterior circulations in patients with ICAS and healthy people, and investigated the relationship between ATT and mCBF in the subjects. We found that in patients with ICAS, the mCBF values of both the anterior circulation and posterior circulation were significantly lower than those of normal healthy people. Furthermore, the ATTs of the patients with ICAS were longer than those of healthy people, which is consistent with the results of previous research (Li et al., 2016; Xu et al., 2016). Stenosis of cerebral arteries caused by ICAS can result in extensive changes in cerebral blood flow distribution, which are closely related to the structure of vessel walls and the hemodynamics across the stenosis (Sangha et al., 2017; Kleindorfer et al., 2021).

We showed significant correlations between ATT and mCBF in ROIs placed in the anterior and posterior circulations in patients with ICAS, as well as in controls. As the mCBF value decreased, the ATT increased. The ATT is a measure of the time taken for the labeled spins to reach the brain tissue of an

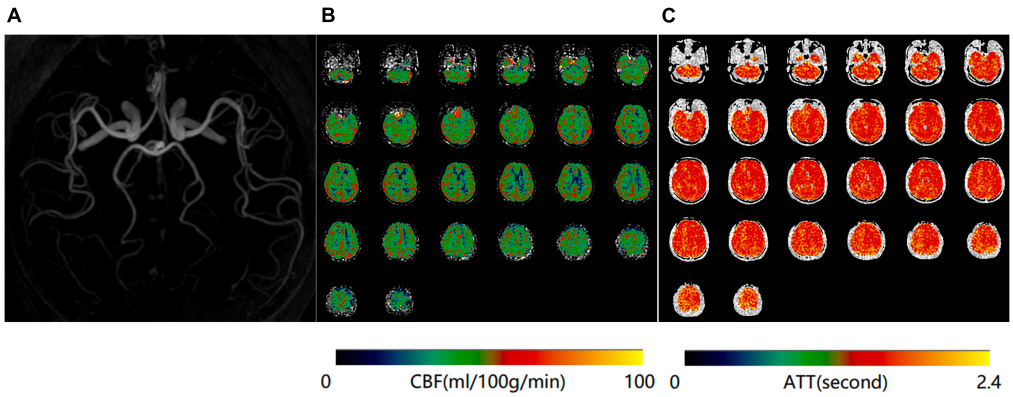

FIGURE 1 | Normal magnetic resonance angiography (MRA) **(A)**, mean cerebral blood flow (mCBF) **(B)**, and arterial transit time (ATT) **(C)** maps of a 65-year-old woman in the control group.

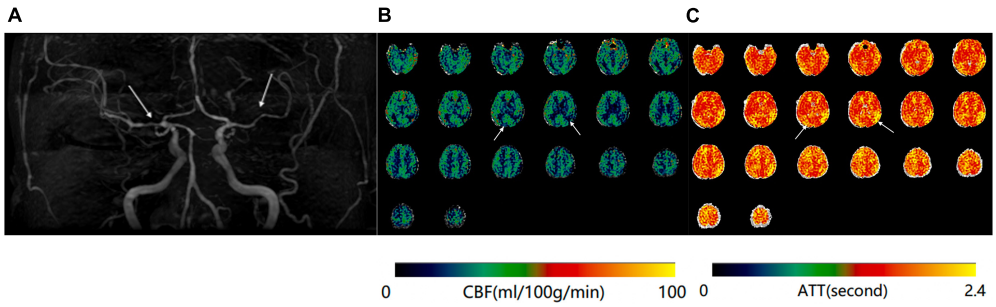

FIGURE 2 | (A) Magnetic resonance angiography (MRA) of a 68-year-old woman shows moderate stenosis of bilateral middle cerebral arteries. **(B)** Mean cerebral blood flow (mCBF) demonstrates decreased blood perfusion in bilateral temporal and parietal lobes. **(C)** Prolongation of arterial transit time (ATT) is demonstrated at the same anatomical regions on the ATT map.

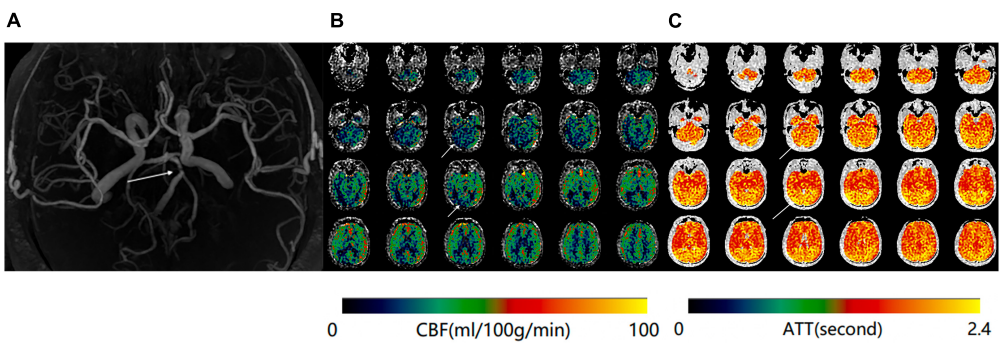

FIGURE 3 | (A) Magnetic resonance angiography (MRA) of a 70-year-old man shows severe stenosis of the basilar artery. **(B)** Maps of mean cerebral blood flow (mCBF) demonstrate markedly decreased blood flow in the bilateral occipital lobes and cerebellum. **(C)** Arterial transit time (ATT) maps shows increased signal at the same anatomical regions.

ROI, and therefore reflects both the arterial flow and intracranial arteriole flow. Because blood flow in the large arteries is very fast and takes little time to flow into the brain, most of the ATT can be attributed to the intracranial arteriole component. Some studies demonstrated the agreement of ATT and MTT in patients with vascular stenosis (Wang et al., 2003; Xu et al., 2021), and previous research suggested a feedback mechanism between the transit time and CBF to maintain stable cerebral perfusion (Haller et al., 2016; Mutsaerts et al., 2017; Cohen et al., 2020). The relationship between ATT and CBF in patients with ICAS is of great importance, especially in the posterior circulation (Jia et al., 2017; Sparaco et al., 2019). Compared with that in the arteries of the anterior circulation, the blood flow velocity in the vessels of the posterior circulation is lower, producing abnormal wall

TABLE 2 | Comparison of the blood flow velocity of the extracranial internal carotid and vertebral arteries between the study and control groups.

Variables	Study group (n = 32)	Control group (n = 32)	p-value
PSV-LICA (cm/s)	61.5625 ± 16.2360	75.5938 ± 18.1745	0.002
EDV-LICA (cm/s)	25.1562 ± 9.2007	30.2500 ± 9.1087	0.030
PSV-RICA (cm/s)	67.7500 ± 21.6661	82.8750 ± 19.4932	0.005
EDV-RICA (cm/s)	23.6250 ± 7.4042	31.0312 ± 9.6067	< 0.001
mPSV-VA (cm/s)	45.9531 ± 8.8976	50.9062 ± 8.5388	0.027
mEDV-VA (cm/s)	14.5625 ± 3.6781	16.7656 ± 4.2445	0.030

PSV, peak systolic velocity; EDV, end-diastolic velocity; mPSV, mean peak systolic velocity; mEDV, mean end-diastolic velocity; LICA, left lateral internal carotid artery; RICA, right lateral internal carotid artery; VA, vertebral artery.

TABLE 3 | Results from multiple linear regression of the extracranial artery flow velocity, ATT on CBF in the anterior and posterior circulations of the control group.

Dependent variable	Independent variable	*B* coefficient	p-value
Frontal lobe mCBF	PSV-ICA	0.065 (−0.012, 0.142)	0.095
	EDV-ICA	−0.074 (−0.083, 0.232)	0.348
	Frontal lobe ATT	−14.371 (−27.736, −1.005)	0.036
Parietal lobe mCBF	PSV-ICA	0.025 (−0.058, 0.107)	0.555
	EDV-ICA	0.105 (−0.061, 0.271)	0.21
	Parietal lobe ATT	−14.230 (−26.347, −2.112)	0.022
Insula mCBF	PSV-ICA	0.093 (0.020, 0.166)	0.013
	EDV-ICA	0.055 (−0.098, 0.208)	0.476
	Insula ATT	−9.059 (−25.012, 6.894)	0.261
Occipital lobe mCBF	mPSA-VA	0.029 (−0.279, 0.337)	0.85
	mEDV-VA	0.686 (−0.079, 1.452)	0.077
	Occipital lobe mATT	−15.104 (−32.847, 2.640)	0.092
Cerebellum mCBF	mPSV-VA	0.001 (−0.344, 0.346)	0.995
	mEDV-VA	0.733 (−0.103, 1.569)	0.083
	Cerebellum mATT	−16.496 (−36.053, 3.061)	0.095

ATT, arterial transit time; mPSV, mean peak systolic velocity; mEDV, mean end-diastolic velocity; mCBF, mean cerebral blood flow; PSV, peak systolic velocity; EDV, end-diastolic velocity; VA, vertebral artery; ICA, internal carotid artery.

TABLE 4 | Results from multiple linear regression of the extracranial artery flow velocity, ATT on CBF in the anterior and posterior circulations of the study group.

Dependent variable	Independent variable	*B* coefficient	p-value
Frontal lobe mCBF	PSV-ICA	0.131 (−0.017, 0.279)	0.081
	EDV-ICA	−0.053 (−0.485, 0.379)	0.807
	Frontal lobe ATT	−12.668 (−28.260, 2.924)	0.109
Parietal lobe mCBF	PSV-ICA	0.130 (−0.022, 0.282)	0.092
	EDV-ICA	0.097 (−0.337, 0.531)	0.656
	Parietal lobe ATT	−9.180 (−22.538, 4.178)	0.174
Insula mCBF	PSV-ICA	0.174 (−0.010, 0.359)	0.063
	EDV-ICA	−0.108 (−0.638, 0.421)	0.683
	Insula ATT	−11.253 (−31.067, 8.560)	0.260
Occipital lobe mCBF	mPSA-VA	0.423 (0.092, 0.754)	0.014
	mEDV-VA	−0.237 (−1.130, 0.657)	0.591
	Occipital lobe mATT	−42.319 (−63.169, −21.469)	<0.001
Cerebellum mCBF	mPSV-VA	0.334 (0.013, 0.655)	0.042
	mEDV-VA	−0.076 (−0.916, 0.764)	0.855
	Cerebellum mATT	−38.432 (−61.545, −15.318)	0.002

ATT, arterial transit time; mPSV, mean peak systolic velocity; mEDV, mean end-diastolic velocity; mCBF, mean cerebral blood flow; PSV, peak systolic velocity; EDV, end-diastolic velocity; VA, vertebral artery; ICA, internal carotid artery.

shear stress, which is a risk factor for thrombosis (Caplan, 2000; Eker et al., 2019). At the same time, atherosclerosis can lead to artery stenosis and occlusion, which slows down blood flow and results in a low perfusion state (Ya et al., 2020). In this situation, compensatory elongation of ATT will help to maintain local perfusion in a steady state. The adjustment of ATT may reflect slow collateral flow compensating for a disrupted blood supply through one of the proximal arteries (van Osch et al., 2018).

In addition to eASL, we used color Doppler ultrasound to examine the extracranial carotid/vertebral arteries and measure their blood flow velocity. Although our patients had no severe stenosis or occlusion of the extracranial carotid and vertebral arteries, there were significant differences in the blood flow velocity of the extracranial carotid and vertebral arteries between the controls and patients. In the patients with ICAS, the mean PSV of the vertebral arteries and local ATT demonstrated a significant association on the mCBF of the occipital lobes and cerebellum, but this phenomenon was not observed in the controls. We suggest that mCBF of the posterior circulation in patients with ICAS is sensitive to the change in the upstream blood supply. Under normal physiological conditions, intracranial hemodynamic mechanisms can well-adjust to pressure and blood flow changes from the extracranial internal carotid and vertebral arteries (McBryde et al., 2017). In contrast, patients with ICAS seem to have a declined ability to cope with the reduced blood inflow, suggesting a vulnerability to the decrease in perfusion (Nixon et al., 2010). We note that the association of the extracranial flow on the mCBF in patients with ICAS was demonstrated exclusively in the posterior circulation. This may be because posterior circulation vessels such as the basilar artery have less sympathetic nerve innervation, which leads to poor vascular regulation (Tissir and Goffinet, 2013). Our study supports the idea that maintenance of extracranial blood flow is of great significance in the preservation of intracranial hemodynamics, especially those of the posterior circulation.

Previous studies mostly used arterial spin labeling technology with a single PLD or three PLDs, but the mismatch between PLD and ATT among individuals is the main reason for inaccurate measurement of CBF (MacIntosh et al., 2010). In this study, eASL based on Hadamard matrix time coding was applied, and the total labeling time was divided into seven short labeling time blocks, which significantly shortened the total time for collecting multiple PLDs and allowed ATT and mCBF to be obtained at the same time (Dai et al., 2013). This sequence also facilitated quick measurement of ATT by low-resolution time coding technology, and choosing of a reasonable PLD based on this known ATT, thereby allowing a more accurate mCBF measurement to be obtained (Teeuwisse et al., 2014; von Samson-Himmelstjerna et al., 2016). CBF measurements using pCASL

with multiple post-label delay acquisitions correlated well with quantitative CBF values derived from ^{15}O-H_2O PET in patients with chronic occlusive cerebrovascular disease (Kamano et al., 2013). The disadvantages of eASL lie in the longer scanning time and low signal-to-noise ratio due to the short label durations (Haller et al., 2016). Optimization of the number of post-label delay acquisitions and excitations to reduce the acquisition time with a sparse model-based image reconstruction (Tsujikawa et al., 2016), and/or use of more complex but efficient Hadamard time-encoding strategies (Amemiya et al., 2021), will be needed to establish guidelines for routine use in future clinical applications.

There are several limitations to this study. First, not all brain regions were included in the analysis, because some brain regions like the thalamus and temporal lobes are supplied by both the anterior and posterior circulation, which may cause confusion when analyzing the perfusion state. Second, the relationship between the stenoses and eASL parameters was not studied. Because some patients had extensive intracranial atherosclerotic lesions, we could not simply classify the vessel territories according to the stenosis of arteries. Sometimes, a vessel territory with a relatively mild stenosis may be ischemic because of the intracerebral steal phenomenon. Third, the CDU examinations were conducted by only one experienced doctor who was blind to the clinical status of the subjects, and we therefore had no measure of the reliability of the ultrasonographic measurements. Finally, the sample size of this study was small, and the influences of age, blood pressure, and vessel diameter on the blood flow of the cervical and vertebral arteries were not analyzed.

Overall, we used eASL to demonstrate changes in ATT and mCBF in patients with ICAS. We found that ATT correlated with mCBF in the healthy controls, as well as in the patients. Furthermore, we found that extracranial blood flow may influence intracranial hemodynamics in the posterior circulation of the patients, indicating the importance of the maintenance of upstream blood flow.

DATA AVAILABILITY STATEMENT

The raw data supporting the conclusions of this article will be made available by the authors, without undue reservation.

ETHICS STATEMENT

The studies involving human participants were reviewed and approved by the Institutional Review Boards of China-Japan Friendship Hospital (approval number: 2015-23). The patients/participants provided their written informed consent to participate in this study. Written informed consent was obtained from the individual(s) for the publication of any potentially identifiable images or data included in this article.

AUTHOR CONTRIBUTIONS

HY acquired, analyzed, and interpreted the eASL data, and drafted the manuscript. YL conducted the statistical analysis. LZ and ZL acquired the clinical information. ZY assisted with the ASL data analysis. YF analyzed and interpreted the head and neck carotid Doppler ultrasound data. WG and YC acquired the MRA data. SX designed the study and revised the manuscript. All authors contributed to the article and approved the submitted version.

REFERENCES

Amemiya, S., Watanabe, Y., Takei, N., Ueyama, T., Miyawaki, S., Koizumi, S., et al. (2021). Arterial transit time-based multidelay combination strategy improves arterial spin labeling cerebral blood flow measurement accuracy in severe steno-occlusive diseases. *J. Magn. Reson. Imaging* 55, 178–187. doi: 10.1002/jmri.27823

Caplan, L. (2000). Posterior circulation ischemia: then, now, and tomorrow. The Thomas Willis Lecture-2000. *Stroke* 31, 2011–2023. doi: 10.1161/01.str.31.8.2011

Cheng, X.-Q., Tian, J.-M., Zuo, C.-J., Liu, J., Zhang, Q., and Lu, G.-M. (2012). Quantitative perfusion computed tomography measurements of cerebral hemodynamics: correlation with digital subtraction angiography identified primary and secondary cerebral collaterals in internal carotid artery occlusive disease. *Eur. J. Radiol.* 81, 1224–1230. doi: 10.1016/j.ejrad.2011.02.046

Cohen, A. D., Agarwal, M., Jagra, A. S., Nencka, A. S., Meier, T. B., Lebel, R. M., et al. (2020). Longitudinal reproducibility of MR perfusion using 3D pseudocontinuous arterial spin labeling with hadamard-encoded multiple postlabeling delays. *J. Magn. Reson. Imaging* 51, 1846–1853. doi: 10.1002/jmri.27007

Dai, W., Shankaranarayanan, A., and Alsop, D. C. (2013). Volumetric measurement of perfusion and arterial transit delay using hadamard encoded continuous arterial spin labeling. *Magn. Reson. Med.* 69, 1014–1022. doi: 10.1002/mrm.24335

Detre, J. A., and Alsop, D. C. (1999). Perfusion magnetic resonance imaging with continuous arterial spin labeling: methods and clinical applications in the central nervous system. *Eur. J. Radiol.* 30, 115–124. doi: 10.1016/s0720-048x(99)00050-9

Eker, O. F., Ameli, R., Makris, N., Jurkovic, T., Montigon, O., Barbier, E. L., et al. (2019). MRI assessment of oxygen metabolism and hemodynamic status in symptomatic intracranial atherosclerotic stenosis: a pilot study. *J. Neuroimaging* 29, 467–475. doi: 10.1111/jon.12615

Ferré, J. C., Bannier, E., Raoult, H., Mineur, G., Carsin-Nicol, B., and Gauvrit, J. Y. (2013). Arterial spin labeling (ASL) perfusion: techniques and clinical use. *Diagn. Interv. Imaging* 94, 1211–1223. doi: 10.1016/j.diii.2013.06.010

Haller, S., Zaharchuk, G., Thomas, D. L., Lovblad, K.-O., Barkhof, F., and Golay, X. (2016). Arterial spin labeling perfusion of the brain: emerging clinical applications. *Radiology* 281, 337–356. doi: 10.1148/radiol.2016150789

Jia, R., Xu, X., Liu, X., Wu, B., Men, W., and An, N. (2017). Value of 3D pseudo-continuous arterial spin labeling magnetic resonance perfusion imaging in evaluating posterior circulation ischemia in the elderly. *Zhongguo Yi Xue Ke Xue Yuan Xue Bao* 39, 272–279. doi: 10.3881/j.issn.1000-503X.2017.02.018

Kamano, H., Yoshiura, T., Hiwatashi, A., Abe, K., Togao, O., Yamashita, K., et al. (2013). Arterial spin labeling in patients with chronic cerebral artery steno-occlusive disease: correlation with (15)O-PET. *Acta Radiol.* 54, 99–106. doi: 10.1258/ar.2012.120450

Kang, K. H., Kim, H. S., and Kim, S. Y. (2008). Quantitative cerebrovascular reserve measured by acetazolamide-challenged dynamic CT perfusion in ischemic adult Moyamoya disease: initial experience with angiographic correlation. *AJNR Am. J. Neuroradiol.* 29, 1487–1493. doi: 10.3174/ajnr.A1129

Kleindorfer, D. O., Towfighi, A., Chaturvedi, S., Cockroft, K. M., Gutierrez, J., Lombardi-Hill, D., et al. (2021). 0.2021 guideline for the prevention of stroke in patients with stroke and transient ischemic attack: a guideline from the

American Heart Association/American Stroke Association. *Stroke* 52, e364–e467. doi: 10.1161/STR.0000000000000375

Leng, X., Lan, L., Ip, H. L., Abrigo, J., Scalzo, F., Liu, H., et al. (2019). Hemodynamics and stroke risk in intracranial atherosclerotic disease. *Ann. Neurol.* 85, 752–764. doi: 10.1002/ana.25456

Li, Z., Li, N., Qu, Y., Gai, F., Zhang, G., and Zhang, G. (2016). Application of 3.0T magnetic resonance arterial spin labeling (ASL) technology in mild and moderate intracranial atherosclerotic stenosis. *Exp. Ther. Med.* 12, 297–301. doi: 10.3892/etm.2016.3318

MacIntosh, B. J., Lindsay, A. C., Kylintireas, I., Kuker, W., Günther, M., Robson, M. D., et al. (2010). Multiple inflow pulsed arterial spin-labeling reveals delays in the arterial arrival time in minor stroke and transient ischemic attack. *AJNR Am. J. Neuroradiol.* 31, 1892–1894. doi: 10.3174/ajnr.A2008

McBryde, F. D., Malpas, S. C., and Paton, J. F. R. (2017). Intracranial mechanisms for preserving brain blood flow in health and disease. *Acta Physiol.* 219, 274–287. doi: 10.1111/apha.12706

Mutsaerts, H. J., Petr, J., Václavů, L., van Dalen, J. W., Robertson, A. D., Caan, M. W., et al. (2017). The spatial coefficient of variation in arterial spin labeling cerebral blood flow images. *J. Cereb. Blood Flow Metab.* 37, 3184–3192. doi: 10.1177/0271678X16683690

Nixon, A. M., Gunel, M., and Sumpio, B. E. (2010). The critical role of hemodynamics in the development of cerebral vascular disease. *J. Neurosurg.* 112, 1240–1253. doi: 10.3171/2009.10.JNS09759

Ravindra, V. M., Kralik, S. F., Griauzde, J., Gadgil, N., LoPresti, M. A., and Lam, S. (2020). Preoperative computed tomography perfusion in pediatric moyamoya disease: a single-institution experience. *J. Neurosurg. Pediatr.* 24, 1–8. doi: 10.3171/2019.10.PEDS19450

Sangha, R. S., Naidech, A. M., Corado, C., Ansari, S. A., and Prabhakaran, S. (2017). Challenges in the medical management of symptomatic intracranial stenosis in an urban setting. *Stroke* 48, 2158–2163. doi: 10.1161/STROKEAHA.116.016254

Sparaco, M., Ciolli, L., and Zini, A. (2019). Posterior circulation ischemic stroke-a review part II: imaging and acute treatment. *Neurol. Sci.* 40, 2007–2015. doi: 10.1007/s10072-019-03936-x

Teeuwisse, W. M., Schmid, S., Ghariq, E., Veer, I. M., and van Osch, M. J. P. (2014). Time-encoded pseudocontinuous arterial spin labeling: basic properties and timing strategies for human applications. *Magn. Reson. Med.* 72, 1712–1722. doi: 10.1002/mrm.25083

Tissir, F., and Goffinet, A. M. (2013). Shaping the nervous system: role of the core planar cell polarity genes. *Nat. Rev. Neurosci.* 14, 525–535. doi: 10.1038/nrn3525

Tsujikawa, T., Kimura, H., Matsuda, T., Fujiwara, Y., Isozaki, M., Kikuta, K.-I., et al. (2016). Arterial transit time mapping obtained by pulsed continuous 3D ASL imaging with multiple post-label delay acquisitions: comparative study with PET-CBF in patients with chronic occlusive cerebrovascular disease. *PLoS One* 11:e0156005. doi: 10.1371/journal.pone.0156005

van der Thiel, M., Rodriguez, C., Giannakopoulos, P., Burke, M. X., Lebel, R. M., Gninenko, N., et al. (2018). Brain perfusion measurements using multidelay arterial spin-labeling are systematically biased by the number of delays. *AJNR Am. J. Neuroradiol.* 39, 1432–1438. doi: 10.3174/ajnr.A5717

van Osch, M. J., Teeuwisse, W. M., Chen, Z., Suzuki, Y., Helle, M., and Schmid, S. (2018). Advances in arterial spin labelling MRI methods for measuring perfusion and collateral flow. *J. Cereb. Blood Flow Metab.* 38, 1461–1480. doi: 10.1177/0271678X17713434

von Samson-Himmelstjerna, F., Madai, V. I., Sobesky, J., and Guenther, M. (2016). Walsh-ordered hadamard time-encoded pseudocontinuous ASL (WH pCASL). *Magn. Reson. Med.* 76, 1814–1824. doi: 10.1002/mrm.26078

Wang, D. J. J., Alger, J. R., Qiao, J. X., Gunther, M., Pope, W. B., Saver, J. L., et al. (2013). Multi-delay multi-parametric arterial spin-labeled perfusion MRI in acute ischemic stroke - Comparison with dynamic susceptibility contrast enhanced perfusion imaging. *Neuroimage Clin.* 3, 1–7. doi: 10.1016/j.nicl.2013.06.017

Wang, J., Alsop, D. C., Song, H. K., Maldjian, J. A., Tang, K., Salvucci, A. E., et al. (2003). Arterial transit time imaging with flow encoding arterial spin tagging (FEAST). *Magn. Reson. Med.* 50, 599–607. doi: 10.1002/mrm.10559

Wang, R., Yu, S., Alger, J. R., Zuo, Z., Chen, J., Wang, R., et al. (2014). Multi-delay arterial spin labeling perfusion MRI in moyamoya disease–comparison with CT perfusion imaging. *Eur. Radiol.* 24, 1135–1144. doi: 10.1007/s00330-014-3098-9

Wang, Y., Zhao, X., Liu, L., Soo, Y. O. Y., Pu, Y., Pan, Y., et al. (2014). Prevalence and outcomes of symptomatic intracranial large artery stenoses and occlusions in China: the Chinese Intracranial Atherosclerosis (CICAS) Study. *Stroke* 45, 663–669. doi: 10.1161/STROKEAHA.113.003508

Wells, J. A., Lythgoe, M. F., Gadian, D. G., Ordidge, R. J., and Thomas, D. L. (2010). In vivo hadamard encoded continuous arterial spin labeling (H-CASL). *Magn. Reson. Med.* 63, 1111–1118. doi: 10.1002/mrm.22266

Xu, X., Tan, Z., Fan, M., Ma, M., Fang, W., Liang, J., et al. (2021). Comparative study of multi-delay pseudo-continuous arterial spin labeling perfusion MRI and CT perfusion in ischemic stroke disease. *Front. Neuroinform.* 15:719719. doi: 10.3389/fninf.2021.719719

Xu, Y., Lü, J.-H., Ma, L., Chen, W.-J., and Lou, X. (2016). Quantitative measurement of cerebral blood flow in enhanced psedo-continuous arterial spin labeling perfusion imaging in patients with intracranial atherosclerotic stenosis. *Zhongguo Yi Xue Ke Xue Yuan Xue Bao* 38, 679–685. doi: 10.3881/j.issn.1000-503X.2016.06.009

Ya, J., Zhou, D., Ding, J., Ding, Y., Ji, X., Yang, Q., et al. (2020). High-resolution combined arterial spin labeling MR for identifying cerebral arterial stenosis induced by moyamoya disease or atherosclerosis. *Ann. Transl. Med.* 8:87. doi: 10.21037/atm.2019.12.140

Zaharchuk, G. (2007). Theoretical basis of hemodynamic MR imaging techniques to measure cerebral blood volume, cerebral blood flow, and permeability. *AJNR Am. J. Neuroradiol.* 28, 1850–1858. doi: 10.3174/ajnr.A0831

Zaharchuk, G., Olivot, J.-M., Fischbein, N. J., Bammer, R., Straka, M., Kleinman, J. T., et al. (2012). Arterial spin labeling imaging findings in transient ischemic attack patients: comparison with diffusion- and bolus perfusion-weighted imaging. *Cerebrovasc. Dis.* 34, 221–228. doi: 10.1159/000339682

Conflict of Interest: ZY was an employee of AnImageTech, who assisted with the ASL data analysis.

The remaining authors declare that the research was conducted in the absence of any commercial or financial relationships that could be construed as a potential conflict of interest.

Publisher's Note: All claims expressed in this article are solely those of the authors and do not necessarily represent those of their affiliated organizations, or those of the publisher, the editors and the reviewers. Any product that may be evaluated in this article, or claim that may be made by its manufacturer, is not guaranteed or endorsed by the publisher.

Copyright © 2022 Yu, Li, Feng, Zhang, Yao, Liu, Gao, Chen and Xie. This is an open-access article distributed under the terms of the Creative Commons Attribution License (CC BY). The use, distribution or reproduction in other forums is permitted, provided the original author(s) and the copyright owner(s) are credited and that the original publication in this journal is cited, in accordance with accepted academic practice. No use, distribution or reproduction is permitted which does not comply with these terms.

frontiers in Neuroscience

ORIGINAL RESEARCH
published: 24 February 2022
doi: 10.3389/fnins.2022.812997

Differentiation of Neoplastic and Non-neoplastic Intracranial Enhancement Lesions Using Three-Dimensional Pseudo-Continuous Arterial Spin Labeling

Wen-zhong Hu[1,2†], Fan Guo[2†], Yong-qiang Xu[2†], Yi-bin Xi[1], Bei He[1], Hong Yin[1,2] and Xiao-wei Kang[1*]*

[1] Department of Radiology, Xi'an People's Hospital, Xi'an Fourth Hospital, Xi'an, China, [2] Department of Radiology, Xijing Hospital, The Fourth Military Medical University, Xi'an, China

OPEN ACCESS

Edited by:
Guolin Ma,
China-Japan Friendship Hospital, China

Reviewed by:
Xuntao Yin,
Army Medical University, China
Danny J. J. Wang,
University of Southern California, United States
Chunmei Li,
Chinese Academy of Medical Sciences, China

***Correspondence:**
Hong Yin
yinnhong@163.com
Xiao-wei Kang
kangxiaowei881123@126.com

[†] These authors have contributed equally to this work

Specialty section:
This article was submitted to Brain Imaging Methods, a section of the journal Frontiers in Neuroscience

Received: 11 November 2021
Accepted: 17 January 2022
Published: 24 February 2022

Citation:
Hu W-z, Guo F, Xu Y-q, Xi Y-b, He B, Yin H and Kang X-w (2022) Differentiation of Neoplastic and Non-neoplastic Intracranial Enhancement Lesions Using Three-Dimensional Pseudo-Continuous Arterial Spin Labeling. Front. Neurosci. 16:812997. doi: 10.3389/fnins.2022.812997

Background and Purpose: It is sometimes difficult to effectively distinguish non-neoplastic from neoplastic intracranial enhancement lesions using conventional magnetic resonance imaging (MRI). This study aimed to evaluate the diagnostic performance of three-dimensional pseudo-continuous arterial spin labeling (3D-pCASL) to differentiate non-neoplastic from neoplastic enhancement lesions intracranially.

Materials and Methods: This prospective study included thirty-five patients with high-grade gliomas (HGG), twelve patients with brain metastasis, and fifteen non-neoplastic patients who underwent conventional, contrast enhancement and 3D-pCASL imaging at 3.0-T MR; all lesions were significantly enhanced. Quantitative parameters including cerebral blood flow (CBF) and relative cerebral blood flow (rCBF) were compared between neoplastic and non-neoplastic using Student's *t*-test. In addition, the area under the receiver operating characteristic (ROC) curve (AUC) was measured to assess the differentiation diagnostic performance of each parameter.

Results: The non-neoplastic group demonstrated significantly lower rCBF values of lesions and perilesional edema compared with the neoplastic group. For the ROC analysis, both relative cerebral blood flow of lesion (rCBF-L) and relative cerebral blood flow of perilesional edema (rCBF-PE) had good diagnostic performance for discriminating non-neoplastic from neoplastic lesions, with an AUC of 0.994 and 0.846, respectively.

Conclusion: 3D-pCASL may contribute to differentiation of non-neoplastic from neoplastic lesions.

Keywords: three-dimensional pseudo-continuous arterial spin labeling, non-neoplastic, high-grade gliomas, metastasis, cerebral blood flow

INTRODUCTION

The incidence of brain and central nervous system tumors has been increasing in recent years. There are about 308,000 new cases of brain tumors worldwide until 2020. The morbidity rates of men and women are 3.9% and 3.0%, respectively, and the mortality rates are 3.2% and 2.4%, respectively (Sung et al., 2021). Conventional MRI has a good value in differentiating diagnosis by assessing the shape, location, and mass effect of lesions (Villanueva-Meyer et al., 2017). Sometimes, conventional MRI of many intracranial non-neoplastic diseases, such as brain abscess, tuberculosis, and cerebral cysticercosis, mimics cerebral high-grade glioma, which could all manifest as space-occupying lesions with cystic, necrosis, and ring enhancement (Omuro et al., 2006). However, the treatment strategies and prognosis of non-neoplastic and neoplastic are completely different, so how to accurately differentiate those two kinds of diseases is quite important (Bush et al., 2017).

Considering the limitations of conventional MRI, a growing number of studies have focused on assessing the physiological and metabolic characteristics of lesions, especially on tumors (Ko et al., 2016). Arterial spin labeling (ASL) is an emerging MRI perfusion technology that uses magnetically labeled arterial blood water protons as an endogenous tracer. ASL can quantitatively measure the relative cerebral blood flow (rCBF) in different lesions and evaluate the malignant degree of lesions from the level of microcirculation (Hernandez-Garcia et al., 2019). According to different labeling methods, ASL can be divided into three types: pulsed ASL (PASL), continuous ASL (CASL), and pseudo-continuous ASL (pCASL). pCASL has advantages including high signal-to-noise ratio, high labeling efficiency, minimal magnetization transfer effect, less radiofrequency energy deposition, low requirements for hardware equipment, and good repeatability (Wu et al., 2014; Alsop et al., 2015). 3D-pCASL is a more advanced technology that can improve the image signal-to-noise ratio further and reduce motion artifacts while achieving whole brain volume perfusion imaging.

Previous studies have proved that ASL is valuable in identifying and grading brain tumors (Haller et al., 2016; Abdel Razek et al., 2019b; Xi et al., 2019). As far as we know, there are few studies regarding using ASL to distinguish intracranial non-neoplastic from neoplastic lesions. In this retrospective study, we collected imaging data of patients with intracranial non-neoplastic and neoplastic lesions and analyzed the difference between them on ASL images. This study aimed to evaluate the additional value of ASL in distinguishing non-neoplastic from neoplastic lesions in intracranial, which manifest as ring-enhancement lesions.

MATERIALS AND METHODS

Subjects

This retrospective study was approved by the Institutional Review Board, and informed consent was obtained from all participants. From September 2015 to September 2020, MRI data of patients from our hospital were retrospectively reviewed. The inclusion criteria were as follows: (1) all patients were newly diagnosed, untreated patients; (2) all patients underwent conventional MRI including T1, T2, post-contrast T1 weighted imaging, and 3D-pCASL preoperatively; (3) all lesions showed obvious ring enhancement from the contrast MRI scanning; and (4) all patients were further confirmed by pathological or clinical examinations. The following were the exclusion criteria: (1) poor image quality, which affects the measurement results, and (2) those who had received therapy prior to MRI. Finally, 35 HGG (21 men, 14 women, mean age 52.9 years, range 12–79 years), 12 metastases (7 men, 5 women, mean age 57.3 years, range 42–77 years), and 15 non-neoplastic cases (9 men, 6 women, mean age 39 years, range 10–64 years) were enrolled. The non-neoplastic lesions contained the following: brain abscess (n = 7), tuberculoma (n = 3), granuloma (n = 3), cerebral cysticercosis, and demyelinating pseudotumor (n = 1). Among the 12 patients with brain metastases, the primary sites of tumors were lung cancer (n = 5), stomach cancer, osteosarcoma, cervical cancer, parotid gland cancer, colon cancer, rectal cancer, and adenocarcinoma (n = 1 each).

Magnetic Resonance Imaging Acquisition

In this experiment, a 3.0-T MR system (Discovery MR750, GE Healthcare, Milwaukee, WI, United States) with an 8-channel head-matrix coil was used. The head of the patient was fixed with a sponge cushion, and the patient was supine on the examination table. The scan sequences included the following: (1) axial T1WI [TR, 1,750 ms; TE, 24 ms; section thickness, 4 mm; inter-slice gap = 0 mm; field of view (FOV), 240 × 240 mm^2; matrix, 320 × 256]; (2) T2WI (TR, 3,976 ms; TE, 92 ms; section thickness, 5 mm; inter-slice gap = 1.5 mm; FOV, 240 × 240 mm^2; matrix size, 512 × 512); (3) fluid-attenuated inversion recovery (FLAIR) (TR, 8,400 ms; TE, 145 ms; section thickness, 5 mm; inter-slice gap = 1.5 mm; FOV, 240 × 240 mm^2; matrix size, 160 × 256); (4) post-contrast T1 was acquired after intravenous administration of 0.1 mmol/kg gadopentetate dimeglumine; (5) ASL was performed with pseudocontinuous labeling, background suppression, and a stack of spiral 3D fast spin-echo imaging sequences using the following acquisition parameters: 512 sampling points on eight spirals, TR = 4,632 ms; TE = 10.5 ms; matrix = 128 × 128; slice thickness = 4 mm, field of view (FOV) = 240 × 240 mm^2; scan time = 4 min 27 s; post-labeling delay = 1 m, 525 ms.

Image Processing and Analysis

The image data were transferred to an offline workstation for post-processing (Advantage Workstation, AW4.5; GE Medical Systems) provided by the supplier, and the CBF images were post-processed by GE FuncTool software. We used T1WI enhancement and FLAIR to define the localization of the lesions and perilesional edema, and then registered these images with 3D-pCASL images. Cerebral blood flow (CBF) values were measured by placing the regions of interest (ROI) above the lesion with the highest perfusion signal. CBF of the solid part of the lesion (CBF-L), CBF of the PLE (CBF-PLE) (within 1 cm from the

lesion), and CBF of contralateral normal gray matter (CBF-CGM) were measured, respectively. CBF-PLE was measured by placing the ROI above the highest perfusion signal seen in the perilesional edema on ASL map. Two experienced neuroradiologists who were blinded to the final diagnosis measured 3 times and then taken the average value. The necrosis, cystic change, hemorrhage, or blood vessel area that may affect the measurement were avoided. To minimize the inter-individual variation in CBF values, the rCBF values (rCBF-L, rCBF-PLE) were calculated by normalizing to the CBF-CGM.

Statistical Analysis

All data were processed by SPSS 23.0 software, and all values were expressed as mean ± standard deviation (SD). Interobserver agreement for the CBF values measured by the two observers was analyzed by calculating the intraclass correlation coefficient (ICC). ICCs greater than 0.74 were considered to be excellent (Yeganeh et al., 2019). Two observers averaged the measured values of each patient for further analysis. The comparison of measurement data that conform to the normal distribution used the independent sample *t*-test, and qualitative data used the chi-square test. The area under the curve (AUC) from receiver operating characteristic (ROC) analysis was used to evaluate the diagnostic performance of the ASL-determined rCBF for differentiating non-neoplastic from neoplastic lesions. p values < 0.05 were considered to be statistically significant.

RESULTS

Patient Demographics and Conventional Magnetic Resonance Imaging Features

The clinical and MRI characteristics of subjects are summarized in **Table 1**. There was no statistical difference in male-to-female ratio between the two groups. The age of the non-neoplastic group was younger than the neoplastic group with statistically significant difference. All intracranial lesions were exhibited as ring-like enhancement and accompanied with perilesional edema. The representative MRI of a patient with HGG, metastasis, and non-neoplastic lesions is shown in **Figure 1**.

TABLE 1 | Clinical and MRI characteristics of patients.

	Neoplastic (n = 47)	Non-neoplastic (n = 15)	p-values
Age (years)	54.09 ± 12.55	39.00 ± 17.03	<0.001
Sex (male:female)	28:19	9:6	0.977
Number of lesions			
Single lesion	37	11	-
Multiple lesions	10	4	-
Enhancing pattern	Ring enhancement	Ring enhancement	-
Necrosis	47	15	-

Values are expressed as mean ± standard deviation (SD).
The Student's t-test was used to compare the age between the two groups, and the chi-square test was used to compare the gender.

Differences in Cerebral Blood Flow and Relative Cerebral Blood Flow Between Neoplastic and Non-neoplastic Groups

Supplementary Table 1 shows the ICCs measured by two observers. Excellent agreement was observed for CBF values. The CBF and rCBF values of the lesions and perilesional edema in the non-neoplastic group were significantly lower than those in the neoplastic group. There was no significant difference in the CBF-CGM values between the two groups, as shown in **Table 2**. The representative ASL images are shown in **Figure 1**.

After comparing the neoplastic group and the non-neoplastic group, the CBF-L, CBF-PLE, rCBF-L, and rCBF-PLE values of the metastatic group and the non-neoplastic group were lower than those of the HGG group, and the difference was statistically significant ($p < 0.001$). The CBF-L and rCBF-L values of the non-neoplastic group were lower than those of the metastatic group, and the difference was statistically significant ($p < 0.001$), while the CBF-PLE and rCBF-PLE were not significantly different between the two groups with p-values of 0.894 and 0.795, respectively. The details are shown in **Supplementary Table 2**.

Diagnostic Values of Relative Cerebral Blood Flow of Lesion and Relative Cerebral Blood Flow of Perilesional Edema

Receiver operating characteristic analysis showed that the AUC of rCBF-L for the diagnosis of non-neoplastic and neoplastic was 0.994 with a sensitivity of 95.7% and a specificity of 100%. The AUC of rCBF-PLE for the diagnosis of non-neoplastic and neoplastic was 0.846 with a sensitivity of 70.2% and a specificity of 93.3%. **Table 3** summarizes the best cutoff values for different parameters that distinguish non-neoplastic from neoplastic lesions. The ROC curves are shown in **Figure 2**.

After the main group comparison, we found that when the rCBF-L cutoff value was selected at 1.545, the AUC for the diagnosis of HGG and metastasis was 0.923 (95% CI 0.839–1.000), with a sensitivity of 91.4% and a specificity of 83.3%. When the rCBF-L cutoff value was selected at 0.940, the AUC for diagnosing metastatic and non-neoplastic lesions was 0.978 (95% CI 0.934–1.000), with a sensitivity of 91.7% and a specificity of 93.3%. When the rCBF-PLE cutoff value was selected at 0.465, the AUC for the diagnosis of HGG and metastases was 0.923 (95% CI 0.949–1.000), with a sensitivity of 94.3% and a specificity of 100%.

DISCUSSION

In the present study, we evaluated the utility of 3D-PCASL for the differentiation of neoplastic and non-neoplastic lesions. We demonstrated that non-neoplastic lesions exhibited lower CBF values based on ASL perfusion MRI compared with neoplastic lesions. We demonstrated that 3D-PCASL MRI techniques could be used for differentiation with high accuracy.

It is essential to distinguish non-neoplastic from neoplastic lesions as the therapeutic strategies and prognosis are different

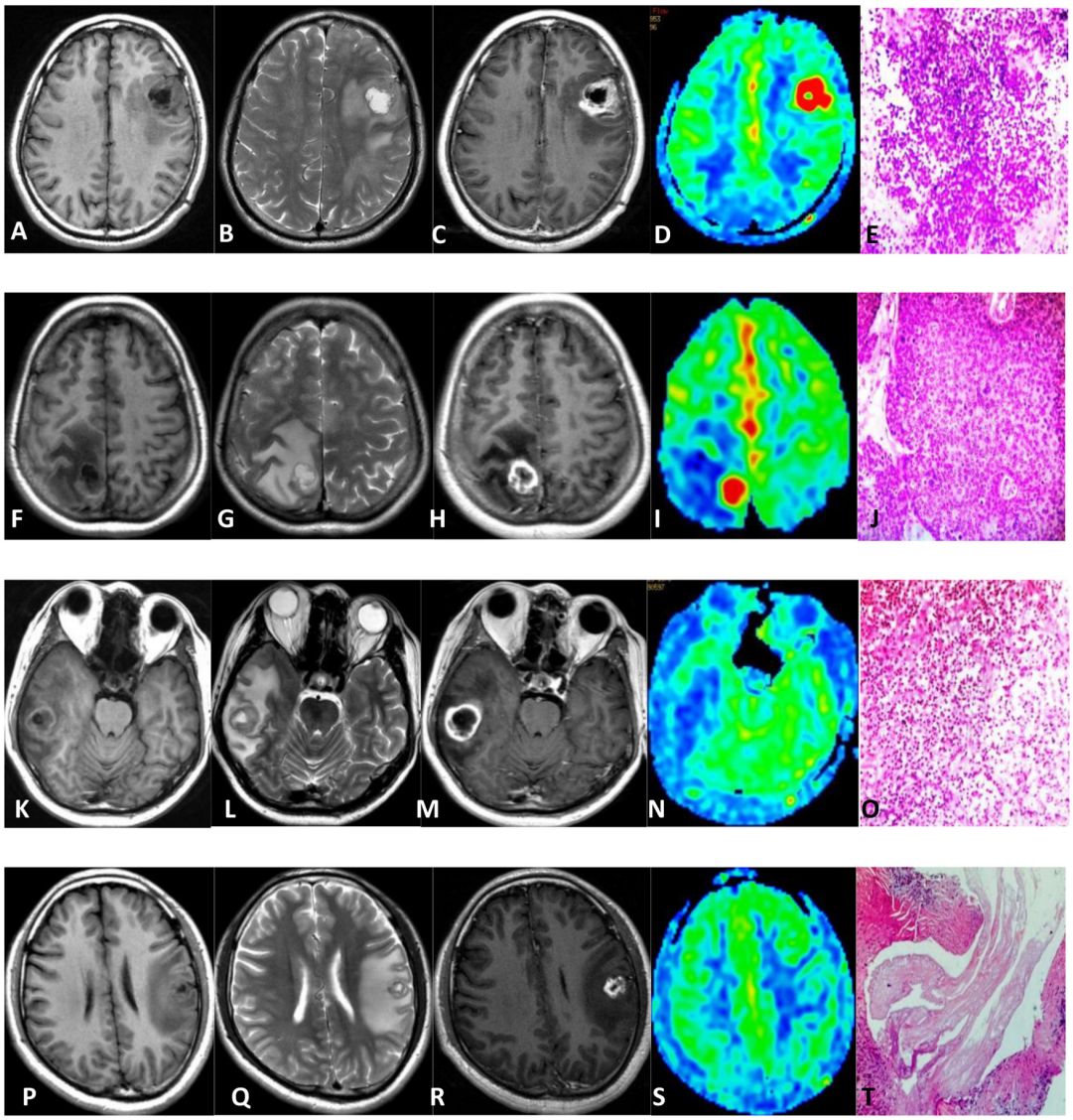

FIGURE 1 | Comparison of HGG **(A–E)**, metastasis **(F–J)**, brain abscess **(K–O)**, and cerebral cysticercosis **(P–T)**. First row: 64-year-old male with an HGG in the left frontal lobe; unenhanced MR scan showed hypointense on T1WI and hyperintense onT2WI **(A,B)**. The contrast-enhanced T1-weighted MRI showed ring enhancement **(C)**. 3D-pCASL exhibited as hyper-perfusion in the region of tumor compared with the contralateral brain **(D)**. Pathologically, the tumor cells were diffusely distributed and showed increased density **(E)**. Second row: 42-year-old woman with a metastatic tumor in the right parietal lobe; MR plain scan showed hypointense on T1WI and hyperintense on T2WI **(F,G)**. The enhanced scan showed ring enhancement **(H)**. 3D-pCASL showed as hyper-perfusion in the region of metastasis **(I)**. Pathology showed the nested atypical cells, which was squamous cell carcinoma **(J)**. Third row: 40-year-old man with a brain abscess in the right temporal lobe. MR plain scan showed hypointense on T1WI and hyperintense on T2WI **(K,L)**. The enhanced scan showed ring enhancement **(M)**. 3D-pCASL showed the lesion demonstrated as hypo-perfusion **(N)**. Pathology showed lymphocyte, neutrophil infiltration, abscess formation, and granulation tissue hyperplasia **(O)**. Fourth row: 28-year-old man with cerebral cysticercosis in the left frontal and parietal lobe. MR plain scan showed hypointense on T1WI and hyperintense on T2WI **(P,Q)**. The enhanced scan showed ring enhancement **(R)**. 3D-pCASL showed that the lesion was iso-hypo-perfusion **(S)**. Pathologically, lace-like parasites can be seen **(T)**.

clinically. However, many non-neoplastic neurological diseases could often mimic brain tumors in neuroimaging (Okamoto et al., 2004a,b). The conventional MR contrast enhancement is affected by the damage of the blood–brain barrier (BBB) and the permeability of neovascularization. Most intracranial tumors could destroy the BBB, while some non-neoplastic lesions could increase vascular permeability (Gupta et al., 2008). Therefore, both intracranial neoplastic and non-neoplastic lesions could show significant enhancement, usually ring enhancement, and thus difficult to distinguish. Most brain abscesses show high signal on MR diffusion-weighted imaging (DWI), which is helpful to distinguish from the necrosis center of neoplastic disease. However, there are reports that some metastases and HGG could also show high signal on DWI (Holtås et al., 2000;

TABLE 2 | 3D-pCASL imaging-derived parameters for non-neoplastic and neoplastic.

	Neoplastic (*n* = 47)	Non-neoplastic (*n* = 15)	*p*-values
CBF-L	115.59 ± 40.83	40.17 ± 6.71	<0.001
CBF-PLE	29.80 ± 6.29	22.22 ± 2.29	<0.001
CBF-CGM	54.05 ± 2.81	53.50 ± 3.13	0.521
rCBF-L	2.13 ± 0.75	0.75 ± 0.14	<0.001
rCBF-PLE	0.55 ± 0.12	0.42 ± 0.04	<0.001

Values are expressed as mean ± standard deviation (SD).
Comparisons between groups were performed by Student's t-test.
CBF-L, cerebral blood flow of lesion; CBF-PLE, cerebral blood flow of perilesional edema; CBF-CGM, cerebral blood flow of contralateral normal gray matter; rCBF-L, relative cerebral blood flow of lesion; rCBF-PLE, relative cerebral blood flow of perilesional edema.

TABLE 3 | Diagnostic performance of rCBF-L and rCBF-PLE for differentiating non-neoplastic from neoplastic lesions.

Model	AUC	Cutoff value	Sensitivity	Specificity
rCBF-L	0.994 (0.983–1.000)	1.095	0.957	1.000
rCBF-PLE	0.846 (0.752–0.940)	0.475	0.702	0.933

Data in parentheses are 95% confidence intervals.
AUC, area under the receiver operating characteristic curve; rCBF-L, relative cerebral blood flow of lesion; rCBF-PLE, relative cerebral blood flow of perilesional edema.

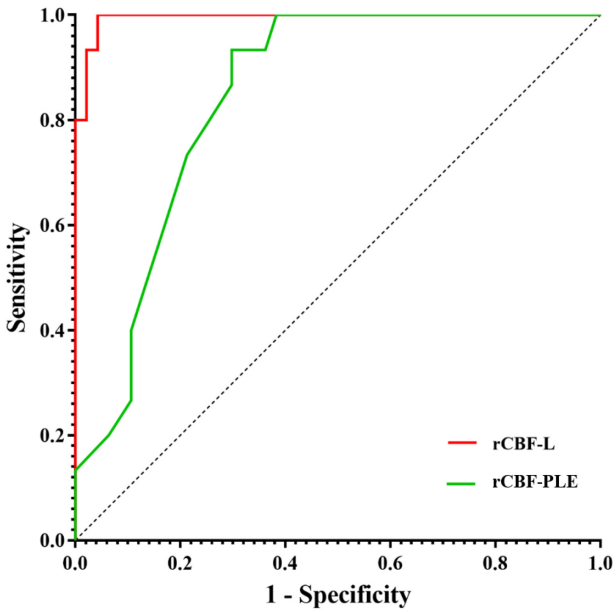

FIGURE 2 | Receiver operating characteristic curves for rCBF and rCBF-PLE for differentiating non-neoplastic from neoplastic lesions. AUC, area under the receiver operating characteristic curve; rCBF-L, relative cerebral blood flow of lesion; rCBF-PLE, relative cerebral blood flow of perilesional edema.

Hakyemez et al., 2005). Tuberculoma and metastasis could both show lipid peaks on magnetic resonance spectroscopy (MRS); as a result, MRS may not be useful when calcification and bleeding exist (Nagar et al., 2007). Misdiagnosis may expose patients to unnecessary surgery. Accordingly, it is particularly important to find a new diagnostic method. All the above-mentioned sequences could not reflect the blood flow distribution and perfusion in the lesions.

In this study, we first focused on the application of 3D-pCASL in intracranial enhancement lesions. Previous examinations of CBF were mostly accomplished through perfusion imaging based on nuclear medicine, dynamic contrast-enhanced computed tomography (CT), or dynamic susceptibility contrast MRI (DSC-MRI) (Noguchi et al., 2016). However, nuclear medicine examinations cannot be routinely performed in clinical practice. Dynamic contrast-enhanced CT requires the use of contrast agents and gives radiation to the patient. DSC-MRI has shown good ability in differentiating non-neoplastic from neoplastic lesions and is widely used. Studies have shown that the relative cerebral blood volume (rCBV) of non-neoplastic lesions was significantly lower than that of neoplastic lesions (Floriano et al., 2013). However, DSC can be easily affected by the destruction of the BBB and requires the injection of contrast agents. ASL is one of the non-contrast-enhanced MR perfusion imaging methods, which has the advantages of non-invasiveness, simple operation, and repeatable inspection. It is widely used in the differential diagnosis between tumors and grading of gliomas (Suh et al., 2018). ASL can more realistically reflect the angiogenesis of the lesion without being affected by blood products, necrosis, or calcification (Furtner et al., 2014). Many previous studies have shown that there is a strong correlation between the perfusion parameters obtained by ASL and DSC (Grade et al., 2015; Soni et al., 2017; Novak et al., 2019), which showed the feasibility of ASL as an alternative to DSC.

In the current study, the CBF-L and rCBF-L of non-neoplastic lesions were lower compared with neoplastic lesions, which is consistent with previous studies (Soni et al., 2018). This result may be attributed to the fact that neoplastic lesions could induce angiogenesis, leading to an increase in blood perfusion. Muccio et al. (2008) found lower rCBV values in patients with brain abscesses, proposing that this was due to the low density of capillaries and the enrichment of collagen fibers in the capsule of abscess lesions. This explanation also applies to the performance of other non-neoplastic lesions with low perfusion. Therefore, when encountering a rare HGG with a high DWI signal in clinical practice (Reiche et al., 2010), ASL could be helpful for the distinguishing diagnosis from brain abscess. At the same time, we found that the CBF-L and rCBF-L of metastatic lesions were lower than HGG, which is also consistent with previous studies (Sunwoo et al., 2016; Abdel Razek et al., 2019a). This can be attributed to the higher density of new blood vessels in HGG.

Secondly, we tested the application of 3D-pCASL in perilesional perfusion. Compared with brain tumors, non-neoplastic lesion has lower CBF-PLE and rCBF-PLE. However, there was no significant difference in CBF PLE and rCBF PLE between metastatic and non-neoplastic lesions. This may be due to the tendency of glioma cells to infiltrate surrounding brain tissues. The PLE of glioma includes not only the invading tumor cells, but also the glial alterations in surrounding normal tissues, such as swelling of astrocytes, aggregation of microglia, and microglia

activation (Engelhorn et al., 2009). The PLE of metastases represents pure vasogenic edema rich in plasma proteins, and its source is the leakage of capillaries in or around the metastasis. In addition, the decrease of CBF-PLE may be caused by local compression of the microcirculation by edema (Lin et al., 2016).

Our study has some limitations. First, there may be a bias of sample selection in retrospective studies. Second, the sample size was not large enough, and the data had a large degree of dispersion. More patients will validate our results in the future. Finally, it has been reported that factors such as MR sequence parameters and postprocessing software may influence the results.

CONCLUSION

In this study, we found that both the rCBF value of the lesion and the peri-edema from the non-neoplastic group were significantly lower than those of the neoplastic group. ASL parameters could be helpful in discriminating non-neoplastic from neoplastic lesions for the intracranial enhancement lesions, thus preventing misdiagnosis and unnecessary surgery.

DATA AVAILABILITY STATEMENT

The original contributions presented in the study are included in the article/**Supplementary Material**, further inquiries can be directed to the corresponding author/s.

ETHICS STATEMENT

Written informed consent was obtained from the individual(s), and minor(s)' legal guardian/next of kin, for the publication of any potentially identifiable images or data included in this article.

AUTHOR CONTRIBUTIONS

HY, Y-BX, and X-WK contributed to conception and design of the study. W-ZH and Y-QX organized the database. Y-QX and FG performed the statistical analysis. W-ZH wrote the first draft of the manuscript. FG and BH wrote sections of the manuscript. All authors contributed to manuscript revision, read, and approved the submitted version.

FUNDING

This work was supported by the National Natural Science Foundation of China (HY, Grant Number 81971594), the Research Incubation Fund of Xi'an People's Hospital (Xi'an Fourth Hospital) (ZD-11), and the Project Supported by Natural Science Basic Research Plan in Shaanxi Province of China (2020JM-325).

SUPPLEMENTARY MATERIAL

The Supplementary Material for this article can be found online at: https://www.frontiersin.org/articles/10.3389/fnins.2022.812997/full#supplementary-material

REFERENCES

Abdel Razek, A. A. K., Talaat, M., El-Serougy, L., Abdelsalam, M., and Gaballa, G. (2019a). Differentiating Glioblastomas from Solitary Brain Metastases Using Arterial Spin Labeling Perfusion- and Diffusion Tensor Imaging-Derived Metrics. *World Neurosurg.* 127, e593–e598. doi: 10.1016/j.wneu.2019.03.213

Abdel Razek, A. A. K., Talaat, M., El-Serougy, L., Gaballa, G., and Abdelsalam, M. (2019b). Clinical Applications of Arterial Spin Labeling in Brain Tumors. *J. Comput. Assist. Tomogr.* 43, 525–532. doi: 10.1097/RCT.0000000000000873

Alsop, D. C., Detre, J. A., Golay, X., Günther, M., Hendrikse, J., Hernandez-Garcia, L., et al. (2015). Recommended implementation of arterial spin-labeled perfusion MRI for clinical applications: A consensus of the ISMRM perfusion study group and the European consortium for ASL in dementia. *Magn. Reson Med.* 73, 102–116. doi: 10.1002/mrm.25197

Bush, N. A., Chang, S. M., and Berger, M. S. (2017). Current and future strategies for treatment of glioma. *Neurosurg. Rev.* 40, 1–14.

Engelhorn, T., Savaskan, N. E., Schwarz, M. A., Kreutzer, J., Meyer, E. P., Hahnen, E., et al. (2009). Cellular characterization of the peritumoral edema zone in malignant brain tumors. *Cancer Sci.* 100, 1856–1862. doi: 10.1111/j.1349-7006.2009.01259.x

Floriano, V. H., Torres, U. S., Spotti, A. R., Ferraz-Filho, J. R., and Tognola, W. A. (2013). The role of dynamic susceptibility contrast-enhanced perfusion MR imaging in differentiating between infectious and neoplastic focal brain lesions: results from a cohort of 100 consecutive patients. *PLoS One.* 8:e81509. doi: 10.1371/journal.pone.0081509

Furtner, J., Schöpf, V., Preusser, M., Asenbaum, U., Woitek, R., Wöhrer, A., et al. (2014). Non-invasive assessment of intratumoral vascularity using arterial spin labeling: A comparison to susceptibility-weighted imaging for the differentiation of primary cerebral lymphoma and glioblastoma. *Eur. J. Radiol.* 83, 806–810. doi: 10.1016/j.ejrad.2014.01.017

Grade, M., Hernandez Tamames, J. A., Pizzini, F. B., Achten, E., Golay, X., and Smits, M. A. (2015). neuroradiologist's guide to arterial spin labeling MRI in clinical practice. *Neuroradiology* 57, 1181–1202. doi: 10.1007/s00234-015-1571-z

Gupta, R. K., Nath, K., Prasad, A., Prasad, K. N., Husain, M., Rathore, R. K., et al. (2008). *In vivo* demonstration of neuroinflammatory molecule expression in brain abscess with diffusion tensor imaging. *AJNR* 29, 326–332. doi: 10.3174/ajnr.A0826

Hakyemez, B., Erdogan, C., Yildirim, N., and Parlak, M. (2005). Glioblastoma multiforme with atypical diffusion-weighted MR findings. *Br. J. Radiol.* 78, 989–992. doi: 10.1259/bjr/12830378

Haller, S., Zaharchuk, G., Thomas, D. L., Lovblad, K. O., Barkhof, F., and Golay, X. (2016). Arterial Spin Labeling Perfusion of the Brain: Emerging Clinical Applications. *Radiology* 281, 337–356. doi: 10.1148/radiol.2016150789

Hernandez-Garcia, L., Lahiri, A., and Schollenberger, J. (2019). Recent progress in ASL. *Neuroimage* 187, 3–16. doi: 10.1016/j.neuroimage.2017.12.095

Holtås, S., Geijer, B., Strömblad, L. G., Maly-Sundgren, P., and Burtscher, I. M. A. (2000). ring-enhancing metastasis with central high signal on diffusion-weighted imaging and low apparent diffusion coefficients. *Neuroradiology* 42, 824–827. doi: 10.1007/s002340000431

Ko, C. C., Tai, M. H., Li, C. F., Chen, T. Y., Chen, J. H., Shu, G., et al. (2016). Differentiation between Glioblastoma Multiforme and Primary Cerebral Lymphoma: Additional Benefits of Quantitative Diffusion-Weighted MR Imaging. *PLoS One.* 11:e0162565. doi: 10.1371/journal.pone.0162565

Lin, L., Xue, Y., Duan, Q., Sun, B., Lin, H., Huang, X., et al. (2016). The role of cerebral blood flow gradient in peritumoral edema for differentiation of

glioblastomas from solitary metastatic lesions. *Oncotarget* 7, 69051–69059. doi: 10.18632/oncotarget.12053

Muccio, C. F., Esposito, G., Bartolini, A., and Cerase, A. (2008). Cerebral abscesses and necrotic cerebral tumours: differential diagnosis by perfusion-weighted magnetic resonance imaging. *Radiol. Med.* 113, 747–757. doi: 10.1007/s11547-008-0254-9

Nagar, V. A., Ye, J., Xu, M., Ng, W. H., Yeo, T. T., Ong, P. L., et al. (2007). Multivoxel MR spectroscopic imaging–distinguishing intracranial tumours from non-neoplastic disease. *Ann. Acad. Med. Singap.* 36, 309–313.

Noguchi, T., Yakushiji, Y., Nishihara, M., Togao, O., Yamashita, K., Kikuchi, K., et al. (2016). Arterial Spin-labeling in Central Nervous System Infection. *Magn. Reson Med. Sci.* 15, 386–394. doi: 10.2463/mrms.mp.2015-0140

Novak, J., Withey, S. B., Lateef, S., MacPherson, L., Pinkey, B., and Peet, A. C. A. (2019). comparison of pseudo-continuous arterial spin labelling and dynamic susceptibility contrast MRI with and without contrast agent leakage correction in paediatric brain tumours. *Br. J. Radiol.* 92:20170872. doi: 10.1259/bjr.20170872

Okamoto, K., Furusawa, T., Ishikawa, K., Quadery, F. A., Sasai, K., and Tokiguchi, S. (2004a). Mimics of brain tumor on neuroimaging: part II. *Radiat. Med.* 22, 135–142.

Okamoto, K., Furusawa, T., Ishikawa, K., Quadery, F. A., Sasai, K., and Tokiguchi, S. (2004b). Mimics of brain tumor on neuroimaging: part I. *Radiat. Med.* 22, 63–76.

Omuro, A. M., Leite, C. C., Mokhtari, K., and Delattre, J. Y. (2006). Pitfalls in the diagnosis of brain tumours. *Lancet Neurol.* 5, 937–948. doi: 10.1016/S1474-4422(06)70597-X

Reiche, W., Schuchardt, V., Hagen, T., Il'yasov, K. A., Billmann, P., and Weber, J. (2010). Differential diagnosis of intracranial ring enhancing cystic mass lesions–role of diffusion-weighted imaging (DWI) and diffusion-tensor imaging (DTI). *Clin. Neurol. Neurosurg.* 112, 218–225. doi: 10.1016/j.clineuro.2009.11.016

Soni, N., Dhanota, D. P. S., Kumar, S., Jaiswal, A. K., and Srivastava, A. K. (2017). Perfusion MR imaging of enhancing brain tumors: Comparison of arterial spin labeling technique with dynamic susceptibility contrast technique. *Neurol. India* 65, 1046–1052. doi: 10.4103/neuroindia.NI_871_16

Soni, N., Srindharan, K., Kumar, S., Mishra, P., Bathla, G., Kalita, J., et al. (2018). Arterial spin labeling perfusion: Prospective MR imaging in differentiating neoplastic from non-neoplastic intra-axial brain lesions. *Neuroradiol. J.* 31, 544–553. doi: 10.1177/1971400918783058

Suh, C. H., Kim, H. S., Jung, S. C., Choi, C. G., and Kim, S. J. (2018). Perfusion MRI as a diagnostic biomarker for differentiating glioma from brain metastasis: a systematic review and meta-analysis. *Eur. Radiol.* 28, 3819–3831. doi: 10.1007/s00330-018-5335-0

Sung, H., Ferlay, J., Siegel, R. L., Laversanne, M., Soerjomataram, I., Jemal, A., et al. (2021). Global Cancer Statistics 2020: GLOBOCAN Estimates of Incidence and Mortality Worldwide for 36 Cancers in 185 Countries. *CA Cancer J. Clin.* 71, 209–249. doi: 10.3322/caac.21660

Sunwoo, L., Yun, T. J., You, S. H., Yoo, R. E., Kang, K. M., Choi, S. H., et al. (2016). Differentiation of Glioblastoma from Brain Metastasis: Qualitative and Quantitative Analysis Using Arterial Spin Labeling MR Imaging. *PLoS One.* 11:e0166662. doi: 10.1371/journal.pone.0166662

Villanueva-Meyer, J. E., Mabray, M. C., and Cha, S. (2017). Current Clinical Brain Tumor Imaging. *Neurosurgery* 81, 397–415.

Wu, B., Lou, X., Wu, X., and Ma, L. (2014). Intra- and interscanner reliability and reproducibility of 3D whole-brain pseudo-continuous arterial spin-labeling MR perfusion at 3T. *J. Magn. Reson Imaging* 39, 402–409. doi: 10.1002/jmri.24175

Xi, Y. B., Kang, X. W., Wang, N., Liu, T. T., Zhu, Y. Q., Cheng, G., et al. (2019). Differentiation of primary central nervous system lymphoma from high-grade glioma and brain metastasis using arterial spin labeling and dynamic contrast-enhanced magnetic resonance imaging. *Eur. J. Radiol.* 112, 59–64. doi: 10.1016/j.ejrad.2019.01.008

Yeganeh, L., Boyle, J. A., Wood, A., Teede, H., and Vincent, A. J. (2019). Menopause guideline appraisal and algorithm development for premature ovarian insufficiency. *Maturitas* 130, 21–31. doi: 10.1016/j.maturitas.2019.09.009

Conflict of Interest: The authors declare that the research was conducted in the absence of any commercial or financial relationships that could be construed as a potential conflict of interest.

Publisher's Note: All claims expressed in this article are solely those of the authors and do not necessarily represent those of their affiliated organizations, or those of the publisher, the editors and the reviewers. Any product that may be evaluated in this article, or claim that may be made by its manufacturer, is not guaranteed or endorsed by the publisher.

Copyright © 2022 Hu, Guo, Xu, Xi, He, Yin and Kang. This is an open-access article distributed under the terms of the Creative Commons Attribution License (CC BY). The use, distribution or reproduction in other forums is permitted, provided the original author(s) and the copyright owner(s) are credited and that the original publication in this journal is cited, in accordance with accepted academic practice. No use, distribution or reproduction is permitted which does not comply with these terms.

frontiers in Neuroscience

ORIGINAL RESEARCH
published: 09 March 2022
doi: 10.3389/fnins.2022.856710

Cerebral Blood Flow Pattern Changes in Unilateral Sudden Sensorineural Hearing Loss

Yue Chen[1†], Haimei Li[2†], Bing Liu[1], Wenwen Gao[1], Aocai Yang[1], Kuan Lv[1], Hui Xia[3], Wenwei Zhang[3], Hongwei Yu[1], Jian Liu[4], Xiuxiu Liu[1], Yige Wang[1], Honglei Han[5] and Guolin Ma[1]**

[1] Department of Radiology, China-Japan Friendship Hospital, Beijing, China, [2] Department of Radiology, Fuxing Hospital, Capital Medical University, Beijing, China, [3] Institute of Electrical Engineering, Chinese Academy of Sciences, Beijing, China, [4] Department of Ultrasound Diagnosis, China-Japan Friendship Hospital, Beijing, China, [5] Department of Otolaryngology, China-Japan Friendship Hospital, Beijing, China

Objective: This study analyzed the differences in the cerebral blood flow (CBF) between unilateral Sudden Sensorineural Hearing Loss (SSNHL) patients and healthy controls (HCs). We also investigated CBF differences in auditory-related areas in patients with left- and right-sided SSNHL (lSSNHL and rSSNHL) and HCs. We further explore the correlation between unilateral SSNHL characteristics and changes in the CBF.

Methods: 36 patients with unilateral SSNHL (15 males and 21 females, 40.39 ± 13.42 years) and 36 HCs (15 males and 21 females, 40.39 ± 14.11 years) were recruited. CBF images were collected and analyzed using arterial spin labeling (ASL). CereFlow software was used for the post-processing of the ASL data to obtain the CBF value of 246 subregions within brainnetome atlas (BNA). The Two-sample *t*-test was used to compare CBF differences between SSNHL patients and HCs. One-way ANOVA or Kruskal-Wallis test was used to compare the CBF difference of auditory-related areas among the three groups (lSSNHL, rSSNHL, and HCs). Then, the correlation between CBF changes and specific clinical characteristics were calculated.

Results: The SSNHL patients exhibited decreased CBF in the bilateral middle frontal gyrus (MFG, MFG_7_1 and MFG_7_3), the contralateral precentral gyrus (PrG, PrG_6_3) and the bilateral superior parietal lobule (SPL, bilateral SPL_5_1, SPL_5_2, and ipsilateral SPL_5_4), $p < 0.0002$. Compared with HCs, unilateral SSNHL patients exhibited increased rCBF in the bilateral orbital gyrus (OrG, OrG_6_5), the bilateral inferior temporal gyrus (ITG, contralateral ITG_7_1 and bilateral ITG_7_7), $p < 0.0002$. lSSNHL showed abnormal CBF in left BA21 caudal ($p = 0.02$) and left BA37 dorsolateral ($p = 0.047$). We found that the CBF in ipsilateral MFG_7_1 of SSNHL patients was positively correlated with tinnitus Visual Analog Scale (VAS) score ($r = 0.485$, $p = 0.008$).

Conclusion: Our preliminary study explored CBF pattern changes in unilateral SSNHL patients in auditory-related areas and non-auditory areas, suggesting that there may exist reduced attention and some sensory compensation in patients with SSNHL. These findings could advance our understanding of the potential pathophysiology of unilateral SSNHL.

Keywords: sudden sensorineural hearing loss, cerebral blood flow, arterial spin labeling, brainnetome atlas, magnetic resonance imaging

OPEN ACCESS

Edited by:
Jun Shi,
Shanghai University, China

Reviewed by:
Bo Gao,
Affiliated Hospital of Guizhou Medical University, China
Ruiwang Huang,
South China Normal University, China
Ni Shu,
Beijing Normal University, China

***Correspondence:**
Guolin Ma
maguolin1007@qq.com
Honglei Han
hanhonglei1972@163.com

† These authors have contributed equally to this work

Specialty section:
This article was submitted to Brain Imaging Methods, a section of the journal Frontiers in Neuroscience

Received: *17 January 2022*
Accepted: *15 February 2022*
Published: *09 March 2022*

Citation:
Chen Y, Li H, Liu B, Gao W, Yang A, Lv K, Xia H, Zhang W, Yu H, Liu J, Liu X, Wang Y, Han H and Ma G (2022) Cerebral Blood Flow Pattern Changes in Unilateral Sudden Sensorineural Hearing Loss. Front. Neurosci. 16:856710. doi: 10.3389/fnins.2022.856710

INTRODUCTION

Sudden Sensorineural Hearing Loss (SSNHL) is defined as a hearing loss of over 30 dB in three sequential frequencies in the pure-tone audiogram within 72 h, and is considered as an otologic emergency (Stachler et al., 2012). SSNHL is often accompanied by tinnitus and vertigo, which affects quality of life of patients, leading to anxiety and depression (Fusconi et al., 2012). Many causes of SSNHL have been proposed, including viral infection, neoplasms, trauma, ototoxicity, autoimmune diseases, and developmental anomalies, but the mechanisms of SSNHL have not yet been clarified. It is difficult to identify the exact cause of SSNHL by routine clinical examinations (Jung da et al., 2016). At present, steroid therapy is the main treatment method for SSNHL. But some SSNHL patients do not respond to conventional treatment, which leads to a low long-term quality of life (Liu et al., 2020). Previous studies have reported that hearing loss induced brain structural changes, brain functional changes and reorganization of functional cerebral networks. From the brain structural perspective, brain morphological changes could be induced by unilateral hearing loss was found, including decreased gray matter volume in temporal/ precuneus/ cingulate and parahippocampal gyrus (Yang et al., 2014). From the functional perspective, a functional magnetic resonance imaging (fMRI) study found the changes of default mode networks (DMN) in patients with long-term unilateral SSNHL might be associated with cognitive ability of patients (Zhang et al., 2015). Another resting-state fMRI found that there existed a shift toward small-worldization in unilateral SSNHL patients functional connectome (Xu et al., 2016). A widespread functional reorganization was found in SSNHL, not only in auditory regions (Minosse et al., 2020). Similarly, a diffusion tensor imaging (DTI) study with graph theoretical analysis found that altered nodal centralities in brain regions involved the auditory network and non-auditory network, including visual network, attention network, DMN, sensorimotor network, and subcortical network in SSNHL patients in the acute period (Zou et al., 2021). A study demonstrated cortical perfusion pattern changes in age-related hearing loss (Ponticorvo et al., 2019). All in all, structural and functional changes were found not only in the auditory-related areas, but also in the non-auditory areas in the above studies. Until now, few studies shed light on the cerebral blood flow (CBF) pattern changes in unilateral SSNHL patients. The changes of CBF following SSNHL remain largely unknown.

Arterial spin labeling (ASL) is an MRI technique used to non-invasively measure CBF by magnetically labeling the arterial water (Haller et al., 2016). Regional brain CBF is tightly coupled with regional metabolism and neuronal activity (Li et al., 2020). This study aimed to use three-dimensional pseudo-continuous (3D-pCASL) to detect regional CBF pattern changes in unilateral SSNHL patients by region of interest (ROI) analysis. We analyzed the differences in the CBF between unilateral SSNHL patients and healthy controls (HCs). We also investigated the CBF differences in auditory-related areas in patients with left- and right-sided SSNHL (lSSNHL and rSSNHL) and HCs. We further explore the correlation between unilateral SSNHL characteristics and changes in the CBF. We hope our results will help to characterize unilateral SSNHL pathophysiology.

MATERIALS AND METHODS

Subjects

Thirty-six patients (19 left-sided SSNHL, 17 right-sided SSNHL) were enrolled in this study. Among them, 13 patients were recruited at the outpatient otorhinolaryngology Department of China-Japan Friendship Hospital, and 23 patients were recruited at Fuxing Hospital affiliated to Capital Medical University. The inclusion criteria for patients were: (1) diagnosed as unilateral SSNHL, according to the Sudden Hearing Loss Clinical Practice Guideline of the American Academy of Otolaryngology-Head and Neck Surgery Foundation (Stachler et al., 2012); (2) SSNHL duration time $\leq$ 3 month; (3) age $<$ 70 years, (4) being right-handedness. The exclusion criteria for patients were: (1) with bilateral SSNHL; (2) have contraindications to MRI examination; (3) suffer from Ménière's disease, hyperacusis, and history of neurological disorders, such as brain trauma and strokes. Thirty six healthy controls (HC) were recruited from the society. The SSNHL patients and HCs were group-matched in terms of age, sex, and education. This study was approved by the Ethics Committee of China-Japan Friendship hospital and Fuxing Hospital, and informed consent of all the participants was obtained.

Clinical Data

Demographic information was collected prior to the MRI scan. Hearing thresholds were determined by pure tone audiometry to determine the hearing loss degree. Pure tone average (PTA) value was calculated by averaging the hearing thresholds at 0.5, 1, 2, and 4 kHz. 28 SSNHL patients were accompanied by tinnitus, and we finally obtained the tinnitus questionnaire results from them. The tinnitus loudness was measured by Visual Analogue Scale (VAS) (Mores et al., 2019). The severity of tinnitus was assessed by Tinnitus Handicap Inventory (THI) (Meng et al., 2012). In addition, we evaluated symptoms of depression and anxiety of SSNHL patients according to the Self-Rating Depression Scale (SDS) (Zung, 1972) and Self-Rating Anxiety Scale (SAS) (Zung, 1971). However, as the overall scores of SDS and SAS for SSNHL patients were less than 50, none of them had anxiety or depression.

Magnetic Resonance Imaging Data Acquisition

13 unilateral SSNHL patients and all 36 HCs were scanned using a 3.0-T MRI scanner (Discovery MR750 scanner, GE Medical Systems, United States) with an 8-channel phased-array head coil in China-Japan Friendship Hospital. 3D-pCASL using the parameters as follows: TR = 4,817 ms, TE = 14.6 ms, slice thickness = 4 mm, slice spacing = 4 mm, flip angle = 111°, post label delay = 1,525 ms, voxel size = 1.875×1.875 mm^2.

The other 23 unilateral SSNHL patients were scanned using a 3.0-T MRI scanner (Discovery MR750w scanner, GE Medical Systems, United States) in Fuxing Hospital. ASL images were obtained with 3D-pCASL using the parameters as follows: TR = 4,640 ms, TE = 10.7 ms, slice thickness = 4 mm, slice spacing = 4 mm, flip angle = 111°, post label delay = 1,525 ms, voxel size = 1.875 × 1.875 mm^2. All the participants were given ear plugs to reduce scanner noise, and foam paddings were given to restrict head motion.

Data Processing

CereFlow software (An-Image Technology Co., China) was used to process ASL data, the steps were as follows: (1) convert the 3D ASL perfusion weighted images and proton density images (generated from GE MR scanner) into the CBF map of cerebral perfusion for each subject by using the simplified one compartment model (St Lawrence and Wang, 2005). (2) normalize the CBF map to the Montreal Neurological Institute (MNI) space with intensity-based image registration where the MNI152 brain template was used as a fixed image, and transform each subject's image as the motion image to match the fixed image. (3) then the Brainnetome Atlas (BNA) (Fan et al., 2016) was overlaid. (4) the average CBF value of each brain region from BNA was finally obtained (**Figure 1**).

Calculation of rCBF

We considered that ASL data acquired from different MR scanners and the individual variance of subjects could affect the study results. The normalized cerebral blood flow value rCBF was calculated for further statistical analysis:

$$rCBF = CBF \div mCBF$$

Where CBF is the average CBF value of each brain region in BNA, and mCBF is the average CBF value of the whole brain.

rCBF in Auditory-Related Areas Analysis

Several studies have confirmed changed neuronal activity of the auditory cortex in SSNHL patients (Minosse et al., 2020; Zou et al., 2021). Considering the lateralization effects of auditory cortex (Tervaniemi and Hugdahl, 2003), we investigated the CBF differences of auditory-related areas among lSSNHL, rSSNHL, and HCs. We conducted an ROI analysis of auditory-related areas for further analysis. Auditory related areas of both hemispheres with in BNA were divided into the following ROIs: auditory cortex (BA41/42; TE1.0 and TE1.2), Wernicke's area (BA22 caudal and rostral) and associative auditory areas (BA21 caudal and rostral; BA37 dorsalateral; and the anterior part of the Superior Temporal Sulcus) (Martín-Fernández et al., 2021; **Figure 2**).

Statistical Analysis

Demographic and Clinical Data Analysis

Differences in demographic data between the SSNHL and HC group were analyzed using Two-sample *t*-test and Chi-square test in SPSS 26.0 software (Chicago, IL, United States).

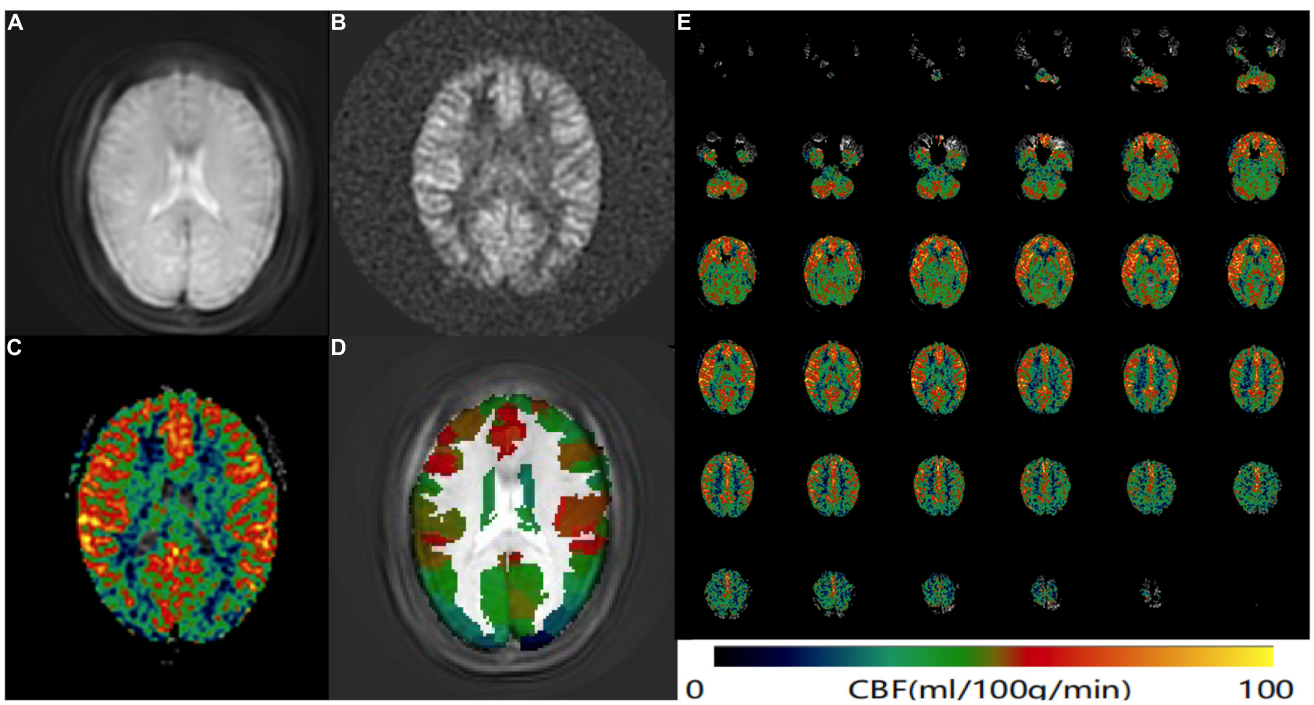

FIGURE 1 | ASL data processing workflow. Convert the **(A)** 3D ASL proton density images and **(B)** perfusion weighted images into the CBF map of cerebral perfusion for each subject. **(C)** The CBF map was normalized to the MNI space and then the BNA was overlaid. **(D)** The average CBF value of each brain region from BNA was obtained. **(E)** An example CBF map of a female SSNHL patient calculated by Cereflow software.

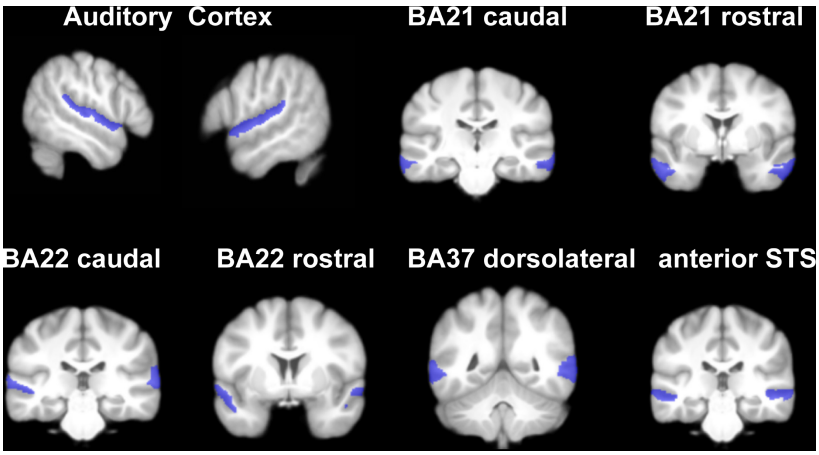

FIGURE 2 | Anatomic representation of the auditory-related areas ROIs within the Brainnetome atlas.

Group rCBF Differences: Sudden Sensorineural Hearing Loss vs. Healthy Controls

For more rigorous statistical analysis, the right side of rSSNHL matched controls (17 cases) was defined as the ipsilateral (affected side), and the left side of lSSNHL matched controls (19 cases) was defined as the ipsilateral. Then, the other side was defined as contralateral in this study. rCBF difference between two groups (all the SSNHL patients and HCs) were compared by Two-sample *t*-test, corrected with the Bonferroni method, 246 comparisons (for there were 246 subregions in BNA). $P < 0.0002$ was considered statistically significant.

Group rCBF Differences in Auditory-Related Areas: lSSNHL vs. rSSNHL vs. Healthy Controls

One-way ANOVA or Kruskal-Wallis test was used to compare the rCBF difference of each auditory ROI among the three groups (lSSNHL, rSSNHL, and HCs), followed by *post hoc* intergroup comparisons (Bonferroni correction). $P < 0.05$ was considered statistically significant.

Correlation Analysis

We used Pearson correlation analysis to calculate the relationships between abnormal rCBF and clinical characteristic data. Partial correlations were calculated after correction for age and gender. $P < 0.05$ was considered statistically significant.

RESULTS

Demographics and Clinical Characteristics: Sudden Sensorineural Hearing Loss vs. Healthy Control

Demographics and clinical characteristic data of all the unilateral SSNHL patients and healthy controls were summarized in **Table 1** and **Figure 3**. No significant differences were found in terms of age, gender, education level.

Group rCBF Differences: Sudden Sensorineural Hearing Loss vs. Healthy Control

The SSNHL patients exhibited decreased rCBF in the bilateral middle frontal gyrus (MFG_7_1 and MFG_7_3), the contralateral precentral gyrus (PrG_6_3) and the bilateral Superior Parietal Lobule (bilateral SPL_5_1, SPL_5_2 and ipsilateral SPL_5_4), $p < 0.0002$ (**Figures 4**, **5A**).

Compared with healthy controls, unilateral SSNHL patients exhibited increased rCBF in the bilateral orbital gyrus (OrG_6_5), the bilateral inferior temporal gyrus (contralateral ITG_7_1 and bilateral ITG_7_7), $p < 0.0002$ (**Figures 4**, **5B**).

Group rCBF Differences: lSSNHL vs. rSSNHL vs. Healthy Control

lSSNHL showed abnormal rCBF in left BA21 caudal ($p = 0.02$, One-way ANOVA, Bonferroni correction) and

TABLE 1 | Demographics and clinical characteristics of unilateral SSNHL patients and HC.

	SSNHL ($n = 36$)	HCs ($n = 36$)	*p*-value
Age (years)	40.39 ± 13.42	40.39 ± 14.11	1.000
Gender (M)	15 (41.67%)	15 (41.67%)	1.000
Education level (years)	15.50 ± 3.39	15.42 ± 3.90	0.923
Handedness (R)	36 (100%)	36 (100%)	–
Duration of hearing loss (day)	16.11 ± 24.41	–	–
Tinnitus	28 (77.8%)	–	–
PTA of affected ear (dB)	54.68 ± 28.71	–	–
VAS score	4.86 ± 2.05	–	–
THI score	44.83 ± 25.84	–	–
SAS score	32.40 ± 8.03	–	–
SDS score	36.53 ± 7.24	–	–

PTA, Pure tone average. VAS, Visual Analog Scale. THI, Tinnitus Handicap Inventory. SAS, Self-Rating Anxiety Scale. SDS, Self-Rating Depression Scale. –, not measured.

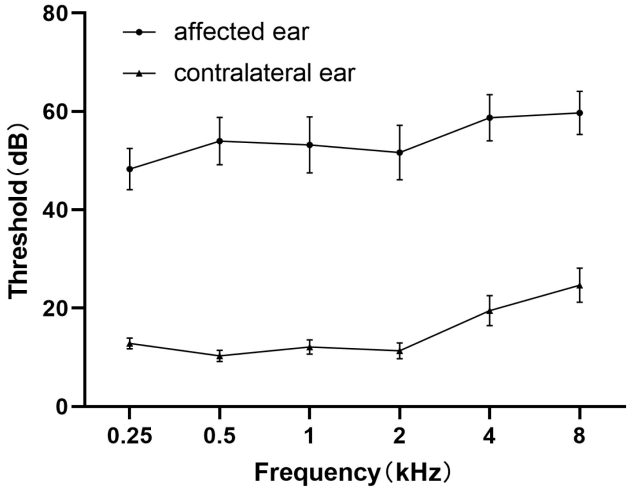

FIGURE 3 | Average pure tone audiograms for patients with SSNHL averaged over both ears at different frequencies. Data are presented as mean ± SEM. SEM, standard error of mean.

left BA37 dorsolateral ($p = 0.047$, Kruskal-Wallis test, Bonferroni correction) compared to HC. There were no significant differences in the rCBF between the rSSNHL group and HC group or lSSNHL group and rSSNHL group (**Figure 6**).

Correlation Analysis

We found that the CBF in ipsilateral MFG_7_1 of SSNHL patients was positively correlated with VAS score ($r = 0.485$, $p = 0.008$) (**Figure 7**).

DISCUSSION

In this study, the CBF changes in patients with unilateral SSNHL, as well as the relationship between the altered CBF and the clinical characteristics was explored. To the best of our knowledge, this study is the first to investigate the CBF changes in unilateral SSNHL patients using 3D-pCASL. We observed the CBF changes in patients with SSNHL in non-auditory areas, such as visual-related (bilateral ITG) and attention-related areas (bilateral dorsolateral prefrontal cortex, dlPFC) compared with the control. lSSNHL patients showed abnormal CBF in auditory-related areas in this study, whereas rSSNHL patients did not.

Unilateral SSNHL patients exhibited increased CBF in visual-related areas (ITG). The ventral part of temporal cortices, which belongs to the ventral stream of the visual system, are involved in the perception in the recognition of object and human faces features, and scenes (Hickok and Poeppel, 2007). When the central auditory system input is reduced, other sensory inputs would be enhanced correspondingly (Lomber et al., 2010). Previous fMRI studies demonstrated that there may exist transmodal neural change in the visual and sensory system in patients with sensorineural hearing loss (SNHL), which reflects

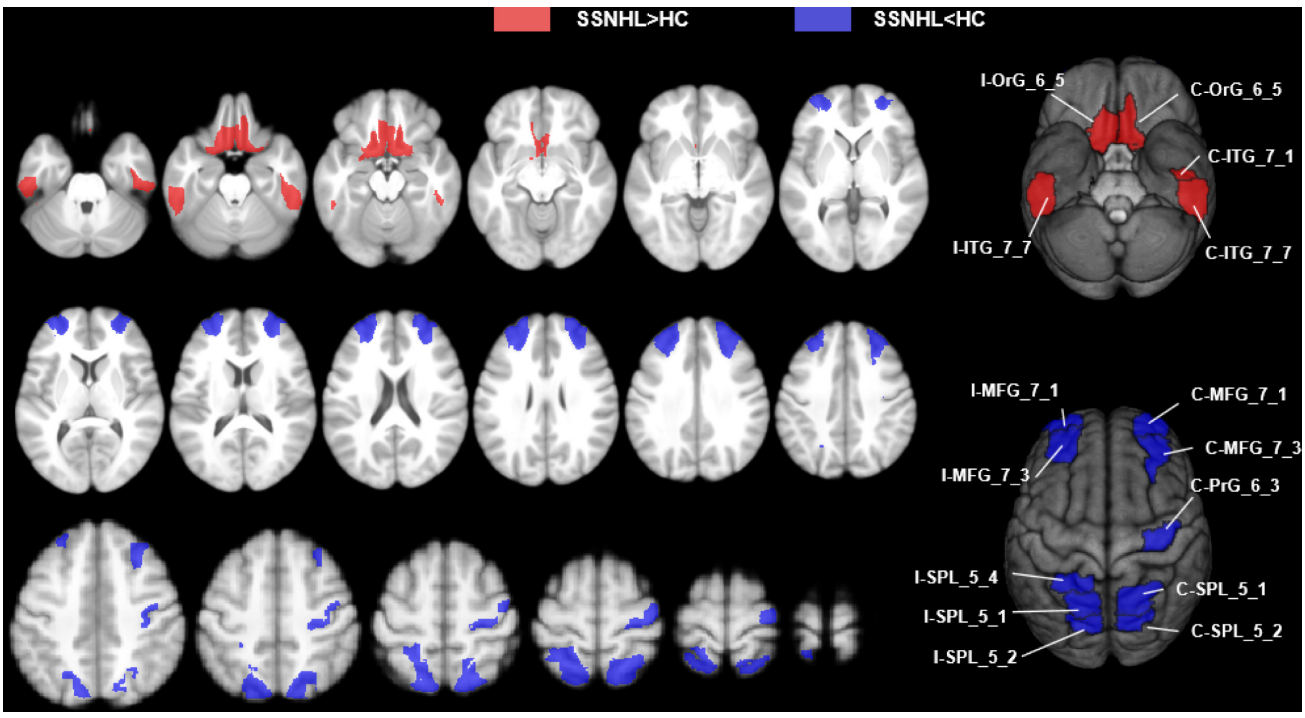

FIGURE 4 | Abnormal CBF subregions in patients with unilateral SSNHL compared with healthy controls. Red, SSNHL (rCBF) > HC (rCBF); Blue, SSNHL (rCBF) < HC (rCBF). l, ipsilateral; C, contralateral; MFG, middle frontal gyrus; PrG, Precentral Gyrus; SPL, superior parietal gyrus; ITG, inferior temporal gyrus; OrG, orbital gyrus.

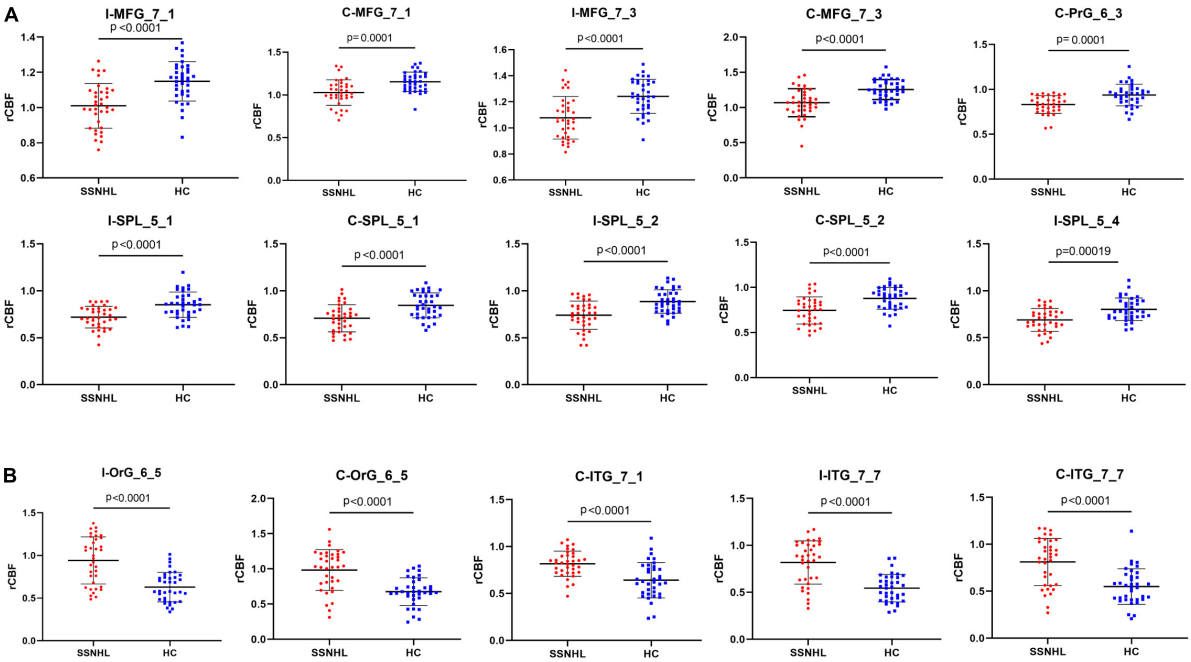

FIGURE 5 | Comparisons of rCBF values between healthy controls and patients with SSNHL. **(A)** Decreased CBF subregions in patients with unilateral SSNHL compared with healthy controls. **(B)** Increased CBF subregions in patients with unilateral SSNHL compared with healthy controls. Data was mean ± SD. I, ipsilateral; C, contralateral; MFG, middle frontal gyrus; PrG, Precentral Gyrus; SPL, superior parietal gyrus; ITG, inferior temporal gyrus; OrG, orbital gyrus; SD, standard deviation.

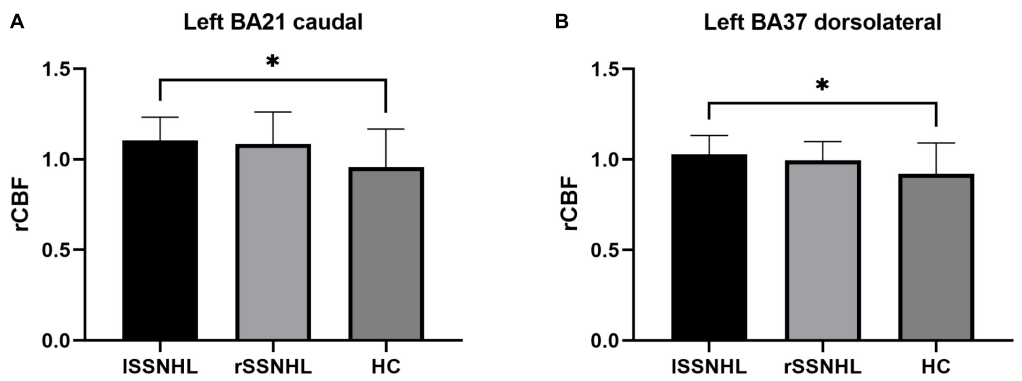

FIGURE 6 | Comparisons of auditory ROIs rCBF values among the three groups (ISSNHL, rSSNHL and HCs). ISSNHL showed increased rCBF in auditory-related areas **(A)** left BA21 caudal ($p = 0.02$) and **(B)** left BA37 dorsolateral ($p = 0.047$) compared to HC. *$p < 0.05$.

the compensation of brain function (Lomber et al., 2010; Chen et al., 2020). In this study, CBF increase in visual-related areas, suggesting that there may be similar visual compensation in patients with SSNHL. In this study, we also found the increased CBF in bilateral OrG. The OrG belongs to the ventromedial prefrontal cortex, and involves in emotional management and guidance of the concentration of attention (Hiser and Koenigs, 2018; Kuusinen et al., 2018). We speculate that the increased CBF in bilateral OrG might be caused by the emotional reaction of patients with SSNHL.

Unilateral SSNHL patients exhibited decreased CBF in attention-related areas (bilateral dlPFC), primary motor cortex (PrG) and the associative somatosensory cortex (bilateral SPL). dlPFC involves in multi-sensory integration (Fuster, 2000), goal-driven attention (Jones and Graff-Radford, 2021), and as a core node in the executive control network (ECN) (Shen et al., 2020). Attention effects were reduced by the dlPFC lesions (Knight et al., 1981). A multimodal MRI Study indicated that the dlPFC plays an important role in the recruitment of the auditory area into cross-sensory processing in long-term bilateral SNHL patients (Luan et al., 2019). A voxel-based morphometry (VBM) analysis revealed gray matter changes in the SFG and MFG, suggesting a decreased use of ECN in chronic hearing loss patients (Husain et al., 2011). Several studies found the

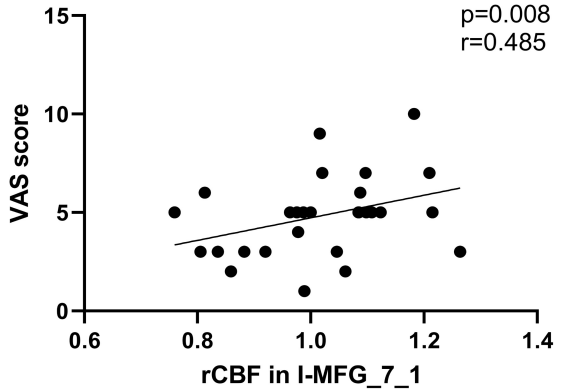

FIGURE 7 | The significant correlations between the CBF changes and the clinical data in unilateral SSNHL patients. CBF in ipsilateral MFG_7_1 of SSNHL patients was positively correlated with VAS score (r = 0.485, p = 0.008).

reduction of cortical thickness in SPL of children with SNHL (Shiohama et al., 2019; Qu et al., 2020), which is involved in processing motion stimuli (Qu et al., 2020) and cognitive control (Job et al., 2020). An age-related hearing loss ASL MRI study found the trend of reduced averaged perfusion involved multiple extra-auditory regions in the parietal and prefrontal cortex (Ponticorvo et al., 2019). Unilateral hearing loss causes the reduced attention of SSNHL patients in noisy environment by the deterioration of auditory processing, including speech perception and understanding (Ponticorvo et al., 2019). We speculate that reduced attention of SSNHL patients was related to CBF changes in the parietal and prefrontal lobes. In addition, we also explored the CBF differences of auditory-related cortex among the three groups (lSSNHL, rSSNHL, and HCs). We found that the increased CBF in left BA21 cadual and BA37 dorsolateral in patients with left-sided SSNHL, indicates that there might be a "superactivation" phenomenon in auditory-related areas (Xia et al., 2017). The same phenomenon was not found in patients with right-sided SSNHL, probably due to lateralization and the asymmetry in auditory processing (Tervaniemi and Hugdahl, 2003). The CBF in ipsilateral MFG_7_1 of SSNHL patients was positively correlated with VAS score tinnitus loudness. An fMRI study showed that the abnormal intensity of brain functional connectivity in patients with chronic tinnitus mainly occurred in the non-auditory brain region, especially in the prefrontal cortex (Araneda et al., 2018). Tinnitus may be produced to reduce perceptual uncertainty caused by peripheral auditory deafferentation (Morcom and Friston, 2012), which can explain the reason most SSNHL patients in this study accompanied by tinnitus.

There were several limitations in this study. First and foremost, the ASL data was acquired using different MR scanners, though we calculated rCBF to minimize the effects, the effects can't be avoided completely. Second, this is a cross-sectional study, and the sample size was small, we first compared the CBF difference between all the SSNHL patients and HCs, then we only investigated CBF differences in auditory-related areas in patients with lSSNHL and rSSNHL. In the future, the CBF changes of all the subregions in patients with lSSNHL and rSSNHL can be studied separately. Third, we cannot completely prevent subjects from hearing some sounds during MRI scans, although we attempted to minimize scanner noise through earplugs in this study.

CONCLUSION

Our preliminary study explored CBF pattern changes in unilateral SSNHL patients in auditory-related areas and non-auditory areas, suggesting that there may exist reduced attention and some sensory compensation in patients with SSNHL. CBF changes in ipsilateral MFG_7_1 may influence the tinnitus loudness of SSNHL patients. These findings could advance our understanding of the potential pathophysiology of unilateral SSNHL.

DATA AVAILABILITY STATEMENT

The original contributions presented in the study are included in the article/supplementary material, further inquiries can be directed to the corresponding author/s.

ETHICS STATEMENT

The studies involving human participants were reviewed and approved by the Ethics Committee of China-Japan Friendship Hospital and Fuxing Hospital. The patients/participants provided their written informed consent to participate in this study.

AUTHOR CONTRIBUTIONS

YC and HL acquired and analyzed the ASL data, and drafted the manuscript. BL, WG, HX, WZ, and JL searched and managed the literature. AY, KL, XL, YW, and HY did the MRI scanning. GM and HH designed the study and revised the manuscript. All authors contributed to the article and approved the submitted version.

FUNDING

This study was supported by the National Key Research and Development Program of China (Nos. 2020YFC2003903 and 2020YFC2007301), the grants from National Natural Science Foundation of China (NSFC) (No. 81971585), Guangzhou Science and Technology Planning Project (No. 202103010001), and Beijing Municipal Science and Technology Project (No. Z211100003521009).

ACKNOWLEDGMENTS

We thank Zeshan Yao from An-Image Technology Co., China for his contribution in processing of the ASL data.

REFERENCES

Araneda, R., Renier, L., Dricot, L., Decat, M., Ebner-Karestinos, D., Deggouj, N., et al. (2018). A key role of the prefrontal cortex in the maintenance of chronic tinnitus: An fMRI study using a Stroop task. *Neuroimage Clin.* 17, 325–334. doi: 10.1016/j.nicl.2017.10.029

Chen, J., Hu, B., Qin, P., Gao, W., Liu, C., Zi, D., et al. (2020). Altered Brain Activity and Functional Connectivity in Unilateral Sudden Sensorineural Hearing Loss. *Neural Plast.* 2020:9460364. doi: 10.1155/2020/9460364

Fan, L., Li, H., Zhuo, J., Zhang, Y., Wang, J., Chen, L., et al. (2016). The Human Brainnetome Atlas: A New Brain Atlas Based on Connectional Architecture. *Cereb. Cortex.* 26, 3508–3526. doi: 10.1093/cercor/bhw157

Fusconi, M., Chistolini, A., de Virgilio, A., Greco, A., Massaro, F., Turchetta, R., et al. (2012). Sudden sensorineural hearing loss: a vascular cause? Analysis of prothrombotic risk factors in head and neck. *Int. J. Audiol.* 51, 800–805. doi: 10.3109/14992027.2012.705904

Fuster, J. M. (2000). Executive frontal functions. *Exp. Brain Res.* 133, 66–70. doi: 10.1007/s002210000401

Haller, S., Zaharchuk, G., Thomas, D. L., Lovblad, K. O., Barkhof, F., and Golay, X. (2016). Arterial Spin Labeling Perfusion of the Brain: Emerging Clinical Applications. *Radiology* 281, 337–356. doi: 10.1148/radiol.2016150789

Hickok, G., and Poeppel, D. (2007). The cortical organization of speech processing. *Nat. Rev. Neurosci.* 8, 393–402. doi: 10.1038/nrn2113

Hiser, J., and Koenigs, M. (2018). The Multifaceted Role of the Ventromedial Prefrontal Cortex in Emotion. Decision Making, Social Cognition, and Psychopathology. *Biol. Psychiatr.* 83, 638–647. doi: 10.1016/j.biopsych.2017.10.030

Husain, F. T., Medina, R. E., Davis, C. W., Szymko-Bennett, Y., Simonyan, K., Pajor, N. M., et al. (2011). Neuroanatomical changes due to hearing loss and chronic tinnitus: a combined VBM and DTI study. *Brain Res.* 1369, 74–88. doi: 10.1016/j.brainres.2010.10.095

Job, A., Jaroszynski, C., Kavounoudias, A., Jaillard, A., and Delon-Martin, C. (2020). Functional Connectivity in Chronic Nonbothersome Tinnitus Following Acoustic Trauma: A Seed-Based Resting-State Functional Magnetic Resonance Imaging Study. *Brain Connect* 10, 279–291.

Jones, D. T., and Graff-Radford, J. (2021). Executive Dysfunction and the Prefrontal Cortex. *Continuum* 27, 1586–1601. doi: 10.1212/con.0000000000001009

Jung da, J., Park, J. H., Jang, J. H., and Lee, K. Y. (2016). The efficacy of combination therapy for idiopathic sudden sensorineural hearing loss. *Laryngoscope* 126, 1871–1876. doi: 10.1002/lary.25751

Knight, R. T., Hillyard, S. A., Woods, D. L., and Neville, H. J. (1981). The effects of frontal cortex lesions on event-related potentials during auditory selective attention. *Electroencephalogr. Clin. Neurophysiol.* 52, 571–582. doi: 10.1016/0013-4694(81)91431-0

Kuusinen, V., Cesnaite, E., Peräkylä, J., Ogawa, K. H., and Hartikainen, K. M. (2018). Orbitofrontal Lesion Alters Brain Dynamics of Emotion-Attention and Emotion-Cognitive Control Interaction in Humans. *Front. Hum. Neurosci.* 12:437. doi: 10.3389/fnhum.2018.00437

Li, X., Zhao, P., Qiu, X., Ding, H., Lv, H., Yang, Z., et al. (2020). Lateralization Effects on Cerebral Blood Flow in Patients With Unilateral Pulsatile Tinnitus Measured With Arterial Spin Labeling. *Front. Hum. Neurosci.* 14:591260. doi: 10.3389/fnhum.2020.591260

Liu, Y., Chen, Q., and Xu, Y. (2020). Research progress in refractory sudden hearing loss: steroid therapy. *J. Int. Med. Res.* 48:300060519889426. doi: 10.1177/0300060519889426

Lomber, S. G., Meredith, M. A., and Kral, A. (2010). Cross-modal plasticity in specific auditory cortices underlies visual compensations in the deaf. *Nat. Neurosci.* 13, 1421–1427. doi: 10.1038/nn.2653

Luan, Y., Wang, C., Jiao, Y., Tang, T., Zhang, J., and Teng, G. J. (2019). Prefrontal-Temporal Pathway Mediates the Cross-Modal and Cognitive Reorganization in Sensorineural Hearing Loss With or Without Tinnitus: A Multimodal MRI Study. *Front. Neurosci.* 13:222. doi: 10.3389/fnins.2019.00222

Martín-Fernández, J., Burunat, I., Modroño, C., González-Mora, J. L., and Plata-Bello, J. (2021). Music Style Not Only Modulates the Auditory Cortex, but Also Motor Related Areas. *Neuroscience* 457, 88–102. doi: 10.1016/j.neuroscience.2021.01.012

Meng, Z., Zheng, Y., Liu, S., Wang, K., Kong, X., Tao, Y., et al. (2012). Reliability and validity of the chinese (mandarin) tinnitus handicap inventory. *Clin. Exp. Otorhinolaryngol.* 5, 10–16. doi: 10.3342/ceo.2012.5.1.10

Minosse, S., Garaci, F., Martino, F., Mauro, R. D., Melis, M., Giuliano, F. D., et al. (2020). Global and local reorganization of brain network connectivity in sudden sensorineural hearing loss. *Annu. Int. Conf. IEEE Eng. Med. Biol. Soc.* 2020, 1730–1733. doi: 10.1109/embc44109.2020.9175688

Morcom, A. M., and Friston, K. J. (2012). Decoding episodic memory in ageing: a Bayesian analysis of activity patterns predicting memory. *Neuroimage* 59, 1772–1782. doi: 10.1016/j.neuroimage.2011.08.071

Mores, J. T., Bozza, A., Magni, C., Casali, R. L., and Amaral, M. (2019). Clinical profile and implications of tinnitus in individuals with and without hearing loss. *Codas* 31:e20180029. doi: 10.1590/2317-1782/20192018029

Ponticorvo, S., Manara, R., Pfeuffer, J., Cappiello, A., Cuoco, S., Pellecchia, M. T., et al. (2019). Cortical pattern of reduced perfusion in hearing loss revealed by ASL-MRI. *Hum. Brain Mapp.* 40, 2475–2487. doi: 10.1002/hbm.24538

Qu, H., Tang, H., Pan, J., Zhao, Y., and Wang, W. (2020). Alteration of Cortical and Subcortical Structures in Children With Profound Sensorineural Hearing Loss. *Front. Hum. Neurosci.* 14:565445. doi: 10.3389/fnhum.2020.565445

Shen, K. K., Welton, T., Lyon, M., McCorkindale, A. N., Sutherland, G. T., Burnham, S., et al. (2020). Structural core of the executive control network: A high angular resolution diffusion MRI study. *Hum. Brain Mapp.* 41, 1226–1236. doi: 10.1002/hbm.24870

Shiohama, T., McDavid, J., Levman, J., and Takahashi, E. (2019). The left lateral occipital cortex exhibits decreased thickness in children with sensorineural hearing loss. *Int. J. Dev. Neurosci.* 76, 34–40. doi: 10.1016/j.ijdevneu.2019.05.009

St Lawrence, K. S., and Wang, J. (2005). Effects of the apparent transverse relaxation time on cerebral blood flow measurements obtained by arterial spin labeling. *Magn. Reson. Med.* 53, 425–433. doi: 10.1002/mrm.20364

Stachler, R. J., Chandrasekhar, S. S., Archer, S. M., Rosenfeld, R. M., Schwartz, S. R., Barrs, D. M., et al. (2012). Clinical practice guideline: sudden hearing loss. *Otolaryngol. Head Neck Surg.* 146, S1–S35. doi: 10.1177/0194599812436449

Tervaniemi, M., and Hugdahl, K. (2003). Lateralization of auditory-cortex functions. *Brain Res. Brain Res. Rev.* 43, 231–246. doi: 10.1016/j.brainresrev.2003.08.004

Xia, S., Song, T., Che, J., Li, Q., Chai, C., Zheng, M., et al. (2017). Altered Brain Functional Activity in Infants with Congenital Bilateral Severe Sensorineural Hearing Loss: A Resting-State Functional MRI Study under Sedation. *Neural Plast.* 2017:8986362. doi: 10.1155/2017/8986362

Xu, H., Fan, W., Zhao, X., Li, J., Zhang, W., Lei, P., et al. (2016). Disrupted functional brain connectome in unilateral sudden sensorineural hearing loss. *Hear Res.* 335, 138–148. doi: 10.1016/j.heares.2016.02.016

Yang, M., Chen, H. J., Liu, B., Huang, Z. C., Feng, Y., Li, J., et al. (2014). Brain structural and functional alterations in patients with unilateral hearing loss. *Hear Res.* 316, 37–43. doi: 10.1016/j.heares.2014.07.006

Zhang, G. Y., Yang, M., Liu, B., Huang, Z. C., Chen, H., Zhang, P. P., et al. (2015). Changes in the default mode networks of individuals with long-term unilateral sensorineural hearing loss. *Neuroscience* 285, 333–342. doi: 10.1016/j.neuroscience.2014.11.034

Zou, Y., Ma, H., Liu, B., Li, D., Liu, D., Wang, X., et al. (2021). Disrupted Topological Organization in White Matter Networks in Unilateral Sudden Sensorineural Hearing Loss. *Front. Neurosci.* 15:666651.

Zung, W. W. (1971). A rating instrument for anxiety disorders. *Psychosomatics* 12, 371–379. doi: 10.1016/s0033-3182(71)71479-0

Zung, W. W. (1972). The Depression Status Inventory: an adjunct to the Self-Rating Depression Scale. *J. Clin. Psychol.* 28, 539–543. doi: 10.1002/1097-4679(197210)28:4<539::aid-jclp2270280427<3.0.co;2-s

Conflict of Interest: The authors declare that the research was conducted in the absence of any commercial or financial relationships that could be construed as a potential conflict of interest.

Publisher's Note: All claims expressed in this article are solely those of the authors and do not necessarily represent those of their affiliated organizations, or those of the publisher, the editors and the reviewers. Any product that may be evaluated in this article, or claim that may be made by its manufacturer, is not guaranteed or endorsed by the publisher.

Copyright © 2022 Chen, Li, Liu, Gao, Yang, Lv, Xia, Zhang, Yu, Liu, Liu, Wang, Han and Ma. This is an open-access article distributed under the terms of the Creative Commons Attribution License (CC BY). The use, distribution or reproduction in other forums is permitted, provided the original author(s) and the copyright owner(s) are credited and that the original publication in this journal is cited, in accordance with accepted academic practice. No use, distribution or reproduction is permitted which does not comply with these terms.

frontiers in Neuroscience

ORIGINAL RESEARCH
published: 14 March 2022
doi: 10.3389/fnins.2022.855483

Altered Brain Function and Causal Connectivity Induced by Repetitive Transcranial Magnetic Stimulation Treatment for Major Depressive Disorder

Muzhen Guan[1,2†], Zhongheng Wang[2†], Yanru Shi[2], Yuanjun Xie[3], Zhujing Ma[4], Zirong Liu[5], Junchang Liu[2], Xinyu Gao[4], Qingrong Tan[2] and Huaning Wang[2*]*

[1] Department of Mental Health, Xi'an Medical University, Xi'an, China, [2] Deptartment of Psychiatry, Xijing Hospital, Air Force Medical University, Xi'an, China, [3] Department of Radiology, Xijing Hospital, Fourth Military Medical University, Xi'an, China, [4] Deptartment of Psychology, Air Force Medical University, Xi'an, China, [5] Deptartment of Psychiatry, Yulin Fifth Hospital, Yuling, China

OPEN ACCESS

Edited by:
Guolin Ma,
China-Japan Friendship Hospital, China

Reviewed by:
Weihua Yue,
Peking University Sixth Hospital, China
Xiaowei Ma,
Central South University, China

***Correspondence:**
Huaning Wang
13609161341@163.com
Muzhen Guan
13484952621@163.com

[†]These authors have contributed equally to this work

Specialty section:
This article was submitted to Brain Imaging Methods, a section of the journal Frontiers in Neuroscience

Received: 15 January 2022
Accepted: 03 February 2022
Published: 14 March 2022

Citation:
Guan M, Wang Z, Shi Y, Xie Y, Ma Z, Liu Z, Liu J, Gao X, Tan Q and Wang H (2022) Altered Brain Function and Causal Connectivity Induced by Repetitive Transcranial Magnetic Stimulation Treatment for Major Depressive Disorder. Front. Neurosci. 16:855483. doi: 10.3389/fnins.2022.855483

Objective: Repetitive transcranial magnetic stimulation (rTMS) can effectively improve depression symptoms in patients with major depressive disorder (MDD); however, its mechanism of action remains obscure. This study explored the neuralimaging mechanisms of rTMS in improving depression symptoms in patients with MDD.

Methods: In this study, MDD patients with first-episode, drug-naive (n = 29) and healthy controls (n = 33) were enrolled. Depression symptoms before and after rTMS treatment were assessed using the Hamilton Depression Rating Scale (HAMD-17). Resting-state functional magnetic resonance imaging (rs-fMRI) data were collected both before and after the treatment. Changes in the brain function after the treatment were compared using the following two indices: the amplitude of the low-frequency fluctuation (ALFF) and regional homogeneity (ReHo), which are sensitive for evaluating spontaneous neuronal activity. The brain region with synchronous changes was selected as the seed point, and the differences in the causal connectivity between the seed point and whole brain before and after rTMS treatment were investigated via Granger causality analysis (GCA).

Results: Before treatment, patients with MDD had significantly lower ALFF in the left superior frontal gyrus ($p < 0.01$), higher ALFF in the left middle frontal gyrus and left precuneus ($p < 0.01$), and lower ReHo in the left middle frontal and left middle occipital gyri ($p < 0.01$) than the values observed in healthy controls. After the rTMS treatment, the ALFF was significantly increased in the left superior frontal gyrus ($p < 0.01$) and decreased in the left middle frontal gyrus and left precuneus ($p < 0.01$). Furthermore, ReHo was significantly increased in the left middle frontal and left middle occipital gyri ($p < 0.01$) in patients with MDD. Before treatment, GCA using the left middle frontal gyrus (the brain region with synchronous changes) as the seed point revealed a weak bidirectional causal connectivity between the middle and superior frontal gyri as well as a weak causal connectivity from the inferior temporal to the middle frontal

gyri. After treatment, these causal connectivities were strengthened. Moreover, the causal connectivity from the inferior temporal gyrus to the middle frontal gyri negatively correlated with the total HAMD-17 score ($r = -0.443$, $p = 0.021$).

Conclusion: rTMS treatment not only improves the local neural activity in the middle frontal gyrus, superior frontal gyrus, and precuneus but also strengthens the bidirectional causal connectivity between the middle and superior frontal gyri and the causal connectivity from the inferior temporal to the middle frontal gyri. Changes in these neuroimaging indices may represent the neural mechanisms underlying rTMS treatment in MDD.

Clinical Trial Registration: This study was registered in the Chinese Clinical Trial Registry (Registration number: ChiCTR1800019761).

Keywords: major depressive disorder, amplitude of the low-frequency fluctuation, regional homogeneity, Granger causality analysis (GCA), repetitive transcranial magnetic stimulation

INTRODUCTION

Major depressive disorder (MDD) is a mental illness characterized by mood disorders and cognitive dysfunction. By the year 2020, MDD had become the second most disabling illness and a major social and public health concern (Cheng et al., 2018). Blood-oxygen-level-dependent magnetic resonance imaging works based on the principle of detecting changes in the magnetic field properties due to the changes in local metabolism and blood oxygen level after neuronal activity (Tian et al., 2020). This imaging method has been widely used in exploring the pathophysiology of and therapeutic mechanism for MDD (Tateishi et al., 2020). The amplitude of the low-frequency fluctuation (ALFF) in the blood-oxygen-level-dependent signal is used to describe the amplitude of the spontaneous activity of the brain neurons, and larger ALFF indicates greater activity in the brain region. Regional homogeneity (ReHo) refers to the correlation of the synchronous activity in the blood-oxygen-level-dependent signal between a given voxel and its neighboring voxels (Dichter et al., 2015). The ALFF and ReHo can evaluate the spontaneous activity of neurons from different perspectives, and these two indices are complementary to each other (Kong et al., 2017).

Patients with MDD have been reported to exhibit abnormal ALFF and ReHo in the brain function (Yao et al., 2014; Li et al., 2018), A recent study investigated the MDD patients with negative bias and showed significantly higher neuronal activation in the frontal lobe (Gollan et al., 2015; Tadayonnejad et al., 2015). Studies have also indicated increased ReHo in the right postcentral gyrus and increased ALFF in the left triangular part of the inferior frontal gyrus (Xia et al., 2019; Rosenbaum et al., 2020; Liu et al., 2021). Liang et al. (2020) demonstrated that compared with healthy controls, patients with MDD had lower ReHo in the calcarine gyrus, insula, right superior temporal gyrus, left cuneus, right precuneus and right postcentral gyrus as well as lower ALFF in the calcarine gyrus, left cuneus, right inferior parietal cortex, right precuneus, and right postcentral gyrus (Kaiser et al., 2015), indicating that brain dysfunction in these patients affects their emotion regulation and social function.

Medication is the primary treatment modality used for patients with MDD. Antidepressants usually begin to show effects after 2 weeks of intake; hence, such medications (e.g., venlafaxine) should be taken for at least 4 weeks before determining the drug efficacy (Gex-Fabry et al., 2004; Otte et al., 2016). However, the first-line medication and psychotherapy often fail to show any improvement in the condition of 20–30% of patients with MDD (Loerinc et al., 2015; Maneeton et al., 2020; Cohen et al., 2021), repetitive transcranial magnetic stimulation—a non-invasive and well-tolerated physical therapy (McGirr et al., 2015) in the domain of antidepressant therapy—has been an important treatment choice (Antonenko et al., 2019; Yin et al., 2020). Zheng et al. (2020) collected the functional magnetic resonance imaging (fMRI) data of 15 patients with MDD both before and after repetitive transcranial magnetic stimulation (rTMS) treatment and found an increase in the ALFF in the left dorsolateral prefrontal cortex and left superior frontal gyrus after 2 weeks of treatment; however, they found no correlation between the change in the ALFF and symptoms of depression.

TABLE 1 | Group demographics and clinical measures (mean ± *SD*).

	MDD ($n = 29$)	Healthy controls ($n = 33$)	p
Age (years)	28.44 ± 7.91	26.53 ± 5.56	0.52
Female/male	20/9	22/11	0.88
Education (years)	14.71 ± 2.01	15.18 ± 1.99	0.36
Duration of illness (months)	4.05 ± 3.77	-	
Dose of venlafaxine (mg/d)	98.27 ± 22.16	-	

TABLE 2 | Comparisons of the score of HAMD-17 between MDD and healthy controls (mean ± *SD*).

	MDD	Healthy controls	t
Pre-rTMS	21.00 ± 5.382	2.85 ± 2.279	18.571***
Post-rTMS	9.52 ± 4.106	-	7.961***

*** *means* $p < 0.001$.

Granger causality analysis (GCA) is a method used for identifying the effective connectivity of the directed functional interactions from time-series data, and it has been widely used in resting-state fMRI studies (Berlim et al., 2014; Gaynes et al., 2014; Yang et al., 2021). Feng et al. (2016) analyzed the data of 23 drug-naive patients with first-onset MDD using GCA. They revealed that these patients had a stronger causal connectivity from the right insula, right putamen, and right caudate nucleus to the cingulate gyrus seed point as well as a weaker causal connectivity from the bilateral dorsolateral prefrontal and left orbitofrontal cortices to the cingulate gyrus seed point than those of the healthy controls (Feng et al., 2016); this indicated the dysfunction of the prefrontal cortex–limbic system in patients with MDD (Ishida et al., 2020).

However, the mechanism through which rTMS improves depression symptoms remains unclear, and few studies have explored the changes in both the ALFF and ReHo of patients with MDD receiving rTMS treatment. In this study, resting-state fMRI (rs-fMRI) was used to evaluate the changes in the abovementioned indices in patients with MDD after rTMS treatment. The brain region with synchronous changes was selected as the seed point, and the causal connectivity between the seed point and whole brain was analyzed via GCA to investigate the mechanism through which rTMS improves the symptoms of depression in patients with MDD.

MATERIALS AND METHODS

Participants

This study included drug-naive patients with first-onset MDD aged 18–45 years who visited the psychiatry outpatient clinic of the First Affiliated Hospital of Air Force Military Medical University, China, from May 2019 to October 2021. The inclusion criteria were as follows: (1) Patients who fulfilled the MDD diagnostic criteria of the Diagnostic and Statistical Manual of Mental Disorders, Fifth Edition, (2) patients with a total score of $\geq$ 18 points on the Hamilton Depression Rating Scale (HAMD-17), and (3) patients who met the enrollment requirements of the study and provided their informed consent. The exclusion criteria were as follows: (1) patients with severe physical diseases, (2) patients with a history of traumatic brain injury or brain surgery, (3) patients with a history of alcohol or substance abuse, and patients with a history of other mental or nervous system disorders.

Healthy controls matching the characteristics of patients with MDD were also recruited in this study. All participants read and understood the experimental procedures and precautions and signed informed consent forms before the commencement of the study.

Clinical Evaluation

In this study, the depression symptoms of patients with MDD were evaluated using the Hamilton Depression Rating Scale (HAMD-17) both before and after rTMS treatment (Hamilton, 1967). Higher HAMD-17 scores indicated more severe depression.

Repetitive Transcranial Magnetic Stimulation Procedure

The repetitive transcranial magnetic stimulator used in this study is a magnetic field stimulator from YIRYIDE Medical (MagPro R30, Dantec Medtronic, Denmark, CCY-IA), and the stimulation coil is a 100 mm figure of eight shaped coil. The treatment was administered at 10 Hz and 110% of the resting motor threshold (RMT) coil. The RMT is the minimum stimulation intensity that can elicit at least 5 motor evoked potential with an amplitude $>$ 50 μV with 10 consecutive stimuli to the patient (Bashir et al., 2019). According to the international 10–20 system, the rTMS treatment target is located at the F3 point of the left dorsolateral prefrontal region, one pulse per second for 10 s, with 10 s interval, consisted of 1,000 pluses. rTMS treatment was provided for 15 min per day on 15 successive days.

Research Procedures

In the current study, we conducted a single-blind, randomized, controlled study at a general hospital. The randomization program was created using a computer and executed by an investigator who is not involved in the treatment and recruitment of patients. The allocation of patients was screened, applying numbered in the sealed and opaque envelopes. The antidepressant taken by the patients was venlafaxine (H32022135). The doses of venlafaxine prescribed were tailored based on clinical considerations determined by the physicians. The patients taken oral venlafaxine were initiated at a dose of 75 mg/d. Based on response and tolerability, the dose could be titrated upward to 150 mg/d at a 2-week interval. The patient with MDD used HAMD to assess the severity of depressive symptoms before and after the treatment rTMS treatment and completed the fMRI scan.

TABLE 3 | Brain regions in ALFF between MDD and healthy controls.

Brain regions	Brodmann areas	Side	MNI coordinates			Cluster size	*t*-values
			X	*Y*	*Z*		
Superior frontal gyrus	11/10	Left	−12	60	−21	133	−8.651
Inferior temporal gyrus	20	Right	69	−27	−27	76	−6.483
Middle occipital gyrus	17	Left	−27	−102	3	207	−7.827
Inferior occipital gyrus	18	Right	30	−99	−15	79	−7.421
Precuneus	40	Left	−42	−42	36	370	6.711
Middle frontal gyrus	8	Left	−36	12	60	313	6.619

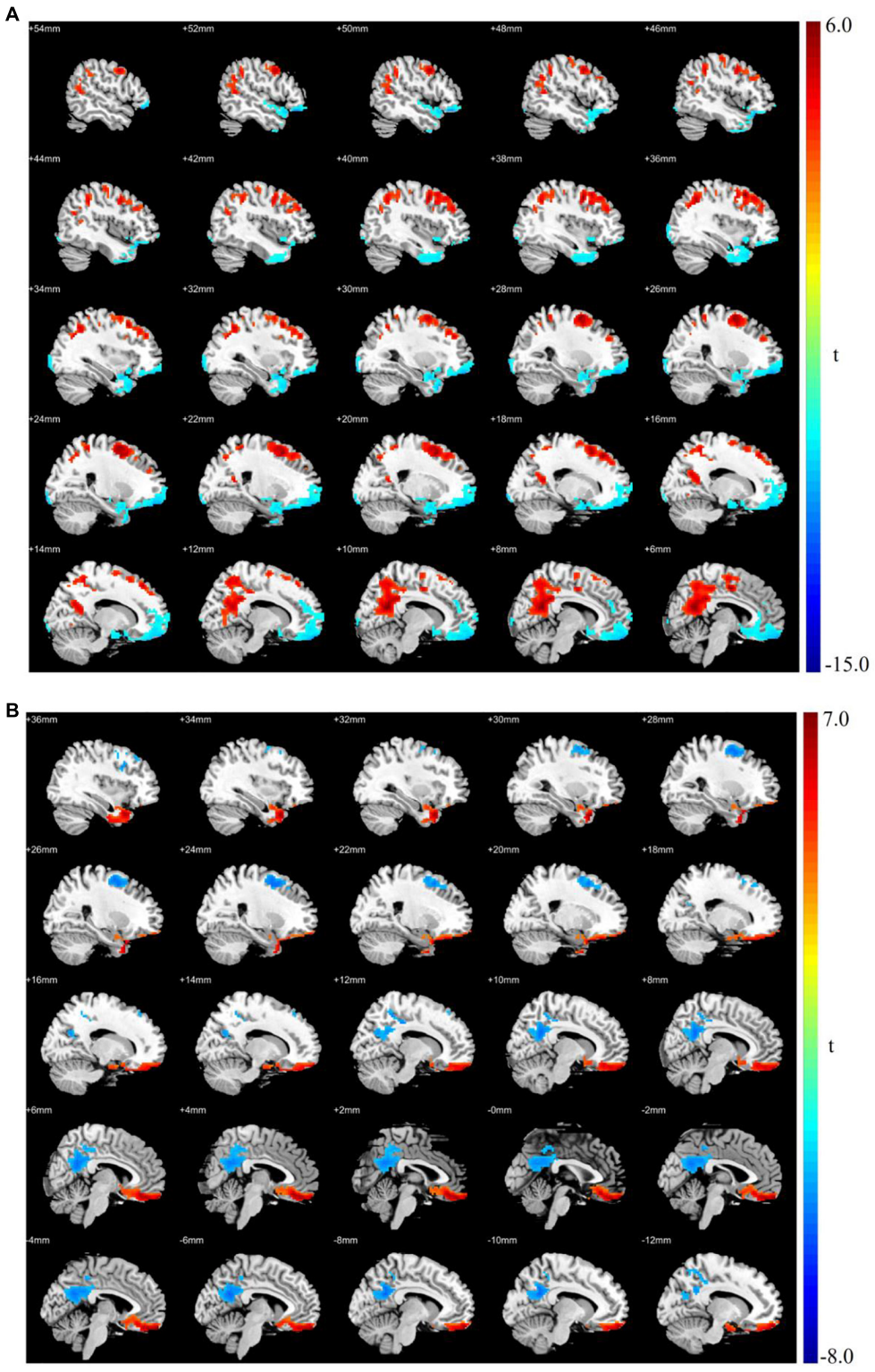

FIGURE 1 | (A) Brain regions showing significant differences of amplitude of low-frequency fluctuation (ALFF) between MDD and healthy controls. **(B)** Brain regions showing significant differences of ALFF between pre- and post-rTMS. The warm color denoted the region where ALFF is higher, and the cool color denotes the region where ALFF is lower.

Imaging Data Acquire and Preprocessing

The patients underwent scanning within 48 h before the commencement of rTMS treatment and on the day following the end of the treatment course. The healthy controls were only scanned at baseline. Imaging data were acquired on a 3.0 Tesla MRI system with a standard 8-channel head coil (GE Medical Systems, Milwaukee, WI, United States). Functional images were acquired using a gradient echo-planar imaging (EPI) sequence (repetition time, 2,000 ms; echo time, 30 ms; FOV = 240 mm × 240 mm; FA = 90; matrix = 64 × 64; slice thickness, 4.5 mm; 45 axial slices no gap. A total of 210 volumes were collected for a total scan time of 420 s.

We performed image preprocessing using DPABI[1] and SPM12.[2] Briefly steps are as follow: (1) The first ten scan volumes were discarded for steady-state magnetization; (2) subsequent images were corrected for temporal differences by slice timing and head motion by alignment; (3) the resulting functional images were spatially normalized to the standard space of the Montreal Neurological Institute (MNI) using an optimum affine transformation and non-linear deformations, and then resampled to 3 mm × 3 mm × 3 mm isotropic voxels. Nuisance signals, including those from Fristo; (4) then all the functional images were smoothed with a 6-mm full-width at half-maximum (FWHM) Gaussian filter; (5) time series linear detrending was conducted to remove low-frequency drifts and high-frequency physiological noise.

Amplitude of the Low-Frequency Fluctuation Analysis

The whole-brain ALFF was calculated using the DPABI software. First, the time series of a given voxel was extracted; next, the amplitude of all frequencies in a frequency range (which was set as 0.01–0.1 Hz in this study) was calculated via Fourier transform; then, it was converted to the power spectrum for radication to determine the ALFF. The ALFF of each voxel was standardized (subtracted from the mean value of the whole-brain signal and then divided by the standard deviation) to obtain the standardized ALFF for each participant, which was used in subsequent statistical analyses.

Regional Homogeneity Analysis

By calculating Kendall's coefficient of concordance of each voxel with a total of 26 voxel time series adjacent to the point, line, and plane of the given voxel, ReHo was determined and then divided by the mean value of the whole-brain signal to get the standardized ReHo; next, the standardized ReHo was subjected to Gaussian smoothing with the full width at a half-maximum of $6 \times 6 \times 6$ mm^3 and then used for subsequent statistical analyses.

Granger Causality Model

In this study, the left middle frontal gyrus with synchronous changes was used as the seed point, and dual-coefficient GCA was used to evaluate the causal connectivity between the time series describing the seed point and that of each voxel in the whole brain. GCA based on the whole-brain voxel level was used in the representational state transfer toolkit; the mean time series of the left middle frontal gyrus was defined as the seed-based time series x, whereas the time series of each voxel in the whole brain was represented by the time series y. A positive value of the causal connectivity from x to y indicated the existence of a causal connectivity between the activity in the middle frontal gyrus and that in the brain in the same direction, whereas a negative value indicated the opposite direction. The seed point was analyzed on the causal connectivity from the seed point to the other voxels in the whole brain (x to y) and that from the other voxels in the whole brain to the seed point (y to x). Afterward, the *Fisher R-to-Z* transformation was performed to obtain the voxel-level connectivity Z-map for subsequent statistical analyses.

[1]https://rfmri.org/DPABIDiscussion

[2]https://www.fil.ion.ucl.ac.uk/spm/software/spm12/

TABLE 4 | Brain regions in ALFF between post- and pre-rTMS.

Brain regions	Brodmann areas	Side	MNI coordinates			Cluster size	*t*-values
			X	*Y*	*Z*		
Superior frontal gyrus	11	Left	−12	57	−21	115	8.5434
Precuneus	23	Left	−6	−57	24	141	−5.859
Middle frontal gyrus	44	Left	−48	12	36	99	−5.747

TABLE 5 | Brain regions in ReHo between MDD and healthy controls.

Brain regions	Brodmann areas	Side	MNI coordinates			Cluster size	*t*-values
			X	*Y*	*Z*		
Inferior temporal gyrus	20	Right	54	−18	−24	164	4.851
Middle occipital gyrus	17	Left	0	−90	−3	488	−7.469
Middle frontal gyrus	24	Left	−34	39	15	87	−5.282
Postcentrol gyrus	3	Left	−57	−21	45	62	−5.8024

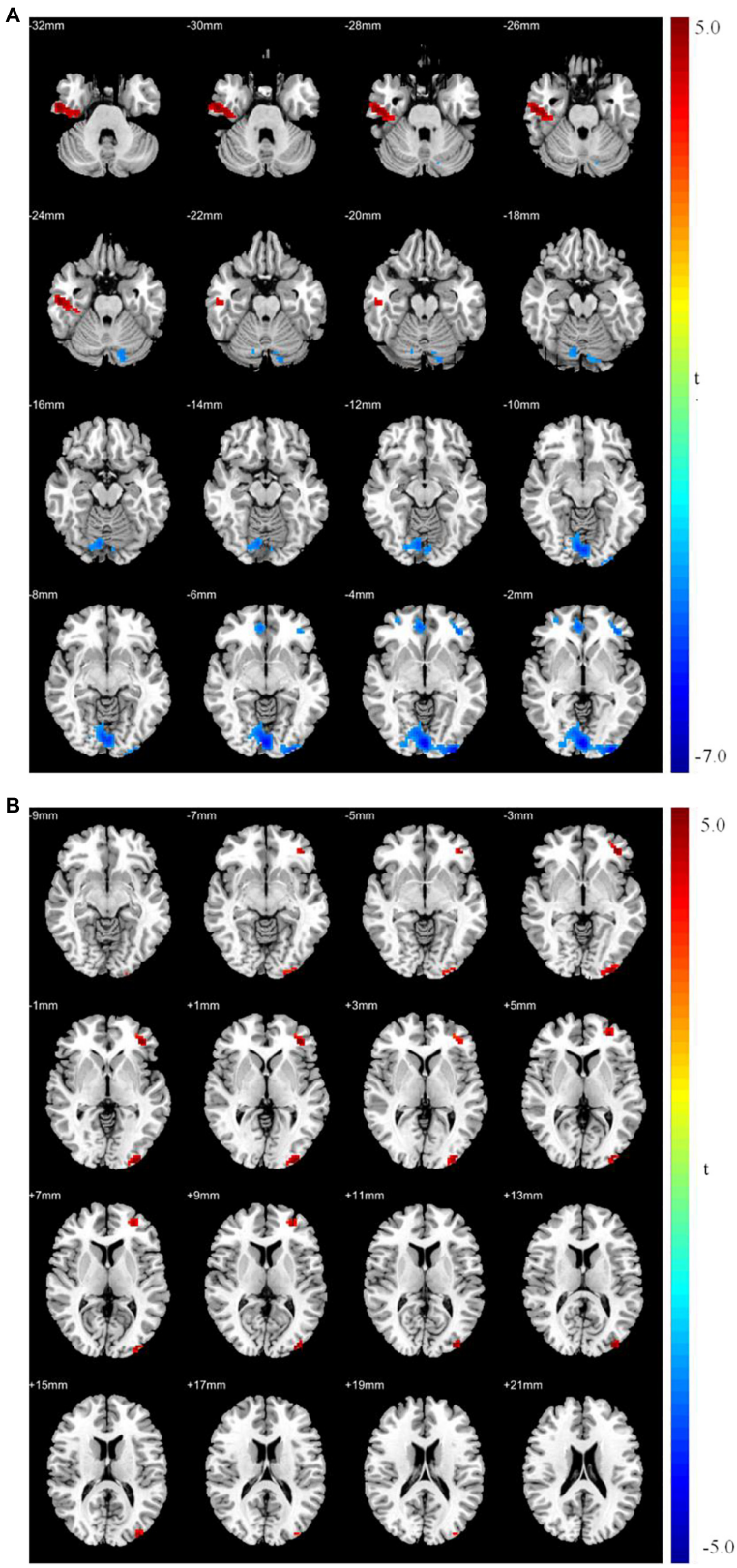

FIGURE 2 | (A) Brain regions showing significant differences of regional homogeneity (ReHo) between MDD and healthy controls. **(B)** Brain regions showing significant differences of ReHo between pre- and post-rTMS. The warm color denoted the region where ReHo is higher, and the cool color denotes the region where ReHo is lower.

Statistical Analysis

Statistical analysis of the clinical data was performed using SPSS 22.0. The paired-samples *t*-test was used to compare the ALFF and ReHo of patients with MDD before and after the treatment, whereas the independent-samples *t*-test was used to compare these neuroimaging indices of patients with MDD before and after the treatment with those of the healthy controls. The results of multiple comparisons were corrected using a Gaussian random field. The cluster level $p < 0.01$ (false discovery rate correction), voxel level $p < 0.001$, and voxel number > 70 were used to identify the brain region that differed significantly between groups. The imaging indices of different brain regions were extracted and their correlations with HAMD-17 scores were analyzed. $p < 0.05$ was considered statistically significant.

RESULTS

Participant Demographics

A total of 29 patients with MDD, with a mean age of 28.44 ± 7.909 years and mean MDD duration of 4.05 ± 3.77 months were included in the treatment group, whereas a total of 33 healthy controls with a mean age of 26.53 ± 5.563 years were included in the control group. There were no significant differences between the two groups in terms of age, sex, and education level ($p > 0.05$; **Table 1**).

HAMD-17 Score

The HAMD-17 total score was significantly higher in patients with MDD than in healthy controls, and the total score after treatment was significantly lower in patients with MDD than that before treatment in ($t = 11.313$, $p < 0.001$; **Table 2**).

Amplitude of the Low-Frequency Fluctuation Analysis

Patients with MDD had lower ALFF in the left superior frontal, right inferior temporal, left middle occipital, and right inferior occipital gyri as well as higher ALFF in the left precuneus and left middle frontal gyrus than the values observed in healthy controls (**Table 3** and **Figure 1**).

After 15 days of rTMS treatment, the ALFF was increased in the left superior frontal gyrus and decreased in the left precuneus and left middle frontal gyrus of patients with MDD (**Table 4** and **Figure 1**).

Regional Homogeneity Analysis

Patients with MDD had higher resting-state ReHo in the right inferior temporal gyrus and lower ReHo in the left middle occipital, left middle frontal, and left postcentral gyri than the values obtained in healthy controls (**Table 5** and **Figure 2**).

After 15 days of rTMS treatment, ReHo was increased in the left middle occipital and frontal gyri (**Table 6** and **Figure 2**).

Granger Causality Analysis Results

The ALFF and ReHo analyses identified the left middle frontal gyrus as a brain region with synchronous changes; therefore, it was used as the seed point for GCA. The results showed that the causal connectivity from the seed point to the left superior frontal gyrus, right middle temporal gyrus, and right caudate nucleus was significantly weak ($p < 0.05$; **Table 7** and **Figure 3**). Moreover, the causal connectivity from the left superior frontal, left inferior

TABLE 6 | Brain regions in ReHo between post- and pre-rTMS.

Brain regions	Brodmann areas	Side	MNI coordinates			Cluster size	*t*-values
			X	*Y*	*Z*		
Middle occipital gyrus	18	Left	−33	−96	0	74	4.189
Middle frontal gyrus	47	Left	−39	39	−3	57	4.237

TABLE 7 | Significant differences in Granger causality analysis between MDD and healthy controls.

Brain regions	Brodmann areas	Side	MNI coordinates			Cluster size	*t*-values
			X	*Y*	*Z*		
x to y							
MDD VS. healthy controls							
Superior frontal gyrus	46	Left	−30	18	39	345	−4.251
Middle temporal gyrus	21	Right	66	−24	0	95	−3.558
Caudate	48	Right	21	6	12	149	−3.964
y to x							
MDD VS. healthy controls							
Superior frontal gyrus	10	Left	−33	54	6	98	−3.258
Inferior temporal gyrus	20	Left	−48	−18	−30	145	−3.707
Middle occipital gyrus	19	Left	−33	−81	15	88	−3.284
Caudate	48	Right	24	0	27	98	3.514

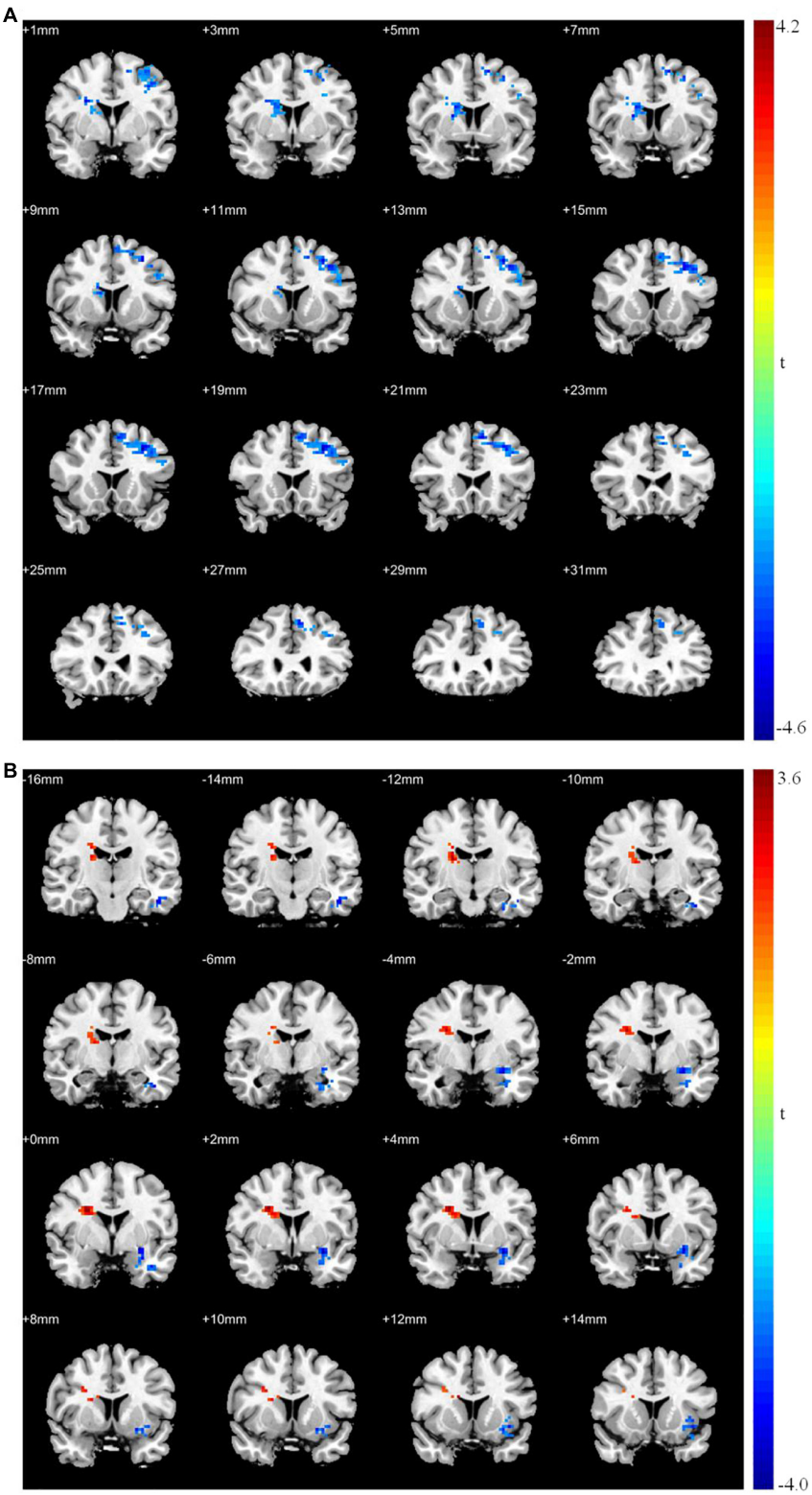

FIGURE 3 | Granger causality analysis between patients with MDD and healthy controls. **(A)** Significant different brain regions from seed point (LMFG) to whole brain regions; **(B)** significant different brain regions from whole brain regions to seed point (LMFG). Red areas show brain regions where patients with MDD had increased causal connectivity than healthy controls; Blue areas show brain regions where patients with MDD had decreased causal connectivity than healthy controls. The color bar represents *t*-values.

temporal, and left middle occipital gyri to the seed point was significantly weak ($p < 0.05$; **Table 7** and **Figure 3**). However, the causal connectivity from the right caudate nucleus to the seed point was significantly strong ($p < 0.05$; **Table 7** and **Figure 3**).

After rTMS treatment, the causal connectivity from the seed point to the superior frontal gyrus of patients with MDD was strengthened significantly ($p < 0.05$; **Table 8** and **Figure 4**) and the causal connectivity from the left superior frontal and left inferior temporal gyri of patients with MDD to the seed point was also strengthened significantly ($p < 0.05$; **Table 8** and **Figure 4**) compared with the causal connectivity before treatment.

Correlation of Granger Causality Analysis Outcomes With HAMD-17 Score in Patients With Major Depressive Disorder After Repetitive Transcranial Magnetic Stimulation Treatment

The bidirectional causal connectivity between the left middle frontal gyri and left superior frontal gyri showed no significant negative correlation with the total HAMD-17 score ($p > 0.05$), whereas the causal connectivity from the left inferior temporal to the left middle frontal gyri showed a significant negative correlation with the total HAMD-17 score ($r = -0.443$, $p = 0.021$; **Figure 5**). The receiver operator characteristic (ROC) analysis was used to assess whether causal connectivity from inferior temporal gyrus to seed point can distinguish patients (pretreatment and posttreatment) and controls. The results showed that causal connectivity from inferior temporal gyrus to seed point successfully distinguished the patient group from the healthy control group and also pretreatment patients from the posttreatment patients (**Figure 5**).

DISCUSSION

In this study, the left dorsolateral prefrontal cortex was selected as the therapeutic target where the depression symptoms of patients with MDD were improved effectively. On the basis of ALFF and ReHo analyses, the ALFF and ReHo in the left superior frontal gyrus, left precuneus, and left middle frontal gyrus were significantly increased after rTMS treatment. GCA with the left middle frontal gyrus as the seed point revealed that after rTMS treatment, the bidirectional causal connectivity between the seed point and superior frontal gyrus was significantly improved and the causal connectivity from the inferior temporal gyrus to the seed point was also significantly improved and showed a remarkable negative correlation with the total HAMD-17 score. These findings demonstrate that the changes in the brain activity and causal connectivity in the frontal, parietal, and temporal regions may constitute the neural mechanisms underlying rTMS treatment in MDD.

As an important part of the prefrontal cortex (Li et al., 2013), the left superior frontal gyrus plays a vital role in self-awareness (Niendam et al., 2012) and negative emotion regulation (Chen et al., 2022), and it is involved in attention control and emotion regulation in patients with MDD (Dutta et al., 2014; Hamilton et al., 2015). In this study, we found that patients with MDD had significantly lower ALFF in the left superior frontal gyrus than healthy controls, which is consistent with the findings of previous studies (Liu et al., 2020; Zhang et al., 2021). The decreased spontaneous activities of brain neurons in the superior frontal gyrus may lead to low mood, anhedonia, and excessive negative self-evaluation in patients with MDD (Guo et al., 2013).

The left precuneus is a part of the superior parietal lobule (Zhu et al., 2018), which is involved in high-level cognitive functions such as episodic memory and self-reflection (Li et al., 2018). Studies have found that the abnormal neuronal activity in the precuneus of patients with MDD (Zhou et al., 2017) weakens the regulation of negative emotions (Zhong et al., 2016). The number of depressive episodes has a significant positive correlation with the ALFF in the precuneus (Jing et al., 2013). The present study demonstrated that patients with MDD had significantly higher ALFF in the left precuneus than healthy controls, indicating an excessive increase and abnormal activation of neuronal activities in this brain region of these patients; this finding is consistent with the that of previous studies (Guo et al., 2013; Yao et al., 2014; Zhang et al., 2021) and may be associated with a stronger negative self-awareness and sensory dysfunction (Gong et al., 2020; Wang et al., 2020).

The middle frontal gyrus is an important part of the ventromedial prefrontal cortex, which is involved in functions such as advanced cognition, autobiographical memory (van Heeringen et al., 2017), and emotion processing (Whalley et al., 2012) and cognition control dysfunction (Han et al., 2014). Evidence shows that an abnormal middle frontal gyrus leads to the dysregulation of top-down emotions and cognitive control disorder in patients with MDD (Lu et al., 2012). The ALFF in the middle frontal gyrus can not only specifically distinguish between the depressive episode and convalescence in MDD but also objectively reflect the severity of depression symptoms to a certain extent (Zhao et al., 2020). In the present study, the ALFF in the resting-state middle frontal gyrus was increased, further supporting the abnormal function of the middle frontal gyrus in patients with MDD. Abnormalities in functions such as abnormal emotional processing and cognitive memory may result from the compensatory increase in local neuronal activities in the middle frontal gyrus of patients with MDD (Guo et al., 2013). ReHo is also a sensitivity index of neuronal activity. The present study found that ReHo in the left middle frontal gyrus of patients with MDD was decreased, which is consistent with the finding of previous studies (Liu et al., 2021). The weakened synchronous and consistent activity of neurons in the middle frontal gyrus may lead to a decline in the ability to regulate emotions, thereby causing low mood with pessimistic and negative emotions in patients with MDD. In essence, abnormal ALFF and ReHo in the middle frontal gyrus reflect the disorders of local neuronal activity in patients with MDD in the resting state, which lead to the dysfunction of the middle frontal gyrus and dysregulation of emotional responses; these may represent important pathophysiological mechanisms of MDD (Geng et al., 2019).

High-frequency rTMS can regulate the excitability of the cerebral cortex (Xie et al., 2021). In this study, the left dorsolateral

TABLE 8 | Significant differences in Granger causality analysis between pre- and post- rTMS.

Brain regions	Brodmann areas	Side	MNI coordinates			Cluster size	*t*-values
			X	*Y*	*Z*		
x to y							
Post-rTMS vs. pre- rTMS							
Superior frontal gyrus	46	Left	−33	18	39	129	4.081
y to x							
Post-rTMS vs. pre- rTMS							
Superior frontal gyrus	10	Left	−24	60	9	76	3.678
Inferior temporal gyrus	48	Left	−30	6	−12	246	3.583

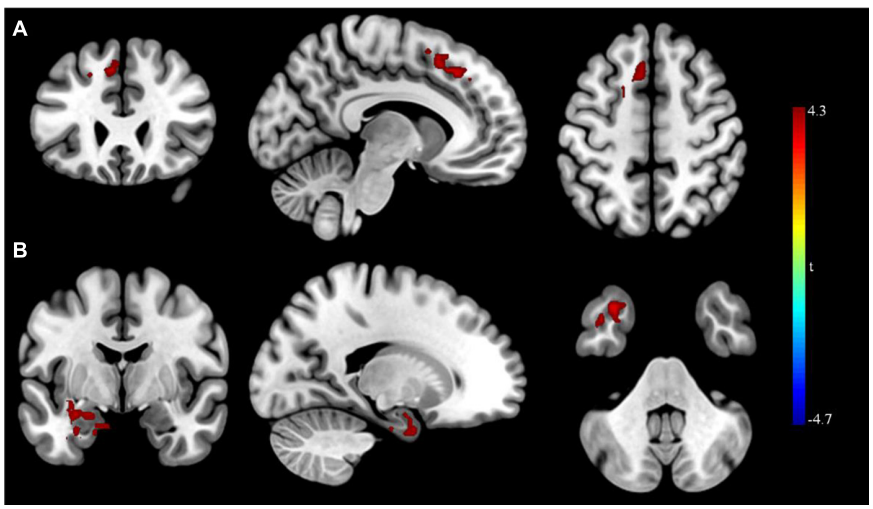

FIGURE 4 | Granger causality analysis pre- and post- rTMS in MDD. **(A)** Brain regions showing group differences in causal connectivity from the seed point (LMFG) to whole brain in pre- and post-rTMS comparison; **(B)** Brain regions showing group differences in causal connectivity from the whole brain to seed point (LMFG) in pre- and post-rTMS comparison. Red areas show brain regions where post- rTMS patients with MDD had increased causal connectivity than pre- rTMS; Blue areas show brain regions where post- rTMS patients with MDD had decreased causal connectivity than pre-rTMS. The color bar represents *t*-values.

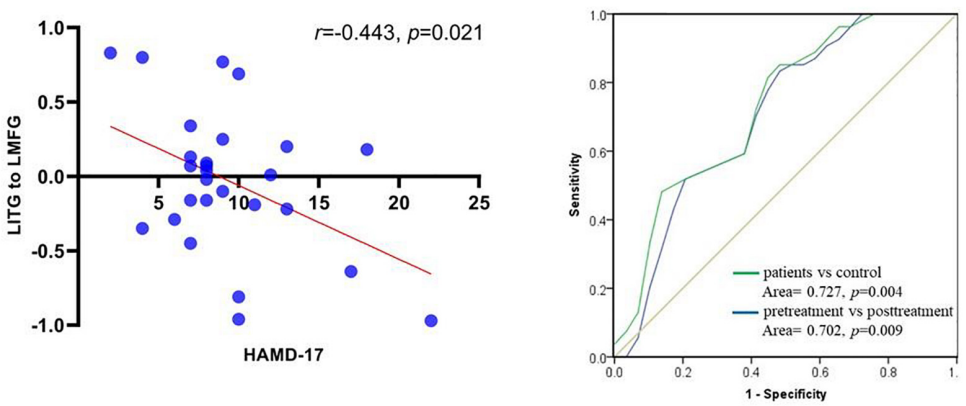

FIGURE 5 | Scatter plot between causal connectivity from left inferior temporal gyrus to left middle frontal gyrus and score of HAMD-17 in post- rTMS of patients with MDD (left); ROC curve for causal connectivity from inferior temporal gyrus to seed point with patients between patients (pretreatment and posttreatment) and control (right).

prefrontal cortex was targeted by high-frequency stimulation at 10 HZ, which directly enhanced the neural activity in the target-related brain region (Du et al., 2018). Therefore, an increase in the ALFF in the left superior frontal gyrus was observed in patients with MDD. The left superior frontal gyrus is the key brain region of the left dorsolateral prefrontal cortex. If it is damaged, the surrounding non-core organization brain regions compensate for the core brain region (Wang et al., 2019). The left middle frontal gyrus and left precuneus have a strong structural and functional connectivity with the left superior frontal gyrus (van den Heuvel and Sporns, 2011). If the function of the superior frontal gyrus is impaired, the middle frontal gyrus and precuneus may compensate for this impairment. Thus, an excessive increase in activity is observed in the left middle frontal gyrus and left precuneus. However, after treatment with high-frequency repetitive transcranial magnetic stimulation (HF-rTMS), the neural activity in the left superior frontal gyrus—the key brain region—was restored and the functions of the left middle frontal gyrus and left precuneus showed a tendency to be normal.

Our findings suggest that rTMS directly improves the neural activity in the target brain region stimulated indirectly improves the activity in local brain regions surrounding the target. The middle frontal gyrus is anatomically connected to the superior frontal gyrus through the uncinate fasciculus (Briggs et al., 2021), and this connection is involved in decision-making and emotional control. The functional connectivity between the middle and superior frontal gyri has been reported to be strengthened after antidepressant therapy (Porta-Casteràs et al., 2020). The findings of the present study are not only consistent with the findings of previous studies but also identify the direction of the causal connectivity between the middle and superior frontal gyri. The causal connectivity between the middle and superior frontal gyri was weak before treatment but strengthened after 15 days of continuous rTMS treatment; this suggests that the functional brain connectivity in patients with MDD tends to be normal and the negative thoughts can be improved, thus alleviating depression (Gröhn et al., 2019). Furthermore, the inferior temporal and middle frontal gyri are anatomically connected through the arcuate fasciculus, and these two also have a close functional connectivity, which is associated with emotional processing and episodic memory (Briggs et al., 2021). After rTMS treatment, the causal connectivity from the inferior temporal to the middle frontal gyri was strengthened and found to be negatively correlated with the total HAMD-17 score, indicating that the strengthening of such causal connectivity leads to the remission of depression symptoms.

CONCLUSION

In this study, the ALFF, ReHo, and GCA were used to explore the mechanisms through which HF-rTMS improves depression symptoms in patients with MDD. Our findings indicate that the rTMS treatment was efficacious for reducing depressive symptoms. And the rTMS treatment could regulate the neuronal activity in frontal gyrus of patients with MDD; It further enhanced the connectivity among the frontal—temporal—parietal regions of the brain after rTMS treatment. These changes may represent the neural mechanism through HF-rTMS treatment and may be used as a clinical biomarker for the objective evaluation of the therapeutic efficacy of rTMS.

LIMITATIONS

This study has some limitations. The sample size was small; this might have influenced the results and conclusion of this study. Moreover, Venlafaxine is the first of the SNRIs that provides dose-dependent norepinephrine reuptake inhibition; a dosage of 150 mg/day or higher is sufficient to produce noradrenergic activity, and it has low affinity for the postsynaptic receptors (Strawn et al., 2018; Zhou et al., 2021). A latest review has demonstrated that the brain function changes at least 4 weeks' antidepressant pharmacotherapy in patients with MDD (Cattarinussi et al., 2021). In current study, venlafaxine, which is added from 75 to 150 mg/d within 15 days during rTMS treatment, may marginally affect brain function, but *post-hoc* test is difficult to control the confusion between drugs and rTMS treatment results. Future studies should ensure a larger sample size and enhance the experimental design to further discuss the therapeutic effects of rTMS in MDD.

DATA AVAILABILITY STATEMENT

The raw data supporting the conclusions of this article will be made available by the authors, without undue reservation.

ETHICS STATEMENT

This study was reviewed and approved by the Medical Ethics Committee of Xijing Hospital (Approval document Number: KY20202055-F-1). The patients/participants provided their written informed consent to participate in this study.

AUTHOR CONTRIBUTIONS

MG, HW, and QT conceived and designed the experiments. MG, YS, ZM, YX, and ZW performed the experiments. MG, ZL, JL, and XG analyzed the data. HW and QT conceived the project and modified the manuscript. All authors read and approved the final manuscript.

FUNDING

This work was supported by the National Nature Science Foundation of China (No. 81974215 to HW), the National Nature Science Founda tion of China (No. 81630032 to QT), and the Project of Natural Science of Shaanxi Science and Technology Department (No. 2021JQ-783).

REFERENCES

Antonenko, D., Thielscher, A., Saturnino, G. B., Aydin, S., Ittermann, B., Grittner, U., et al. (2019). Towards precise brain stimulation: is electric field simulation related to neuromodulation? *Brain Stimul.* 12, 1159–1168. doi: 10.1016/j.brs.2019.03.072

Bashir, S., Ahmad, S., Alatefi, M., Hamza, A., Sharaf, M., and Fecteau, S. (2019). Effects of anodal transcranial direct current stimulation on motor evoked potentials variability in humans. *Physiol. Rep.* 7:e14087. doi: 10.14814/phy2.14087

Berlim, M. T., van den, Eynde, F., Tovar-Perdomo, S., and Daskalakis, Z. J. (2014). Response, remission and drop-out rates following high-frequency repetitive transcranial magnetic stimulation (rTMS) for treating major depression: a systematic review and meta-analysis of randomized, double-blind and sham-controlled trials. *Psychol. Med.* 44, 225–239. doi: 10.1017/S0033291713000512

Briggs, R. G., Lin, Y.-H., Dadario, N. B., Kim, S. J., Young, I. M., Bai, M. Y., et al. (2021). Anatomy and white matter connections of the middle frontal gyrus. *World Neurosurg.* 150, e520–e529. doi: 10.1016/j.wneu.2021.03.045

Cattarinussi, G., Delvecchio, G., Maggioni, E., Bressi, C., and Brambilla, P. (2021). Ultra-high field imaging in major depressive disorder: a review of structural and functional studies. *J. Affect Disord.* 290, 65–73. doi: 10.1016/j.jad.2021.04.056

Chen, Z., Zhao, S., Tian, S., Yan, R., Wang, H., Wang, X., et al. (2022). Diurnal mood variation symptoms in major depressive disorder associated with evening chronotype: evidence from a neuroimaging study. *J. Affect. Disord.* 298, 151–159. doi: 10.1016/j.jad.2021.10.087

Cheng, W., Rolls, E. T., Ruan, H., and Feng, J. (2018). Functional connectivities in the brain that mediate the association between depressive problems and sleep quality. *JAMA Psychiatry* 75, 1052–1061. doi: 10.1001/jamapsychiatry.2018.1941

Cohen, S. E., Zantvoord, J. B., Wezenberg, B. N., Bockting, C. L. H., and Van Wingen, G. A. (2021). Magnetic resonance imaging for individual prediction of treatment response in major depressive disorder: a systematic review and meta-analysis. *Transl. Psychiat.* 11, 1–10. doi: 10.1038/s41398-021-01286-x

Dichter, G. S., Gibbs, D., and Smoski, M. J. (2015). A systematic review of relations between resting-state functional-MRI and treatment response in major depressive disorder. *J. Affect. Disord.* 172, 8–17. doi: 10.1016/j.jad.2014.09.028

Du, L., Liu, H., Du, W., Chao, F., Zhang, L., Wang, K., et al. (2018). Stimulated left DLPFC-nucleus accumbens functional connectivity predicts the anti-depression and anti-anxiety effects of rTMS for depression. *Transl. Psychiat.* 7, 1–10. doi: 10.1038/s41398-017-0005-6

Dutta, A., Mckie, S., and Deakin, J. F. W. (2014). Resting state networks in major depressive disorder. *Psychiatry Res.* 224, 139–151. doi: 10.1016/j.pscychresns.2014.10.003

Feng, Z., Xu, S., Huang, M., Shi, Y., Xiong, B., and Yang, H. (2016). Disrupted causal connectivity anchored on the anterior cingulate cortex in first-episode medication-naive major depressive disorder. *Prog. Neuro-Psychoph.* 64, 124–130. doi: 10.1016/j.pnpbp.2015.07.008

Gaynes, B. N., Lloyd, S. W., Lux, L., Gartlehner, G., Hansen, R. A., Brode, S., et al. (2014). Repetitive transcranial magnetic stimulation for treatment-resistant depression: a systematic review and meta-analysis. *J. Clin. Psychiatry* 75, 477–489.

Geng, J., Yan, R., Shi, J., Chen, Y., Mo, Z., Shao, J., et al. (2019). Altered regional homogeneity in patients with somatic depression: A resting-state fMRI study. *J. Affect Disord.* 246, 498–505. doi: 10.1016/j.jad.2018.12.066

Gex-Fabry, M., Balant-Gorgia, A. E., Balant, L. P., Rudaz, S., Veuthey, J.-L., and Bertschy, G. (2004). Time course of clinical response to venlafaxine: relevance of plasma level and chirality. *Eur. J. Clin. Pharmacol.* 59, 883–891. doi: 10.1007/s00228-003-0710-3

Gollan, J. K., Connolly, M., Buchanan, A., Hoxha, D., Rosebrock, L., Cacioppo, J., et al. (2015). Neural substrates of negativity bias in women with and without major depression. *Biol. Psychol.* 109, 184–191. doi: 10.1016/j.biopsycho.2015.06.003

Gong, J., Wang, J., Qiu, S., Chen, P., Luo, Z., Wang, J., et al. (2020). Common and distinct patterns of intrinsic brain activity alterations in major depression and bipolar disorder: voxel-based meta-analysis. *Transl. Psychiat.* 10, 1–13. doi: 10.1038/s41398-020-01036-5

Gröhn, H., Gillick, B. T., Tkáč, I., Bednařík, P., Mascali, D., Deelchand, D. K., et al. (2019). Influence of repetitive transcranial magnetic stimulation on human neurochemistry and functional connectivity: a Pilot MRI/MRS study at 7 T. *Front. Neurosci.* 13:1260. doi: 10.3389/fnins.2019.01260

Guo, W.-B., Liu, F., Xun, G.-L., Hu, M.-R., Guo, X.-F., Xiao, C.-Q., et al. (2013). Reversal alterations of amplitude of low-frequency fluctuations in early and late onset, first-episode, drug-naive depression. *Prog. Neuro-Psychoph.* 40, 153–159.

Hamilton, J. P., Farmer, M., Fogelman, P., and Gotlib, I. H. (2015). Depressive rumination, the default-mode network, and the dark matter of clinical neuroscience. *Biol. Psychiatry* 78, 224–230. doi: 10.1016/j.biopsych.2015.02.020

Hamilton, M. A. X. (1967). Development of a rating scale for primary depressive illness. *Br. J. Soc. Clin. Psychol.* 6, 278–296. doi: 10.1111/j.2044-8260.1967.tb00530.x

Han, K.-M., Choi, S., Jung, J., Na, K.-S., Yoon, H.-K., Lee, M.-S., et al. (2014). Cortical thickness, cortical and subcortical volume, and white matter integrity in patients with their first episode of major depression. *J. Affect. Disord.* 155, 42–48. doi: 10.1016/j.jad.2013.10.021

Ishida, T., Dierks, T., Strik, W., and Morishima, Y. (2020). Converging Resting State Networks Unravels Potential Remote Effects of Transcranial Magnetic Stimulation for Major Depression. *Front. Psychia.* 11, 1–13. doi: 10.3389/fpsyt.2020.00836

Jing, B., Liu, C.-H., Ma, X., Yan, H.-G., Zhuo, Z.-Z., Zhang, Y., et al. (2013). Difference in amplitude of low-frequency fluctuation between currently depressed and remitted females with major depressive disorder. *Brain Res.* 1540, 74–83. doi: 10.1016/j.brainres.2013.09.039

Kaiser, R. H., Andrews-Hanna, J. R., Wager, T. D., and Pizzagalli, D. A. (2015). Large-scale network dysfunction in major depressive disorder: a meta-analysis of resting-state functional connectivity. *JAMA Psychiatry* 72, 603–611. doi: 10.1001/jamapsychiatry.2015.0071

Kong, X.-M., Xu, S.-X., Sun, Y., Wang, K.-Y., Wang, C., Zhang, J., et al. (2017). Electroconvulsive therapy changes the regional resting state function measured by regional homogeneity (ReHo) and amplitude of low frequency fluctuations (ALFF) in elderly major depressive disorder patients: an exploratory study. *Psychiat. Res. Neuroim.* 264, 13–21. doi: 10.1016/j.pscychresns.2017.04.001

Li, G., Rossbach, K., Zhang, A., Liu, P., and Zhang, K. (2018). Resting-state functional changes in the precuneus within first-episode drug-naive patients with MDD. *Neuropsych. Dis. Treat.* 14:1991. doi: 10.2147/NDT.S168060

Li, W., Qin, W., Liu, H., Fan, L., Wang, J., Jiang, T., et al. (2013). Subregions of the human superior frontal gyrus and their connections. *Neuroimage* 78, 46–58. doi: 10.1016/j.neuroimage.2013.04.011

Liang, S., Xue, K., Wang, W., Yu, W., Ma, X., Luo, S., et al. (2020). Altered brain function and clinical features in patients with first-episode, drug naïve major depressive disorder: A resting-state fMRI study. *Psychiat. Res. Neuroim.* 303:111134. doi: 10.1016/j.pscychresns.2020.111134

Liu, P., Tu, H., Zhang, A., Yang, C., Liu, Z., Lei, L., et al. (2021). Brain functional alterations in MDD patients with somatic symptoms: A resting-state fMRI study. *J. Affect. Disord.* 295, 788–796. doi: 10.1016/j.jad.2021.08.143

Liu, X., Hou, Z., Yin, Y., Xie, C., Zhang, H., Zhang, H., et al. (2020). Dopamine multilocus genetic profile, spontaneous activity of left superior temporal gyrus, and early therapeutic effect in major depressive disorder. *Front. Psychiatry* 11:1432. doi: 10.3389/fpsyt.2020.591407

Loerinc, A. G., Meuret, A. E., Twohig, M. P., Rosenfield, D., Bluett, E. J., and Craske, M. G. (2015). Response rates for CBT for anxiety disorders: Need for standardized criteria. *Clin. Psychol. Rev.* 42, 72–82. doi: 10.1016/j.cpr.2015.08.004

Lu, Q., Li, H., Luo, G., Wang, Y., Tang, H., Han, L., et al. (2012). Impaired prefrontal–amygdala effective connectivity is responsible for the dysfunction of emotion process in major depressive disorder: a dynamic causal modeling study on MEG. *Neurosci. Lett.* 523, 125–130. doi: 10.1016/j.neulet.2012.06.058

Maneeton, B., Maneeton, N., Woottiluk, P., and Likhitsathian, S. (2020). Repetitive transcranial magnetic stimulation combined with anti-depressants for the first episode of major depressive disorder. *Curr. Neuropharmacol.* 18, 852–860. doi: 10.2174/1570159X18666200221113134

McGirr, A., Van Den Eynde, F., Tovar-Perdomo, S., Fleck, M. P. A., and Berlim, M. T. (2015). Effectiveness and acceptability of accelerated repetitive transcranial magnetic stimulation (rTMS) for treatment-resistant major depressive disorder: an open label trial. *J. Affect. Disord.* 173, 216–220. doi: 10.1016/j.jad.2014.10.068

Niendam, T. A., Laird, A. R., Ray, K. L., Dean, Y. M., Glahn, D. C., and Carter, C. S. (2012). Meta-analytic evidence for a superordinate cognitive control network subserving diverse executive functions. *Cogn. Affect Behav. Neurosci.* 12, 241–268.

Otte, C., Gold, S. M., Penninx, B. W., Pariante, C. M., Etkin, A., Fava, M., et al. (2016). Major depressive disorder. *Nat. Rev. Dis. Prim.* 2, 1–20. doi: 10.1093/med/9780198810940.003.0001

Porta-Casteràs, D., Cano, M., Camprodon, J. A., Loo, C., Palao, D., Soriano-Mas, C., et al. (2020). A multimetric systematic review of fMRI findings in patients with MDD receiving ECT. *Prog. Neuro-Psychoph* 2020:110178. doi: 10.1016/j.pnpbp.2020.110178

Rosenbaum, D., Int-Veen, I., Kroczek, A., Hilsendegen, P., Velten-Schurian, K., Bihlmaier, I., et al. (2020). Amplitude of low frequency fluctuations (ALFF) of spontaneous and induced rumination in major depression: an fNIRS study. *Sci. Rep. UK* 10, 1–13. doi: 10.1038/s41598-020-78317-y

Strawn, J. R., Geracioti, L., Rajdev, N., Clemenza, K., and Levine, A. (2018). Pharmacotherapy for generalized anxiety disorder in adult and pediatric patients: an evidencebased treatment review. *Expert Opin. Pharmacother.* 19, 1057–1070. doi: 10.1080/14656566.2018.1491966

Tadayonnejad, R., Yang, S. L., Kumar, A., and Ajilore, O. (2015). Clinical, cognitive, and functional connectivity correlations of resting-state intrinsic brain activity alterations in unmedicated depression. *J. Affect. Disord.* 172, 241–250. doi: 10.1016/j.jad.2014.10.017

Tateishi, H., Mizoguchi, Y., Kawaguchi, A., Imamura, Y., Matsushima, J., Kunitake, H., et al. (2020). Changes in interleukin-1 beta induced by rTMS are significantly correlated with partial improvement of cognitive dysfunction in treatment-resistant depression: a pilot study. *Psychiat. Res.* 289:112995. doi: 10.1016/j.psychres.2020.112995

Tian, L., Sun, S. S., Cui, L. B., Wang, S. Q., Peng, Z. W., Tan, Q. R., et al. (2020). Repetitive transcranial magnetic stimulation elicits antidepressant- and anxiolytic-like effect via nuclear factor-E2-related factor 2-mediated anti-inflammation mechanism in rats. *Neuroscience* 429, 119–133. doi: 10.1016/j.neuroscience.2019.12.025

van den Heuvel, M. P., and Sporns, O. (2011). Rich-club organization of the human connectome. *J. Neurosci.* 31, 15775–15786. doi: 10.1523/JNEUROSCI.3539-11.2011

van Heeringen, K., Wu, G.-R., Vervaet, M., Vanderhasselt, M.-A., and Baeken, C. (2017). Decreased resting state metabolic activity in frontopolar and parietal brain regions is associated with suicide plans in depressed individuals. *J. Psychiatric. Res.* 84, 243–248. doi: 10.1016/j.jpsychires.2016.10.011

Wang, M., Ju, Y., Lu, X., Sun, J., Dong, Q., Liu, J., et al. (2020). Longitudinal changes of amplitude of low-frequency fluctuations in MDD patients: A 6-month follow-up resting-state functional magnetic resonance imaging study. *J. Affect. Disord.* 276, 411–417. doi: 10.1016/j.jad.2020.07.067

Wang, X., Qin, J., Zhu, J., Bi, K., Zhang, S., and Yan, R. (2019). Rehabilitative compensatory mechanism of hierarchical subnetworks in major depressive disorder: a longitudinal study across multi-sites. *Eur. Psychiat.* 58, 54–62. doi: 10.1016/j.eurpsy.2019.02.004

Whalley, M. G., Rugg, M. D., and Brewin, C. R. (2012). Autobiographical memory in depression: an fMRI study. *Psychiatry Res.* 201, 98–106.

Xia, M., Si, T., Sun, X., Ma, Q., Liu, B., Wang, L., et al. (2019). Reproducibility of functional brain alterations in major depressive disorder: Evidence from a multisite resting-state functional MRI study with 1,434 individuals. *Neuroimage* 189, 700–714. doi: 10.1016/j.neuroimage.2019.01.074

Xie, Y., Guan, M., Wang, Z., Ma, Z., Wang, H., Fang, P., et al. (2021). rTMS induces brain functional and structural alternations in schizophrenia patient with auditory verbal hallucination. *Front. Neurosci.* 2021:15. doi: 10.3389/fnins.2021.722894

Yang, L., Wei, A. H., Ouyang, T. T., Cao, Z. Z., Duan, A. W., and Zhang, H. H. (2021). Functional plasticity abnormalities over the lifespan of first-episode patients with major depressive disorder: a resting state fMRI study. *Ann. Transl. Med.* 9:349. doi: 10.21037/atm-21-367

Yao, Z., Yan, R., Wei, M., Tang, H., Qin, J., and Lu, Q. (2014). Gender differences in brain activity and the relationship between brain activity and differences in prevalence rates between male and female major depressive disorder patients: a resting-state fMRI study. *Clin. Neurophysiol.* 125, 2232–2239. doi: 10.1016/j.clinph.2014.03.006

Yin, M., Liu, Y., Zhang, L., Zheng, H., Peng, L., Ai, Y., et al. (2020). Effects of rTMS Treatment on cognitive impairment and resting-state brain activity in stroke patients: a randomized clinical trial. *Front. Neural. Circuits* 14:62. doi: 10.3389/fncir.2020.563777

Zhang, B., Qi, S., Liu, S., Liu, X., Wei, X., and Ming, D. (2021). Altered spontaneous neural activity in the precuneus, middle and superior frontal gyri, and hippocampus in college students with subclinical depression. *BMC Psychiatry* 21, 1–10. doi: 10.1186/s12888-021-03292-1

Zhao, P., Yan, R., Wang, X., Geng, J., Chattun, M. R., Wang, Q., et al. (2020). Reduced resting state neural activity in the right orbital part of middle frontal gyrus in anxious depression. *Front. Psychiatry* 10:994. doi: 10.3389/fpsyt.2019.00994

Zheng, A., Yu, R., Du, W., Liu, H., Zhang, Z., Xu, Z., et al. (2020). Two-week rTMS-induced neuroimaging changes measured with fMRI in depression. *J. Affect. Disord.* 270, 15–21. doi: 10.1016/j.jad.2020.03.038

Zhong, X., Pu, W., and Yao, S. (2016). Functional alterations of fronto-limbic circuit and default mode network systems in first-episode, drug-naïve patients with major depressive disorder: a meta-analysis of resting-state fMRI data. *J. Affect. Disord.* 206, 280–286. doi: 10.1016/j.jad.2016.09.005

Zhou, M., Hu, X., Lu, L., Zhang, L., Chen, L., Gong, Q., et al. (2017). Intrinsic cerebral activity at resting state in adults with major depressive disorder: a meta-analysis. *Prog. Neuropsychopharmacol. Biol. Psychiatry* 75, 157–164. doi: 10.1016/j.pnpbp.2017.02.001

Zhou, J. J., Wang, X., Feng, L., Xiao, L., Yang, R., Zhu, X. Q., et al. (2021). Venlafaxine vs. fluoxetine in postmenopausal women with major depressive disorder: an 8-week, randomized, single-blind, active-controlled study. *BMC. psychia.* 21, 1–10. doi: 10.1186/s12888-021-03253-8

Zhu, J., Lin, X., Lin, C., Zhuo, C., and Yu, Y. (2018). Selective functional dysconnectivity of the dorsal-anterior subregion of the precuneus in drug-naive major depressive disorder. *J. Affect. Disord.* 225, 676–683. doi: 10.1016/j.jad.2017.08.084

Conflict of Interest: The authors declare that the research was conducted in the absence of any commercial or financial relationships that could be construed as a potential conflict of interest.

Publisher's Note: All claims expressed in this article are solely those of the authors and do not necessarily represent those of their affiliated organizations, or those of the publisher, the editors and the reviewers. Any product that may be evaluated in this article, or claim that may be made by its manufacturer, is not guaranteed or endorsed by the publisher.

Copyright © 2022 Guan, Wang, Shi, Xie, Ma, Liu, Liu, Gao, Tan and Wang. This is an open-access article distributed under the terms of the Creative Commons Attribution License (CC BY). The use, distribution or reproduction in other forums is permitted, provided the original author(s) and the copyright owner(s) are credited and that the original publication in this journal is cited, in accordance with accepted academic practice. No use, distribution or reproduction is permitted which does not comply with these terms.

frontiers in Neuroscience

ORIGINAL RESEARCH
published: 14 March 2022
doi: 10.3389/fnins.2022.839485

Preoperative Collateral Perfusion Using Arterial Spin Labeling: A Predictor of Surgical Collaterals in Moyamoya Angiopathy

Maoxue Wang[1†], Yi Wang[2†], Wen Zhang[1], Xiance Zhao[3], Yongbo Yang[2] and Bing Zhang[1,4*]*

[1] Department of Radiology, The Affiliated Drum Tower Hospital of Nanjing University Medical School, Nanjing, China, [2] Department of Neurosurgery, The Affiliated Drum Tower Hospital of Nanjing University Medical School, Nanjing, China, [3] Philips Healthcare, Shanghai, China, [4] Institute of Brain Science, Nanjing University, Nanjing, China

OPEN ACCESS

Edited by:
Long-Biao Cui,
Fourth Military Medical University, China

Reviewed by:
Binbin Sui,
Capital Medical University, China
Huilin Zhao,
Shanghai Jiao Tong University, China

***Correspondence:**
Yongbo Yang
yangyongbo2000@163.com
Bing Zhang
zhangbing_nanjing@nju.edu.cn

[†]These authors have contributed equally to this work and share first authorship

Specialty section:
This article was submitted to Brain Imaging Methods, a section of the journal Frontiers in Neuroscience

Received: 20 December 2021
Accepted: 25 January 2022
Published: 14 March 2022

Citation:
Wang M, Wang Y, Zhang W, Zhao X, Yang Y and Zhang B (2022) Preoperative Collateral Perfusion Using Arterial Spin Labeling: A Predictor of Surgical Collaterals in Moyamoya Angiopathy. Front. Neurosci. 16:839485. doi: 10.3389/fnins.2022.839485

Objectives: Various degrees of surgical collateral circulation are often found in moyamoya angiopathy (MMA) patients after revascularization. Little is known about arterial spin labeling (ASL) that affects surgical collateral circulation. This study aimed to investigate the effect of ASL on surgical collaterals in patients with MMA after combined bypass surgery.

Methods: MMA patients with complete radiological and clinical information, who had undergone combined bypass, were enrolled in this study. Surgical collaterals were classified as good or poor based on the Matsushima standard. Cerebral perfusion on ASL was quantitatively analyzed as relative cerebral blood flow (rCBF). The qualitative collateral score was calculated using a four-grade scale. Univariable and multivariable logistic regressions were performed to identify the predictors for surgical collaterals after combined bypass.

Results: In total, 66 hemispheres of 61 patients (47 years old ± 8.66) were prospectively included (29 and 37 hemispheres with good and poor surgical collaterals, respectively). The presurgical collateral score was significantly lower in patients with good surgical collaterals (13.72 scores ± 7.83) than in those with poor surgical collaterals (19.16 scores ± 6.65, $P = 0.005$). The presurgical rCBF and modified Rankin scale (mRS) scores were not significantly different between the two groups ($P_{rCBF} = 0.639$, $P_{mRS} = 0.590$). The collateral score was significantly elevated (good: 13.72 scores ± 7.83 *vs*. 20.79 scores ± 6.65, $P < 0.001$; poor: 19.16 scores ± 6.65 *vs*. 22.84 scores ± 5.06, $P < 0.001$), and the mRS was reduced (good: 1.66 scores ± 1.14 *vs*. 0.52 scores ± 0.83, $P < 0.001$; poor: 1.49 scores ± 0.90 *vs*. 0.62 scores ± 0.76, $P < 0.001$) in patients after revascularization. Multivariable logistic regression showed that preoperative collateral scores [odds ratio (OR): 0.791; 95% confidence interval (CI): 0.695, 0.900; $P < 0.001$], age (OR: 0.181; 95% CI: 0.039, 0.854; $P = 0.031$), sex (OR: 0.154; 95% CI: 0.035, 0.676; $P = 0.013$), and hypertension (OR: 0.167; 95%

CI: 0.038, 0.736; P = 0.018) were predictors of surgical collaterals after combined revascularization.

Conclusion: The preoperative collateral score based on ASL could be a predictor for surgical collaterals in patients with MMA after combined bypass surgery. Combined with age, sex, and hypertension, it may have a better predictive effect.

Keywords: arterial spin labeling, collateral circulation, revascularization, moyamoya angiopathy, predictors

INTRODUCTION

Moyamoya angiopathy (MMA) is a chronic and progressive cerebrovascular disease that is characterized by stenosis of the distal internal carotid artery (ICA), proximal, middle cerebral artery, and anterior cerebral artery. Ischemic stroke, cerebral hemorrhage, headache, and dizziness often occur in patients with MMA (Herve et al., 2018). Revascularization, including direct bypass, indirect bypass, and combined bypass, was recommended to reduce the risk of cerebrovascular events by improving cerebral perfusion (Miyamoto et al., 2014; Zhang et al., 2020). Direct and combined bypass was often used in adults; in addition, the combined bypass had the advantages of both direct and indirect bypass (Kronenburg et al., 2014; Esposito et al., 2018).

Various degrees of surgical collateral circulation are often found in MMA patients after revascularization. Good surgical collateral circulation has been found to be associated with better long-term outcomes compared with the poor group (Zhao et al., 2019). Hemorrhagic onset and ICA moyamoya vessels have an important role in the formation of surgical collateral circulation in MMA patients after indirect bypass surgery (Zhao et al., 2019). Moreover, presurgical collateral stage, p.R4810K variant, and age were also found to be correlated with good surgical collateral circulation in MMA patients after 10 years of indirect bypass surgery (Wang Q. N. et al., 2021).

The presurgical collateral stage was evaluated in a previous study according to the Suzuki stage and leptomeningeal system, which need to be based on digital subtraction angiography (DSA; Liu et al., 2019; Wang Q. N. et al., 2021). However, DSA is an invasive and radiative exam that requires contrast media. Arterial spin labeling (ASL) is a noninvasive magnetic resonance (MR) imaging method without radiation and contrast media, which uses hydrogen protons in the blood as endogenous tracers (Hernandez-Garcia et al., 2019). Three-dimensional (3D) pseudo-continuous ASL (pCASL) was recommended while considering the sufficient image quality (Alsop et al., 2015).

Recently, 4D magnetic resonance angiography (MRA) based on ASL had been shown to have a high consistency with DSA in the presence of distal collaterals in MMA patients (Togao et al., 2018; Wang M. et al., 2021). In addition, ASL can also evaluate cerebral perfusion changes and predict the intensity of collateral flow in patients with MMA compared with DSA (Zaharchuk et al., 2011; Lee et al., 2018). However, little is known about the factors based on ASL that affect surgical collateral circulation after combined bypass surgery.

The purpose of this study was to investigate the effect of ASL on surgical collateral circulation in patients with MMA after combined bypass surgery.

MATERIALS AND METHODS

The local institutional review board approved the study protocol before trial initiation (2021-026-02). Written consent was obtained from all subjects before the examinations.

Subjects

Moyamoya angiopathy patients in a single center from December 2019 to December 2021 were enrolled in this prospective study. Inclusion criteria included the following: (1): MMA patients were diagnosed on MRA or DSA; (2) pre- and postoperative ASL, postoperative super-selective 4D MRA, and susceptibility-weighted imaging (SWI) was acquired; (3) the follow-up time was more than 3 months; and (4) all patients underwent combined bypass surgery. The exclusion criteria were as follows: (1) postoperative intracranial hemorrhage occurring at the anastomosis; (2) motion artifacts on MR images; and (3) contraindications for MR exams. Hypertension, hyperlipidemia, diabetes, history of smoking, drinking, onset type, and pre- and postoperative mRS were collected. The time interval of the preoperative MR exam to bypass surgery and the follow-up time were acquired.

Magnetic Resonance Imaging

Magnetic resonance images were acquired on a 3.0T scanner (Ingenia CX, Philips Healthcare) using a 32-element phased-array head coil. Three-dimensional pCASL was performed with the following parameters: 3D gradient and spin-echo imaging; 20 sections; 8 control/label pairs, repetition time (TR)/echo time (TE), 3,903/11 ms; SENSE factor, 1.3; labeling duration, 1,800 s; post-labeling delay (PLD), 1.5 s; scan time, 3 min 31 s.

Four-dimensional MRA images were collected based on super-selective pCASL combined with the keyhole and view-sharing techniques (4D-sPACK), which was described in a previous study and used for labeling the external carotid artery (Wang M. et al., 2021). The parameters were the same as those in a previous study, in which scan time was 4 min 52 s (Wang M. et al., 2021). It could be an alternative method for visualization of intracranial collaterals from the external carotid artery after bypass surgery.

Susceptibility-weighted imaging was acquired using the following parameters: 3D fast field echo imaging; TR/TE1/delta TE, 31/7.2/6.2 ms; Echoes, 4; Compressed SENSE factor: 4; voxel size: $0.60 \times 0.60 \times 2$ mm^3; scan time, 3 min.

Image Analysis

Arterial spin labeling was quantitatively analyzed as relative cerebral blood flow (rCBF) using Statistical Parametric

Mapping software. CBF images were generated from 3D pCASL automatically. The preprocessing was as follows: coregistered CBF images to the corresponding 3D T1-weighted images for each subject, normalized the coregistered T1 images to Montreal Neurological Institute, applied the transformation matrix to CBF images, and then smoothed them with a 6-mm Gaussian kernel. The smoothed CBF image was divided by the averaged CBF of whole cerebral gray matter using Data Processing and Analysis of Brain Imaging. The rCBF values of gray matter in each hemisphere were extracted.

Two neuroradiologists (W.M. and C.F., with 11 and 7 years of experience, respectively) qualitatively analyzed the pre- and postsurgical collateral scores on CBF images by consensus with a 2-week interval. They were blinded to the postsurgical collateral circulation on 4D MRA and mRS. A four-point grading scale was used on two slices of ASL images corresponding to the Alberta Stroke Program Early CT Score locations. The scale was as follows: 0, no or minimal perfusion signal; 1, moderate perfusion signal with arterial transit artifact (ATA); 2, high perfusion signal with ATA; and 3, normal perfusion signal without ATA (Zaharchuk et al., 2011; Lee et al., 2018). Ten regions in each hemisphere were evaluated (a total of 30 scores).

The MRA scores of intracranial arteries were assessed on preoperative maximum intensity projection images by two neuroradiologists (W.M. and C.F., with 11 and 7 years of experience, respectively) according to the criteria in a previous report (Houkin et al., 2005). The ICA score was defined as follows: 0, normal; 1, stenosis of C1; 2, discontinuity of C1 signal; and 3, invisible. The score definition of MCA-M1 was similar to ICA. ACA scores were defined as follows: 0, normal A2 and its distal; 1, A2 and its distal signal decrease or loss; and 2, invisible. The score definition of PCA was similar to ACA. The total MRA score of each hemisphere was 0–10.

Hemorrhage on anastomosis site was assessed on SWI images by one neuroradiologist (W.M. with 11 years of experience). Hemorrhage was considered if hemosiderin deposition was newly found in the anastomosis site after revascularization, which was an irregular patchy low signal on SWI images.

Follow-Up Evaluation

Follow-up MR exams were collected after more than 3 months. Surgical collaterals were evaluated on super-selective 4D MRA using the Matsushima standard (Zhao et al., 2019): 0–3, null, localized, moderate, and abundant. A score of 0–1 indicated poor surgical collaterals, and a score of 2–3 indicated good surgical collaterals. Evaluations were conducted by a neurosurgeon (W.Y., with 16 years of experience) and a radiologist (C.C., with 4 years of experience), who were blinded to the baseline results. mRS was collected by another neurosurgeon (Y.Y., with 20 years of experience) and another radiologist (W.K., with 10 years of experience), who were blinded to the baseline results and surgical collaterals. The time interval between the MR exam and mRS evaluation was less than 1 week. Disagreements in the qualitative analysis were resolved by consensus.

TABLE 1 | Demographic and radiological information of included subjects.

	Surgical collaterals		
	Good (*n* = 29)	**Poor (*n* = 37)**	***P***
Age (years)	46.59 ± 10.83	47.83 ± 6.58	0.586
Sex (male)	13	23	0.160
Personal history			
Hypertension	10	20	0.113
Diabetes	10	11	0.681
Hyperlipidemia	5	12	0.161
Smoking	1	4	0.262
Drinking alcohol	1	3	0.431
Onset type			
Hemorrhagic	5	10	0.346
Nonhemorrhagic	24	27	
Side			
Right	15	23	0.394
Light	14	14	
MRA score (scores)	4.55 ± 1.97	3.95 ± 1.73	0.216
ASL			
$rCBF_{pre}$	0.81 ± 0.13	0.83 ± 0.08	0.639
$Collaterals_{pre}$ (scores)	13.72 ± 7.83	19.16 ± 6.65	0.005
$rCBF_{post}$	0.83 ± 0.11	0.82 ± 0.08	0.682
$Collaterals_{post}$ (scores)	20.79 ± 6.65	22.84 ± 5.06	0.279
Follow-up time (months)	8.07 ± 3.51	7.78 ± 4.06	0.765
Presurgical time interval (days)	4.72 ± 2.74	5.14 ± 2.21	0.502
mRS_{pre}	1.66 ± 1.14	1.49 ± 0.90	0.590
mRS_{post}	0.52 ± 0.83	0.62 ± 0.76	0.475

Presurgical time interval: time interval between presurgical MR exam and combined bypass surgery.

Statistical Analysis

Statistical analysis was performed with SPSS 25.0 software (IBM). $P < 0.05$ was considered statistically significant. Interobserver agreement of the collateral score, MRA scores, surgical collaterals, and mRS were assessed using Cohen's weighted kappa statistic. Kappa values were interpreted as follows: ≤0.20, slight; 0.21–0.40, fair; 0.41–0.60, moderate; 0.61–0.80, substantial; 0.81–1.00, almost perfect. Independent samples *T*-tests and Mann–Whitney U-tests were used to evaluate differences in continuous and categorical variables between the good and poor surgical collateral groups. Paired sample *T*-tests and Wilcoxon signed-rank tests were used to assess the differences between pre- and postsurgical rCBF, collateral score, and mRS. Univariable and multivariable logistic regressions were performed to identify the predictors for surgical collaterals after combined bypass. Two models of multivariable logistic regression were adopted because of the limited sample size. Continuous variables were converted to dichotomous variables according to the largest Youden's index. The area under the curve was calculated to predict postsurgical collaterals.

RESULTS

Subject Characteristics

Pre- and postoperative ASL and 4D MRA were obtained in 63 MMA patients (68 hemispheres). Two hemispheres were

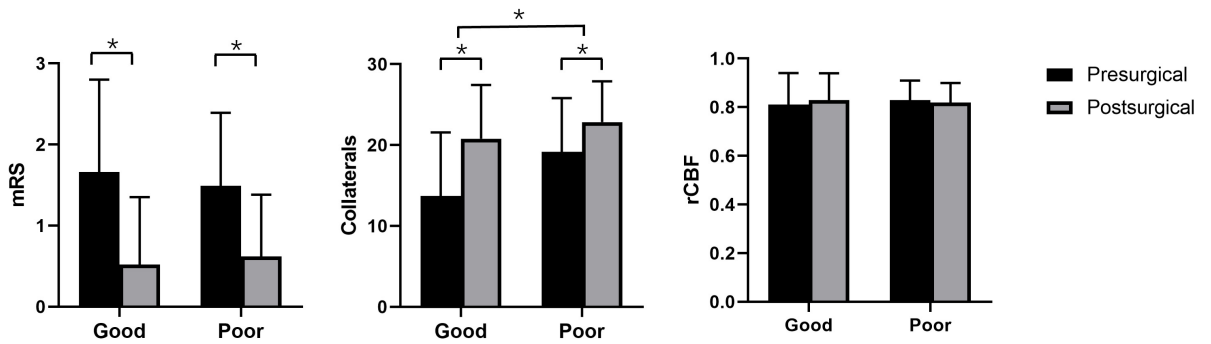

FIGURE 1 | Pre- and postsurgical modified Rankin Scale, collateral perfusion, and relative cerebral blood flow based on arterial spin labeling between good and poor surgical collaterals. *$p < 0.05$ between two groups.

TABLE 2 | Univariable and multivariable logistic regression results.

	Univariable regression		Multivariable regression			
			Model 1		Model 2	
	OR (95% CI)	P	OR (95% CI)	P	OR (95% CI)	P
Sex	0.495 (0.184, 1.329)	0.163	0.146 (0.031, 0.695)	0.016	0.154 (0.035, 0.676)	0.013
Age	0.317 (0.10, 1.002)	0.05	0.135 (0.026, 0.718)	0.019	0.181 (0.039, 0.854)	0.031
Hypertension	0.447 (0.164, 1.219)	0.116	0.161 (0.033, 0.776)	0.023	0.167 (0.038, 0.736)	0.018
Hyperlipidemia	0.434 (0.133, 1.418)	0.167	0.339 (0.066, 1.729)	0.193		
Diabetes	1.244 (0.439, 3.522)	0.681				
Smoking	0.295 (0.031, 2.791)	0.287				
Drinking	0.405 (0.04, 4.110)	0.444				
Hemorrhage	0.563 (0.168, 1.879)	0.350				
MRA	1.201 (0.914, 1.576)	0.188	0.796 (0.495, 1.281)	0.347		
Side	0.652 (0.243, 1.748)	0.395				
$Collaterals_{pre}$	0.902 (0.838, 0.971)	0.006	0.769 (0.649, 0.912)	0.002	0.791 (0.695, 0.900)	<0.001
$rCBF_{pre}$	0.277 (0.065, 1.188)	0.084	0.650 (0.065, 6.474)	0.713		
Follow-up time	0.739 (0.264, 2.070)	0.565				
mRS_{pre}	1.183 (0.726, 1.929)	0.499				

excluded because of a cerebral hemorrhage at the anastomosis site. Totally, 61 patients (66 hemispheres) were included. They were divided into good and poor surgical collateral groups according to follow-up results. Five hemispheres in the good surgical collateral group and 10 in the poor group had hemorrhagic onset. The time interval of the preoperative MR exam to bypass surgery and follow-up time were not significantly different between the two groups (**Table 1**).

Presurgical Comparisons

The MRA score was significantly correlated with the presurgical collateral score ($r = -0.523$, $p < 0.001$). The rCBF and mRS in the good surgical collateral group were not significantly different from those in the poor group (rCBF: $P = 0.639$; mRS: $P = 0.590$). However, the poor group had a higher collateral score (19.16 scores ± 6.65) than the good group (13.72 scores ± 7.83) ($P = 0.005$).

Follow-Up Results

Postsurgical rCBF was not significantly elevated compared with presurgical rCBF in the good ($P = 0.119$) and poor ($P = 0.233$) groups. Postsurgical collateral scores were significantly elevated in the good (13.72 scores ± 7.83 *vs.* 20.79 scores ± 6.65, $p < 0.001$) and poor (19.16 scores ± 6.65 *vs.* 22.84 scores ± 5.06, $p < 0.001$) groups. Moreover, the elevation of collateral scores in the good group (7.07 scores ± 4.32) was higher than that in the poor group (3.68 scores ± 3.52, $P = 0.001$) (**Figure 1**). Postsurgical mRS was significantly reduced compared with presurgical (good: 0.52 ± 0.83 *vs.* 1.66 ± 1.14, $P < 0.001$; poor: 1.49 ± 0.90 *vs.* 0.62 ± 0.76, $P < 0.001$) mRS in the good and poor groups.

Potential Predictors for Surgical Collaterals After Combined Bypass Surgery

The results of univariable and multivariable logistic regressions are listed in **Table 2**. Lower presurgical collateral scores (OR: 0.791; 95% CI: 0.695, 0.90; $P < 0.001$), female sex (OR: 0.154; 95% CI: 0.035, 0.676; $P = 0.013$), younger age (OR: 0.181; 95% CI: 0.039, 0.854; $P = 0.031$), and non-hypertension (OR: 0.167; 95% CI: 0.038, 0.736; $P = 0.018$) were associated with good surgical

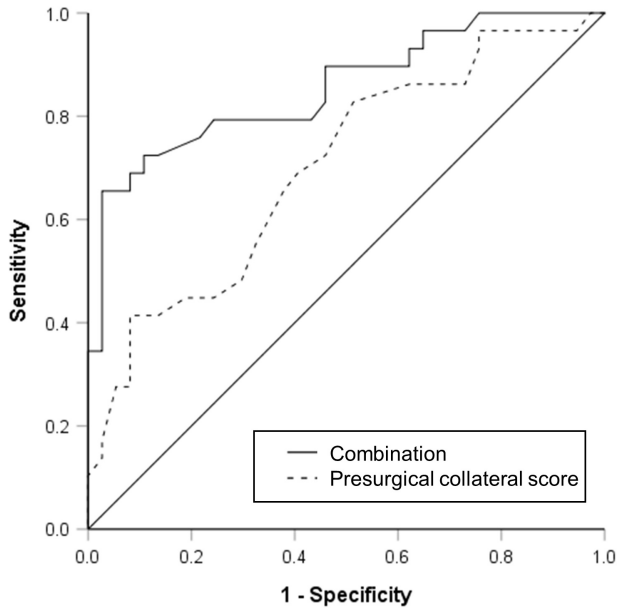

FIGURE 2 | Receiver operating characteristic curve used to evaluate presurgical collateral score (area under curve was 0.702) and combination of presurgical collateral score, sex, age, and hypertension (area under curve was 0.855) for predicting moyamoya angiopathy patients with good surgical collateral circulation after combined bypass surgery.

collaterals. The area under the curve of the combined presurgical collateral score, sex, age, and hypertension for predicting surgical collaterals was 0.855 (**Figure 2**). **Figure 3** shows a bilateral MMA patient with poor surgical collaterals, and the collateral score was increased by approximately 2 after 9 months. **Figure 4** shows a unilateral MMA patient with good surgical collaterals after 7 months of follow-up. The postsurgical collateral score obviously increased from 1 to 12.

Reproducibility

Interobserver reproducibility was almost excellent for the assessment of the MRA score (κ = 0.811), surgical collateral circulation (κ = 0.815), and presurgical collateral score (κ = 0.821). The postsurgical collateral score (κ = 0.790) and pre- (κ = 0.764) and postsurgical (κ = 0.786) mRS had substantial interobserver reproducibility.

DISCUSSION

In this study, we analyzed the characteristics of pre- and postsurgical ASL images in MMA patients who underwent combined bypass surgery to explore the possible role of presurgical ASL in predicting the occurrence of good surgical collateral circulation. We found that the presurgical collateral score was correlated with the MRA score and was lower in patients with good surgical collaterals than in those with poor surgical collaterals. The collateral score increased, and mRS improved after combined bypass surgery. The presurgical collateral score, sex, age, and hypertension may be predictors of surgical collaterals.

The presurgical collateral score based on ASL in this study was evaluated according to the presence of ATA in Alberta Stroke Program Early CT Score areas. ATA is a characteristic artifact in the cerebral cortex and sulcus and is affected by the PLD value (Deibler et al., 2008). ATA on ASL images with a PLD of 1,500 ms has been reported to be correlated with the MRA score in MMA patients. In addition, PLDs of 1,500 ms had a wider range median of the ATA values and a higher correlation coefficient compared with PLDs of 1,000 and 2,000 ms (Ukai et al., 2020). In this study, a PLD of 1,500 ms was adopted in the ASL exam. We also found that the presurgical collateral score based on the ATA was correlated with the MRA score.

Revascularization can improve the clinical outcome in MMA patients with a long median follow-up time (18 and 26.3 months, 12 years) (Duan et al., 2012; Ha et al., 2019; Zhang et al., 2020). In this study, the clinical outcome was improved in all MMA patients, and the postoperative mRS score increased in both good and poor surgical collateral circulation. None of the MMA patients had recurrent cerebrovascular events. This may be due to a shorter median follow-up time of 7 months in our subjects. All MMA patients in our study will be followed in the future continuously.

Collateral circulation is a critical determinant of cerebral perfusion in cerebral ischemia (Liebeskind, 2003). Leptomeningeal collateral circulation plays an important role in the blood supply of ischemic stroke in the anterior cerebral artery and MCA territories in MMA patients (Wang Q. N. et al., 2021). A significantly lower presurgical collateral score on ASL was found in MMA patients with good surgical collateral circulation, which often indicates more severe cerebral hypoperfusion. However, presurgical rCBF in the two groups was not significantly different. This might be because of lower PLD (1,500 ms). Long delay (4,000 ms) and multi-delay ASL can provide more accurate cerebral blood flow in MMA patients compared with positron emission tomography (Fan et al., 2017; Hara et al., 2017). We chose rCBF instead of CBF to reduce the effect of lower PLD in this study. In addition, perfusion differences were calculated using the rCBF of one hemisphere without using an intergroup analysis based on voxels, which may be another reason. The presence of presurgical transdural collaterals trended better surgical collaterals in MMA patients, which also indicated a severe cerebral perfusion defect (Storey et al., 2017). After combined bypass surgery, a higher elevation of the collateral score was found in patients with good surgical collateral circulation.

Younger age was reported to be associated with good surgical collaterals after indirect bypass surgery (Wang Q. N. et al., 2021). It has been demonstrated to be more effective for younger patients than older patients in the long term (Goda et al., 2004). In this study, youth age was also found to be a predictor of good surgical collateral circulation after combined bypass surgery. Moreover, predictors included sex and hypertension. Hypertension was an independent risk factor for unfavorable clinical outcomes and may be a risk factor

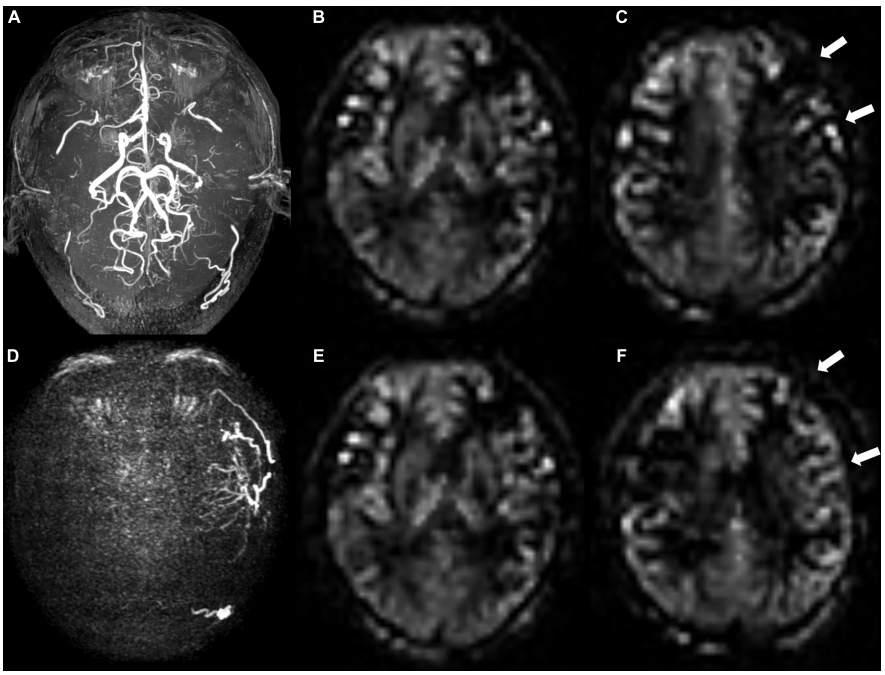

FIGURE 3 | A 48-year-old male patient with moyamoya angiopathy. **(A)** Presurgical MR angiography image. **(B,C)** Two-slice ASL images of ASPECT regions, and preoperative collateral score was 10 in **(B)** and 9 in **(C)**. **(D)** Postoperative super-selective 4D MRA images of external carotid artery. Postsurgical collaterals were defined as poor (1 score according to Matsushima standard). **(E,F)** Same postoperative two-slice ASL images as **(B,C)**. Postoperative collateral scores increased (white arrows) to 10 in **(E)** and 11 in **(F)**.

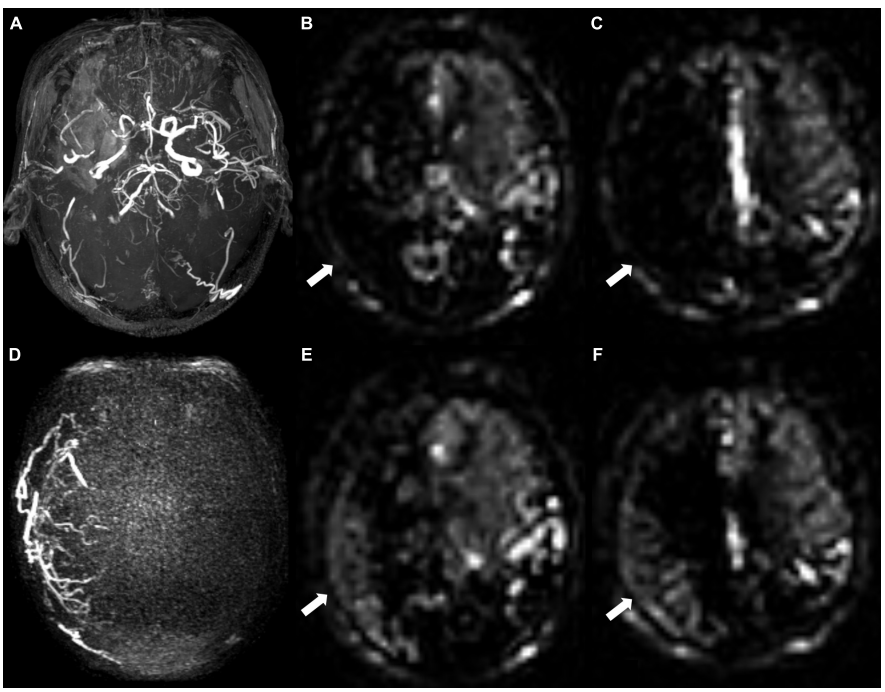

FIGURE 4 | A 68-year-old male patient with unilateral moyamoya angiopathy. **(A)** Presurgical MR angiography image. Right middle cerebral artery was occluded. **(B,C)** Two-slice ASL images of ASPECT regions, and cerebral perfusion was significantly reduced. Preoperative collateral score was almost 0 in **(B)** and 1 in **(C)**. **(D)** Postoperative super-selective 4D MRA images of external carotid artery. Postsurgical collaterals were defined as good (2 scores according to Matsushima standard). **(E,F)** ASL images at same level as **(B,C)**. Postoperative collateral scores increased (white arrows), which were 6 in **(E)** and 6 in **(F)**.

for decreased bypass patency (superficial temporal artery to MCA) in patients with cerebral atherosclerotic disease (Matano et al., 2016; Ma et al., 2020). This might be the cause of poor surgical collateral circulation. Khan et al. (2012) reported that females might be at a higher risk of postoperative adverse events despite successful bypass surgery in MMA patients. However, in previous studies, sex was not a predictor in MMA patients with good surgical collaterals after indirect bypass surgery (Zhao et al., 2019; Wang Q. N. et al., 2021), which was different from this study. The reason might be the limited sample size.

Several limitations existed in this study. First, different surgeons performing bypass surgery may have an effect on surgical collaterals. The number of surgeons performing bypass surgery in this study was three in the same group. This may need to be confirmed in the future to choose patients from the same surgeon. Second, the current study aimed to explore potential clinical and radiographic predictors based on ASL for good surgical collateral circulation after combined bypass surgery. Some of the other potential biomarkers, such as gene type, were not included. Third, perioperative hyperperfusion reaction was not recorded because this information was not clear in electronic medical records. However, a hemorrhagic event in the anastomosis site was considered according to the deposition of hemosiderin on SWI. Finally, limited sample size was used in this study. We will continuously follow up with more MMA patients after cerebral bypass surgery in the future.

CONCLUSION

Patients with good surgical collaterals had lower presurgical collateral scores and higher increased collateral scores on ASL. Lower presurgical collateral scores, youth, female sex, and nonhypertension may indicate good surgical collateral circulation. This may play an important role in improving the management of adult MMA patients and therapeutic decisions.

DATA AVAILABILITY STATEMENT

The raw data supporting the conclusions of this article will be made available by the authors, without undue reservation.

ETHICS STATEMENT

The studies involving human participants were reviewed and approved by Medical Ethics Committee of the Nanjing Drum Tower Hospital. The patients/participants provided their written informed consent to participate in this study. Written informed consent was obtained from the individual(s) for the publication of any potentially identifiable images or data included in this article.

AUTHOR CONTRIBUTIONS

MW, YW, and BZ designed the study. WZ and XZ performed the statistical analyses. MW and YW contributed to data preparation and drafting of the original manuscript. MW was responsible for MR scanning. MW, YW, and YY evaluated radiological and clinical information. YW and YY managed the subject recruitment. BZ and YY modified and confirmed the final article. All authors contributed to the article and approved the submitted version.

FUNDING

This work was supported by the National Natural Science Foundation of China (81720108022 BZ); the social development project of science and technology project in Jiangsu Province (BE2017707); key medical talents of the Jiangsu province, the "13th Five-Year" health promotion project of the Jiangsu province (ZDRCA2016064); and the project of the sixth peak of talented people (WSN -138). The funders had no role in the study design, data collection and analysis, decision to publish, or preparation of the manuscript.

REFERENCES

Alsop, D. C., Detre, J. A., Golay, X., Günther, M., Hendrikse, J., Hernandez-Garcia, L., et al. (2015). Recommended implementation of arterial spin–labeled perfusion MRI for clinical applications: a consensus of the ISMRM perfusion study group and the European consortium for ASL in dementia. *Magn. Reson. Med.* 73, 102–116. doi: 10.1002/mrm.25197

Deibler, A. R., Pollock, J. M., Kraft, R. A., Tan, H., Burdette, J. H., and Maldjian, J. A. (2008). Arterial spin–labeling in routine clinical practice, part 1: technique and artifacts. *AJNR Am. J. Neuroradiol.* 29, 1228–1234. doi: 10.3174/ajnr.A1030

Duan, L., Bao, X. Y., Yang, W. Z., Shi, W. C., Li, D. S., Zhang, Z. S., et al. (2012). Moyamoya disease in China: its clinical features and outcomes. *Stroke* 43, 56–60. doi: 10.1161/STROKEAHA.111.621300

Esposito, G., Sebök, M., Amin-Hanjani, S., and Regli, L. (2018). Cerebral bypass surgery: level of evidence and grade of recommendation. *Acta Neurochir. Suppl.* 129, 73–77. doi: 10.1007/978-3-319-73739-3_10

Fan, A. P., Guo, J., Khalighi, M. M., Gulaka, P. K., Shen, B., Park, J. H., et al. (2017). Long–delay arterial spin labeling provides more accurate cerebral blood flow measurements in moyamoya patients: a simultaneous positron emission tomography/MRI study. *Stroke* 48, 2441–2449. doi: 10.1161/STROKEAHA.117.017773

Goda, M., Isono, M., Ishii, K., Kamida, T., Abe, T., and Kobayashi, H. (2004). Long–term effects of indirect bypass surgery on collateral vessel formation in pediatric moyamoya disease. *J. Neurosurg.* 100, 156–162. doi: 10.3171/ped.2004.100.2.0156

Ha, E. J., Kim, K. H., Wang, K. C., Phi, J. H., Lee, J. Y., Choi, J. W., et al. (2019). Long–term outcomes of indirect bypass for 629 children with moyamoya disease longitudinal and cross–sectional analysis. *Stroke* 50, 3177–3183. doi: 10.1161/STROKEAHA.119.025609

Hara, S., Tanaka, Y., Ueda, Y., Hayashi, S., Inaji, M., Ishiwata, K., et al. (2017). Noninvasive evaluation of CBF and perfusion delay of moyamoya disease using arterial spin–labeling MRI with multiple postlabeling delays: comparison with (15)O-Gas PET and DSC-MRI. *AJNR Am. J. Neuroradiol.* 38, 696–702. doi: 10.3174/ajnr.A5068

Hernandez-Garcia, L., Lahiri, A., and Schollenberger, J. (2019). Recent progress in ASL. *Neuroimage* 187, 3–16. doi: 10.1016/j.neuroimage.2017.12.095

Herve, D., Kossorotoff, M., Bresson, D., Blauwblomme, T., Carneiro, M., Touze, E., et al. (2018). French clinical practice guidelines for moyamoya angiopathy. *Rev. Neurol. (Paris)* 174, 292–303. doi: 10.1016/j.neurol.2017.12.002

Houkin, K., Nakayama, N., Kuroda, S., Nonaka, T., Shonai, T., and Yoshimoto, T. (2005). Novel magnetic resonance angiography stage grading for moyamoya disease. *Cerebrovasc. Dis.* 20, 347–354. doi: 10.1159/000087935

Khan, N., Achrol, A. S., Guzman, R., Burns, T. C., Dodd, R., Bell-Stephens, T., et al. (2012). Sex differences in clinical presentation and treatment outcomes in moyamoya disease. *Neurosurgery* 71, 587–593. doi: 10.1227/NEU.0b013e3182600b3c

Kronenburg, A., Braun, K. P., van der Zwan, A., and Klijn, C. J. (2014). Recent advances in moyamoya disease: pathophysiology and treatment. *Curr. Neurol. Neurosci. Rep.* 14:423. doi: 10.1007/s11910-013-0423-7

Lee, S., Yun, T. J., Yoo, R. E., Yoon, B. W., Kang, K. M., Choi, S. H., et al. (2018). Monitoring cerebral perfusion changes after revascularization in patients with moyamoya disease by using arterial spin–labeling MR imaging. *Radiology* 288, 565–572. doi: 10.1148/radiol.2018170509

Liebeskind, D. S. (2003). Collateral circulation. *Stroke* 34, 2279–2284. doi: 10.1161/01.STR.0000086465.41263.06

Liu, Z. W., Han, C., Zhao, F., Qiao, P. G., Wang, H., Bao, X. Y., et al. (2019). Collateral circulation in moyamoya disease: a new grading system. *Stroke* 50, 2708–2715. doi: 10.1161/STROKEAHA.119.024487

Ma, Y., Zhao, M., Deng, X., Zhang, D., Wang, S., Zeng, Z., et al. (2020). Comparison of clinical outcomes and characteristics between patients with and without hypertension in moyamoya disease. *J. Clin. Neurosci.* 75, 163–167. doi: 10.1016/j.jocn.2019.12.016

Matano, F., Murai, Y., Tateyama, K., Tamaki, T., Mizunari, T., Matsukawa, H., et al. (2016). Long–term patency of superficial temporal artery to middle cerebral artery bypass for cerebral atherosclerotic disease: factors determining the bypass patent. *Neurosurg. Rev.* 39, 655–661. doi: 10.1007/s10143-016-0736-5

Miyamoto, S., Yoshimoto, T., Hashimoto, N., Okada, Y., Tsuji, I., Tominaga, T., et al. (2014). Effects of extracranial–intracranial bypass for patients with hemorrhagic moyamoya disease: results of the Japan adult moyamoya trial. *Stroke* 45, 1415–1421. doi: 10.1161/STROKEAHA.113.004386

Storey, A., Michael Scott, R., Robertson, R., and Smith, E. (2017). Preoperative transdural collateral vessels in moyamoya as radiographic biomarkers of disease. *J. Neurosurg. Pediatr.* 19, 289–295. doi: 10.3171/2016.9.PEDS16161

Togao, O., Hiwatashi, A., Obara, M., Yamashita, K., Kikuchi, K., Kamei, R., et al. (2018). Acceleration–selective arterial spin–labeling MR angiography used to visualize distal cerebral arteries and collateral vessels in moyamoya disease. *Radiology* 286, 611–621. doi: 10.1148/radiol.2017162279

Ukai, R., Mikami, T., Nagahama, H., Wanibuchi, M., Akiyama, Y., Miyata, K., et al. (2020). Arterial transit artifacts observed by arterial spin labeling in moyamoya disease. *J. Stroke Cerebrovasc. Dis.* 29:105058. doi: 10.1016/j.jstrokecerebrovasdis.2020.105058

Wang, M., Yang, Y., Wang, Y., Li, M., Zhang, J., and Zhang, B. (2021). Vessel–selective 4D MRA based on ASL might potentially show better performance than 3D TOF MRA for treatment evaluation in patients with intra–extracranial bypass surgery: a prospective study. *Eur. Radiol.* 31, 5263–5271. doi: 10.1007/s00330-020-07503-3

Wang, Q. N., Yang, R. M., Zou, Z. X., Wang, X. P., Zhang, Q., Li, D. S., et al. (2021). Predictors of neoangiogenesis after indirect revascularisation in moyamoya disease: a 10-year follow-up study. *J. Neurol. Neurosurg. Psychiatry* 92, 1361–1362. doi: 10.1136/jnnp-2020-325401

Zaharchuk, G., Do, H. M., Marks, M. P., Rosenberg, J., Moseley, M. E., and Steinberg, G. K. (2011). Arterial spin-labeling MRI can identify the presence and intensity of collateral perfusion in patients with moyamoya disease. *Stroke* 42, 2485–2491. doi: 10.1161/STROKEAHA.111.616466

Zhang, M., Tang, J., Liu, N., Xue, Y., Ren, X., and Fu, J. (2020). Postoperative functional outcomes and prognostic factors in two types of adult moyamoya diseases. *J. Stroke Cerebrovasc. Dis.* 29:104846. doi: 10.1016/j.jstrokecerebrovasdis.2020.104846

Zhao, Y., Li, J., Lu, J., Zhang, Q., Zhang, D., Wang, R., et al. (2019). Predictors of neoangiogenesis after indirect revascularization in moyamoya disease: a multicenter retrospective study. *J. Neurosurg.* 132, 98–108. doi: 10.3171/2018.9.JNS181562

Conflict of Interest: XZ was employed by the company Philips Healthcare, Shanghai.

The remaining authors declare that the research was conducted in the absence of any commercial or financial relationships that could be construed as a potential conflict of interest.

Publisher's Note: All claims expressed in this article are solely those of the authors and do not necessarily represent those of their affiliated organizations, or those of the publisher, the editors and the reviewers. Any product that may be evaluated in this article, or claim that may be made by its manufacturer, is not guaranteed or endorsed by the publisher.

Copyright © 2022 Wang, Wang, Zhang, Zhao, Yang and Zhang. This is an open-access article distributed under the terms of the Creative Commons Attribution License (CC BY). The use, distribution or reproduction in other forums is permitted, provided the original author(s) and the copyright owner(s) are credited and that the original publication in this journal is cited, in accordance with accepted academic practice. No use, distribution or reproduction is permitted which does not comply with these terms.

frontiers | Frontiers in Neuroscience

ORIGINAL RESEARCH
published: 14 April 2022
doi: 10.3389/fnins.2022.864040

The Local Topological Reconfiguration in the Brain Network After Targeted Hub Dysfunction Attacks in Patients With Juvenile Myoclonic Epilepsy

Ming Ke[1], Huimin Li[1] and Guangyao Liu[2]**

[1] School of Computer and Communication, Lanzhou University of Technology, Lanzhou, China, [2] Department of Magnetic Resonance, Lanzhou University Second Hospital, Lanzhou, China

The central brain regions of brain networks have been extensively studied in terms of their roles in various diseases. This study provides a direct measure of the brain's responses to targeted attacks on central regions, revealing the critical role these regions play in patients with juvenile myoclonic epilepsy (JME). The resting-state data of 37 patients with JME and 37 healthy subjects were collected, and brain functional networks were constructed for the two groups of data according to their Pearson correlation coefficients. The left middle cingulate gyrus was defined as the central brain region by the eigenvector centrality algorithm and was attacked by the CLM sequential failure model. The rich-club connection differences between the patients with JME and healthy controls before and after the attacks were compared according to graph theory indices and the number of rich-club connections. We found that the numbers of rich connections in the brain networks of the healthy control group and the group of patients with JME were significantly reduced [$p < 0.05$, false discovery rate (FDR) correction] before the CLM sequential failure attacks, and no significant differences were observed between the feeder connections and local connections. In the healthy control group, significant rich connection differences were obtained ($p < 0.01$, FDR correction), and no statistically significant differences were observed regarding the feeder connections and local connections in the brain network before and after CLM failure attacks on the central brain region. No significant differences were obtained between the rich connections, feeder connections, and local connections in patients with JME before and after CLM successive failure attacks on the central brain area. The rich connections, feeder connections, and local connections were not significantly different in the brain networks of the healthy control group and the group of patients with JME after CLM successive failure attacks on the central brain region. We concluded that the damage to the left middle cingulate gyrus is closely linked to various brain disorders, suggesting that this region is of great importance for understanding the pathophysiological basis of myoclonic seizures in patients with JME.

Keywords: rich-club, eigenvector centrality, Crucitti-Latora-Marchiori, resting-state network, juvenile myoclonic epilepsy

OPEN ACCESS

Edited by:
Long-Biao Cui, Fourth Military Medical University, China

Reviewed by:
Baojuan Li, Massachusetts General Hospital and Harvard Medical School, United States
Xiaoming Chen, Fourth Military Medical University, China

****Correspondence:***
Ming Ke
keming@lut.edu.cn
Guangyao Liu
lgy362263779@163.com

Specialty section:
This article was submitted to Brain Imaging Methods, a section of the journal Frontiers in Neuroscience

Received: *28 January 2022*
Accepted: *15 March 2022*
Published: *14 April 2022*

Citation:
Ke M, Li H and Liu G (2022) The Local Topological Reconfiguration in the Brain Network After Targeted Hub Dysfunction Attacks in Patients With Juvenile Myoclonic Epilepsy. Front. Neurosci. 16:864040. doi: 10.3389/fnins.2022.864040

INTRODUCTION

Juvenile myoclonic epilepsy (JME) is a highly prevalent genetic generalized epilepsy syndrome, which accounts for up to 10% of all epilepsy cases (Camfield et al., 2013; Scheffer et al., 2017). JME is a common type of idiopathic generalized epilepsy that occurs mostly in people aged 12–18 years, and it accounts for 8–10% of the prevalence in the epileptic population. The clinical manifestations of JME are mainly myoclonic seizures, disorientation seizures, generalized tonic-clonic seizures, cognitive impairment, and motor impairment (Wolf et al., 2015). At present, the complex network method of functional magnetic resonance imaging (fMRI)-based data analysis has been widely used in the study of neuropsychiatric diseases. JME studies conducted with complex networks based on graph theory suggest that JME episodes likely originate in cortical networks associated with movement (Krauss, 2011). The associations between identified discharge-affecting networks and the relationships among resting-state networks might be influenced by aspects of epilepsy in patients with JME (Dong et al., 2016). Brain network studies have pointed to the fact that alterations in brain network organization are closely associated with brain disorders (Liu et al., 2008; Bassett and Bullmore, 2009; Fornito et al., 2015). Our existing CLM sequential failure model for adolescent myoclonic epilepsy revealed that the left middle frontal lobe might be a potential focal area regarding the initiation of generalized tonic-clonic seizures (Ke et al., 2019).

However, there is currently no clear understanding of the internal causes of these large-scale network changes. A key hypothesis was that central brain region dysfunction was likely to be associated with disease (van den Heuvel et al., 2013). A highly central and interconnected organization was presented for the brain network, which played a crucial role in the integration process of the brain, forming the central backbone of global brain communication. The hub region at the center of the brain network topology is the center of information integration between different subsystems of the human brain, and it is capable of collaboratively integrating multisensory information (Zamora-Lopez et al., 2010; Zuo et al., 2012). Central nodes play pivotal roles in the overall architectures of functional brain networks (Sporns et al., 2007; Sporns, 2011; van den Heuvel and Sporns, 2011). These regions of information transmission form highly aggregated brain communication hubs that make important contributions to cross-regional information transmission (van den Heuvel et al., 2013). It is known from past studies of diseases that abnormalities in the central brain regions of patients with schizophrenia lead to brain network topology reorganization, resulting in reduced connectivity within the brain network (van den Heuvel et al., 2013). Moreover, a neuroimaging study reported that the presence of abnormal brain network topologies in patients with JME increased the importance of the motor-related cortex in functional brain networks, which implied a reorganization of the central network nodes in the patients with JME. The changed topologies of the brain networks in the patients with JME caused connectivity to decrease within these brain networks (Ray et al., 2014). From the above description of the central region, we know that the central region plays an important role in brain network topology and information transmission. Once abnormalities occur in the central region, the brain network is greatly affected. Therefore, it is crucial to comprehensively understand the causal relationship between the central nodes of the brain network and the network topology.

We used the CLM sequential failure model to assess the role played by lesions of the central brain regions in brain networks. The CLM sequential failure model is a submodel of the load-capacity model, also known as the node-edge hybrid dynamic model, which does not separate the two factors of nodes and edges but rather considers the importance of both and the role they play in load distribution. Unlike previous approaches to node failure, the CLM model does not remove the node directly but, instead, reduces the efficiency of the edges associated with the node (Crucitti et al., 2004). Kinney et al. (2005) applied the CLM sequential failure model to a North American power network and found that the overall performance of the network degrades relative to the normal state when attacking the highest-loaded generation or transmission nodes. Using the CLM sequential failure model to simulate seizures and their dynamic propagation process in patients with epilepsy, our laboratory found that the left middle frontal lobe may be a potential focal area in the onset of generalized tonic-clonic seizures (Ke et al., 2019). CLM successive failures are already present in the application of the model to complex networks. The model is an important inspiration for our study.

This research adopted the eigenvector centrality (EC) algorithm by choosing the left cingulate gyrus regions of the brain network as central brain regions. The CLM sequential failure model was used to attack the central brain network regions of the healthy control group and the JME group. To study the influence of the central node abnormalities on brain networks, as well as the relationships between these abnormalities and the causes of disease, a rich-club connection analysis was performed on the brain networks of the two groups before and after the attacks. The results showed that the abnormal central nodes in the brain networks of patients with JME led to brain network topology reorganization, affected the functional connections of the brain networks, and obstructed functional information transmission. This is of great significance for understanding the pathophysiological mechanism of JME and indicates that these central brain regions are central brain regions of adolescent clonic epilepsy.

MATERIALS AND METHODS

Participants

Resting-state fMRI data were collected from 37 patients with JME (with average illness duration of 4.03 years) admitted to the Epilepsy Center of Lanzhou University Second Hospital. The patients were diagnosed with JME according to the criteria for epilepsy classification contained in the International League Against Epilepsy (ILAE) guidelines of 2001. Patients were excluded if they had any of the following characteristics: (1) a history of antiepileptic medication intake, (2) other neurological or psychiatric illness, (3) other developmental disabilities, such

as autism and intellectual impairment, and (4) an acute physical illness that would affect the scanning. To evaluate the severity of the epilepsy cases, each patient was required to complete the National Hospital Seizure Severity Scale (NHS3) before the MRI examination. This scale contains six seizure-related factors and produces a total score from 1 to 23. The patients included 21 males and 16 females with an average age of 17.757 ± 5.33 years. No structural abnormalities were found during the routine MRI examinations; the electroencephalography (EEG) results obtained during seizures exhibited extensive multispinous slow waves or compound spinous slow waves at 4∼6 Hz; and none of the patients had received formal treatment. At the same time, the fMRI and 3DT1 images of 37 normal volunteers, including 13 males and 24 females with an average age of 20.081 ± 4.723 years, were selected. The subjects in both groups were right-handed. No significant differences in age, handedness, or sex were observed between the two groups after conducting intragroup paired false discovery rate (FDR) correction ($p > 0.05$). The normal volunteers were recruited through advertising and excluded before excluding those with acute physical illness, substance abuse or dependence, a history of loss of consciousness due to craniocerebral injury, and neurological or psychiatric disorders. This study was approved by the Ethics Committee of the Second Hospital of Lanzhou University, and written informed consent was obtained from each subject or his or her legal guardian after the experimental protocol. Subject information is shown in **Table 1**.

TABLE 1 | Subject information.

Variables	JME (n = 37)	HC (n = 37)
Sex	21/16	13/24
Mean age (year)	17.757 ± 5.33	20.081 ± 4.723
Mean disease duration (months)	46.919 ± 10.627	0
Handedness (right/left)	37/0	37/0
Mean score of the NHS3	9.054 ± 3.778	0
Mean first time of onset	3.185 ± 2.661	0

NHS3, National Hospital Seizure Severity Scale.

Data Acquisition

All data were collected by a Siemens Verio 3.0 T MR scanner. The data collection process required each subject to lie supine, fix his or her head, close his or her eyes, plug his or her ears, and try not to perform specific thinking. The fMRI data were collected *via* a gradient-echo echo-planar imaging (GRE-EPI) sequence. The specific parameters were as follows: the repetition time (RT) = 2,000 ms, echo time (TE) = 30 ms, slice thickness = 4 mm, slice gap = 0.40 mm, number of layers = 33 layers, field of view (FOV) = 240 mm × 240 mm, in-plane matrix resolution = 64 × 64, and flip angle (FA) = 90°, and 200 time points were collected in total. T1-weighted images were acquired by a 3D magnetization-prepared rapid gradient echo sequence (3D MP-RGE). The specific parameters were as follows: the repetition time (TR) = 1,900 ms, TE = 30 ms, slice thickness = 0.9 mm, FOV = 256 mm × 230 mm, matrix = 256 × 256, FA = 90°.

Data Preprocessing

We implemented the data preparation process in MATLAB version 2013a, which ran on the Windows 10 operating system. The graph theoretical network analysis toolbox (GRETNA)[1] (Wang et al., 2015), which ran on MATLAB, was also used to preprocess the data. The main steps of preprocessing included (1) formatted conversion of the DICOM data (conversion of the two-dimensional images in the DICOM format into three-dimensional images in the NIFTI format); (2) removal of the first few time points: the first 10 time points were selected to eliminate data instability caused by reasons such as the starting of the mcassociations between identifiedahine; (3) slice-timing correction, in which all scan time points were corrected to the same reference point. The interval time is 2 s, and there are 33 time layers in total. Using interlayer scanning, the scanning order alternated in the positive direction starting with odd-numbered slices (i.e., 1, 3, 5,... 2, 4, 6, . . .); (4) head movement correction if the translation was greater than 1 mm, and the rotation was greater than 1 degree; (5) within-subject coregistration of the T1 image to a mean functional image; (6) spatial normalization: each scan was stretched, compressed, and coiled to make the scanned brain consistent with a standard brain template; (7) removal of linear drift: removing linear trends that arose from warming or subjects not adapting due to the functioning of the machine; (8) low-pass filtering: the range of low-pass filtering was 0.01–0.08 Hz; and (9) regressing out of the covariates: for the fMRI datasets, several nuisance signals were typically removed from each voxel's time series to reduce the effects of non-neuronal fluctuations, including head motion profiles, cerebrospinal fluid signals, white matter signals, and global signals.

[1]https://github.com/sandywang/GRETNA

Brain Network Construction

In graph theory, the brain network refers to a collection of nodes (brain areas) and edges (connections). The automated anatomical labeling (AAL) brain atlas was employed to define the regions of interest (ROIs), and the ROI function was employed to compute the functional connectivities between the 90 nodes. To construct the brain functional network, the response sequence of each brain region of each subject was extracted over time. The Pearson correlation coefficient was used to obtain the correlation coefficient matrix over time. The expression is as follows:

$$r(x_n, y_n) = \frac{\sum (x_n - \bar{x})(y_n - \bar{y})}{\sqrt{\sum (x_n - \bar{x})^2 \sum (y_n - \bar{y})^2}} \quad (1)$$

x_n is the time series of the n-th brain region. $\bar{x}$ is the mean value across all scan layers in the brain region. y_n and $\bar{y}$ are the time series and mean value of another brain region. When the correlation coefficient $r(x_n, y_n)$ was greater than a given threshold value Tm, it was considered that there was a functional connection between x_n and y_n ; i.e., an edge connection existed between them.

In this experiment, we performed Fisher's z-transformation on the brain functional connectivity. First, binarization was performed on the brain network; when the connection value

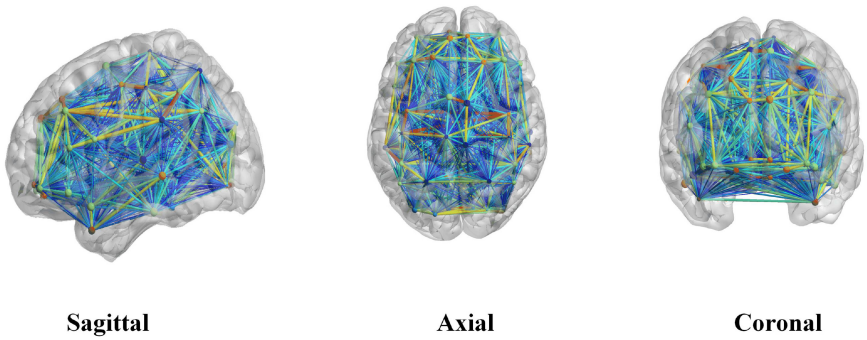

FIGURE 1 | A brain network connectivity map generated using the BrainNet Viewer toolbox.

between two brain regions was greater than the threshold value, they were considered to have an edge, whose value was set to 1; otherwise, the edge value was set to 0. In this experiment, we chose 0.3 as the threshold value in constructing the binary brain network; at this value, the network density is between 10 and 50%, and the average network degree $< k >$ is greater than two times the natural logarithm of the number of network nodes N. In this case, this also yielded no isolated nodes in the brain network, and so the entire network has connectivity. These are the two rules to follow when building a brain network, and choosing this value for the threshold ensures that our brain network satisfies these two rules. **Figure 1** shows the connectivity graph of the brain network generated using the BrainNet Viewer toolbox.

Eigenvector Centrality

Eigenvector centrality is a measure of the importance of a node and depends on both the number (i.e., the degree of the node) and the importance of its neighbor nodes. The EC of a node was proportional to the sum of the centrality scores of its neighbor nodes. The centrality of the eigenvector vectors emphasized the surrounding environment (the number and quality of node neighbors), which, in essence, meant that a node's score was the sum of its neighbors' scores. A node could increase its importance by connecting to many other important nodes. A node with a high score could be connected to either a large number of ordinary nodes or a small number of other high-scoring nodes. From the perspective of transmission, the centrality of eigenvectors was suitable for describing the long-term influence of nodes. For example, during the spread of a disease or spread, a larger EC score indicates that the corresponding node is more likely to be closer to the source of infection and is a key node that needs to be prevented (Bonacich and Lloyd, 2001).

The expression is as follows: if x_i is an important measure of node I, then:

$$EC(i) = x_i = c\sum_{j=1}^{n} a_{ij}x_j \tag{2}$$

where, c is a proportionality constant, $x = (x_1, x_2, x_3,..., x_n)^T$, and when the steady state is reached after multiple iterations, it can be written as the following expression:

$$x = cAx \tag{3}$$

This means that x was the eigenvector corresponding to the eigenvalue c of Matrix A minus 1. The basic method for calculating the vector x was to give an initial value $x(0)$ and then use the following iterative algorithm:

$$x(t) = cAx(t-1),\ t = 1, 2... \tag{4}$$

Then, it was normalized: $x'(t) = x'(t-1)$. During each iteration step, if x was divided by λ, a convergent non-zero solution $x = Ax/\lambda$ could be obtained for this equation, where λ is the principal eigenvalue of the binarized brain network adjacency Matrix A, i.e., the constant $c = 1/\lambda$.

From the perspective of the method itself, EC identifies the importance of a node (within network) by considering the quality of its connections (not only how many connections it has but also whether the connections are formed with important nodes). An increasingly popular centrality metric, the EC is unique in that it considers the centrality of immediate neighbors when computing the centrality of a node. Mathematically, EC is a positive multiple of the sum of the adjacent centralities and is based on the philosophy that a node is more central if its neighbors are also highly central. The novelty of the approach is that it assigns an "importance" score to each feature by considering all other features mapped as nodes on the graph, bypassing the combinatorial problem in a methodologically sound fashion. Indeed, EC differs from other measurements (e.g., degree centrality) since a node (feature) with many links does not necessarily have a high EC because not all nodes are equivalent, some are more relevant than others, and, reasonably, endorsements from important nodes count more. The analysis presented by Lohmann et al., shows that feature vector centrality is an effective computational tool for capturing intrinsic neural structure at the voxel level. Therefore, the method is informative in measuring the importance of nodes.

We used the principle of EC to obtain the EC value of each node and selected the central nodes of the brain network according to the ranked values. This node represents the attack node in subsequent CLM failure attacks.

Successive Failure of CLM

The CLM model not only separated the two factors of nodes and edges but also considered the importance of nodes and edges in terms of load allocation by studying their joint effects. The CLM model did not remove nodes directly but instead reduced the efficiency of the edges associated with the nodes. The principle was that the information passing through a faulty node would choose other alternative transmission paths.

From the point of view of graph theory, assuming that the network was an undirected weighted graph G, the transmission of network information between any two points was always conducted along the shortest path, namely, the optimal path with respect to transmit efficiency. The value of the edge between nodes i and j was e_{ij}, which was expressed by the reciprocal of the shortest path length L_{ij} between the nodes (when there was no path between nodes i and j, the reciprocal of the shortest path length value L_{ij} was 0), which represented the transmission efficiency between nodes i and j at time t; the associated formula is:

$$\varepsilon ij = 1/dij \tag{5}$$

The construction of this model was divided into two parts: the load distribution without node failure and the load distribution after node failure.

(1) Before a node failure occurred, $L_i(t)$ was defined to represent the load of node i at time t. Additionally, $L_i(t)$ represented the number of paths passing through the shortest distance from node i at time t. When t was 0, the initial load was $L_i(0)$. C_i was the capacity of node i, and its calculation expression was:

$$C_i = a \cdot L_i(0)(a \geq 1) \tag{6}$$

where, C_i represents the capacity coefficient, which represents the ability of nodes to handle the load and transmit information.

(2) When a failure occurred, an attack on a node inevitably changed the shortest paths between nodes, resulting in a redistribution of the total load. The load redistribution among the nodes might have led to the overload of other nodes, which, in turn, led to a new round of load redistribution, leading to successive failures. In this model, when a node was overloaded, the load allocated to this point was gradually reduced by reducing the transmission efficiency of the edge connected to it. When the load was less than the capacity, the node worked normally again. The internode efficiency iteration formula at time t is:

$$e_{ij}(t+1) = \begin{cases} e_{ij}(0) \cdot \frac{C_i}{L_i(t)}, L_i(t) > C_i \\ e_{ij}(0), L_i(t) \leq C_i \end{cases} \tag{7}$$

In this study, we focused on the calculation of the brain network matrices before and after attacks. The successive brain network fault matrix removed all edges related to the central node (when the edge value of the node connected to the central node was reduced to 0; otherwise, the value remained unchanged). The edge connection values of the remaining nodes did not change. The brain networks before and after successive failures were taken as the input values of the rich-club structure, and the rich club was used to analyze the results.

To study the changes in brain network topology before and after successive fault attacks, we used the graph theory indices of complex networks to study the difference in brain network information transmission before and after successive CLM fault attacks. The topological changes in the brain networks before and after successive failures were measured by rich-club connections.

Graph Theory Indicators

To study the role of the cingulate gyrus in disease, we adopted a CLM sequential failure model to attack the cingulate gyrus and simulate the process of cingulate gyrus damage. Then, we used the graph theory indices of complex networks to analyze the difference between the brain networks after successive CLM failure attacks occurred. In this experiment, we used the clustering coefficient and global efficiency as two graph theory indicators for study and analysis.

Clustering Coefficient

The clustering coefficient was an important parameter that was used to describe the nodes' tightness in the network. For a node i with a degree value of k_i, its clustering coefficient c_i was defined as the ratio of the actual number of edges between the k_i nodes connected to node i and the possible number of edges between these nodes e_i, namely:

$$c_i = \frac{2e_i}{k_i(k_i - 1)} \tag{8}$$

The clustering coefficient C of the entire network was defined as the mean clustering coefficient c_i across all nodes in the network, namely:

$$C = \frac{1}{N}\sum_{i=1}^{N} c_i \tag{9}$$

Global Efficiency

When isolated nodes were contained in the network, the shortest path length of the network was infinite. To avoid this problem, someone put forward the concept of efficiency. In-network efficiency (the global efficiency), which measured the global information transmission ability, was E_{glob}.

The global efficiency was defined as the mean of the reciprocals of the shortest path lengths between all pairs of nodes in the network, i.e.,

$$Eglob = \frac{1}{N(N-1)}\sum_{i,j\in V, i\neq j}\frac{1}{l_{ij}} \tag{10}$$

where, N represents the number of nodes in the brain network and l_{ij} represents the length of the shortest path between nodes i and j in the subgraph.

Rich Club

A rich club is defined as a group of nodes in a random network whose connectivity level exceeds the expected connectivity level. Here, the degree value k of each node in the functional network of the healthy control group was first calculated. The detection process involved the following steps. (1) We discarded all nodes

in the network whose degrees were less than k. (2) Then, we calculated the ratio of the connections between the remaining nodes and the total number of possible connections when the network was in a fully connected state. (3) For each k, the normalized rich-club coefficient was divided by the average rich-club coefficient of 100 random networks (Colizza et al., 2006).

The normalized rich-club coefficient $\varphi norm(k)$ was the ratio of the rich-club coefficient $\varphi(k)$ to $\varphi random(k)$, where, $\varphi random(k)$ represents 100 random brain networks. The expression is as follows:

$$\phi norm(k) = \frac{\phi(k)}{\phi random(k)} \tag{11}$$

where, $\varphi(k)$ is expressed as:

$$\phi(k) = \frac{2E_{>k}}{N_{>k}(N_{>k} - 1)} \tag{12}$$

In the formula, $E_{>k}$ represents the number of connections between nodes whose degrees were greater than k in the network, and the denominator represents the total number of possible connections between the nodes when the degree was set to "full connection." $N_{>k}$ denotes the number of nodes whose degree was greater than k. $E_{>k}$ took the node degree K as the threshold and constantly adjusted k to remove the nodes whose node degrees were less than or equal to K from the network. In this experiment, the value of K ranged from 1 to 89, and each value was utilized one time to obtain a corresponding normalized rich-club coefficient. Through the three steps of the rich-club test, this paper found that the normalized rich-club coefficients of the two groups of brain networks were greater than 1 in a certain range, which was consistent with the results obtained by existing studies (Li et al., 2016). The normalized rich-club coefficients were obtained through a one-sample t-test. It was proved that the brain functional networks of both the healthy control group and the JME group had rich-club characteristics, which could be used for subsequent rich-club studies.

Rich-club connections refer to the three types of connections that can be formed according to the utilized node selection standard: (1) rich connections, i.e., connections between rich-club nodes; (2) feeder connections, i.e., connections between rich-club and non-rich-club nodes; and (3) local connections, i.e., connections between non-rich-club nodes.

In this study, the brain networks of 37 healthy controls were first calculated, and the average brain network of the 37 healthy controls was constructed. On this basis, the degree value of each node in the average brain network was obtained. The node selection criteria included that the top 10% of nodes among the 90 ranked nodes in terms of their degrees were selected as "rich nodes," and the rest were defined as "non-rich nodes" (Yan et al., 2018). According to the node selection criteria, nine regions in the brain network satisfied the "rich node" selection criteria, including the left middle cingulate gyrus, the left anterior central gyrus, the right anterior central gyrus, the left precuneus, the left dorsolateral superior frontal gyrus, the right dorsolateral superior frontal gyrus, the left supplementary motor area, the left parahippocampal gyrus, and the left middle frontal gyrus. Therefore, these nine brain regions were defined as "rich nodes," while the other 81 brain regions were defined as "non-rich nodes." The rich nodes and non-rich nodes were used to classify the three kinds of connections. To ensure the reliability of the control experiment, the same "rich nodes" and "non-rich nodes" were selected from the healthy control group and the group of patients JME for the division of the three kinds of connections instead of selecting the "rich nodes" from the healthy control group. In the group of patients with JME, the "rich nodes" of the brain network for the patients with JME were selected according to the node selection criteria, and then the three connection values were calculated. The rich connection value was calculated as the sum of the weights of the connections between all rich nodes in the brain network. The feeder connection value was calculated as the sum of the weights of the connections existing between rich nodes and non-rich nodes. The local connection value was the sum of the weights of all connections that existed between non-rich nodes.

TABLE 2 | Eigenvector centrality results.

Brain area	Eigenvector centrality results
Left middle cingulate gyrus	0.1650
Right middle cingulate gyrus	0.1568
Right inferior temporal gyrus	0.1559
Right orbital inferior frontal gyrus	0.1475
Right supplementary motor area	0.1436
Left supplementary motor area	0.1434
Right middle frontal gyrus	0.1425
Left superior temporal gyrus	0.1413
Left inferior temporal gyrus	0.1405

RESULTS

The Eigenvector Centrality Results

The EC results for the top 10% of the node degrees in the 90 brain regions are shown in **Table 2**. The left side shows the top nine brain regions among the 90 brain regions in terms of EC, and the right side shows the top nine EC values among the 90 brain regions as calculated by the EC algorithm. The EC value of the left middle cingulate gyrus was the highest in **Table 2**.

According to the principle of feature vector centrality, the higher the value of feature vector centrality of a particular node, the more important the node is. Therefore, in this experiment, we selected the left middle cingulate region as the core region, as it had the highest EC value.

Statistical Analysis Results Before and After CLM Successive Failure Attacks

In this experiment, we used the clustering coefficient and global efficiency as two graph theory indicators for study and analysis.

The statistical results for the clustering coefficients are shown in **Figure 2A**. The left side of **Figure 2A** shows the clustering coefficients before the CLM attack for the healthy control group and the JME group. The right side of **Figure 2A** shows the clustering coefficients after the CLM attack for the healthy control group and the JME group. The results showed that the cluster

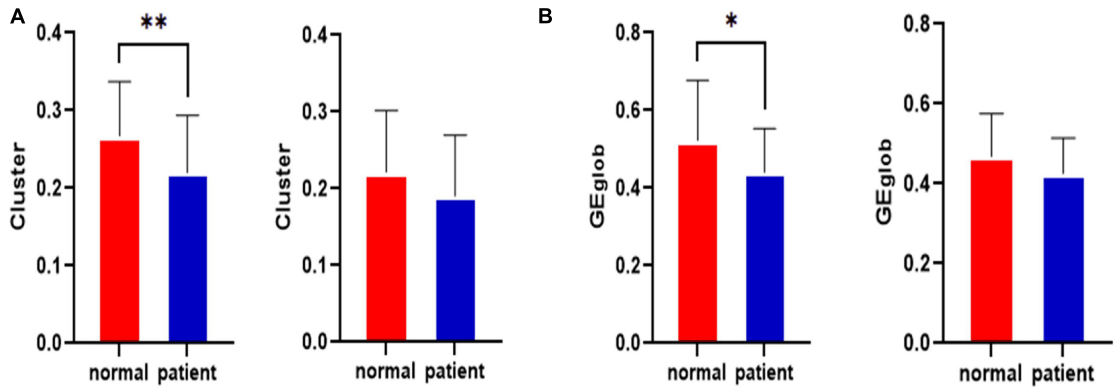

FIGURE 2 | Statistical clustering coefficient and global efficiency results for the left middle cingulate gyrus before and after the attacks in the healthy control group and the JME group. **(A)** Clustering coefficient results. **(B)** Global efficiency results. *$p < 0.05$, **$p < 0.01$, FDR-corrected.

values of the brain networks were significantly different between groups before the CLM successive failure attacks ($p < 0.01$, FDR-corrected). The cluster values of the brain networks were not significantly different after the CLM attack between the healthy control group and the JME group.

The statistical results regarding global efficiency are shown in **Figure 2B**. The left side of **Figure 2B** shows the global efficiency values before the CLM attack for the healthy control group and the JME group. The right side of **Figure 2B** contains the global efficiency results obtained after the CLM attack for the healthy control group and the JME group. The results showed that the global efficiency values of the brain networks were significantly different between groups before the CLM successive failure attacks ($p < 0.05$, FDR-corrected). The global efficiency values of brain networks were not significantly different after the CLM attacks between the healthy control group and the JME group.

The Rich-Club Results

In this study, the rich-club organization of the brain network was studied to explore the changes in the brain network before and after the occurrence of successive failures. Two-sample *t*-tests and a variance analysis were performed on the three types of connections (rich connections, local connections, and feeder connections) before and after CLM sequential failure attacks in the healthy control group and the JME patient group.

The rich-club connections before and after the left middle cingulate gyrus that was attacked for the healthy control group and the JME group are shown in **Figure 3**. **Figure 3A** shows the rich-club junction in the attacked left middle cingulate gyrus for the healthy control group. **Figure 3A** shows that the rich connections in the brain network exhibited statistically significant differences before and after the CLM attacks ($p < 0.01$, FDR-corrected), while there were no significant differences in the feeder and local connections. **Figure 3B** shows the rich-club junction in the attacked left middle cingulate gyrus of the JME group. The results showed that the rich, feeder, and local connections were not statistically different in the brain network before and after the CLM attack ($p > 0.05$, FDR-corrected) for the JME group.

The rich-club connections before the left cingulate gyrus attack for the healthy control and JME groups are shown in **Figure 4A**. The results in **Figure 4A** show that the rich-club organization of the brain network in the JME patient group was changed from that in the healthy control group before the CLM attack. The number of rich connections was significantly reduced ($p < 0.05$, FDR-corrected), while the feeder connections and local connections were not significantly different. The rich-club connections after attacking the left middle cingulate gyrus in the healthy control group and the JME group are shown in **Figure 4B**. The results showed that there were no significant differences in the rich, feeder, and local connections after the CLM attacks in the healthy control group and the JME group ($p > 0.05$, FDR-corrected).

The variance analysis results for the rich clubs before the attack in the healthy control group and JME group show that there were fewer rich connections in the brain networks of the patients with JME ($p < 0.05$) than in those of the healthy controls before the CLM attack. The feeder and local connections were not significantly different.

The variance analysis results for the rich clubs before and after the attack in the healthy control group show that there were fewer rich connections in the brain networks of the healthy controls ($p < 0.01$) before the CLM attack. The feeder and local connections were not significantly different. No statistically significant differences were observed among the rich connections, feeder, or local connections after the CLM attacks for the healthy controls.

The variance analysis results for the rich clubs before and after the attack in the JME group show that the rich, feeder, and local connections in the JME group before and after the CLM attacks were not significantly different.

The variance analysis results for the rich clubs after the attacks in the healthy control group and the JME group show that the rich, feeder, and local connections after the CLM attacks were not significantly different between the healthy control group and the

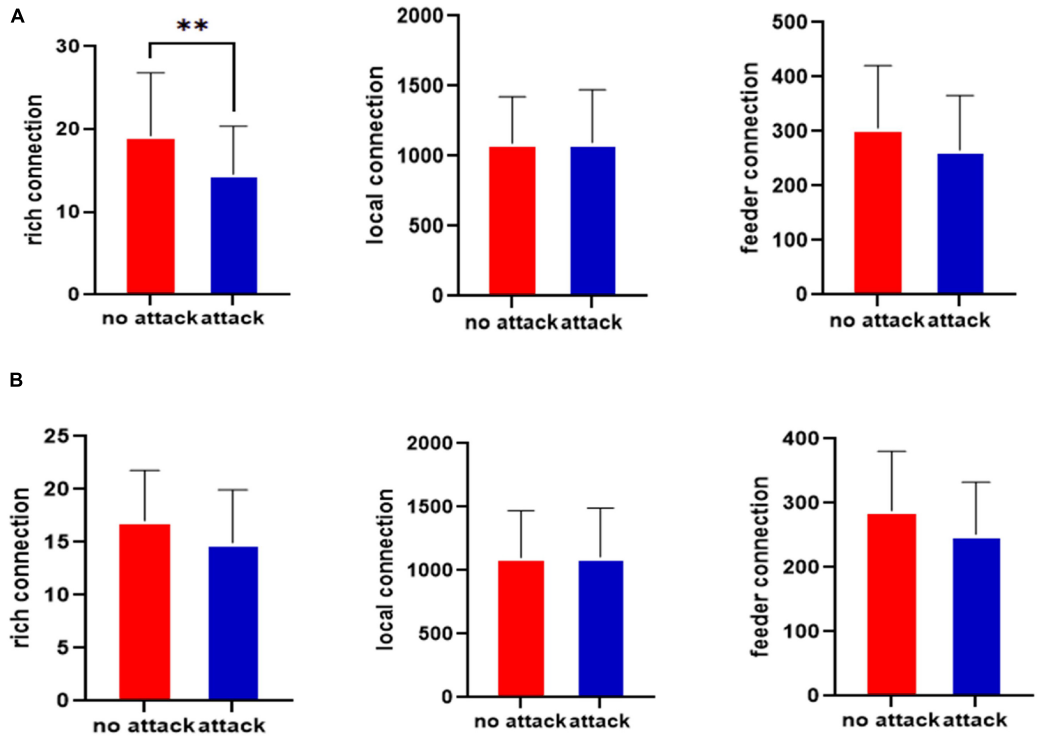

FIGURE 3 | Statistical testing results for the rich-club junction of the left middle cingulate gyrus before and after the attacks in the healthy control group **(A)** and JME group **(B)**. $^{**}p < 0.01$, FDR-corrected.

JME group. These results were consistent with those of the rich-club single-sample *t*-test.

Additionally, to better understand the relationships between the damage to the rich-club topological structure and patients' diseases, we performed a correlation study between the rich connections and patient disease durations.

The relationship between disease duration and the number of rich connections is shown in **Figure 5**. The abscissa represents the disease duration for patients with JME, and the ordinate denotes the patient's rich connection weights. The results showed that there was a negative correlation between the rich connection weights and the patients' disease durations. This result showed that the weight values of rich connections in the brain network decreased as the illness duration increased.

DISCUSSION

In this paper, we examined JME disorders in terms of network modularity and network topological organization. The EC algorithm was used to calculate the EC values of 90 brain regions. The left middle cingulate gyrus was determined as a core brain region, and its role in JME disease was studied. This method was more feasible than the previous method of selecting core nodes according to their degree centrality (Yu et al., 2018).

Previous studies of the cingulate gyrus have shown that atrophy of the right caudal anterior cingulate cortex (cACC) may contribute to reduced performance in functional tasks such as the stroop and auditory consonant trigrams (ACT), although this may be only one node of a broad brain network involved in these cognitive processes (Merkley et al., 2013). Functional connectivity between the cingulate gyrus and other brain regions is abnormal in cortical areas that facilitate motor function and sensory-motor integration (Clemens et al., 2013). The anterior cingulate cortex (ACC) is known to be involved in functions such as emotion, pain, and cognitive control (Parvizi et al., 2013). The cingulate motor areas project to the spinal cord and red nucleus and have premotor functions, while the nociceptive area is engaged in both response selection and cognitively demanding information processing. Cingulate epilepsy syndrome provides important support from experimental animal and human functional imaging studies for the role of anterior cingulate cortex in movement, affect, and social behaviors. Excessive cingulate activity in patients with seizures confirmed in the anterior cingulate cortex *via* subdural electrode recordings can impair consciousness, alter affective state and expression, and influence skeletomotor and autonomic activity. The above findings suggest that, in JME, the cingulate gyrus is involved in both cognitive and motor activity in the brain network. Abnormalities in this brain region cause abnormalities in both cognitive and motor activity in the brain network. This is consistent with the clinical appearance of cognitive and motor deficits in JME and suggests that the cingulate gyrus has an important role in the study of JME. This corroborates the previous results on feature vector centrality. Both in conjunction with the feature vector centrality algorithm and in relation to previous studies of the middle cingulate gyrus,

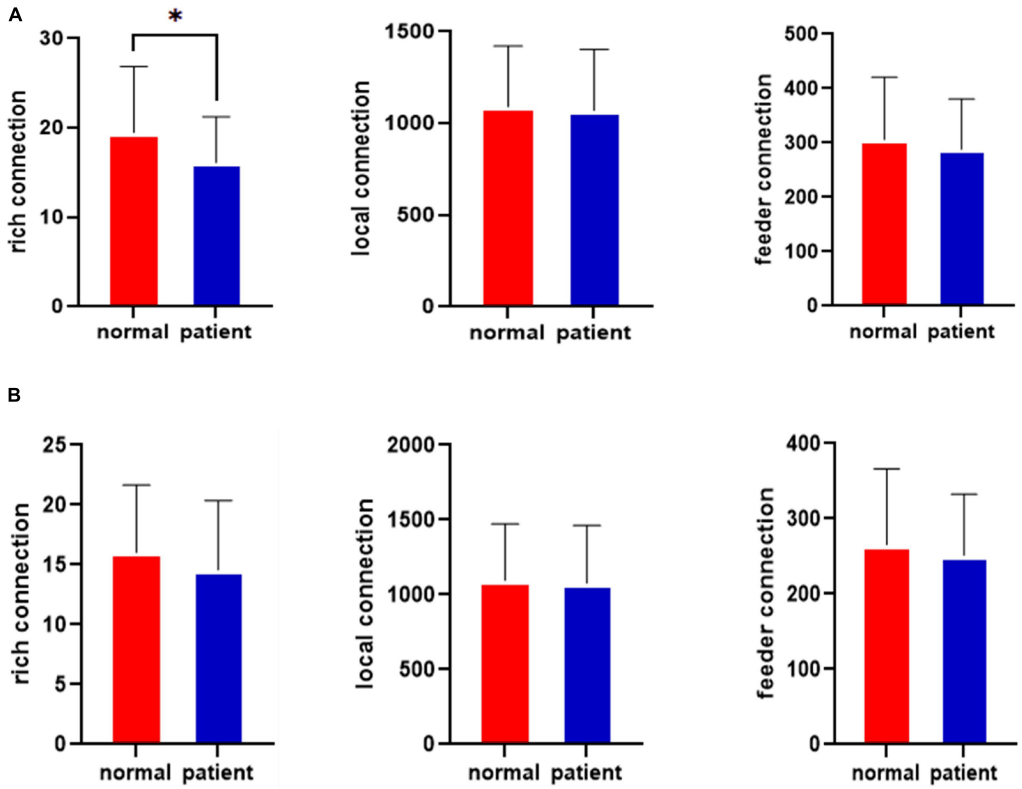

FIGURE 4 | Results for the rich-club junctions in the healthy control group and the JME group. **(A)** Results for the rich-club junctions before the attacks. **(B)** Results for the rich-club junctions after the attacks. *$p < 0.05$, FDR-corrected.

our selected left middle cingulate brain region does play an important role in the brain network.

To study the influence of cingulate gyrus malfunction on the brain network, the clustering coefficient and global efficiency of the brain network were calculated, and the results were statistically analyzed. We found that the clustering coefficient and global efficiency results before and after successive CLM failure attacks exhibited significant differences. The clustering coefficient represented an important parameter regarding the degree of node connections. The observed significant reduction in the clustering coefficient indicated that the node connections related to the left middle cingulate gyrus were blocked after successive failure attacks, which led to a significant decrease in the clustering coefficient results. Global efficiency represents the global information transmission capability of the brain network. After successive failure attacks, the transmitted and received information that passed through the middle cingulate gyrus in the brain network was interrupted. This phenomenon led to information transmission capability changes.

To investigate the effect of the left cingulate gyrus on the network topology, we used CLM successive failure attacks on the central brain region to study the rich-club organization differences in the brain networks of healthy controls and patients with JME before and after the attacks. First, we calculated the rich-club connections of the healthy controls and patients with JME before executing CLM successive failure attacks. The results

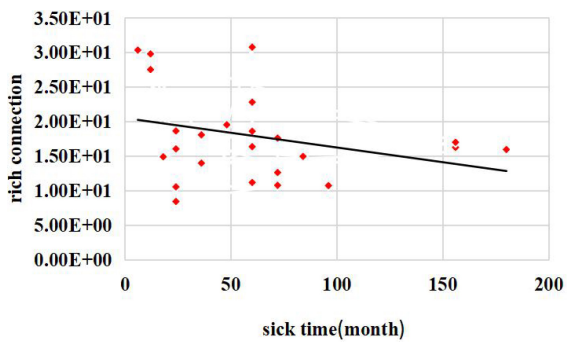

FIGURE 5 | Relationship between disease duration and the number of rich connections.

showed a statistically significant difference between the numbers of rich connections in the group of patients with JME and the healthy control group. The number of rich connections was significantly reduced ($p < 0.05$, FDR-corrected). The feeder connection and local connection results showed no significant difference between the two groups. The above results suggest that there were fewer rich-club connections in the brain networks of patients with JME than in those of the healthy controls before CLM successively failed to attack the left middle cingulate gyrus. The most significant results were for the rich connections,

which indicated that the rich-club tissue in the brain networks of the patients was damaged. A comparison between the rich-club results of the healthy subjects and patients with JME before and after CLM successive failure attacks showed that only the rich connections in the healthy controls exhibited statistically significant differences before and after the attacks ($p < 0.01$, FDR-corrected). There was no significant difference between the feeder connections and local connections. No significant differences were observed among the rich connections, local connections, and feeder connections in the patients with JME before and after successive CLM failure attacks on the left middle cingulate gyrus. This indicated that left middle cingulate gyrus lesions were already present in the group of patients with JME, so there were no significant differences before and after successive CLM failure attacks. The rich-club organization results of healthy subjects and patients with JME after successive CLM failure attacks showed no significant differences in terms of the rich connections, feeder connections, and local connections ($p > 0.05$, FDR-corrected) after successive CLM failure attacks. This means that the results changed from a significant difference regarding the rich connections before the attack to no significant difference in the healthy controls after successive CLM failure attacks on the left middle cingulate gyrus. This suggested that the rich-club connections in the healthy control brain networks after successive failure attacks were similar to the rich-club connections in the patients with JME. The hub regions were damaged in the patients with JME relative to those of normal subjects, and the left middle cingulate gyrus abnormalities might be related to the physiological mechanism of juvenile myoclonic seizures. Damage to the left middle cingulate gyrus in healthy controls was likely to induce disease in healthy subjects. At the same time, to better understand the relationship between the impairment of the rich-club topological structure and disease, we performed a correlation study between rich connections and patients' disease durations. We found that there was a negative correlation between the rich connection weights and patients' illness durations. This result showed that the weight values of rich connections in the brain network decreased as the duration of illness increased.

These results suggested that the left middle cingulate gyrus in patients with JME was impaired compared with that in normal subjects; this may be related to the physiological mechanism of adolescent clonic seizures. The rich-club organization was made up of three types of connections. Rich connections in the rich club referred to the connections between rich nodes, which were located in the central position of brain network. Rich connections played a key role in achieving whole-brain neural signal reception and communication between brain regions, which affected many structural and functional properties of the network, including its topology, path efficiency, and load distribution (Csigi et al., 2017). The left middle cingulate fell within the category of rich nodes. Therefore, for healthy controls before the successively CLM failure attacks, the central brain region functioned normally in terms of the rich-club connections and graph theory indicators, and the rich connection weight values were normal. In the JME group, the left middle cingulate gyrus was damaged, and the rich connection weight values were outside of the normal range. On this basis, the rich-club connections in the healthy control group and the group of patients with JME were significantly different before the successive CLM failures. The left middle cingulate gyrus lesions were simulated after successive CLM failure attacks on the core brain region. After the lesions, the neural signals passing through the rich nodes and the communication information between the functional network regions were greatly reduced. This caused more information that should be transmitted through this road in the brain network to be blocked. Then, the communication information of the whole brain was greatly reduced in terms of a reduction in the number of rich connections. The topology and function connections of the brain network and the graph theory indicators were reorganized (Zhu et al., 2016). Therefore, the rich connections exhibited significant differences for the healthy controls before and after the CLM attacks. The impacts of the left middle cingulate gyrus on the local connections and feeder connections were smaller. No significant differences were observed between the local connections and feeder connections. Similarly, the "rich node" of the midbrain network of the left middle cingulate node was diseased before the CLM attacks in each patient with JMEt, which resulted in the reorganization of the topological structure of the rich-club connections of the brain network, and the weight values of the rich connections were reduced. Therefore, the CLM sequential failure attack was carried out again. There was no significant change in the weight values of the rich connections. No significant differences were observed between the rich connections before and after the CLM attacks in the group of patients with JME. The middle cingulate gyrus had little influence on the local connections and feeder connections. There were no significant differences between the local connections and feeder connections. After the CLM attacks, left middle cingulate gyrus legions were found in both the healthy control group and the group of patients with JME, and the changes in the left middle cingulate gyrus legions of the brain networks of the two groups were relatively consistent. The results showed that the rich-club connections in the two brain networks changed from exhibiting a significant difference before the attacks to presenting no significant difference. This suggested that damage to the left middle cingulate gyrus in healthy controls is likely to induce disease in healthy subjects. Research papers have shown a link between damaged brain connectivity and disease (Ansari et al., 2019).

It is worth noting that the cingulate gyrus could also integrate other neural networks and had close connections between its interneurons (Bagla and Skidmore, 2011; Unnwongse et al., 2012). The middle cingulate gyrus is a part of the cingulate gyrus and plays a role in communication between the anterior and posterior cingulate gyri. Therefore, the function of the left middle cingulate gyrus might be similar to that of the cingulate gyrus, and it may play an important role in communicating with other neural networks. Studies on the cingulate gyrus have confirmed that the middle cingulate gyrus is also known as the cingulate motor area (CMA). The middle cingulate gyrus is located below the pre-supplementary motor area (SMA) between the vertical commissure anterior (VCA) and vertical

commissure posterior (VCP) lines (McConachie and King, 1997), and it is another cortical area that is associated with the motor area (Vogt et al., 1992). The middle cingulate gyrus, which lies below the presubjective motor area (pre-SMA), had projections to the anterior part of the subjective motor area, the dorsolateral prefrontal cortex, the primary motor cortex, the inferior parietal cortex, the reticular formation and motor thalamus, the red nucleus, and the spinal cord. The middle cingulate gyrus exhibited three characteristics with respect to information processing; i.e., it had a unique way of processing emotional, sensory, motor, and cognitive information. It could also integrate inputs from multiple sources, including motivation formations, error predictions, and cognitive and affective network reappearances. It also affected activity in other brain regions, such as the regulation of motor, cognitive, endocrine, and visceral responses (Devinsky et al., 1995; Bagla and Skidmore, 2011; Unnwongse et al., 2012). From an anatomical point of view, the cingulate has a unique emotional, sensory, motor, and cognitive information process (Bagla and Skidmore, 2011; Unnwongse et al., 2012). At the functional level of the brain, the middle cingulate might be involved in the ability to communicate with other neural networks of the brain and the ability to modulate executive functions. Combined with the role of the middle cingulate gyrus regarding the anatomy and functional connectivity of the brain network, it is known that left middle cingulate gyrus lesions can, indeed, cause abnormalities in neural network communication within the brain network and abnormalities in terms of motor area function, which would lead to physiological abnormalities at the motor level in patients. This is consistent with the descriptions of myoclonic seizures, atonic seizures, generalized tonic-clonic seizures, cognitive impairment, and motor impairment in the clinical presentation of JME. This result suggested that left middle cingulate gyrus lesions had the potential to cause abnormalities in the functional interactions among brain networks, which, in turn, led to motor impairment in patients with JME.

Studies of patients with middle cingulate epilepsy have suggested that middle cingulate epilepsy might be associated with paramotor movements and might manifest clinically as generalized tonic-clonic seizures (GTCSs), tonic seizures or paroxysmal seizures (Devinsky et al., 1995). Lim et al. reported that the main manifestations of middle cingulate epilepsy are spastic seizures (Lim et al., 2004). It has also been shown that the clinical manifestations of middle cingulate epilepsy are spastic seizures (Schrader et al., 2009). A recent study has reported protean manifestations of epileptic seizures that have been ascribed to the cingulate gyrus (Lim et al., 2004). These studies suggested that the left cingulate gyrus plays a role in the disease not only by regulating the communication between brain networks and other neural networks and regulating executive functions but also by affecting motor area function. The left middle cingulate gyrus lesions exhibited spastic seizures, which was consistent with the descriptions of the physiological phenomena of JME clinical manifestations (myoclonic seizures, motor seizures, generalized tonic-clonic seizures, cognitive impairment, and motor deficits). It was further demonstrated that the abnormalities of the left middle cingulate gyrus were, indeed, related to the functional interactions among brain networks and motor disorders from a pathological perspective. Therefore, the findings of our study showed that abnormalities in the left middle cingulate gyrus might lead to brain network topological reorganization and motor deficits. Our findings suggested that the left middle cingulate gyrus is a key brain region in patients with JME and is strongly associated with the pathogenesis of JME. However, the present experiment also has limitations. Brain mapping was performed in the present experiment with the AAL-90 without the cerebellum. According to the function of the cerebellum, abnormalities in this region are also associated with motor deficits. Therefore, the absence of the cerebellar template in the AAL-90 brain atlas could have affected the results of our experiment. We will address this limitation in subsequent experiments.

DATA AVAILABILITY STATEMENT

The raw data supporting the conclusions of this article will be made available by the authors, without undue reservation.

ETHICS STATEMENT

The studies involving human participants were reviewed and approved by the Epilepsy Center of Lanzhou University Second Hospital. Written informed consent to participate in this study was provided by the participants' legal guardian/next of kin.

AUTHOR CONTRIBUTIONS

MK, HL, and GL designed the experiment and revised the manuscript. MK and HL wrote the manuscript. GL recorded and collected the data. HL performed the data analysis. All authors contributed to the article and approved the submitted version.

FUNDING

This work was supported by the National Natural Science Foundation of China under (project nos. 61966023 and 82160326).

REFERENCES

Ansari, M., Adib, M., Ghazi, S., Hedayatnia, A., and Mohammad, H. (2019). Comparison of structural connectivity in Parkinson's disease with depressive symptoms versus non-depressed: a diffusion MRI connectometry study. *Int. Psychogeriatr.* 31, 5–12. doi: 10.1017/S1041610218000170

Bagla, R., and Skidmore, C. T. (2011). Frontal lobe seizures. *Neurologist* 17, 125–135. doi: 10.1097/NRL.0b013e31821733db

Bassett, D. S., and Bullmore, E. T. (2009). Human brain networks in health and disease. *Curr. Opin. Neurol.* 22:340. doi: 10.1097/WCO.0b013e32832d93dd

Bonacich, P., and Lloyd, P. (2001). Eigenvector-like measures of centrality for asymmetric relations. *Soc. Netw.* 23, 191–201. doi: 10.1016/S0378-8733(01)00038-7

Camfield, C. S., Striano, P., and Camfield, P. R. (2013). Epidemiology of juvenile myoclonic epilepsy. *Epilepsy Behav.* 28, S15–S17. doi: 10.1016/j.yebeh.2012.06.024

Clemens, B., Puskás, S., Besenyei, M., Spisák, T., Opposits, G., Hollódy, K., et al. (2013). Neurophysiology of juvenile myoclonic epilepsy: EEG-based network and graph analysis of the interictal and immediate preictal states. *Epilepsy Res.* 106, 357–369. doi: 10.1016/j.epplepsyres.2013.06.017

Colizza, V., Flammini, A., Serrano, M. A., and Vespignani, A. (2006). Detecting rich-club ordering in complex networks. *Nat. Phys.* 2, 110–115. doi: 10.1038/nphys209

Crucitti, P., Latora, V., and Marchiori, M. (2004). Model for cascading failures in complex networks. *Phys. Rev. E* 69:045104. doi: 10.1103/PhysRevE69.045104

Csigi, M., Kőrösi, A., Bíró, J., Heszberger, Z., Malkov, Y., and Gulyás, A. (2017). Geometric explanation of the rich-club phenomenon in complex networks. *Sci. Rep.* 7:1730. doi: 10.1038/s41598-017-01824-y

Devinsky, O., Morrell, M. J., and Vogt, B. A. (1995). Contributions of anterior cingulate cortex to behaviour. *Brain* 118, 279–306. doi: 10.1093/brain/118.1.279

Dong, L., Luo, C., Zhu, Y., Hou, C., Jiang, S., Wang, P., et al. (2016). Complex discharge-affecting networks in juvenile myoclonic epilepsy: a simultaneous EEG-fMRI study. *Hum. Brain Mapp.* 37, 3515–3529. doi: 10.1002/hbm.23256

Fornito, A., Zalesky, A., and Breakspear, M. (2015). The connectomics of brain disorders. *Nat. Rev. Neurosci.* 16, 159–172. doi: 10.1038/nrn3901

Ke, M., Cao, L., and Liu, G. (2019). Model for cascading failures in functional networks: application to epileptic patients with generalized tonic-clonic seizures. *J. Integr. Neurosci.* 18, 133–139. doi: 10.31083/j.jin.2019.01.102

Kinney, R., Crucitti, P., Albert, R., and Latora, V. (2005). Modeling cascading failures in the North American power grid. *Eur. Phys. J. B Condens. Matter Complex Syst.* 46, 101–107. doi: 10.1140/epjb/e2005-00237-9

Krauss, G. L. (2011). Cognitive activation of "Hyperexcitable Cortex" in JME: can it trigger seizures? "Hyperexcitable Cortex" in JME. *Epilepsy Curr.* 11, 184–185. doi: 10.5698/1535-7511-11.6.184

Li, R., Liao, W., Li, Y., Yu, Y., Zhang, Z., Lu, G., et al. (2016). Disrupted structural and functional Rich Club organization of the brain connectome in patients with generalized tonic-clonic seizure. *Hum. Brain Mapp.* 37, 4487–4499. doi: 10.1002/hbm.23323

Lim, E. C. H., Tan, J. J. H., Ong, B. K. C., and Wilder-Smith, E. P. V. (2004). Generalized myoclonus evolving into epilepsia partialis continua due to a cingulated gyrus lesion: case report and review of the literature. *Park. Relat. Disord.* 10, 447–449. doi: 10.1016/j.parkreldis.2004.04.010

Liu, Y., Liang, M., Zhou, Y., He, Y., Hao, Y., Song, M., et al. (2008). Disrupted small-world networks in schizophrenia. *Brain* 131, 945–961. doi: 10.1093/brain/awn018

McConachie, N. S., and King, M. D. (1997). Celastic seizures in a child with focal cortical dysplasia the cingulate gyrus. *Neuroradiology* 39, 44–45. doi: 10.1007/s002340050365

Merkley, T. L., Larson, M. J., Bigler, E. D., Good, D. A., and Perlstein, W. M. (2013). Structural and functional changes of the cingulate gyrus following traumatic brain injury: relation to attention and executive skills. *J. Int. Neuropsychol. Soc.* 19, 899–910. doi: 10.1017/S135561771300074X

Parvizi, J., Rangarajan, V., Shirer, W. R., Desai, N., and Greicius, M. D. (2013). The will to persevere induced by electrical stimulation of the human cingulate gyrus. *Neuron* 80, 1359–1367. doi: 10.1016/j.neuron.2013.10.057

Ray, S., Miller, M., Karalunas, S., Robertson, C., Grayson, D. S., Cary, R. P., et al. (2014). Structural and functional connectivity of the human brain in autism spectrum disorders and attention-defificit/ hyperactivity disorder:A Rich Club-organization study. *Hum. Brain Mapp.* 35, 6032–6048. doi: 10.1002/hbm.22603

Scheffer, I. E., Berkovic, S., Capovilla, G., Connolly, M. B., French, J., Guilhoto, L., et al. (2017). ILAE classification of the epilepsies: position paper of the ILAE commission for classification and terminology. *Epilepsia* 58, 512–521. doi: 10.1111/epi.13709

Schrader, D., Langill, L., Singhal, A., Steinbok, P., and Connolly, M. B. (2009). Cingulate lesions presenting with epileptic spasms. *J. Clin. Neurophysiol.* 26, 342–347. doi: 10.1097/WNP.0b013e3181baaacf

Sporns, O. (2011). The human connectome: a complex network. *Ann. N. Y. Acad. Sci.* 1224, 109–125. doi: 10.1111/j.1749-6632.2010.05888.x

Sporns, O., Honey, C. J., and Kotter, R. (2007). Identification and classifification of hubs in brain networks. *PLoS One* 2:e1049. doi: 10.1371/journal.pone.0001049

Unnwongse, K., Wehner, T., and Foldvary-Schaefer, N. (2012). Mesial frontal lobe epilepsy. *J. Clin. Neurophysiol.* 29, 371–378. doi: 10.1097/WNP.0b013e31826b3c60

van den Heuvel, M. P., and Sporns, O. (2011). Rich-club organization of the human connectome. *J. Neurosci.* 31, 15775–15786. doi: 10.1523/JNEUROSCI.3539-11.2011

van den Heuvel, M. P., Sporns, O., Collin, G., Scheewe, T., Mandl, R. C. W., Cahn, W., et al. (2013). Abnormal rich club organization and functional brain dynamics in schizophrenia. *JAMA Psychiatry* 70, 783–792. doi: 10.1001/jamapsychiatry.2013.1328

Vogt, B. A., Finch, D. M., and Olson, C. R. (1992). Functional heterogeneity in cingulate cortex: the anterior executive and posterior evaluative regions. *Cereb. Cortex* 2, 435–443. doi: 10.1093/cercor/2.6.435-a

Wang, J., Wang, X., Xia, M., Liao, X., Evans, A., and He, Y. (2015). GRETNA: a graph theoretical network analysis toolbox for imaging connectomics: corrigendum. *Front. Hum. Neurosci.* 9:458. doi: 10.3389/fnhum.2015.00386

Wolf, P., Yacubian, E. M. T., Avanzini, G., Sander, T., Schmitz, B., Wandschneider, B., et al. (2015). Juvenile myoclonic epilepsy: a system disorder of the brain. *Epilepsy Res.* 114, 2–12. doi: 10.1016/j.eplepsyres.2015.04.008

Yan, T., Wang, W., Yang, L., Chen, K., Chen, R., and Han, Y. (2018). Rich club disturbances of the human connectome from subjective cognitive decline to Alzheimer's disease. *Theranostics* 8:3237. doi: 10.7150/thno.23772

Yu, Y., Chen, C., Zhou, J., Zang, C., and Huang, S. (2018). Research on eigenvector centrality ranking under heterogeneous information network. *Comput. Sci. Appl.* 8, 1452–1458. doi: 10.12677/CSA.2018.89159

Zamora-Lopez, G., Zhou, C., and Kurths, J. (2010). Cortical hubs form a module for multisensory integration on top of the hierarchy of cortical networks. *Front. Neuroinform.* 4:1. doi: 10.3389/neuro.11.001.2010

Zhu, Y., Song, X., Xu, M., Hu, X., Li, E., Liu, J., et al. (2016). Impaired interhemispheric synchrony in Parkinson's disease with depression. *Sci. Rep.* 6:27477. doi: 10.1038/srep27477

Zuo, X., Ehmke, R., Mennes, M., Imperati, D., Castellanos, F. X., Sporns, O., et al. (2012). Network centrality in the human functional connectome. *Cereb. Cortex* 22, 1862–1875. doi: 10.1093/cercor/bhr269

Conflict of Interest: The authors declare that the research was conducted in the absence of any commercial or financial relationships that could be construed as a potential conflict of interest.

Publisher's Note: All claims expressed in this article are solely those of the authors and do not necessarily represent those of their affiliated organizations, or those of the publisher, the editors and the reviewers. Any product that may be evaluated in this article, or claim that may be made by its manufacturer, is not guaranteed or endorsed by the publisher.

Copyright © 2022 Ke, Li and Liu. This is an open-access article distributed under the terms of the Creative Commons Attribution License (CC BY). The use, distribution or reproduction in other forums is permitted, provided the original author(s) and the copyright owner(s) are credited and that the original publication in this journal is cited, in accordance with accepted academic practice. No use, distribution or reproduction is permitted which does not comply with these terms.

frontiers | Frontiers in Neuroscience

ORIGINAL RESEARCH
published: 09 May 2022
doi: 10.3389/fnins.2022.912665

Cerebral Perfusion Patterns of Anxiety State in Patients With Pulmonary Nodules: A Study of Cerebral Blood Flow Based on Arterial Spin Labeling

Xiao-Hui Wang[1], Xiao-Fan Liu[2], Min Ao[1], Ting Wang[1], Jinglan He[3], Yue-Wen Gu[4], Jing-Wen Fan[4], Li Yang[1], Renqiang Yu[5]* and Shuliang Guo[1]**

[1] Department of Pulmonary and Critical Care Medicine, The First Affiliated Hospital of Chongqing Medical University, Chongqing, China, [2] School of Medical Technology, Shaanxi University of Chinese Medicine, Xianyang, China, [3] Department of Psychiatry, The First Affiliated Hospital of Chongqing Medical University, Chongqing, China, [4] Department of Clinical Psychology, Fourth Military Medical University, Xi'an, China, [5] Department of Radiology, The First Affiliated Hospital of Chongqing Medical University, Chongqing, China

OPEN ACCESS

Edited by:
Guolin Ma,
China-Japan Friendship Hospital, China

Reviewed by:
Xia Zhe,
Shaanxi Provincial People's Hospital, China
Hu Liu,
The First Affiliated Hospital of China Medical University, China

***Correspondence:**
Li Yang
315764694@qq.com
Renqiang Yu
yurenqiang@hospital.cqmu.edu.cn
Shuliang Guo
guosl999@sina.com
orcid.org/0000-0003-3572-7421

Specialty section:
This article was submitted to Brain Imaging Methods, a section of the journal Frontiers in Neuroscience

Received: 04 April 2022
Accepted: 21 April 2022
Published: 09 May 2022

Citation:
Wang X-H, Liu X-F, Ao M, Wang T, He J, Gu Y-W, Fan J-W, Yang L, Yu R and Guo S (2022) Cerebral Perfusion Patterns of Anxiety State in Patients With Pulmonary Nodules: A Study of Cerebral Blood Flow Based on Arterial Spin Labeling. Front. Neurosci. 16:912665. doi: 10.3389/fnins.2022.912665

Background and Purpose: The proportion of patients with somatic diseases associated with anxiety is increasing each year, and pulmonary nodules have become a non-negligible cause of anxiety, the mechanism of which is unclear. The study focus on the cerebral blood flow (CBF) of anxiety in patients with pulmonary nodules to explore the cerebral perfusion pattern of anxiety associated with pulmonary nodules, blood perfusion status and mode of pulmonary nodule induced anxiety state.

Materials and Methods: Patients with unconfirmed pulmonary nodules were evaluated by Hamilton Anxiety Scale (HAMA). The total score $>$ 14 was defined as anxiety group, and the total score $\leq$ 14 points was defined as non-anxiety group. A total of 38 patients were enrolled, of which 19 patients were the anxiety group and 19 were the non-anxiety group. All subjects underwent arterial spin labeling imaging using a 3.0 T MRI. A two-sample *t*-test was performed to compare the CBF between the two groups. The CBF was extracted in brain regions with difference, and Spearman correlation was used to analyze the correlation between CBF and HAMA scores; ROC was used to analyze the performance of CBF to distinguish between the anxiety group and the non-anxiety group.

Results: The CBF in the right insula/Heschl's cortex of the anxiety group decreased (cluster = 109, peak t = 4.124, and $P < 0.001$), and the CBF in the right postcentral gyrus increased (cluster = 53, peak t = −3.912, and $P < 0.001$) in the anxiety group. But there was no correlation between CBF and HAMA score. The ROC analysis of the CBF of the right insula/Heschl's cortex showed that the AUC was 0.856 (95%CI, 0.729, 0.983; $P < 0.001$), the optimal cutoff value of the CBF was 50.899, with the sensitivity of 0.895, and specificity of 0.789. The ROC analysis of CBF in the right postcentral gyrus

showed that the AUC was 0.845 (95%CI, 0.718, 0.972; $P < 0.001$), the optimal cutoff value of CBF was 43.595, with the sensitivity of 0.737, and specificity of 0.842.

Conclusion: The CBF of the right insula/Heschl's cortex decreased and the CBF of the right postcentral gyrus increased in patients with pulmonary nodules under anxiety state, and the CBF of the aforementioned brain regions can accurately distinguish the anxiety group from the non-anxiety group.

Keywords: pulmonary nodules, anxiety, arterial spin labeling, cerebral blood flow, cerebral perfusion

INTRODUCTION

Anxiety disorder is a group of mental disorders that mainly manifested by pathological anxiety symptoms. According to the clinical manifestations and pathogenesis, it mainly includes generalized anxiety disorder (GAD), specific phobia (animal, natural environment and blood-injection-injury, etc.), panic disorder, anxiety disorders due to another medical condition, etc. In recent years, the proportion of patients with somatic diseases accompanied by anxiety disorders has increased significantly. The somatic diseases highly related to anxiety mainly include neurological diseases, non-cardiac chest pain, diabetes, gastrointestinal diseases, and cardiovascular and respiratory diseases. Somatic and mental disorders are inextricably linked (Wang et al., 2019). Psychological abnormalities caused by somatic diseases can lead to damage to social functions that required timely intervention. Currently, pulmonary nodules have become a non-negligible somatic disease of anxiety.

Low-dose computed tomography (LDCT) has been widely recommended to screen lung cancer for high risk adults (Zhou et al., 2018), and lung cancer mortality and overall mortality might decrease by 20 and 6.7%, respectively (Aberle et al., 2011). As the increasing number of people undergo LDCT screening, millions of people are found to have pulmonary nodules every year (Slatore and Wiener, 2018). However, the vast majority of pulmonary nodules are benign (Fan et al., 2019; Lin et al., 2019), individuals with which may experience psychological harm as a result of a "near-cancer" diagnosis (Slatore and Wiener, 2018; Li L. et al., 2020). Previous studies show the incidence of anxiety in patients with pulmonary nodules ranges from 39.8 to 59.3% (Freiman et al., 2016; Li L. et al., 2020; Wang et al., 2020). But the neural basis of anxiety in patients with pulmonary nodules is still complex and vague.

The neuroimaging, especially magnetic resonance imaging (MRI), may provide critical information for understanding the disease. The cerebral perfusion is fundamental for the function of brain, and perfusion imaging can be used to indirectly or directly understand these changes. Arterial spinal labeling (ASL) is a imaging method with greater reliability over blood oxygen level-dependent functional magnetic resonance imaging (BOLD-fMRI) that can measure the regional cerebral blood flow (CBF) quantitatively (Tuite, 2017). In recent years, CBF is closely related to normal brain function, so it has attracted much attention in the research of brain function, and may provide a large amount of brain physiological information (Liang et al., 2013), particularly in neurological and psychiatric disorders (Cui et al., 2017a,b; Yu et al., 2021; Chen et al., 2022; Hu et al., 2022; Wang et al., 2022). However, no study has researched the changes of CBF in anxiety of patients with pulmonary nodules.

Therefore, we conducted CBF research based on ASL to explore the cerebral perfusion pattern of anxiety associated with pulmonary nodules, blood perfusion status and mode of pulmonary nodule anxiety induced state, so as to contribute to a more comprehension of its neuroimaging phenotype and provide the basis and possibility for exploring new and more effective intervention measures.

MATERIALS AND METHODS

Patients

From March 2021 to September 2021, 42 patients with unconfirmed pulmonary nodules from the Pulmonary and Critical Care Medicine, the First Affiliated Hospital of Chongqing Medical University underwent MRI. Four patients were excluded, two of which were found obvious demyelinating lesions, and the other 2 patients' image quality could not meet the analysis standards. A total of 38 patients were included in this study, of which 19 patients entered the anxiety group and 19 entered the non-anxiety group. The patients of the two groups were matched for sex, age, and years of education. The inclusion criteria were as follows: (1) all patients were aged from 18 to 65 years old; (2) pulmonary nodules were found by chest CT examination without definite pathological diagnosis by puncture or surgery, diameter of which $\leq$3 cm; and (3) they were right handed. The exclusion criteria were as follows: (1) a history of mental illness; (2) communication impairments, such as hearing or speech impairments; (3) suffering from a severely unstable physical condition; (4) combined with hypertension, diabetes, thyroid disease, heart disease, chronic obstructive pulmonary disease, bronchiectasis, narrow-angle glaucoma, previous head trauma, cerebral infarction, cerebral hemorrhage, intracranial mass, epilepsy, disturbance of consciousness, and other intracranial organic lesions; (5) pregnant or breast-feeding women, or those planning to become pregnant; (6) presence of fixed dentures or tattoos; (7) MRI examination revealed intracranial dysplasia, mass, severe multiple lacunar infarction and demyelinating lesions; (8) metal implants in the body, such as the skull and mouth, which affect the quality of image data; and (9) contraindications to MRI scanning.

The demographic characteristics of the patients were collected, including gender, age, ethnicity, marital status, years of

education, occupation, alcohol consumption, smoking history, second-hand smoke exposure, malignant tumor history, and family history of malignancy. The clinical data were collected, including respiratory symptoms, course of pulmonary nodules, number of pulmonary nodules, diameter of the largest pulmonary nodule, and the decision of doctors. The written informed consent of all individuals were obtained. The study was approved by the institutional of the First Affiliated Hospital of Chongqing Medical University Ethics Board (2019-083).

Clinical Assessment

Patients were evaluated by Hamilton Anxiety Scale (HAMA) in a quiet studio before undertaking MRI. The HAMA is a 14-item rating scale that measures the severity of anxiety based on the frequency and impairment of symptoms during the past week. Each item ranges from 0 (not present) to 4 (very severe). Higher scores indicate a greater degree of anxiety. The total score > 14 was defined as anxiety group, and the total score ≤ 14 points was defined as non-anxiety group.

Image Acquisition

The subjects were required to lie down quietly and with their eyes closed. During the scanning process, they were required to stay awake and not fall asleep. Both ears were plugged with earplugs to protect their hearing. The head was fixed with a sponge to reduce head movement. A standard 8-channel head coil was used with a GE signal Signa HDx 3.0 T MRI scanner (United States). Intracranial lesions and structural abnormalities were excluded using 3D high-resolution T1WI, T2WI, and T2 FLAIR sequences, followed by ASL. ASL parameters: TR 4639 ms, TE 9.8 ms, slice thickness 4.0 mm, acquisition slices 40, NEX 3, FOV 24 mm $\times$ 240 mm, matrix 512 $\times$ 8 (3D spiral filling), PLD 1525 ms, acquisition time 4 min 20 s.

Image Processing

The DICOM images were converted into NIFTI format by dcm2nii software, and then SPM12 was run in the Matlab13b, and the image of each subject was registered by the one-step registration method, and the image quality after registration was checked. Then, dpabi4.3 was used for image normalization; SPM12 was used for spatial smoothing, and the full width at half-maximum of the Gaussian kernel was 6 mm. As performed by a previous study (He et al., 2019), the data were standardized by the signal of whole brain.

Statistical Analysis

Two-sample *t*-test was used to compare CBF between groups, and age, gender, and years of education were used as covariates for regression. The *P* value was set as 0.001 (cluster > 50). The above steps was completed based on SPM12. Xjview10 was used to visualize the results, combined with DPABI 4.3 to extract the CBF values of the brain regions with difference. Spearman correlation analysis was used to evaluate the correlation between the CBF value and HAMA score; ROC analysis was used to assess the capacity of the CBF for distinguishing the anxiety group from the non-anxiety group, and $P < 0.05$ were considered statistically significant.

RESULTS

Demographic and Clinical Data

The proportion of single pulmonary nodules in the anxiety group was significantly lower than that in the non-anxiety group (15.79% vs. 47.37%, $P = 0.039$). There were no significant difference between the two groups in gender, marital status, daily alcohol consumption, smoking history, secondhand smoke exposure history, malignant tumor history, tumor family history, occupational exposure history, pulmonary nodules detected by physical examination, respiratory symptoms, decision of doctors, age, years of education, course of pulmonary nodules, and the diameter of the largest pulmonary nodule ($P > 0.05$, **Table 1**).

Difference of Cerebral Blood Flow Between Anxiety Group and Non-anxiety Group

Compared with the non-anxiety group, CBF decreased in the right insula/Heschl's cortex (cluster = 109, peak $t = 4.124$, and $P < 0.001$; **Figure 1A**), and increased in the right postcentral gyrus (cluster = 53, peak $t = -3.912$, and $P < 0.001$; **Figure 1B**) in anxiety group. Two-sample *t*-test revealed that CBF in the right insula/Heschl's cortex of anxiety group was significantly lower than non-anxiety (49.34 ± 4.76 vs. 56.42 ± 5.21, $t = -4.374$, and $P < 0.001$; **Figure 2**), while CBF in the right postcentral gyrus of anxiety group was significantly higher than non-anxiety (45.37 ± 2.25 vs. 41.31 ± 3.77, $t = 4.024$, and $P < 0.001$; **Figure 3**).

Correlation Between Cerebral Blood Flow and Hamilton Anxiety Scale Score

There was no correlation of CBF in the right insula/Heschl's cortex and HAMA in both anxiety and non-anxiety groups ($r = -0.115$, $P = 0.640$; $r = -0.062$, $P = 0.802$; **Figure 4**). There was no correlation between CBF in the right postcentral gyrus with difference and HAMA in both anxiety and non-anxiety groups ($r = 0.059$, $P = 0.811$; $r = 0.081$, $P = 0.740$; **Figure 5**).

Capacity of Cerebral Blood Flow in Anxiety Classification

The ROC analysis of CBF in the right insula/Heschl's cortex showed an AUC of 0.856 (95%CI, 0.729, 0.983; $P < 0.001$). When the optimal cutoff value of CBF was 50.899, the Youden index was 0.684, the sensitivity was 0.895, the specificity was 0.789, and the accuracy was 0.821 (**Figure 6**). The ROC analysis of CBF in the right postcentral gyrus showed an AUC of 0.845 (95%CI, 0.718, 0.972; $P < 0.001$). When the optimal cutoff value of CBF was 43.595, the Youden index was 0.579, the sensitivity was 0.737, the specificity was 0.842, and the accuracy was 0.789 (**Figure 7**).

DISCUSSION

In this study, we performed ASL imaging and calculated CBF. It was found that in patients with pulmonary nodules combined with anxiety, the CBF of the right insula/Heschl's cortex decreased, and the CBF of the right postcentral gyrus increased.

TABLE 1 | Comparison of demographic characteristics and clinical data between anxiety group and non-anxiety group.

	Anxiety group	Non-anxiety group	χ^2 or *t* or Z value	*P* value
Gender				
Female, *n* (%)	13 (68.42%)	11 (57.89%)	0.440	0.507
Male, *n* (%)	6 (31.58%)	8 (42.11%)		
Marital status				
Married, *n* (%)	15 (78.95%)	18 (94.74%)	2.018	0.155
No spouse, *n* (%)	4 (21.05%)	1 (5.26%)		
Daily alcohol consumption				
Yes, *n* (%)	1 (5.26%)	1 (5.26%)	0.000	1.000
No, *n* (%)	18 (94.74%)	18 (94.74%)		
Smoking				
Yes, *n* (%)	4 (21.05%)	4 (21.05%)	0.000	1.000
No, *n* (%)	15 (78.95%)	15 (78.95%)		
Malignant tumor history				
Yes, *n* (%)	1 (5.26%)	0 (0.00%)	1.000	0.317
No, *n* (%)	18 (94.74%)	19 (100.00%)		
Family history of tumor				
Yes, *n* (%)	9 (47.37%)	8 (42.11%)	0.104	0.748
No, *n* (%)	10 (52.63%)	11 (57.89%)		
Occupational exposure history				
Yes, *n* (%)	2 (10.53%)	0 (0.00%)	2.056	0.152
No, *n* (%)	17 (89.47%)	19 (100.00%)		
Secondhand smoke exposure history				
Yes, *n* (%)	8 (42.11%)	3 (15.79%)	3.114	0.078
No, *n* (%)	11 (57.89%)	16 (84.21%)		
Pulmonary nodules detected by physical examination				
Yes, *n* (%)	13 (68.42%)	13 (68.42%)	0.000	1.000
No, *n* (%)	6 (31.58%)	6 (31.58%)		
Respiratory symptoms				
Yes, *n* (%)	3 (15.79%)	3 (15.79%)	0.000	1.000
No, *n* (%)	16 (84.21%)	16 (84.21%)		
Numbers of pulmonary nodules				
Single, *n* (%)	3 (15.79%)	9 (47.37%)	4.269	0.039
≥2 nodules, *n* (%)	16 (84.21%)	10 (52.63%)		
Decision of doctors				
Follow-up, *n* (%)	12 (63.16%)	16 (84.21%)	2.114	0.146
Puncture or surgery, *n* (%)	7 (36.84%)	3 (15.79%)		
Age (years), $-x \pm s$	48.58 ± 7.11	43.37 ± 10.67	1.771	0.086
Years of education, M (Q1, Q3)	12 (9, 15)	14 (10, 15)	−0.747	0.455[&]
Course of pulmonary nodules (month), M (Q1, Q3)	4 (1, 12)	8 (1, 17)	−0.927	0.354[&]
The diameter of the largest pulmonary nodule (mm), M (Q1, Q3)	5 (4, 10)	5 (4, 7)	−0.695	0.487[&]

"&" Years of education, course of pulmonary nodules, and the diameter of the largest pulmonary nodule showed non-normal distribution, using Mann–Whitney U test.

And the CBF values of the above-mentioned brain regions with difference can accurately distinguish the anxiety group from the non-anxiety group. ASL is a non-invasive imaging technique that can quantitatively reflect tissue perfusion. Blood flow is the blood delivered to a unit of tissue per unit time, reflecting the metabolic and functional state of the tissue. It has been used for the research in brain tumors (Batalov et al., 2021), vascular cognitive impairment (Malojcic et al., 2017), brain injury (Li N. et al., 2020), ischemic stroke (Aracki-Trenkic et al., 2020), depression (Zhang et al., 2020), Alzheimer's disease (Malojcic et al., 2017), kidney disease (Nery et al., 2019), musculoskeletal tumor (Xu et al., 2018), and even lung cystic fibrosis (Hernandez-Garcia et al., 2019), at the same time, it has also been widely used in clinical practice.

From a cognitive neuroscience perspective, anxiety is a state of distress and arousal prototypically evoked by uncertain danger (Hur et al., 2020), and anxiety disorder is the most common familial mental disorder (Collaborators, 2016). Persistent state of anxiety can cause social and physical dysfunction sometimes (Conway et al., 2019). Existing treatments still need to improve on the effectiveness and the side effects (Griebel and Holmes, 2013). Therefore, it is urgent to explore its neurobiological mechanism further. Previous studies have proved the high incidence of anxiety in patients with pulmonary nodules (Freiman et al., 2016; Li L. et al., 2020; Wang et al., 2020), so pulmonary nodules have become a non-negligible cause of anxiety, the CBF changes of which is still unclear.

This study has explored the CBF in anxiety patients with pulmonary nodules and found decreased CBF in the right insula/Heschl's cortex and increased CBF in the right postcentral gyrus. Although there was no correlation of CBF in the aforementioned brain regions and HAMA scores, they contribute to the differentiation of anxiety group from the non-anxiety group. When the CBF value was selected at the optimal cutoff point, the accuracy of CBF in right insula/Heschl's cortex is higher than right postcentral gyrus.

Cerebral blood flow has been used to investigate the neurobiological mechanisms of other anxiety disorders. Anxiety may lead to poor performance in cognitive tests and neuroimaging differences in patients with somatic diseases. Studies have shown that individuals with comorbid symptoms of anxiety and depression have lower performance in all cognitive tests, and reduced CBF in gray matter (Raffield et al., 2016). Anxiety and depression are the most common symptoms in neuropsychiatric systemic lupus erythematosus (NPSLE; Moustafa et al., 2020), that may have significant impact on mental health and health-related quality of life. Reduced prefrontal white matter perfusion was reported in a group of patients with NPSLE, which was associated with more severe anxiety symptoms (Papadaki et al., 2019). The frontal lobe is also considered to be an essential part of emotion assessment and regulation networks (Dixon et al., 2017).

Further studies have shown that individual differences in anxiety symptoms in NPSLE are related to specific and complex hemodynamics in the limbic system and prefrontal brain regions, as anxiety symptoms are mainly related to the increased perfusion dynamics in the right amygdala (Antypa et al., 2021). This study found changes in the CBF of the right insula/Heschl's cortex and postcentral gyrus in anxiety patients with pulmonary nodules, of which the insula is currently considered to belong to the limbic system. The connectivity of subcortical areas to insula plays a pivotal role in anxiety (Robinson et al., 2019). However, the present study did not find abnormal perfusion in the frontal lobe of patients with pulmonary nodules combined with anxiety, which may be related to different underlying diseases.

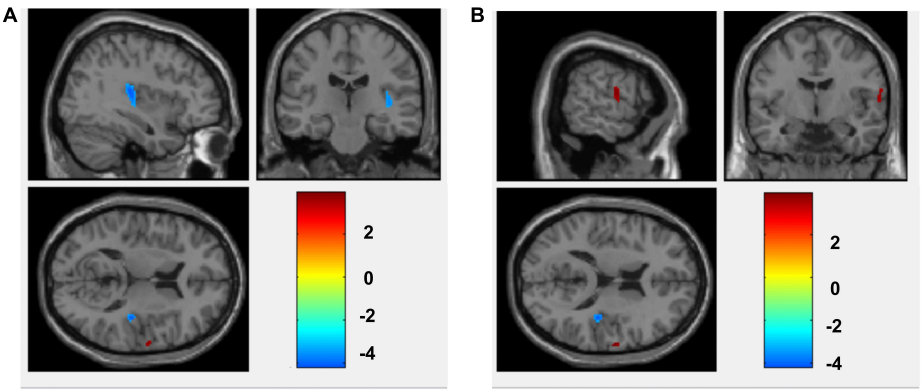

FIGURE 1 | CBF differences between anxiety and non-anxiety group patients with pulmonary nodules. **(A)** The blue area represents CBF decrease (Insula_R/Heschl_R). **(B)** The red area represents CBF increase (Postcentral_R).

A previous study reported increased CBF in the posterior temporal-occipital area of patients with GAD when dealing with sentences induced anxiety, meanwhile, no significant between-group difference was observed between the patients and healthy control (Andreescu et al., 2011). In addition, when patients with GAD were instructed to suppress their worries through reassessment, reduced CBF was found in the striatum, prefrontal cortex, middle cingulate, and sensorimotor areas (Karim et al., 2017a). In patients with chronic traumatic brain injury, voxel-wise analysis showed that CBF in the hippocampus, parahippocampus, rostral anterior cingulate, inferior frontal gyrus, and other temporal regions were negatively associated with self-reported anxiety. Moreover, region of interest (ROI) analysis revealed that CBF in hippocampal and rostral anterior cingulate were negatively associated with symptoms of anxiety (Thomas et al., 2021).

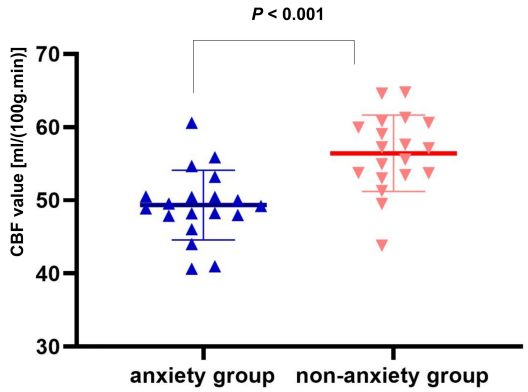

FIGURE 2 | Two-sample *t* test of CBF in the right insula/Heschl's cortex between anxiety group and non-anxiety group.

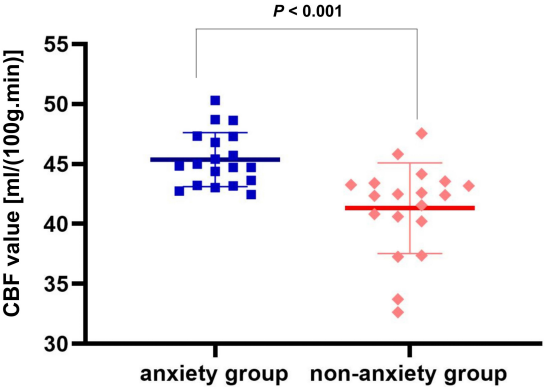

FIGURE 3 | Two-sample *t* test of CBF in the right postcentral gyrus between anxiety group and non-anxiety group.

Notably, the changed brain areas are not common areas in anxiety disorders-related studies. The subcortical areas (the bed nucleus of the stria terminalis, the amygdala, and the hippocampus) are highlighted in the neural circuitry of anxiety (Robinson et al., 2019). However, somatic diseases are risk factors for developing anxiety symptom by causing neurohumoral dysfunction, and there is a bidirectional association between anxiety and somatic disease (Henning et al., 2020). The underlying mechanisms of comorbid anxiety in individuals with somatic diseases comprise unhealthy lifestyles, low treatment adherence, and dysregulations of psychobiological stress systems (Penninx et al., 2021), differing from anxiety disorders. As the first research of CBF in patients with pulmonary nodules complicated with anxiety, it was found that CBF decreased in the right insula/Heschl's cortex and increased in the right postcentral gyrus, which is inconsistent with the abnormal CBF brain region found in the above study, suggesting that patients with pulmonary nodules complicated with anxiety have a different cerebral perfusion pattern from other anxious people. But, in another study revealed group differences in CBF in the inferior parietal lobule and in the postcentral and precentral gyri during anxiety induction of patients (Karim et al., 2017b), and the CBF alteration in the postcentral gyrus was consistent with the present study, suggesting a common neuroimaging phenotype in certain types of anxiety.

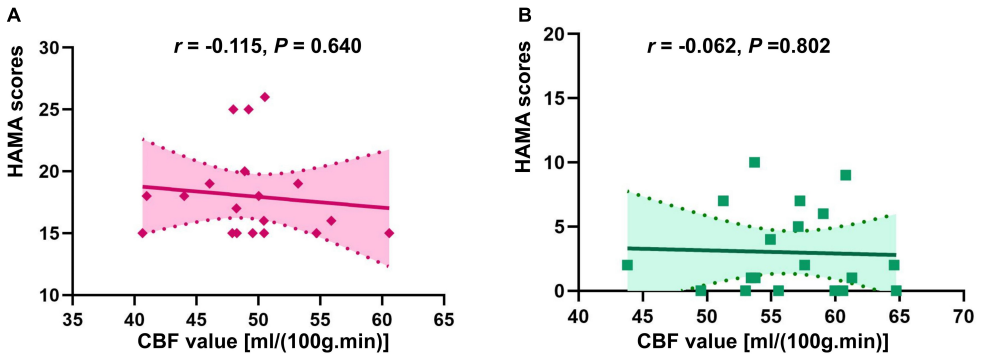

FIGURE 4 | Correlation analysis of CBF in brain regions with difference (Insula_R/Heschl_R) and HAMA score in two groups. **(A)** The correlation analysis in anxiety group. **(B)** The correlation analysis in non-anxiety group.

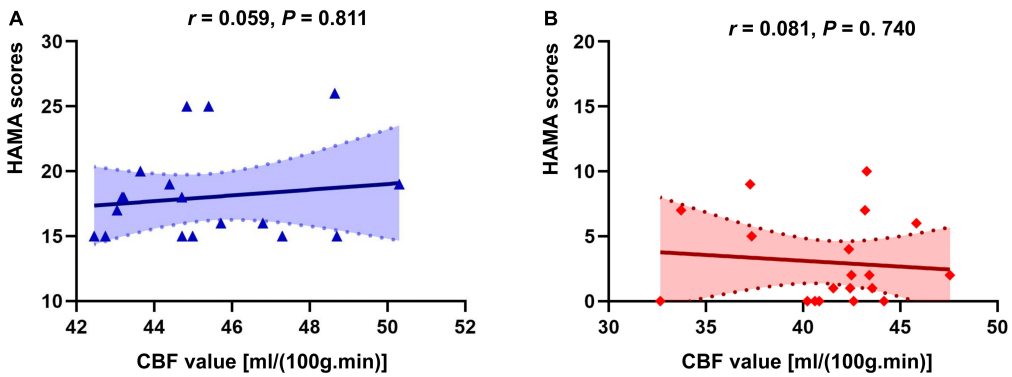

FIGURE 5 | Correlation analysis of CBF in brain regions with difference (Postcentral_R) and HAMA score in two groups. **(A)** The correlation analysis in anxiety group. **(B)** The correlation analysis in non-anxiety group.

However, the mechanisms of anxiety are quite complex. Lots of studies show that anxiety-fear stimuli affect multiple regions, including the anterior insula, middle cingulate cortex, thalamus, and amygdala (Fullana et al., 2018). A meta-analysis showed that both induced anxiety and pathological anxiety showed increased activity in the left and right insula and cingulate cortex/medial prefrontal cortex; however, When the analyses were split by disorder, specific phobia appeared the most, and GAD the least, similar to induced anxiety (Chavanne and Robinson, 2021). Even

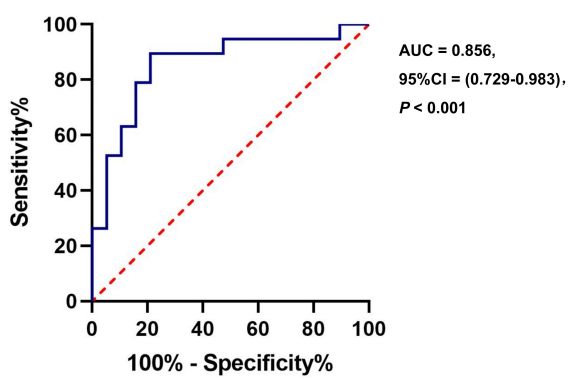

FIGURE 6 | The ROC curve of CBF in the brain regions with difference (Insula_R/Heschl_R) for distinguishing the anxiety group from the non-anxiety group.

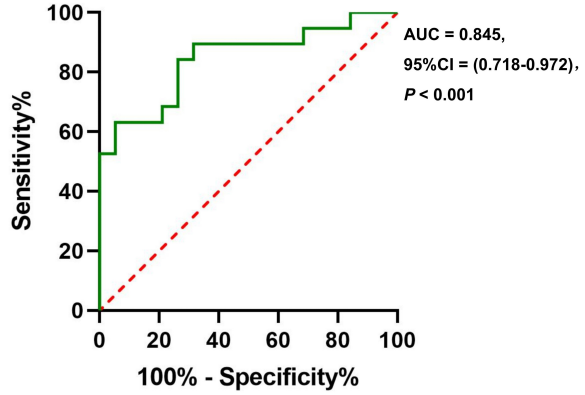

FIGURE 7 | The ROC curve of CBF in the brain regions with difference (Postcentral_R) for distinguishing the anxiety group from the non-anxiety group.

Murty et al. (2022) found that the effect of anxious apprehension was distributed across the brain and that the temporal evolution of the responses was quite varied, including more transient and more sustained profiles, as well as signal increases and decreases with threat. Hence, more researches need to be performed to validate the results.

There are some limitations of our study. First, a single-modality study sequence was used in our study. Diffusion tensor imaging and fMRI will be needed in the future. Second, the sample size was not large. Although our study was able to detect clinically relevant effects, it is important to conduct large sample research in the future.

CONCLUSION

Therefore, decreased CBF in the right insula cortex of the anxiety group found by the current study demonstrates the neurobiological basis of the anxiety state to some extent. CBF in the right insula/Heschl's cortex and right postcentral gyrus has a capability to distinguish anxiety group from the non-anxiety group. This study broadens the perspective for analyzing the brain phenotype of patients with pulmonary nodules complicated with anxiety.

DATA AVAILABILITY STATEMENT

The raw data supporting the conclusions of this article will be made available by the authors, without undue reservation.

ETHICS STATEMENT

The studies involving human participants were reviewed and approved by the institutional of the First Affiliated Hospital of Chongqing Medical University Ethics Board. The patients/participants provided their written informed consent to participate in this study.

AUTHOR CONTRIBUTIONS

X-HW and SG contributed to the conception and design of the study. X-HW and X-FL were in charge of the manuscript draft. X-HW, RY, TW, and MA collected and confirmed data and image accuracy. LY was responsible for the management of pulmonary nodules. JH was responsible for anxiety evaluation and consultation. X-HW, Y-WG, J-WF, and RY were responsible for statistical analysis of data. All authors made substantial revisions to the manuscript and approved the submitted revision.

FUNDING

This work was supported by: (1) the Fourth Military Medical University (2021JSTS30); (2) Chongqing Science and Technology Commission, Chongqing People's Municipal Government (cstc2019jscx-msxmX0184 and CSTC2021jscx-gksb-N0023); (3) Chongqing Research project on key disease prevention and control technology (2019ZX002); (4) Chongqing Pulmonary Nodule Management Studio; and (5) Discipline Innovation Fund discipline training project of the First Affiliated Hospital of Chongqing Medical University (XKST134).

ACKNOWLEDGMENTS

We would like to thank the support of Longbiao Cui from the Department of Clinical Psychology, Fourth Military Medical University in data analysis.

REFERENCES

Aberle, D. R., Adams, A. M., Berg, C. D., Black, W. C., Clapp, J. D., Fagerstrom, R. M., et al. (2011). Reduced lung-cancer mortality with low-dose computed tomographic screening. *N. Engl. J. Med.* 365, 395–409. doi: 10.1056/NEJMoa1102873

Andreescu, C., Gross, J. J., Lenze, E., Edelman, K. D., Snyder, S., Tanase, C., et al. (2011). Altered cerebral blood flow patterns associated with pathologic worry in the elderly. *Depress. Anxiety* 28, 202–209. doi: 10.1002/da.20799

Antypa, D., Simos, N. J., Kavroulakis, E., Bertsias, G., Fanouriakis, A., Sidiropoulos, P., et al. (2021). Anxiety and depression severity in neuropsychiatric SLE are associated with perfusion and functional connectivity changes of the frontolimbic neural circuit: a resting-state f(unctional) MRI study. *Lupus Sci. Med.* 8:473. doi: 10.1136/lupus-2020-000473

Aracki-Trenkic, A., Law-Ye, B., Radovanovic, Z., Stojanov, D., Dormont, D., and Pyatigorskaya, N. (2020). ASL perfusion in acute ischemic stroke: the value of CBF in outcome prediction. *Clin. Neurol. Neurosurg.* 194:105908. doi: 10.1016/j.clineuro.2020.105908

Batalov, A. I., Goryaynov, S. A., Zakharova, N. E., Solozhentseva, K. D., Kosyrkova, A. V., Potapov, A. A., et al. (2021). Prediction of Intraoperative Fluorescence of Brain Gliomas: correlation between Tumor Blood Flow and the Fluorescence. *J. Clin. Med.* 10:10112387. doi: 10.3390/jcm10112387

Chavanne, A. V., and Robinson, O. J. (2021). The Overlapping Neurobiology of Induced and Pathological Anxiety: a Meta-Analysis of Functional Neural Activation. *Am. J. Psychiatry* 178, 156–164. doi: 10.1176/appi.ajp.2020.19111153

Chen, Y., Li, H., Liu, B., Gao, W., Yang, A., Lv, K., et al. (2022). Cerebral Blood Flow Pattern Changes in Unilateral Sudden Sensorineural Hearing Loss. *Front. Neurosci.* 16:856710. doi: 10.3389/fnins.2022.856710

Collaborators, G. B. O. D. (2016). Global, regional, and national incidence, prevalence, and years lived with disability for 310 diseases and injuries, 1990-2015: a systematic analysis for the Global Burden of Disease Study 2015. *Lancet* 388, 1545–1602. doi: 10.1016/S0140-6736(16)31678-6

Conway, C. C., Forbes, M. K., Forbush, K. T., Fried, E. I., Hallquist, M. N., Kotov, R., et al. (2019). A Hierarchical Taxonomy of Psychopathology Can Transform Mental Health Research. *Perspect. Psychol. Sci.* 14, 419–436. doi: 10.1177/1745691618810696

Cui, L. B., Chen, G., Xu, Z. L., Liu, L., Wang, H. N., Guo, L., et al. (2017a). Cerebral blood flow and its connectivity features of auditory verbal hallucinations in schizophrenia: a perfusion study. *Psychiatry Res. Neuroimag.* 260, 53–61. doi: 10.1016/j.pscychresns.2016.12.006

Cui, L. B., Wang, L. X., Tian, P., Wang, H. N., Cai, M., Guo, F., et al. (2017b). Aberrant perfusion and its connectivity within default mode network of first-episode drug-naive schizophrenia patients and their unaffected first-degree relatives. *Sci. Rep.* 7:16201. doi: 10.1038/s41598-017-14343-7

Dixon, M. L., Thiruchselvam, R., Todd, R., and Christoff, K. (2017). Emotion and the prefrontal cortex: an integrative review. *Psychol. Bull.* 143, 1033–1081. doi: 10.1037/bul0000096

Fan, L., Wang, Y., Zhou, Y., Li, Q., Yang, W., Wang, S., et al. (2019). Lung Cancer Screening with Low-Dose CT: Baseline Screening Results in Shanghai. *Acad. Radiol.* 26, 1283–1291. doi: 10.1016/j.acra.2018.12.002

Freiman, M. R., Clark, J. A., Slatore, C. G., Gould, M. K., Woloshin, S., Schwartz, L. M., et al. (2016). Patients' Knowledge, Beliefs, and Distress Associated with Detection and Evaluation of Incidental Pulmonary Nodules for Cancer: results from a Multicenter Survey. *J. Thorac. Oncol.* 11, 700–708. doi: 10.1016/j.jtho.2016.01.018

Fullana, M. A., Albajes-Eizagirre, A., Soriano-Mas, C., Vervliet, B., Cardoner, N., Benet, O., et al. (2018). Fear extinction in the human brain: a meta-analysis of fMRI studies in healthy participants. *Neurosci. Biobehav. Rev.* 88, 16–25. doi: 10.1016/j.neubiorev.2018.03.002

Griebel, G., and Holmes, A. (2013). 50 years of hurdles and hope in anxiolytic drug discovery. *Nat. Rev. Drug Discov.* 12, 667–687. doi: 10.1038/nrd4075

He, Z., Sheng, W., Lu, F., Long, Z., Han, S., Pang, Y., et al. (2019). Altered resting-state cerebral blood flow and functional connectivity of striatum in bipolar disorder and major depressive disorder. *Prog Neuropsychopharmacol Biol Psychiatry* 90, 177–185. doi: 10.1016/j.pnpbp.2018.11.009

Henning, M., Subic-Wrana, C., Wiltink, J., and Beutel, M. (2020). Anxiety Disorders in Patients With Somatic Diseases. *Psychosom. Med.* 82, 287–295. doi: 10.1097/PSY.0000000000000779

Hernandez-Garcia, L., Lahiri, A., and Schollenberger, J. (2019). Recent progress in ASL. *Neuroimage* 187, 3–16. doi: 10.1016/j.neuroimage.2017.12.095

Hu, W. Z., Guo, F., Xu, Y. Q., Xi, Y. B., He, B., Yin, H., et al. (2022). Differentiation of Neoplastic and Non-neoplastic Intracranial Enhancement Lesions Using Three-Dimensional Pseudo-Continuous Arterial Spin Labeling. *Front. Neurosci.* 16:812997. doi: 10.3389/fnins.2022.812997

Hur, J., Smith, J. F., DeYoung, K. A., Anderson, A. S., Kuang, J., Kim, H. C., et al. (2020). Anxiety and the Neurobiology of Temporally Uncertain Threat Anticipation. *J. Neurosci.* 40, 7949–7964. doi: 10.1523/JNEUROSCI.0704-20.2020

Karim, H. T., Tudorascu, D. L., Butters, M. A., Walker, S., Aizenstein, H. J., and Andreescu, C. (2017a). Erratum: In the grip of worry: cerebral blood flow changes during worry induction and reappraisal in late-life generalized anxiety disorder. *Transl. Psychiatry* 7, e1244. doi: 10.1038/tp.2017.215

Karim, H. T., Tudorascu, D. L., Butters, M. A., Walker, S., Aizenstein, H. J., and Andreescu, C. (2017b). In the grip of worry: cerebral blood flow changes during worry induction and reappraisal in late-life generalized anxiety disorder. *Transl. Psychiatry* 7:e1204. doi: 10.1038/tp.2017.180

Li, L., Zhao, Y., and Li, H. (2020). Assessment of anxiety and depression in patients with incidental pulmonary nodules and analysis of its related impact factors. *Thorac. Cancer* 11, 1433–1442. doi: 10.1111/1759-7714.13406

Li, N., Wingfield, M. A., Nickerson, J. P., Pettersson, D. R., and Pollock, J. M. (2020). Anoxic Brain Injury Detection with the Normalized Diffusion to ASL Perfusion Ratio: implications for Blood-Brain Barrier Injury and Permeability. *AJNR Am. J. Neuroradiol.* 41, 598–606. doi: 10.3174/ajnr.A6461

Liang, X., Zou, Q., He, Y., and Yang, Y. (2013). Coupling of functional connectivity and regional cerebral blood flow reveals a physiological basis for network hubs of the human brain. *Proc. Natl. Acad. Sci. U S A* 110, 1929–1934. doi: 10.1073/pnas.1214900110

Lin, Y., Ma, J., Feng, J., Zhang, Q., and Huang, Y. (2019). [Results of Lung Cancer Screening among Urban Residents in Kunming]. *Zhongguo Fei Ai Za Zhi* 22, 413–418. doi: 10.3779/j.issn.1009-3419.2019.07.02

Malojcic, B., Giannakopoulos, P., Sorond, F. A., Azevedo, E., Diomedi, M., Oblak, J. P., et al. (2017). Ultrasound and dynamic functional imaging in vascular cognitive impairment and Alzheimer's disease. *BMC Med.* 15:27. doi: 10.1186/s12916-017-0799-3

Moustafa, A. T., Moazzami, M., Engel, L., Bangert, E., Hassanein, M., Marzouk, S., et al. (2020). Prevalence and metric of depression and anxiety in systemic lupus erythematosus: a systematic review and meta-analysis. *Semin. Arthritis Rheum* 50, 84–94. doi: 10.1016/j.semarthrit.2019.06.017

Murty, D., Song, S., Morrow, K., Kim, J., Hu, K., and Pessoa, L. (2022). Distributed and Multifaceted Effects of Threat and Safety. *J. Cogn. Neurosci.* 34, 495–516. doi: 10.1162/jocn_a_01807

Nery, F., De Vita, E., Clark, C. A., Gordon, I., and Thomas, D. L. (2019). Robust kidney perfusion mapping in pediatric chronic kidney disease using single-shot 3D-GRASE ASL with optimized retrospective motion correction. *Magn. Reson. Med.* 81, 2972–2984. doi: 10.1002/mrm.27614

Papadaki, E., Kavroulakis, E., Bertsias, G., Fanouriakis, A., Karageorgou, D., Sidiropoulos, P., et al. (2019). Regional cerebral perfusion correlates with anxiety in neuropsychiatric SLE: evidence for a mechanism distinct from depression. *Lupus* 28, 1678–1689. doi: 10.1177/0961203319887793

Penninx, B. W., Pine, D. S., Holmes, E. A., and Reif, A. (2021). Anxiety disorders. *Lancet* 397, 914–927. doi: 10.1016/S0140-6736(21)00359-7

Raffield, L. M., Brenes, G. A., Cox, A. J., Freedman, B. I., Hugenschmidt, C. E., Hsu, F. C., et al. (2016). Associations between anxiety and depression symptoms and cognitive testing and neuroimaging in type 2 diabetes. *J. Diabetes Compl.* 30, 143–149. doi: 10.1016/j.jdiacomp.2015.09.010

Robinson, O. J., Pike, A. C., Cornwell, B., and Grillon, C. (2019). The translational neural circuitry of anxiety. *J. Neurol. Neurosurg. Psychiatry* 90, 1353–1360. doi: 10.1136/jnnp-2019-321400

Slatore, C. G., and Wiener, R. S. (2018). Pulmonary Nodules: a Small Problem for Many, Severe Distress for Some, and How to Communicate About It. *Chest* 153, 1004–1015. doi: 10.1016/j.chest.2017.10.013

Thomas, B. P., Tarumi, T., Wang, C., Zhu, D. C., Tomoto, T., Munro, C. C., et al. (2021). Hippocampal and rostral anterior cingulate blood flow is associated with affective symptoms in chronic traumatic brain injury. *Brain Res.* 1771:147631. doi: 10.1016/j.brainres.2021.147631

Tuite, P. (2017). Brain Magnetic Resonance Imaging (MRI) as a Potential Biomarker for Parkinson's Disease (PD). *Brain Sci* 7:7060068. doi: 10.3390/brainsci7060068

Wang, L., Wei, Y., Hu, H., Zhang, X., Zheng, M., and Fei, G. (2020). Correlation between Anxiety, Depression and Changes in Th17/Treg and Inflammatory Levels in Patients with Pulmonary Nodules. *Zhongguo Fei Ai Za Zhi* 23, 554–560. doi: 10.3779/j.issn.1009-3419.2020.102.30

Wang, M., Wang, Y., Zhang, W., Zhao, X., Yang, Y., and Zhang, B. (2022). Preoperative Collateral Perfusion Using Arterial Spin Labeling: a Predictor of Surgical Collaterals in Moyamoya Angiopathy. *Front. Neurosci* 16:839485. doi: 10.3389/fnins.2022.839485

Wang, X. H., Yu, A., Zhu, X., Yin, H., and Cui, L. B. (2019). Cardiopulmonary Comorbidity, Radiomics and Machine Learning, and Therapeutic Regimens for a Cerebral fMRI Predictor Study in Psychotic Disorders. *Neurosci. Bull.* 35, 955–957. doi: 10.1007/s12264-019-00409-1

Xu, L., Xu, L., and Zhu, H. (2018). Evaluation of three-dimensional arterial spin labeling perfusion imaging for the pathological investigation of musculoskeletal tumors. *Exp. Ther. Med.* 15, 5029–5034. doi: 10.3892/etm.2018.6030

Yu, H., Li, Y., Feng, Y., Zhang, L., Yao, Z., Liu, Z., et al. (2021). Enhanced Arterial Spin Labeling Magnetic Resonance Imaging of Cerebral Blood Flow of the Anterior and Posterior Circulations in Patients With Intracranial Atherosclerotic Stenosis. *Front. Neurosci.* 15:823876. doi: 10.3389/fnins.2021.823876

Zhang, N., Qin, J., Yan, J., Zhu, Y., Xu, Y., Zhu, X., et al. (2020). Increased ASL-CBF in the right amygdala predicts the first onset of depression in healthy young first-degree relatives of patients with major depression. *J. Cereb. Blood Flow Metab.* 40, 54–66. doi: 10.1177/0271678X19861909

Zhou, Q., Fan, Y., Wang, Y., Qiao, Y., Wang, G., Huang, Y., et al. (2018). China National Lung Cancer Screening Guideline with Low-dose Computed Tomography (2018 version). *Zhongguo Fei Ai Za Zhi* 21, 67–75. doi: 10.3779/j.issn.1009-3419.2018.02.01

Conflict of Interest: The authors declare that the research was conducted in the absence of any commercial or financial relationships that could be construed as a potential conflict of interest.

Publisher's Note: All claims expressed in this article are solely those of the authors and do not necessarily represent those of their affiliated organizations, or those of the publisher, the editors and the reviewers. Any product that may be evaluated in this article, or claim that may be made by its manufacturer, is not guaranteed or endorsed by the publisher.

Copyright © 2022 Wang, Liu, Ao, Wang, He, Gu, Fan, Yang, Yu and Guo. This is an open-access article distributed under the terms of the Creative Commons Attribution License (CC BY). The use, distribution or reproduction in other forums is permitted, provided the original author(s) and the copyright owner(s) are credited and that the original publication in this journal is cited, in accordance with accepted academic practice. No use, distribution or reproduction is permitted which does not comply with these terms.

frontiers | Frontiers in Neuroscience

ORIGINAL RESEARCH
published: 06 July 2022
doi: 10.3389/fnins.2022.934166

Abnormal Cerebral Blood Flow and Volumetric Brain Morphometry in Patients With Obstructive Sleep Apnea

*Ping Xiao[1,2], Kelei Hua[3], Feng Chen[3], Yi Yin[3], Jurong Wang[3], Xiangjun Fu[2], Jiasheng Yang[4], Qingfeng Liu[4], Queenie Chan[5] and Guihua Jiang[1,3]**

[1] The Second School of Clinical Medicine, Southern Medical University, Guangzhou, China, [2] Department of Otolaryngology-Head & Neck Surgery, Guangdong Second Provincial General Hospital, Guangzhou, China, [3] Department of Medical Imaging, Guangdong Second Provincial General Hospital, Guangzhou, China, [4] Department of Respiratory and Critical Care Medicine, Center for Sleep Medicine, Guangdong Second Provincial General Hospital, Guangzhou, China, [5] Philips Healthcare, Hong Kong, Hong Kong SAR, China

OPEN ACCESS

Edited by:
Long-Biao Cui, Fourth Military Medical University, China

Reviewed by:
Ruiwang Huang, South China Normal University, China
Chao Li, The First Affiliated Hospital of China Medical University, China

***Correspondence:**
Guihua Jiang
GH.jiang2002@163.com

Specialty section:
This article was submitted to Brain Imaging Methods, a section of the journal Frontiers in Neuroscience

Received: *02 May 2022*
Accepted: *30 May 2022*
Published: *06 July 2022*

Citation:
Xiao P, Hua K, Chen F, Yin Y, Wang J, Fu X, Yang J, Liu Q, Chan Q and Jiang G (2022) Abnormal Cerebral Blood Flow and Volumetric Brain Morphometry in Patients With Obstructive Sleep Apnea. Front. Neurosci. 16:934166. doi: 10.3389/fnins.2022.934166

Obstructive sleep apnea (OSA) is a serious breathing disorder, leading to myocardial infarction, high blood pressure, and stroke. Brain morphological changes have been widely reported in patients with OSA. The pathophysiological mechanisms of cerebral blood flow (CBF) changes associated with OSA are not clear. In this study, 20 patients with OSA and 36 healthy controls (HCs) were recruited, and then pseudo-continuous arterial spin labeling (pCASL) and voxel-based morphometry (VBM) methods were utilized to explore blood perfusion and morphological changes in the patients with OSA. Compared with the HC group, the OSA group showed increased CBF values in the right medial prefrontal cortex (mPFC), left precentral gyrus, and right insula and showed decreased CBF values in the right temporal pole (TP) and the right cerebellum_Crus2. Compared with the HC group, the patients with OSA showed decreased gray matter volume (GMV) in the right dorsal lateral prefrontal cortex (DLPFC), the right occipital pole, and the vermis. There were no significantly increased GMV brain regions found in patients with OSA. Pearson correlation analysis showed that the reduced GMV in the right DLPFC and the right occipital pole was both positively correlated with Mini-Mental State Examination (MMSE) ($r = 0.755$, $p < 0.001$; $r = 0.686$, $p = 0.002$) and Montreal Cognitive Assessment (MoCA) scores ($r = 0.716$, $p = 0.001$; $r = 0.601$, $p = 0.008$), and the reduced GMV in the right occipital pole was negatively correlated with duration of illness ($r = -0.497$, $p = 0.036$). Patients with OSA have abnormal blood perfusion metabolism and morphological changes in brain regions including the frontal lobe and the cerebellum and were closely related to abnormal behavior, psychology, and cognitive function, which play an important role in the pathophysiological mechanism of OSA.

Keywords: obstructive sleep apnea, pseudo-continuous arterial spin labeling, cerebral blood flow, voxel-based morphometry, Montreal Cognitive Assessment

INTRODUCTION

Obstructive sleep apnea (OSA) is a frequently but insufficiently recognized breathing disorder, associated with prominent comorbidities, especially cerebrovascular and cardiovascular diseases such as high blood pressure, myocardial infarction, and stroke (Arzt et al., 2005; Yaggi et al., 2005; Chang et al., 2014; Lamberts et al., 2014). Obstructive sleep apnea can cause sleep fragmentation, daytime sleepiness, reduced work performance, increased risk of traffic accidents, and reduced quality of life (Bennett et al., 1999). The deficits in attention, memory, and visuoconstructive abilities frequently accompany OSA. Intermittent episodes of hypoxia during sleep and significant hemodynamic changes during apnea are considered to be central to the pathophysiology of the development of ischemic brain injury (Pizza et al., 2012; Winklewski and Frydrychowski, 2013). Previous studies have reported morphological brain changes that could underlie those symptoms in patients with OSA (Macey et al., 2002; Morrell et al., 2003; Canessa et al., 2011; O'Donoghue et al., 2012). However, the pathophysiological mechanisms of cerebral blood flow (CBF) changes associated with OSA are not fully understood.

During the past three decades, neuroimaging studies explored abnormal functional metabolism neural regions of various medical disorders such as OSA, by analyzing CBF and metabolic processes. A considerable number of studies focus on the CBF and the continuous positive air pressure therapy for the possible improvement of CBF in OSA. CBF is controlled by a variety of automatic regulatory mechanisms, including chemical, metabolic, and neurogenic regulation, with changes in carbon dioxide and oxygen (to a lesser extent) being the most powerful stimuli leading to changes in cerebrovascular flow. Acute hypoxia stimulates cerebral vasodilation and increases CBF as a compensatory mechanism. Single-photon emission computed tomography (SPECT) and positron emission tomography (PET) have been previously used for the observed brain hemometabolic process. However, SPECT and PET scans take a long time, need to inject invasive radiotracers, cause strong ionizing radiation, and have a low spatial resolution of SPECT and PET images. Compared with SPECT and PET, pseudo-continuous arterial spin labeling (pCASL) is a recent non-invasive MRI technique that can rapidly quantify local CBF using endogenous contrast agents instead of invasive radiotracers and has a high temporal and spatial resolution. Resting CBF is closely related to brain metabolisms such as glucose utilization, oxygen consumption, and aerobic glycolysis. Resting CBF indicator was widely used in bipolar disorder, major depressive disorder, schizophrenia, and multiple sclerosis to identify abnormal hemometabolic brain regions. However, no studies have focused on abnormal CBF changes in OSA using the pCASL technique.

In addition, voxel-based morphometry (VBM) is a widely used neuroimaging technique for measuring changes in gray matter and white matter volumes (GMV and WMV) in a non-invasive and region-specific manner. It is also an automatic whole-brain method that can calculate the local volume of gray matter in an unbiased manner. Several previous VBM studies found abnormal GMV brain regions in OSA. However, these results are inconsistent such as gray matter loss in the frontal and parietal cortex (Canessa et al., 2011), anterior cingulate (Macey et al., 2012), hippocampus (Morrell et al., 2003; Canessa et al., 2011), and cerebellum (Macey et al., 2002). Moreover, Fergal et al., found no GMV deficits nor focal structural changes in severe OSA (O'Donoghue et al., 2005). These differences may be related to the differences in methodologies, study population, or disease severity. However, with continuous positive airway pressure (CPAP) therapy, most of the VBM differences in GMV in patients with OSA were observed to be reversible, possibly due to changes in neuronal blood flow caused by changes in neurons or angiogenesis (Canessa et al., 2011; O'Donoghue et al., 2012). Furthermore, previous studies adopted a separate CBF method or VBM method to investigate OSA, abnormal CBF is closely related to GMV changes (Gonchigsuren et al., 2022), and therefore more efforts should be made to concentrate on CBF and VBM imaging modalities to explore the common changes and specific changes of CBF and VBM and to identify whether abnormal changes in GMV are the basis of abnormal CBF or abnormal CBF leading to abnormal GMV in OSA.

Thus, we aimed to obtain an understanding of the correlation between hemodynamic differences and morphological abnormalities in patients with OSA by using pCASL and VBM imaging and to detect shared and specific patterns of neuronal blood flow and GMV in OSA. The characteristic altered patterns of CBF and GMV may play important roles in the pathophysiological mechanism of OSA.

MATERIALS AND METHODS

Participants

A total of 20 outpatients diagnosed with moderate-to-severe OSA [apnea-hypopnea index (AHI) $>$ 15 events/h] were recruited from the Center for Sleep Medicine of Second People's Hospital of Guangdong Province. And 36 healthy control sex-, age-, and education-matched participants as healthy controls (HCs) (AHI $<$ 5) were recruited through local advertisements. All participants were right-handed and drug-naive. The exclusion criteria included the presence of severe lung, heart, or kidney disease; history of mental retardation, neurological disorders, organic brain disorder, or any comorbid somatic disorders; body mass index (BMI) $>$ 40 kg/m^2; malignant disease; pregnancy or breastfeeding; use of antidepressants, hypnotics, morphine, other respiratory-depressant medication, or non-psychiatric drugs; comorbidity with any other Axis-I mental disorders or Axis-II personality disorder; any clinical sign of previous stroke or transient ischemic attack; and drink more than 14 units per week. During the three days before the imaging period, the Epworth Sleepiness Scale (ESS), which is a validated questionnaire, was used to evaluate subjective daytime sleepiness in the context of sleep disorders for each participant. The Mini-Mental State Examination (MMSE) was published more than 30 years ago in 1975 as a practical method of grading cognitive impairment (Folstein et al., 1975). The Montreal Cognitive Assessment

(MoCA) is an increasingly popular cognitive screening tool that has good sensitivity and specificity in detecting cognitive impairment and includes an assessment of multiple cognitive domains (Shi et al., 2018). The MMSE and MoCA were used to assess the psychological state and cognitive impairment of each participant.

This study was approved by the Ethics Committee of the Second People's Hospital of Guangdong Province, and the ethics approval was given in March 2022. This study was carried out in accordance with the World Medical Association's Declaration of Helsinki. All participants agreed in writing to participate in this study.

Image Acquisition

Imaging data were performed using a 3.0 T MRI scanner (Ingenia; Philips, Best, The Netherlands). The pCASL sequence was used for three-dimensional (3D) fast spin-echo acquisition and background suppression in the resting-state perfusion imaging. The acquisition parameters were the following: repetition time (TR) = 4,155 ms, echo time (TE) = 33 ms, post-labeling delay (PLD) = 2,000 ms, field of view (FOV) = 240 × 240 mm^2, in-plane matrix = 64 × 59, in-plane voxel size = 3.75 × 3.75 × 6.00, slice thickness/gap = 6.0/0 mm, 20 axial slices covering the whole brain, number of signals averaged (NSA) = 1, and acquisition time = 4 min 51 s. In addition, a 3D T1-weighted brain volume imaging sequence covering the whole brain was used for structural data acquisition with the following: TR/TE = 7.8/3.6 ms, flip angle = 8°, slice thickness/gap = 1.0/0 mm, FOV = 240 × 240 mm, matrix = 256 × 256, NSA = 1, and acquisition time = 5 min 56 s. Routine MRI images were also collected to exclude anatomical abnormalities. All participants were found by two experienced radiologists to confirm that there were no brain structural abnormalities.

Cerebral Blood Flow Processing

The pCASL images were analyzed on a Philips post-processing workstation. Quantification of CBF was calculated using the following equation:

$$CBF = \frac{6000\lambda\,(SI_{control} - SI_{label})\,e^{\frac{PLD}{T_{1,blood}}}}{2\alpha T_{1,blood} SI_{PD}(1 - e^{-\frac{\tau}{T_{1,blood}}})}[ml/100g/min],$$

where T1 of blood ($T_{1,blood}$) was assumed to be 1,650 ms at 3.0T, partition coefficient (λ) 0.9, labeling efficiency (α) 0.85, labeling duration (τ) 1,800 ms, and PLD 2,000 ms. $SI_{control}$ and SI_{label} are the time-averaged signal intensities in the control and label images, respectively, SI_{PD} is the signal intensity of a proton density-weighted image. Using the Statistical Parametric Mapping (SPM12[1]) software standardizes the CBF maps into a standard Montreal Neurological Institute (MNI) space: (1) the individual 3D T1-weighted structure images and the individual CBF brain maps were co-registered to obtain the individual T1' brain maps; (2) all the individual T1' brain maps were non-linearly normalized to T1 template in standard space; (3) using the normalization parameters estimated in step (2), all the CBF images were normalized to MNI space and resampled to the voxel size of 2 × 2 × 2 mm^3. (4) For standardization, the z-transform was performed on the CBF value of each voxel: zCBF = (single voxel CBF - mean CBF of whole-brain)/standard deviation of the whole brain CBF. (5) The zCBF maps were smoothed using a Gaussian smoothing kernel with a half maximum and full width (FWHM) of 6 mm.

TABLE 1 | Demographic and clinical data and (standard deviations) by group.

	OSAS	HCs	*p* values
Number of subjects	18	36	
Age (years)	43.00 (15.73)	40.61 (12.01)	0.538*
Education (years)	13.50 (3.47)	13.42 (3.36)	0.933*
Sex (male/female)	13/5	27/9	0.826†
TIV (mm^3)	1514.61 (93.54)	1439.58 (126.68)	0.031*
BMI (kg/m^2)	25.42 (3.86)	21.49 (1.50)	< 0.001*
AHI (times/min)	37.86 (25.96)	2.26 (1.01)	< 0.001*
MMSE	28.28 (1.56)	29.36 (0.83)	< 0.001*
MoCA	27.56 (2.06)	29.08 (1.20)	< 0.001*
ESS	10.33 (4.59)	3.14 (1.59)	< 0.001*
Duration of illness (years)	13.72 (13.55)	n/a	

*Means (with standard deviations in parentheses) are reported unless otherwise noted. OSAS, Obstructive sleep apnea syndrome; HCs, healthy controls; TIV, total intracranial volume; BMI, Body Mass Index; AHI, apnea-hypopnea index; MMSE, Mini-mental State Examination; MoCA, Montreal Cognitive Assessment; ESS, Epworth Sleepiness Scale. *The p values were obtained by independent-sample t-tests. †The p value for sex distribution was obtained by chi-square test.*

Voxel-Based Morphometry Processing

All T1-weighted brain structure images were processed using CAT12[2] based on the SPM12 software[3]. For the VBM analysis, diffeomorphic anatomical registration through an exponentiated Lie algebra algorithm (DARTEL) (Ashburner, 2007) was used to improve the quality of structural image registration (Klein et al., 2009). The preprocessing process of structural MRI data is as follows: (1) the original individual T1-weighted images were segmented into white matter (WM), gray matter (GM), and cerebrospinal fluid (CSF). (2) After segmenting GM and WM images of all subjects, a study-specific template was created using DARTEL. (3) The individual segmented images were warped to a special template for the study and spatially normalized to the MNI space using modulation. (4) The modulated GM images were smoothed using a Gaussian smoothing kernel with an FWHM of 6 mm.

Statistical Analysis

SPSS for the Windows software, version 19.0 (SPSS Inc., Chicago, IL, United States) was performed for statistical analyses. The Kolmogorov-Smirnov test was used to evaluate the normality of age, years of education, total intracranial volume (TIV), BMI, AHI, MMSE, MoCA, and ESS. In addition, age, years of education, TIV, BMI, AHI, MMSE, MoCA, and ESS follow

[1]http://www.fil.ion.ucl.Ac.uk/spm

[2]http://dbm.neuro.uni-jena.de/cat/

[3]http://www.fil.ion.ucl.ac.uk/spm/software/spm12/

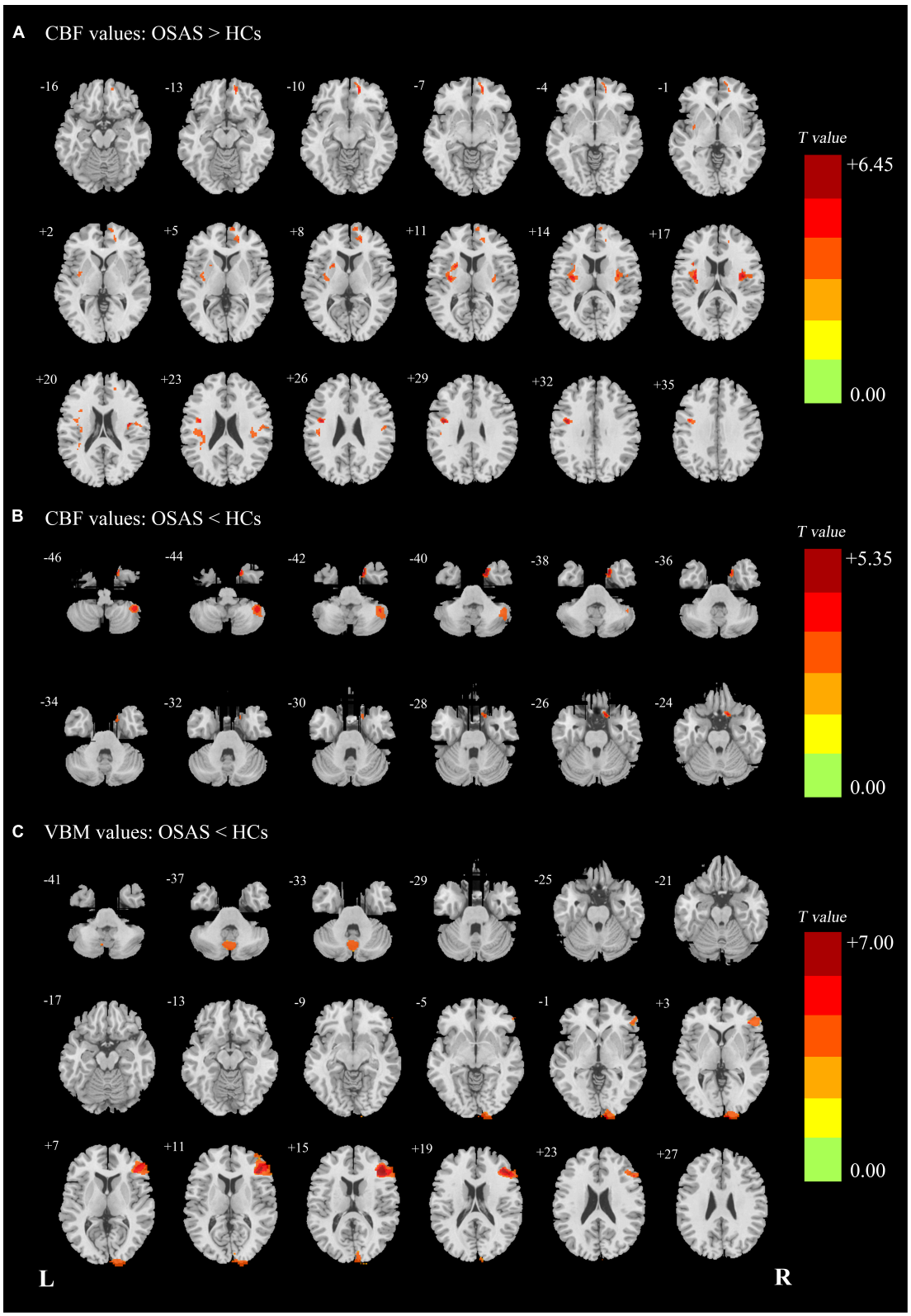

FIGURE 1 | (A) Patients with OSA showed significantly increased CBF clusters than HCs. **(B)** Patients with OSA showed significantly decreased cerebral CBF clusters than HCs. **(C)** Patients with OSA showed significantly decreased VBM clusters than HCs. OSA, obstructive sleep apnea syndrome; HCs, healthy controls; CBF, cerebral blood flow; VBM, voxel-based morphometry; L (R), left (right) hemisphere.

the normal distribution. The independent-sample *t*-test was used to compare age, years of education, TIV, BMI, AHI, MMSE, MoCA, and ESS between the OSA and HC groups. $\mathcal{X}^2$ test was used to compare the gender differences between two groups. All tests were two-tailed, and $p < 0.05$ was considered statistically significant.

For comparisons of CBF and VBM maps, a voxel-based comparison of CBF maps and VBM maps was performed between OSA and HCs groups using two-sample *t*-tests, with individuals' age, sex, years of education, and TIV as nuisance covariates. A family wise error (FWE) cluster-level correction for multiple comparisons ($p < 0.001$, cluster level $p < 0.05$, cluster > 165 voxels) was used in all group comparisons.

Once the clusters showing significant group differences in CBF and VBM maps between two groups were identified, the cluster was saved as a binary mask to extract the CBF and GMV values. Then, we further calculated the Pearson's correlation coefficients between these CBF and GMV values and the MMSE, MoCA, ESS, and duration of illness. The Bonferroni correction was used for multiple comparisons.

RESULTS

Demographic Information

Table 1 shows the demographic information and clinical characteristics of all recruited participants. Two patients with OSA were excluded from further analyses due to image artifacts. Two experienced radiologists confirmed that all participants have no brain structural abnormalities from routine MRI images. Finally, 18 patients with OSA and 36 HCs were included. There were no significant differences in age, education, and sex between two groups. The TIV, BMI, AHI, and ESS of patients with OSA were greater than those in HCs. The scores of MMSE and MoCA in the OSA group were lower than those in the HC group.

Differences in Cerebral Blood Flow Values Between Two Groups

Compared with the HC group, the OSA group showed increased CBF values in the right medial prefrontal cortex (mPFC), left precentral gyrus (extending to the left insula and left putamen), and right insula (extending to the right rolandic_oper) and showed decreased CBF values in the right TP and the right cerebellum_Crus2 (**Figures 1A,B** and **Table 2**).

Differences in Voxel-Based Morphometry Values Between Two Groups

Compared with the HC group, the patients with OSA showed decreased GMV in the right DLPFC, the right occipital pole, and the vermis. There were no significantly increased GMV brain regions found in patients with OSA (**Figure 1C** and **Table 2**).

Correlation Analysis

Pearson correlation analysis showed that the reduced GMV in the right DLPFC and the right occipital pole was positively correlated with both MMSE ($r = 0.755$, $p < 0.001$; $r = 0.686$, $p = 0.002$) and MoCA scores ($r = 0.716$, $p = 0.001$; $r = 0.601$, $p = 0.008$), and the reduced GMV in the right occipital pole was negatively correlated with duration of illness ($r = -0.497$, $p = 0.036$) ($p < 0.05/32 = 0.0016$, Bonferroni corrected) (**Figure 2**). There were no significant correlations between the left precentral gyrus, right insula, right TP, right cerebellum_Crus2, and vermis and the MMSE, MoCA, ESS, and duration of illness.

TABLE 2 | The areas of significantly different CBF and VBM values between the OSAS patients and the HCs. ($p < 0.001$, cluster level $p < 0.05$, cluster > 165, FWE corrected).

Brain regions	Extending regions	Brodman Area	Montreal Neurological Institute Coordinates			Peak *t* Value	Cluster Size (voxel numbers)
			X	Y	Z		
CBF values: OSAS > HCs							
R mPFC		11	14	52	−10	5.23	262
L precentral gyrus		6	−42	−2	30	6.43	606
	L insula	48	−33	−9	16	5.11	
	L putamen	NA	−23	8	10	4.285	
R insula		48	36	−6	18	5.66	244
	R rolandic_oper	48	37	−4	16	5.07	
CBF values: OSAS < HCs							
R TP		36	20	7	−40	5.31	165
R cerebellum_Crus2		NA	45	−49	−44	4.195	202
VBM values: OSAS < HCs							
R DLPFC		45	42	35	17	6.65	2494
R occipital pole		17	14	−101	2	4.21	1163
Vermis		NA	−3	−68	−35	4.46	541

CBF, cerebral blood flow; VBM, voxel Based morphometry; OSAS, obstructive sleep apnea syndrome; HCs, healthy controls; FWE, family wise error; mPFC, medial prefrontal cortex; TP, temporal pole; DLPFC, dorsal lateral prefrontal cortex; R, right hemisphere.

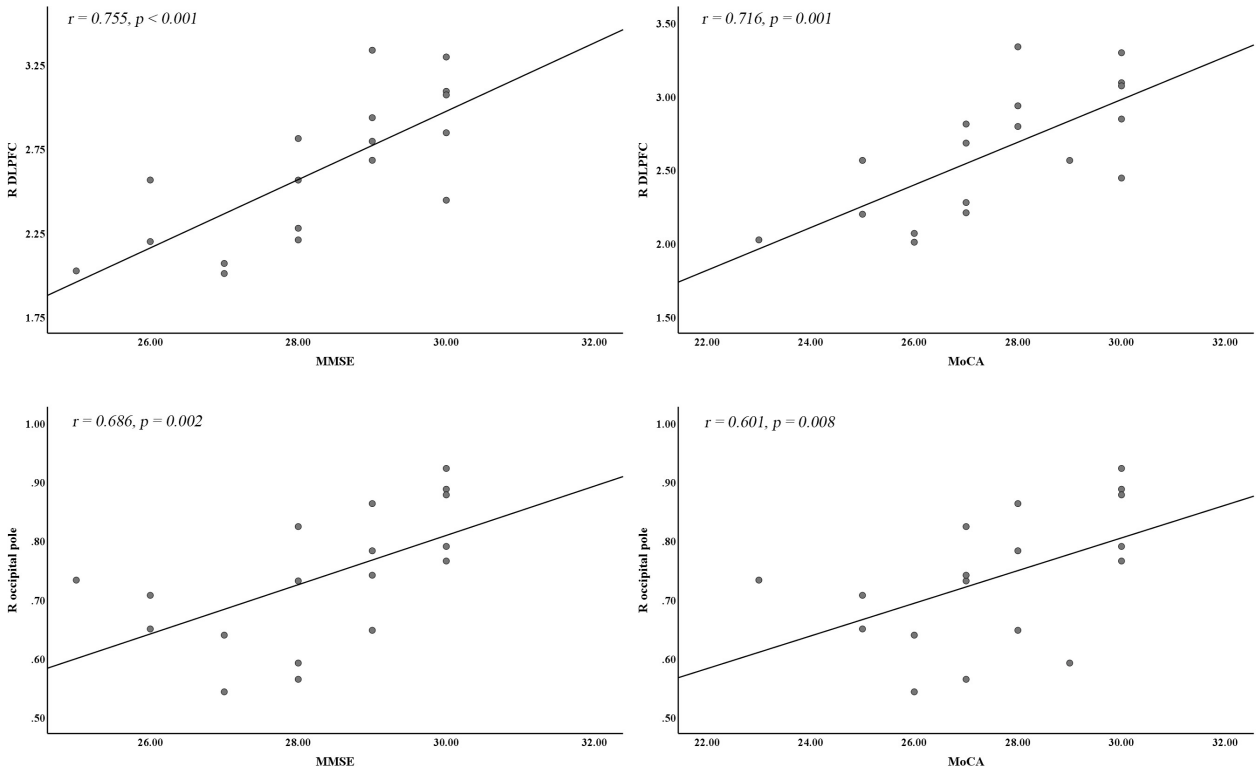

FIGURE 2 | Correlation analysis between significantly different CBF or VBM clusters and cognitive and clinical variables. DLPFC, dorsal lateral prefrontal cortex; MMSE, Mini-Mental State Examination; MoCA, Montreal Cognitive Assessment; R, right hemisphere.

DISCUSSION

To the best of our knowledge, this is the first study to combine VBM and CBF modalities to detect the pathophysiological mechanism in patients with OSA. The results showed that, for VBM modality, compared with HCs, the patients with OSA showed decreased GMV in the right DLPFC, the right occipital pole, and the vermis. The reduced GMV in the right DLPFC and the right occipital pole was positively correlated with both MMSE and MoCA scores, and the reduced GMV in the occipital pole was negatively correlated with the duration of illness. For CBF modality, compared with HCs, the patients with OSA showed decreased CBF values in the right TP and the right cerebellum_Crus2 and increased CBF values in the right mPFC, the left precentral gyrus, and the right insula. All the results suggested that disturbed brain volume and blood flow mainly located in the frontal lobe, cerebellum, primary functional area (including precentral gyrus and occipital pole), insula, and TP and were closely related to the psychological problems and cognitive deficits.

In this study, in OSA, GMV reductions and CBF increases were observed in the right DLPFC and the right mPFC, respectively. In addition, the reduced GMV in OSA was positively correlated with MMSE and MoCA scores. The prefrontal cortex, particularly DLPFC, is the area of the brain that controls various executive functions, such as behavioral inhibition, environmental switching, emotional self-regulation, and arousal (Beebe and Gozal, 2002). The mPFC is the hub of the default mode network (DMN) and is generally more active at rest than during cognitive activity. Recently, the executive dysfunction associated with OSA cannot be explained by sleepiness itself (Harrison and Horne, 2000) but may be a manifestation of neuronal damage in the prefrontal cortex (including DLPFC and mPFC) (Nofzinger, 2005). A previous VBM meta-analysis reported GMV reductions in the frontal lobe in OSA (Shi et al., 2017), and Bai et al. (2021) found decreased fractional amplitude of low-frequency fluctuation and regional homogeneity in the prefrontal cortex in childhood OSA, which supported our findings. In DMN (such as mPFC), changes in functional connectivity and regional brain activity were observed in resting states (Li et al., 2016), and abnormal inactivation was observed in working memory tasks in patients with OSA (Prilipko et al., 2011). Previous studies have found that prefrontal CBF decreases in patients with OSA during exercise stimulation, explaining the intolerance of exercise in patients with OSA (Marillier et al., 2018). OSA is associated with loss of slow-wave sleep, and there are behavioral deficits that reflect changes in prefrontal cortex function in OSA (Nofzinger, 2005). Studies of the metabolic and cognitive consequences of sleep deprivation suggest that sleep plays a role in the restoration of prefrontal cortex function (Thomas et al., 2000). Combined with our results, the GMV atrophy of the DLPFC may be caused by poor sleep quality and sleep hypoxia, which could lead

to abnormal cognitive function and psychological status, and the increased CBF in the mPFC may be a compensatory response to the GMV reduction of prefrontal lobe in OSA.

The cerebellum is considered a crucial module in motor control systems, closely related to movement and balance. It also connects to a wide range of areas of the brain, including cortex-associated and limbic regions (Schmahmann and Pandya, 1997). In this study, patients with OSA showed decreased GMV and CBF values in the cerebellum, suggesting impairment in both atrophy and blood metabolism in the cerebellum in OSA. The cerebellum is known to be susceptible to hypoxia or ischemia and is proved to be an important role in maintaining sleep, and lack of sleep may interfere with the function of the cerebellum (DelRosso and Hoque, 2014). Exposure to sleep apnea with recurrent intermittent hypoxia may be associated with abnormal GMV and CBF in the cerebellum. Several previous studies have reported decreased GMV of the cerebellum in patients with OSA when compared with HCs (Celle et al., 2009; Yaouhi et al., 2009; Joo et al., 2010; Kim et al., 2016), and Celle et al. found inverse correlations between the GMV of cerebellum and AHI scores in OSA (Celle et al., 2009), which were consistent with our results. In addition, in sensorimotor tasks, sleep deprivation interferes with functional MRI signals from many brain regions, including the cerebellum (Gazes et al., 2012). Combined with this study, the cerebellum is important for motor and cognitive networks to function properly, and reduced GMV and CBF in the cerebellum may lead to abnormal behavior in patients with OSA.

Moreover, decreased GMV in the right occipital pole, decreased CBF values in the right TP, increased CBF values in the left precentral gyrus, and the right insula were also observed in patients with OSA when compared with HCs, and the GMV loss of the occipital pole was negatively correlated with the duration of illness. Previous studies revealed reduced scattered sites of GM concentration in the temporo-parieto-occipital cortices (Yaouhi et al., 2009) and abnormal white matter volume in the occipital gyrus in patients with OSA (Huynh et al., 2014), which supported our results. After 6 weeks of continuous positive airway pressure treatment, CBF of the occipital and temporal lobe increased in patients with OSA (Maresky et al., 2019). Joo et al. (2010) reported reduced GM density in the left precentral gyrus and right insula in patients with OSA when compared with HCs, and combined with our results, we speculated that the increased CBF values of the left precentral gyrus and the right insula could be a compensatory response to GMV deficits of the left precentral and the right insula. It should be noted that GM atrophy (Joo et al., 2010; Kim et al., 2016) and hypertrophy (Fatouleh et al., 2014; Lin et al., 2016) were both found in the insula in OSA. In addition, reduced GMV of the hippocampus was reported in patients with OSA in previous studies (Morrell et al., 2003; Yaouhi et al., 2009; Canessa et al., 2011; Torelli et al., 2011; Kim et al., 2016) that did not survive in this study after FWE correction. The possible reasons accounting for these discrepancies may include small samples, demographic information, methodology (e.g., different statistical correction methods), and the duration and severity of the OSA.

The strength of this study is that it is the first time to utilize two modalities (VBM and CBF index) in patients with OSA. However, there were several limitations in this study. First, the sample size of this study was relatively small, and the findings should be verified in a larger sample study in the future. Second, as this was a cross-sectional design study, longitudinal studies such as taking CPAP therapy combined with VBM and CBF methods should be considered in the future. Finally, several potentially important new imaging markers have recently been identified that we were unable to analyze, such as cortical microinfarcts and brain atrophy.

In conclusion, this study suggested that patients with OSA had widely structural and hemometabolic abnormalities, particularly in the frontal lobe and cerebellum, and were closely related to abnormal behavior, psychology, and cognitive function, which may contribute to the pathogenesis of OSA. Large-scale, longitudinally designed randomized controlled studies are needed to further evaluate the correlation between efficacy of treatment and brain structural and blood metabolic in patients with OSA.

DATA AVAILABILITY STATEMENT

The raw data supporting the conclusions of this article will be made available by the authors, without undue reservation.

ETHICS STATEMENT

The studies involving human participants were reviewed and approved by the Ethics Committee of the Second People's Hospital of Guangdong Province. The patients/participants provided their written informed consent to participate in this study.

AUTHOR CONTRIBUTIONS

GJ designed this study and revised the manuscript. PX, KH, FC, YY, JW, XF, JY, QL, and QC contributed to data acquisition. PX contributed to data analysis and wrote the manuscript. All authors contributed and approved the final manuscript.

FUNDING

This study was funded by grants from the National Natural Science Foundation of China (Grant Nos. U1903120, 81771807, and 81901729) and the Science and Technology Planning Project of Guangzhou (Grant No. 202002030234).

REFERENCES

Arzt, M., Young, T., Finn, L., Skatrud, J. B., and Bradley, T. D. (2005). Association of sleep-disordered breathing and the occurrence of stroke. *Am. J. Respir. Crit. Care Med.* 172, 1447–1451. doi: 10.1164/rccm.200505-702OC

Ashburner, J. (2007). A fast diffeomorphic image registration algorithm. *Neuroimage.* 38, 95–113. doi: 10.1016/j.neuroimage.2007.07.007

Bai, J., Wen, H., Tai, J., Peng, Y., Li, H., Mei, L., et al. (2021). Altered Spontaneous Brain Activity Related to Neurologic and Sleep Dysfunction in Children With Obstructive Sleep Apnea Syndrome. *Front. Neurosci.* 15:595412. doi: 10.3389/fnins.2021.595412

Beebe, D. W., and Gozal, D. (2002). Obstructive sleep apnea and the prefrontal cortex: towards a comprehensive model linking nocturnal upper airway obstruction to daytime cognitive and behavioral deficits. *J. Sleep Res.* 11, 1–16. doi: 10.1046/j.1365-2869.2002.00289.x

Bennett, L. S., Barbour, C., Langford, B., Stradling, J. R., and Davies, R. J. (1999). Health status in obstructive sleep apnea: relationship with sleep fragmentation and daytine sleepiness, and effects of continuous positive airway pressure treatment. *Am. J. Respir. Crit. Care Med.* 159, 1884–1890. doi: 10.1164/ajrccm.159.6.9808107

Canessa, N., Castronovo, V., Cappa, S. F., Aloia, M. S., Marelli, S., Falini, A., et al. (2011). Obstructive sleep apnea: brain structural changes and neurocognitive function before and after treatment. *Am. J. Respir. Crit. Care Med.* 183, 1419–1426. doi: 10.1164/rccm.201005-0693OC

Celle, S., Peyron, R., Faillenot, I., Pichot, V., Alabdullah, M., Gaspoz, J. M., et al. (2009). Undiagnosed sleep-related breathing disorders are associated with focal brainstem atrophy in the elderly. *Hum. Brain Mapp.* 30, 2090–2097. doi: 10.1002/hbm.20650

Chang, C. C., Chuang, H. C., Lin, C. L., Sung, F. C., Chang, Y. J., Hsu, C. Y., et al. (2014). High incidence of stroke in young women with sleep apnea syndrome. *Sleep Med.* 15, 410–414. doi: 10.1016/j.sleep.2013.12.011

DelRosso, L. M., and Hoque, R. (2014). The cerebellum and sleep. *Neurol. Clin.* 32, 893–900. doi: 10.1016/j.ncl.2014.07.003

Fatouleh, R. H., Hammam, E., Lundblad, L. C., Macey, P. M., McKenzie, D. K., Henderson, L. A., et al. (2014). Functional and structural changes in the brain associated with the increase in muscle sympathetic nerve activity in obstructive sleep apnoea. *Neuroimage Clin.* 6, 275–283. doi: 10.1016/j.nicl.2014.08.021

Folstein, M. F., Folstein, S. E., and McHugh, P. R. (1975). Mini-mental state". A practical method for grading the cognitive state of patients for the clinician. *J. Psychiatr. Res.* 12, 189–198. doi: 10.1016/0022-3956(75)90026-6

Gazes, Y., Rakitin, B. C., Steffener, J., Habeck, C., Lisanby, S. H., Butterfield, B., et al. (2012). Dual-tasking alleviated sleep deprivation disruption in visuomotor tracking: an fMRI study. *Brain Cogn.* 78, 248–256. doi: 10.1016/j.bandc.2012.01.004

Gonchigsuren, O., Harada, M., Hisaoka, S., Higashi, K., Matsumoto, Y., Sumida, N., et al. (2022). Brain abnormalities in children with attention-deficit/hyperactivity disorder assessed by multi-delay arterial spin labeling perfusion and voxel-based morphometry. *Jpn J. Radiol.* 40, 568–577. doi: 10.1007/s11604-021-01239-w

Harrison, Y., and Horne, J. A. (2000). The impact of sleep deprivation on decision making: a review. *J. Exp. Psychol. Appl.* 6, 236–249. doi: 10.1037/1076-898X.6.3.236

Huynh, N. T., Prilipko, O., Kushida, C. A., and Guilleminault, C. (2014). Volumetric Brain Morphometry Changes in Patients with Obstructive Sleep Apnea Syndrome: Effects of CPAP Treatment and Literature Review. *Front. Neurol.* 5:58. doi: 10.3389/fneur.2014.00058

Joo, E. Y., Tae, W. S., Lee, M. J., Kang, J. W., Park, H. S., Lee, J. Y., et al. (2010). Reduced brain gray matter concentration in patients with obstructive sleep apnea syndrome. *Sleep.* 33, 235–241. doi: 10.1093/sleep/33.2.235

Kim, H., Joo, E., Suh, S., Kim, J. H., Kim, S. T., and Hong, S. B. (2016). Effects of long-term treatment on brain volume in patients with obstructive sleep apnea syndrome. *Hum. Brain Mapp.* 37, 395–409. doi: 10.1002/hbm.23038

Klein, A., Andersson, J., Ardekani, B. A., Ashburner, J., Avants, B., Chiang, M. C., et al. (2009). Evaluation of 14 nonlinear deformation algorithms applied to human brain MRI registration. *Neuroimage.* 46, 786–802. doi: 10.1016/j.neuroimage.2008.12.037

Lamberts, M., Nielsen, O. W., Lip, G. Y., Ruwald, M. H., Christiansen, C. B., Kristensen, S. L., et al. (2014). Cardiovascular risk in patients with sleep apnoea with or without continuous positive airway pressure therapy: follow-up of 4.5 million Danish adults. *J. Intern. Med.* 276, 659–666. doi: 10.1111/joim.12302

Li, H. J., Nie, X., Gong, H. H., Zhang, W., Nie, S., and Peng, D. C. (2016). Abnormal resting-state functional connectivity within the default mode network subregions in male patients with obstructive sleep apnea. *Neuropsychiatr. Dis. Treat.* 12, 203–212. doi: 10.2147/NDT.S97449

Lin, W. C., Huang, C. C., Chen, H. L., Chou, K. H., Chen, P. C., Tsai, N. W., et al. (2016). Longitudinal brain structural alterations and systemic inflammation in obstructive sleep apnea before and after surgical treatment. *J. Transl. Med.* 14:139. doi: 10.1186/s12967-016-0887-8

Macey, P. M., Henderson, L. A., Macey, K. E., Alger, J. R., Frysinger, R. C., Woo, M. A., et al. (2002). Brain morphology associated with obstructive sleep apnea. *Am. J. Respir. Crit. Care Med.* 166, 1382–1387. doi: 10.1164/rccm.200201-050OC

Macey, P. M., Kumar, R., Yan-Go, F. L., Woo, M. A., and Harper, R. M. (2012). Sex differences in white matter alterations accompanying obstructive sleep apnea. *Sleep.* 35, 1603–1613. doi: 10.5665/sleep.2228

Maresky, H. S., Shpirer, I., Klar, M. M., Levitt, M., Sasson, E., and Tal, S. (2019). Continuous positive airway pressure alters brain microstructure and perfusion patterns in patients with obstructive sleep apnea. *Sleep Med.* 57, 61–69. doi: 10.1016/j.sleep.2018.12.027

Marillier, M., Gruet, M., Baillieul, S., Wuyam, B., Tamisier, R., Levy, P., et al. (2018). Impaired cerebral oxygenation and exercise tolerance in patients with severe obstructive sleep apnea syndrome. *Sleep Med.* 51, 37–46. doi: 10.1016/j.sleep.2018.06.013

Morrell, M. J., McRobbie, D. W., Quest, R. A., Cummin, A. R., Ghiassi, R., and Corfield, D. R. (2003). Changes in brain morphology associated with obstructive sleep apnea. *Sleep Med.* 4, 451–454. doi: 10.1016/S1389-9457(03)00159-X

Nofzinger, E. A. (2005). Neuroimaging and sleep medicine. *Sleep Med. Rev.* 9, 157–172. doi: 10.1016/j.smrv.2004.07.003

O'Donoghue, F. J., Briellmann, R. S., Rochford, P. D., Abbott, D. F., Pell, G. S., Chan, C. H., et al. (2005). Cerebral structural changes in severe obstructive sleep apnea. *Am. J. Respir. Crit. Care Med.* 171, 1185–1190. doi: 10.1164/rccm.200406-738OC

O'Donoghue, F. J., Wellard, R. M., Rochford, P. D., Dawson, A., Barnes, M., Ruehland, W. R., et al. (2012). Magnetic resonance spectroscopy and neurocognitive dysfunction in obstructive sleep apnea before and after CPAP treatment. *Sleep* 35, 41–48. doi: 10.5665/sleep.1582

Pizza, F., Biallas, M., Kallweit, U., Wolf, M., and Bassetti, C. L. (2012). Cerebral hemodynamic changes in stroke during sleep-disordered breathing. *Stroke* 43, 1951–1953. doi: 10.1161/STROKEAHA.112.656298

Prilipko, O., Huynh, N., Schwartz, S., Tantrakul, V., Kim, J. H., Peralta, A. R., et al. (2011). Task positive and default mode networks during a parametric working memory task in obstructive sleep apnea patients and healthy controls. *Sleep* 34:293–301A. doi: 10.1093/sleep/34.3.293

Schmahmann, J. D., and Pandya, D. N. (1997). The cerebrocerebellar system. *Int. Rev. Neurobiol.* 41, 31–60. doi: 10.1016/S0074-7742(08)60346-3

Shi, D., Chen, X., and Li, Z. (2018). Diagnostic test accuracy of the Montreal Cognitive Assessment in the detection of post-stroke cognitive impairment under different stages and cutoffs: a systematic review and meta-analysis. *Neurol. Sci.* 39, 705–716. doi: 10.1007/s10072-018-3254-0

Shi, Y., Chen, L., Chen, T., Li, L., Dai, J., Lui, S., et al. (2017). A Meta-analysis of Voxel-based Brain Morphometry Studies in Obstructive Sleep Apnea. *Sci. Rep.* 7:10095. doi: 10.1038/s41598-017-09319-6

Thomas, M., Sing, H., Belenky, G., Holcomb, H., Mayberg, H., Dannals, R., et al. (2000). Neural basis of alertness and cognitive performance impairments during sleepiness. I. Effects of 24 h of sleep deprivation on waking human regional brain activity. *J. Sleep Res.* 9, 335–352. doi: 10.1046/j.1365-2869.2000.00225.x

Torelli, F., Moscufo, N., Garreffa, G., Placidi, F., Romigi, A., Zannino, S., et al. (2011). Cognitive profile and brain morphological changes in obstructive sleep apnea. *Neuroimage.* 54, 787–793. doi: 10.1016/j.neuroimage.2010.09.065

Winklewski, P. J., and Frydrychowski, A. F. (2013). Cerebral blood flow, sympathetic nerve activity and stroke risk in obstructive sleep apnoea. Is there a direct link? *Blood Press.* 22, 27–33. doi: 10.3109/08037051.2012.701407

Yaggi, H. K., Concato, J., Kernan, W. N., Lichtman, J. H., Brass, L. M., and Mohsenin, V. (2005). Obstructive sleep apnea as a risk factor for stroke and death. *N. Engl. J. Med.* 353, 2034–2041. doi: 10.1056/NEJMoa043104

Yaouhi, K., Bertran, F., Clochon, P., Mézenge, F., Denise, P., Foret, J., et al. (2009). A combined neuropsychological and brain imaging study of obstructive sleep apnea. *J. Sleep Res.* 18, 36–48. doi: 10.1111/j.1365-2869.2008.00705.x

Conflict of Interest: QC was employed by Philips Healthcare.

The remaining authors declare that the research was conducted in the absence of any commercial or financial relationships that could be construed as a potential conflict of interest.

Publisher's Note: All claims expressed in this article are solely those of the authors and do not necessarily represent those of their affiliated organizations, or those of the publisher, the editors and the reviewers. Any product that may be evaluated in this article, or claim that may be made by its manufacturer, is not guaranteed or endorsed by the publisher.

Copyright © 2022 Xiao, Hua, Chen, Yin, Wang, Fu, Yang, Liu, Chan and Jiang. This is an open-access article distributed under the terms of the Creative Commons Attribution License (CC BY). The use, distribution or reproduction in other forums is permitted, provided the original author(s) and the copyright owner(s) are credited and that the original publication in this journal is cited, in accordance with accepted academic practice. No use, distribution or reproduction is permitted which does not comply with these terms.

frontiers | Frontiers in Neuroscience

ORIGINAL RESEARCH
published: 22 July 2022
doi: 10.3389/fnins.2022.934471

Potential Diagnostic Applications of Multi-Delay Arterial Spin Labeling in Early Alzheimer's Disease: The Chinese Imaging, Biomarkers, and Lifestyle Study

Mengfan Sun[1†], Yan-Li Wang[1,2†], Runzhi Li[1], Jiwei Jiang[1], Yanling Zhang[3], Wenyi Li[1], Yuan Zhang[1], Ziyan Jia[1], Michael Chappell[4,5] and Jun Xu[1,2]*

[1] Department of Neurology, Beijing Tiantan Hospital, Capital Medical University, Beijing, China, [2] China National Clinical Research Center for Neurological Diseases, Beijing Tiantan Hospital, Capital Medical University, Beijing, China, [3] Department of Radiology, Beijing Tiantan Hospital, Capital Medical University, Beijing, China, [4] Mental Health and Clinical Neurosciences and Sir Peter Mansfield Imaging Centre, School of Medicine, University of Nottingham, Nottingham, United Kingdom, [5] Nottingham Biomedical Research Centre, Queen's Medical Centre, University of Nottingham, Nottingham, United Kingdom

OPEN ACCESS

Edited by:
Guolin Ma,
China-Japan Friendship Hospital, China

Reviewed by:
Liping Fu,
China-Japan Friendship Hospital, China
Jiu Chen,
Nanjing Medical University, China

***Correspondence:**
Jun Xu
neurojun@126.com

[†] These authors have contributed equally to this work and share first authorship

Specialty section:
This article was submitted to Brain Imaging Methods, a section of the journal Frontiers in Neuroscience

Received: 02 May 2022
Accepted: 21 June 2022
Published: 22 July 2022

Citation:
Sun M, Wang Y-L, Li R, Jiang J, Zhang Y, Li W, Zhang Y, Jia Z, Chappell M and Xu J (2022) Potential Diagnostic Applications of Multi-Delay Arterial Spin Labeling in Early Alzheimer's Disease: The Chinese Imaging, Biomarkers, and Lifestyle Study. Front. Neurosci. 16:934471. doi: 10.3389/fnins.2022.934471

Background: Cerebral blood flow (CBF) alterations are involved in the onset and progression of Alzheimer's disease (AD) and can be a potential biomarker. However, CBF measured by single-delay arterial spin labeling (ASL) for discrimination of mild cognitive impairment (MCI, an early stage of AD) was lack of accuracy. Multi-delay ASL can not only provide CBF quantification but also provide arterial transit time (ATT). Unfortunately, the technique was scarcely applied to the diagnosis of AD. Here, we detected the utility of ASL with 1-delay and 7-delay in ten regions of interest (ROIs) to identify MCI and AD.

Materials and Methods: Pseudocontinuous ASL (pCASL) MRI was acquired on a 3T GE scanner in adults from the Chinese Imaging, Biomarkers, and Lifestyle (CIBL) Study of AD cohort, including 26 normal cognition (NC), 37 MCI, and 39 AD. Receiver operating characteristic (ROC) analyses with 1-delay and 7-delay ASL were performed for the identification of MCI and AD. The DeLong test was used to compare ROC curves.

Results: For CBF of 1-delay or 7-delay the AUCs showed moderate-high performance for the AD/NC and AD/MCI comparisons (AUC = 0.83∼0.96) ($p < 0.001$). CBF of 1-delay performed poorly in MCI/NC comparison (AUC = 0.69) ($p < 0.001$), but CBF of 7-delay fared well with an AUC of 0.79 ($p < 0.001$). The combination of CBF and ATT of 7-delay showed higher performance for AD/NC, AD/MCI, and MCI/NC comparisons with AUCs of 0.96, 0.89, and 0.89, respectively ($p < 0.001$). Furthermore, combination of CBF, ATT, sex, age, *APOE* ε4, and education improved further the accuracy ($p < 0.001$). In subgroups analyses, there were no significant differences in CBF of 7-delay ASL for identification of AD or MCI between age subgroups ($p > 0.05$).

Conclusion: The combination of CBF and ATT with 7-delay ASL showed higher performance for identification of MCI than CBF of 1-delay, when adding to sex, age, *APOE* ε4 carrier status, and education years, the diagnostic performance was further increased, presenting a potential imaging biomarker in early AD.

Keywords: Alzheimer's disease, mild cognitive impairment, diagnosis, multi-delay arterial spin labeling, cerebral blood flow, arterial transit time

INTRODUCTION

Alzheimer's disease (AD) is the most common neurodegenerative disorder and is neuropathologically hallmarked by extracellular β-amyloid (Aβ) plaques and by intracellular neurofibrillary tangles consisting of hyperphosphorylated tau protein, which starts 10–20 years before the onset of clinical symptoms (Frisoni et al., 2011; Dubois et al., 2016; Jack et al., 2018). Specific biomarkers of AD, Aβ, and Tau could be detected on positron emission tomography (PET) or in cerebrospinal fluid (CSF), which are expensive, invasive, and limiting widespread application clinically (Verberk et al., 2018). For this reason, studies have increasingly focused on affordable and non-invasive methods for the detection of AD at an earlier stage [such as mild cognitive impairment (MCI) and predementia phase of AD] to delay and prevent the progression of the disease (Alzheimer's Association, 2018; Thomas et al., 2021). Cerebral blood flow (CBF) changes are part of neurovascular unit impairment that is considered as an essential role in AD pathogenesis (Bell and Zlokovic, 2009; Zlokovic, 2011). The two-hit vascular hypothesis of AD states that cerebrovascular damage ("hit one"), including blood-brain barrier (BBB) breakdown and CBF reductions, contributes to the accumulation of neurotoxic molecules and hypoperfusion that can directly initiate neuronal injury; subsequently, there is Aβ deposition ("hit two") leading to the onset and progression of AD dementia (Nelson et al., 2016; Kisler et al., 2017). CBF has gained attention, which is measured by arterial spin labeling (ASL) MRI, and ASL is a non-invasive technique using magnetically labeled arterial water as an endogenous tracer (Sierra-Marcos, 2017; Zhang et al., 2017).

Using ASL, several studies have supported the pattern of spread of hypoperfusion in AD starting from the precuneus, spreading to the rest of the parietal cortex and the cingulate gyrus, then the frontal and temporal lobes and eventually the occipital cortex (Dai et al., 2009; Binnewijzend et al., 2013; Wierenga et al., 2014; Xekardaki et al., 2015; Love and Miners, 2016; Duan et al., 2021). In cross-sectional studies, positive correlations have been found between general cognition and cortical CBF in the precuneus and posterior cingulate, parietal, frontal, temporal, and occipital lobes (Binnewijzend et al., 2013; Leeuwis et al., 2017; Duan et al., 2020). Decreased CBF of all of the above-mentioned regions and entorhinal cortex has also been reported to be a useful predictor of future cognitive decline in longitudinal studies (De Vis et al., 2018; Sanchez et al., 2020; Bangen et al., 2021; Duan et al., 2021). Moreover, areas of hypoperfusion measured with ASL have a significant agreement with areas of hypometabolism measured by ^{18}F-fluorodeoxyglucose PET (^{18}F-FDG PET) in bilateral parietotemporal cortex, precuneus, and posterior cingulate cortex in patients with AD and MCI compared with healthy control participants (Riederer et al., 2018; Dolui et al., 2020); and studies have shown that these imaging modalities had similar associations with amyloid deposition in regions of frontal, parietal, and temporal cortex performed with voxel-wise regression based on cross-sectional analyses (McDade et al., 2014; Yan et al., 2018). Although these studies indicate that ASL-MRI CBF may be a valuable biomarker for AD, only a few studies explored the diagnostic performance for discrimination of MCI stage, which did not show high sensitivity and specificity (Binnewijzend et al., 2013; Xekardaki et al., 2015; Dolui et al., 2020).

Notably, ASL studies in AD to date have mostly been performed using a single post-labeling delay (PLD), the time between labeling and acquisition of the image for evaluating CBF. The main limitation of single-delay ASL is that any variation in arterial transit time (ATT) is ignored. ATT represents the duration for labeled blood to travel from the labeling region to the point of delivery to the brain tissue, which varies widely with vascular pathology and normal aging and can have a significant effect on quantifying CBF (Liu et al., 2012; Wang et al., 2013). Multi-delay ASL, with multiple PLDs, can not only improve the accuracy of CBF quantification by calculating mean values of CBF at each PLD corrected by ATT but also enable the calculation of ATT itself (Yoshiura et al., 2009; Wang et al., 2013). Little is known about how CBF and ATT change with multi-delay ASL in AD and whether the multi-delay is better than single-delay ASL for the identification of MCI.

Considering spiral readout and background suppression, 3D fast-spin-echo pseudocontinuous ASL (pCASL) is recommended as the standard method for ASL image in the clinical setting (Alsop et al., 2015), the current study investigated the changes in CBF and ATT using 7-delay ASL and compared the diagnostic value between 1-delay and 7-delay ASL in ten regions of interest (ROIs): left and right regions of olfactory, posterior cingulate, hippocampus, cuneus, and precuneus. Besides, we also examined associations of cognitive performance with CBF and ATT in ROIs.

MATERIALS AND METHODS

Participants

Subjects (n = 102) with ASL-MRI data were included in the Chinese Imaging, Biomarkers, and Lifestyle (CIBL) Study of AD cohort from April to October 2021. They were carefully screened with a medical history, neuropsychological assessment, and brain MRI. In this study, all participants from both

genders with minimum primary school education, and were clinically diagnosed with normal cognition (NC), MCI, and AD. Patients with AD fulfilled the clinical criteria of probable AD dementia defined by the National Institute on Aging and Alzheimer's Association (NIA-AA, 2011) (McKhann et al., 2011). Patients with MCI had memory complaints and fulfilled the criteria defined by NIA-AA (Albert et al., 2011). NC subjects had no cognitive impairment and had Mini-Mental State Examination (MMSE) scores of 25–30 and Montreal Cognitive Assessment (MOCA) scores of 26–30. Subjects with the evidence that might affect cognition, including cerebrovascular diseases (e.g., stroke, multiple infarcts, and severe white matter hyperintensity burden), other neurodegenerative diseases (e.g., frontotemporal dementia and dementia with Lewy bodies), and other neurological diseases (e.g., head injury, hydrocephalus, and encephalitis), were excluded. Subjects who suffered from organ failure, cancer, severe depression, psychiatric illness, drugs or alcohol abuse, and inability to perform MRI scan were also excluded. The study was approved by the Institutional Review Board of Beijing Tiantan Hospital of Capital Medical University (KY2021-028-01). And the CIBL study had been registered at http://www.chictr.org.cn/index.aspx (ChiCTR2100049131), before enrolling participants. Written informed consent was acquired from each participant or their guardians.

MRI Acquisition

Imaging data were acquired on a 3T MR scanner (SIGNA Premier; GE HealthCare, Milwaukee, WI, United States) with a 48-channel head coil. A high-resolution 3D T1-weighted sequence was acquired with the following parameters: repetition time (TR)/echo time (TE)/inversion time (TI) = 7.3/3.0/450 ms, flip angle = 12°, field of view (FOV) = 256 mm × 256 mm, matrix size = 256 × 256, and slice thickness = 1.0 mm. A high-resolution 3D T2-weighted FLAIR sequence was acquired with the following parameters: TR/TE/TI = 5,000/106/1,515 ms, FOV = 256 mm × 256 mm, matrix size = 256 × 256, and slice thickness = 1.0 mm. ASL images were acquired with a background-suppressed 3D stack-of-spirals fast-spin-echo sequence preceded by a Hadamard-encoded pCASL module. ASL imaging parameters with 1-delay were acquired with the following parameters: TR/TE = 4,849/10.6 ms, FOV = 220 mm × 220 mm, slice thickness = 4.0 mm, label duration = 1,450 ms, and PLD = 2,025 ms, with these the proton density image and the perfusion weighted image were generated; and with 7-delay were acquired with the following parameters: pCASL module modified to acquire an additional control-only phase, TR/TE = 7,152/11.2 ms, FOV = 220 mm × 220 mm, slice thickness = 3.0 mm, label durations = 220, 260, 300, 370, 480, 680, and 1,180 ms, and PLDs = 1,000, 1,220, 1,480, 1,780, 2,150, 2,620, and 3,320 ms.

Arterial Spin Labeling Processing

Arterial spin labeling data were quantitatively analyzed through an automatic software "CereFlow" by AnImage (Beijing) Technology Co., Ltd. with the following steps: (i) brain perfusion images were calculated from the raw ASL data [CBF for 1-delay ASL (Alsop et al., 2015) and CBF/ATT for 7-delay ASL (van der Thiel et al., 2018)]; (ii) the M0 image and the T1-weighted image were coregistered (rigid-body transformation with mutual information as similarity metric optimized with exhaustive method); (iii) T1-weighted image was normalized (non-linear transformation, minimizing the bending energies of the deformation fields, and the residual squared difference) onto Montreal Neurological Institute (MNI) template (Binnewijzend et al., 2013), and the M0 image and the perfusion images were then transformed onto the same space as the template as well; (iv) the gray matter regions were further mapped into different cortical regions by masking with automated anatomical labeling (AAL) atlas (Rolls et al., 2015); and (v) ten ROIs were chosen: left and right of olfactory, posterior cingulate, hippocampus, cuneus, and precuneus from the masked regions.

Total Gray Matter Volume

Total gray matter volume was acquired through the software "Dr. Brain" by YIWEI medical technology Co., Ltd. (Wei et al., 2020). Briefly, (i) the T1-weighted image was segmented into gray matter, white matter, and CSF; (ii) a template is created using the Dartel algorithm from the subjects' tissue probability maps obtained at the previous step; (iii) iterate the created template, register the subject's organization probability map with the previous template in each iteration, average the registered organization probability map again to obtain a new template, and finally register the probability map to MNI space; and (iv) total gray matter was then computed based on neuromorphometrics atlas.

White Matter Hyperintensity Volume

Detailed methods for WMH volumetric quantification have been previously described (Jiang et al., 2020). First, all T2-weighted FLAIR images uniformly went through preprocessing operations (bias correction and spatial normalization), followed by a segmentation stage where the WMH was delineated. Sequentially, coregistration of T2-weighted FLAIR image with MNI template and Hammers atlas is used to analyze the distribution of WMH.

Covariates

Demographic information included sex, age, education years, apolipoprotein E (*APOE*) ε4 carrier status, pulse pressure (systolic-diastolic blood pressure), and body mass index (BMI). The presence of *APOE* ε4 genotype was tested by using restriction enzyme isoform genotyping on deoxyribonucleic acid (DNA) extracts. *APOE* ε4 carriers were defined as subjects with at least one ε4 allele (ε4/ε4, ε4/ε3, or ε4/ε2). WMH volume and total gray matter volume were also selected as covariates.

Statistical Analyses

For continuous variables, differences between groups were analyzed using one-way ANOVA with *post-hoc* least significance difference (LSD) tests. Chi-squared tests were used to compare frequency distributions of categorical variables. Differences in CBF and ATT between diagnostic groups were analyzed using ANOVA with *post-hoc* LSD tests, followed by correction with sex, age, pulse pressure, BMI, WMH volume, and total gray matter

volume. Linear regression analyses were performed to assess relationships between CBF or ATT of each ROI (independent variables) and cognition tested by MMSE and MoCA scores (dependent variables) across the diagnostic groups. Sex, age, education years, *APOE* ε4 carrier status, WMH volume, and total gray matter volume were entered into each model as covariates. The area under the curves (AUCs) between 1-delay and 7-delay ASL for identification of AD were compared through receiver operating characteristic (ROC) analyses in leave-one-out cross-validation, in which the predicted values were calculated using a binary logistic regression model. The ROC curves were compared using the DeLong test. All tests were two-tailed, and $p < 0.05$ was considered statistically significant. All statistical analyses were performed using SPSS 24.0 and Medcalc software, and ROC figures were generated with GraphPad Prism 8.0.

RESULTS

Participants and Characteristics

Table 1 summarized demographic and clinical data of 102 subjects, namely, 26 NC, 37 MCI, and 39 AD. AD group had significantly older age, lower MMSE and MoCA scores, less BMI and total gray matter volume, and more WMH volume compared with MCI and NC groups ($p < 0.05$). Patients with AD had a higher proportion of *APOE* ε4 carrier status than patients with MCI and had lower education years than NC subjects ($p < 0.05$). MoCA scores and gray matter volume were lower in the MCI group than in the NC group ($p < 0.05$). There were no significant differences in sex, pulse pressure, hypertension, diabetes, and heart disease between groups ($p > 0.05$). **Supplementary Figure 1** showed the example images of CBF and ATT changes in NC, MCI, and AD subjects.

Cerebral Blood Flow and Arterial Transit Time Changes

The patients with AD had decreased CBF from 1-delay ASL in all ROIs compared with MCI and NC groups ($p < 0.05$), which consisted of 7-delay ASL except in the left hippocampus ($p = 0.051$) (**Table 2**). ATT was prolonged in patients with AD compared with MCI and NC groups in each ROI ($p < 0.05$) (**Table 3**). There were no significant differences between MCI and NC in CBF and ATT ($p > 0.05$). Additional correction for sex, age, WMH volume, total gray matter volume, pulse pressure, and BMI did not change the differences between groups.

Associations of Cognitive Performance With Cerebral Blood Flow and Arterial Transit Time

Across diagnostic groups, CBFs of posterior cingulate, cuneus, and precuneus in 1-delay ASL were associated with MMSE and MoCA adjusted for sex, age, education years, *APOE* ε4 carrier status, gray matter volume, and WMH volume ($\beta = 0.207 \sim 0.306$, $p < 0.05$) (**Supplementary Table 1**). This relationship in 7-delay had appeared in the left posterior cingulate, left hippocampus, cuneus, and precuneus ($\beta = 0.186 \sim 0.305$, $p < 0.05$ except for the relationship between CBF in cuneus and MMSE) (**Supplementary Table 1**). Regional ATT of right olfactory, left hippocampus, and right hippocampus was significantly correlated with MMSE ($\beta = -0.212$, -0.193, and -0.204, respectively, $p < 0.05$). There was no significant relationship between regional ATT and MoCA ($p > 0.05$).

Receiver Operating Characteristic Analyses

To compare 1-delay and 7-delay ASL for the diagnostic accuracy, we applied ROC analyses on perfusion parameters in all ROIs.

TABLE 1 | Demographic and clinical characteristics of participants.

	NC (*n* = 26)	MCI (*n* = 37)	AD (*n* = 39)	*P*-value‡
Age, year	59.77 ± 7.83	63.00 ± 7.06	68.15 ± 8.71*†	**<0.001**
Female, *n* (%)	17 (65.4)	28 (75.7)	20 (51.3)	0.085
Education, year	12.35 ± 3.73	11.57 ± 3.36	10.05 ± 3.53*	**0.030**
APOE ε4 carrier, *n* (%)	7 (26.9)	4 (10.8)	19# (50.0)†	**0.001**
BMI, kg/m^2	24.40 ± 2.59	24.11 ± 3.90	22.33 ± 3.22*†	**0.020**
Pulse pressure, mmHg	43.15 ± 14.17	46.35 ± 10.56	49.59 ± 14.20	0.150
MMSE score	29.04 ± 0.87	27.14 ± 1.57	17.10 ± 6.12*†	**<0.001**
MoCA score	27.31 ± 1.49	21.70 ± 1.87*	11.03 ± 5.94*†	**<0.001**
Gray matter volume, cm^3	622.32 ± 61.33	570.56 ± 57.90*	535.37 ± 52.54*†	**<0.001**
WMH volume, cm^3	1.45 ± 2.90	1.62 ± 1.73	5.67 ± 5.47*†	**<0.001**
Hypertension, *n* (%)	8 (30.8)	12 (32.4)	10 (25.6)	0.797
Diabetes, *n* (%)	3 (11.5)	8 (21.6)	5 (12.8)	0.457
Heart disease§ , *n* (%)	2 (7.7)	10 (27.0)	5 (12.8)	0.092

Data are mean ± standard deviation for continuous variables, and percentage (%) and number (n) of participants for categorical variables. Abbreviations: NC, normal cognition; MCI, mild cognitive impairment; AD, Alzheimer's disease; APOE, apolipoprotein E; BMI, body mass index; MMSE, mini-mental state examination; MoCA, Montreal cognitive assessment; WMH, white matter hyperintensity; LSD, least significance difference.

‡*Analysis of variance and chi-squared tests.*

§*Including coronary atherosclerotic heart disease and heart arrhythmia (such as atrial fibrillation).*

#*One patient had missing value.*

*Bolded values means the significant differences between AD/MCI/HC comparison. *refers to the significant differences between AD and NC. †refers to the significant differences between AD and MCI.*

TABLE 2 | Regions of interest (ROI)-based CBF with 1-delay and 7-delay ASL in groups.

	1-delay				7-delay			
	NC	**MCI**	**AD**	***P*-value‡**	**NC**	**MCI**	**AD**	***P*-value‡**
Olfactory L	46.82 ± 9.41	45.12 ± 10.30	37.19 ± 6.91*†	**<0.001**	50.44 ± 10.64	51.74 ± 13.96	43.73 ± 10.70*†	**0.011**
Olfactory R	46.62 ± 9.70	44.61 ± 10.13	37.63 ± 6.99*†	**<0.001**	49.73 ± 12.10	50.44 ± 14.48	42.55 ± 9.98*†	**0.012**
Posterior Cingulate L	67.27 ± 12.77	64.57 ± 18.07	47.06 ± 14.36*†	**<0.001**	60.18 ± 13.52	61.00 ± 21.80	43.73 ± 16.22*†	**<0.001**
Posterior Cingulate R	56.50 ± 11.12	55.08 ± 14.77	40.67 ± 11.08*†	**<0.001**	48.56 ± 12.63	53.63 ± 18.24	38.45 ± 12.42*†	**<0.001**
Hippocampus L	43.94 ± 8.79	44.39 ± 9.44	37.13 ± 6.75*†	**<0.001**	44.27 ± 9.46	48.69 ± 14.83	38.29 ± 10.22†	**0.001**
Hippocampus R	43.23 ± 7.73	42.99 ± 10.29	36.16 ± 7.34*†	**0.001**	44.30 ± 9.00	47.83 ± 14.58	37.93 ± 9.53*†	**0.001**
Cuneus L	52.86 ± 10.66	51.90 ± 16.79	37.06 ± 12.11*†	**<0.001**	53.94 ± 13.87	55.66 ± 20.59	38.65 ± 12.23*†	**<0.001**
Cuneus R	53.22 ± 12.15	52.91 ± 17.29	38.33 ± 13.69*†	**<0.001**	52.18 ± 13.87	56.58 ± 21.71	39.62 ± 13.85*†	**<0.001**
Precuneus L	54.40 ± 10.48	53.02 ± 15.07	40.33 ± 10.60*†	**<0.001**	55.45 ± 13.73	56.10 ± 19.70	40.47 ± 13.01*†	**<0.001**
Precuneus R	53.57 ± 9.62	52.32 ± 14.07	38.88 ± 10.54*†	**<0.001**	52.42 ± 12.42	55.00 ± 18.07	39.53 ± 11.18*†	**<0.001**

Data are mean ± standard deviation (in milliliters per 100 g/min). Abbreviations: NC, normal cognition; MCI, mild cognitive impairment; AD, Alzheimer's disease; ROI, region of interest; CBF, cerebral blood flow; ASL, arterial spin labeling; L, left; R, right; LSD, least significance difference.
‡*Analysis of variance.*
**$p < 0.05$ compared to the NC group with LSD tests.*
†*$p < 0.05$ compared to the MCI group with LSD tests.*

TABLE 3 | Region of interest (ROI)-based ATT with 7-delay ASL in groups.

	NC	**MCI**	**AD**	***P*-value‡**
Olfactory L	1.28 ± 0.16	1.29 ± 0.13	1.38 ± 0.25*†	**0.037**
Olfactory R	1.30 ± 0.19	1.27 ± 0.11	1.42 ± 0.24*†	**0.003**
Posterior Cingulate L	1.60 ± 0.19	1.57 ± 0.20	1.71 ± 0.19*†	**0.005**
Posterior Cingulate R	1.52 ± 0.17	1.52 ± 0.19	1.64 ± 0.20*†	**0.009**
Hippocampus L	1.34 ± 0.14	1.34 ± 0.14	1.49 ± 0.20*†	**<0.001**
Hippocampus R	1.40 ± 0.16	1.37 ± 0.14	1.49 ± 0.20*†	**0.008**
Cuneus L	1.73 ± 0.20	1.71 ± 0.20	1.86 ± 0.20*†	**0.003**
Cuneus R	1.77 ± 0.18	1.72 ± 0.20	1.87 ± 0.20*†	**0.003**
Precuneus L	1.70 ± 0.18	1.65 ± 0.18	1.80 ± 0.19*†	**0.002**
Precuneus R	1.66 ± 0.18	1.64 ± 0.18	1.78 ± 0.20*†	**0.003**

Data are mean ± standard deviation (in seconds). Abbrevaitions: NC, normal cognition; MCI, mild cognitive impairment; AD, Alzheimer's disease; ROI, region of interest; ATT, arterial transit time; ASL, arterial spin labeling; L, left; R, right; LSD, least significance difference.
‡*Analysis of variance.*
**$p < 0.05$ compared to the NC group with LSD tests.*
†*$p < 0.05$ compared to the MCI group with LSD tests.*

As a result, for CBF of 1-delay the AUCs for the AD/NC and AD/MCI comparisons were 0.94 ($p < 0.001$) and 0.83 ($p < 0.001$), respectively, which were similar to CBF of 7-delay (AUC = 0.96, $p < 0.001$ for AD/NC comparison; AUC = 0.83, $p < 0.001$ for AD/MCI comparison) (**Figures 1A,B** and **Supplementary Table 2**). While the AUC for CBF of 7-delay in MCI/NC comparison was higher (AUC = 0.79, $p < 0.001$) compared with that for CBF of 1-delay (AUC = 0.69, $p < 0.001$) (**Figure 1C** and **Supplementary Table 2**). We compared the diagnostic capacities of combination of CBF and ATT of 7-delay and found that was more discriminative performance for AD/NC, AD/MCI, and MCI/NC comparisons with AUCs of 0.96 ($p < 0.001$), 0.89 ($p < 0.001$), and 0.89 ($p < 0.001$), respectively (**Figures 1A–C** and **Supplementary Table 2**). Furthermore, the AUCs of combination of CBF and ATT of 7-delay, sex, age, *APOE* ε4 carrier status, and educational years (as a composite biomarker) were higher than those mentioned above (AUC = 0.98, $p < 0.001$ for AD/NC comparison; AUC = 0.96, $p < 0.001$ for AD/MCI comparison; and AUC = 0.90, $p < 0.001$ for MCI/NC comparison) (**Figure 1D** and **Supplementary Table 2**). In comparison of AUCs between groups, there were no differences in AUCs between AD and NC groups ($p > 0.05$). The AUC of composite showed higher diagnostic efficiency than other methods in AD/MCI comparison ($p < 0.05$). The AUCs of CBF and ATT of 7-delay and composite were more powerful than that of CBF in 1-delay for MCI/NC identification ($p < 0.05$) (**Supplementary Table 3**).

Subgroup Receiver Operating Characteristic Analyses by Age

We performed subgroup ROC analyses according to age (middle-aged group [<65 years] and old-aged group [≥65 years]) in CBF of 7-delay ASL. CBF of 7-delay ASL in middle-age group had a significantly discriminative performance for the AD/NC, AD/MCI, and MCI/NC comparisons (AUC = 0.97, 0.95, and 0.83, respectively, $p < 0.05$). The method still had significantly

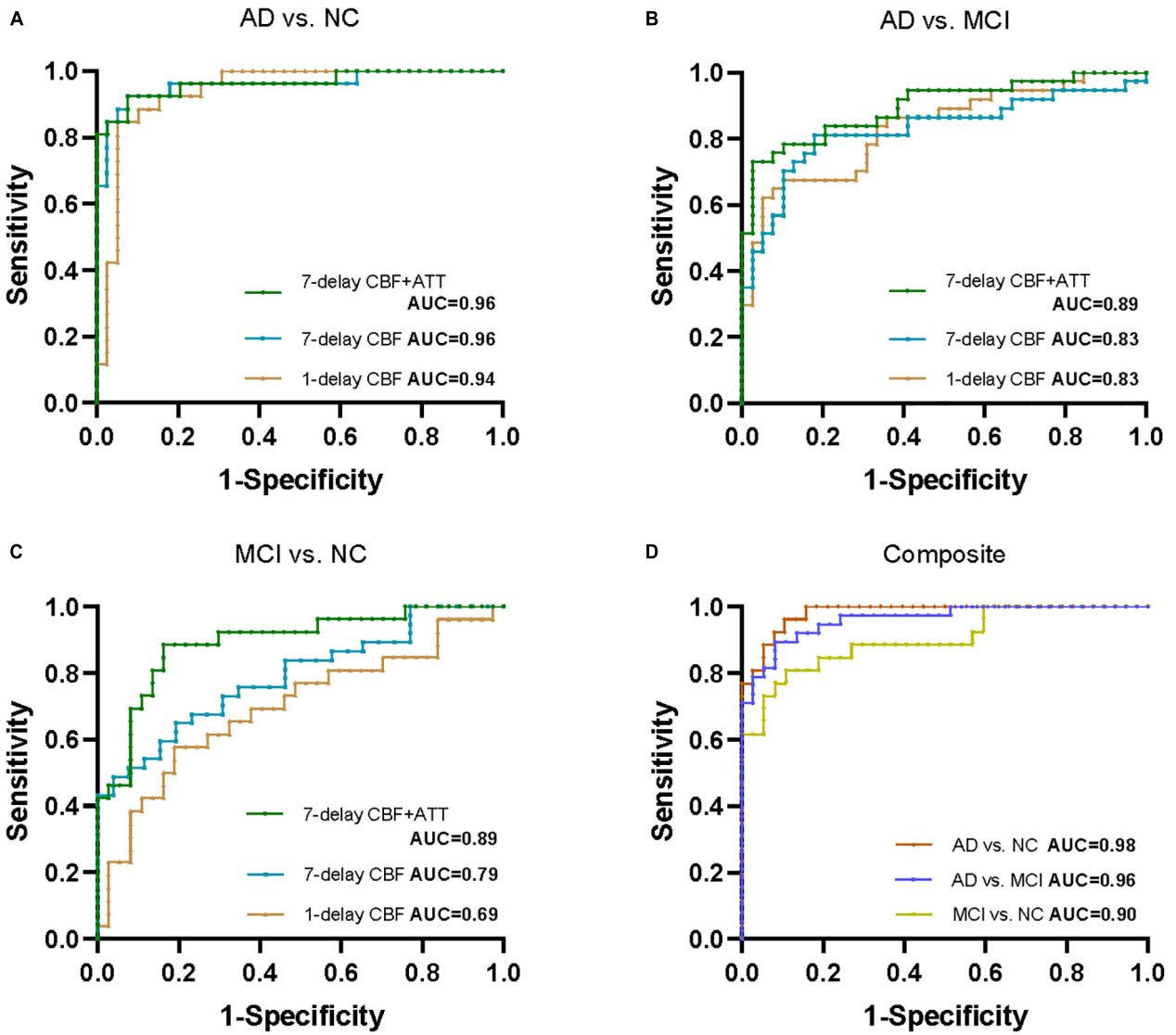

FIGURE 1 | Receiver operating characteristic (ROC) analyses for perfusion parameters of 1-delay and 7-delay ASL in all ROIs in distinguishing different stages of AD. ROC curves for CBF of 1-delay, CBF of 7-delay, or the combination of CBF and ATT of 7-delay in differentiating AD from NC **(A)** and MCI **(B)** and MCI from NC **(C)**. **(D)** AUCs for the combination of CBF and ATT of 7-delay, sex, age, *APOE* ε4 carrier status, and education years (composite) in NC, patients with AD and MCI. NC, normal cognition; MCI, mild cognitive impairment; AD, Alzheimer's disease; *APOE*, apolipoprotein E; ROI, region of interest; CBF, cerebral blood flow; ATT, arterial transit time; AUC, area under the curve; ROC, receiver operating characteristic.

diagnostic performance in old-age group (AUC = 0.97, 0.78, and 0.94, respectively, $p < 0.05$). Besides, there were no significant differences in CBF of 7-delay ASL for identification of AD or MCI between age subgroups ($p > 0.05$) (**Supplementary Table 4**).

DISCUSSION

Our study revealed significant CBF decrease and ATT prolongation in the ten ROIs in patients with AD. Correlation analysis showed a strong association between regional CBF and cognitive function across the diagnostic groups. Combining CBF and ATT of 7-delay ASL based on ROIs showed a higher performance for the differentiation of MCI compared with CBF of 1-delay.

The regional hypoperfusion changes measured by 1-delay ASL of patients with AD compared with patients with MCI and NC subjects in this study were consistent with previous studies (Asllani et al., 2008; Dai et al., 2009; Binnewijzend et al., 2013; Ma et al., 2017), similar to CBF changes measured with 7-delay ASL, supporting the theory that patients with AD have a greater decrease of CBF in the widespread brain than MCI and NC groups. It was found that patients with MCI exhibited decreased CBF in the precuneus and posterior cingulate compared to healthy control or subjective cognitive impairment subjects (Dai et al., 2009; Binnewijzend et al., 2013; Soman et al., 2021).

Dai et al. (2009) observed increased CBF in the hippocampus and limbic system in patients with MCI, which suggests a compensatory mechanism during the MCI stage of AD. However, our results showed no significant differences in CBF of these ROIs measured by 1-delay or 7-delay ASL in patients with MCI compared to NC. Another prominent abnormality using 7-delay ASL was a significant prolongation of ATT in patients with AD compared to MCI and NC subjects. Such findings might support the hypothesis that there is a neurovascular impairment with the AD pathologic process (Østergaard et al., 2013; Love and Miners, 2016; Nelson et al., 2016). While Yoshiura et al. (2009) using multi-TI pulsed ASL reported patients with AD had no significant ATT prolongation in the hypoperfusion area of the bilateral precunei and the left posterior cingulate compared to NC. The lower signal-to-noise ratio with pulsed ASL and different sample sizes might contribute to the discrepancy in our results (Alsop et al., 2015).

There were positive correlations between CBF with 1-delay and MMSE or MoCA in the posterior cingulate, precuneus, and cuneus with all subjects after adjusting for sex, age, education years, *APOE* ε4 carrier status, total gray matter volume, and WMH volume, consistent with the previous studies (Binnewijzend et al., 2013; Liu et al., 2015; Soman et al., 2021; Zhang et al., 2021). We also found the association between CBF with 7-delay and cognition was prominent in the left posterior cingulate, left hippocampus, left cuneus, and precuneus; and ATT was negatively associated with MMSE but not MoCA in the hippocampus and right olfactoffff0100a0210000ffff0100a0210000ry. The results may suggest that multi-delay ASL can also add value to objective cognitive evaluation.

According to previous literature, CBF in the precuneus and posterior cingulate using pCASL identified patients with AD from NC or subjective cognitive impairment with an AUC up to 0.80, but the predicted probability was poor in distinguishing MCI from AD or NC with AUCs of 0.59 and 0.78, respectively (Binnewijzend et al., 2013; Thomas et al., 2019). Liu et al. (2015) found similar AUC for CBF of posterior cingulate measured by pCASL with PLD of 1.5 s and 2.5 s in AD and NC (0.891 and 0.882, respectively), whereas Dolui et al. (2020) reported AUC of 0.77 for CBF in the same region using pCASL with PLD of 1.5 s. In the present study, given the pattern of spread of hypoperfusion in AD starting from the precuneus, spreading to the rest of the parietal cortex and the cingulate gyrus, then the frontal and temporal lobes, we selected the ten ROIs, namely, the left and right regions of olfactory, posterior cingulate, hippocampus, cuneus, and precuneus to perform ROC analyses (Dai et al., 2009; Binnewijzend et al., 2013; Wierenga et al., 2014; Xekardaki et al., 2015; Love and Miners, 2016; Duan et al., 2021). As a result, ROIs-based CBF with 1-delay performed well in distinguishing AD from MCI and NC, but not MCI from NC. A similar observation was found in predicting AD with 7-delay pCASL, with higher performance in differentiating MCI from NC with an AUC of 0.79. Combining CBF and ATT with 7-delay showed higher discriminatory power in predicting AD or MCI with AUCs up to 90%, when adding to sex, age, *APOE* ε4 carrier status, and education years, the diagnostic performance was further increased. Our study indicated that the combination of regional CBF and ATT of the ten ROIs measured by 7-delay pCASL could be a potential sensitive biomarker for the identification of early AD.

Our study had several limitations. First, the sample size was limited to a single center and some analyses may lack sufficient power. More subjects need to be recruited from multi-centers to validate the current findings. Second, the diagnosis of MCI or AD was based on clinical symptoms and neuropsychological assessment with no evidence of specific biomarkers for Aβ and tau pathology. However, we screened subjects carefully with a medical history, detailed neuropsychological evaluations to exclude those with MCI or dementia not due to AD, and the final consensus diagnosis was decided by the experienced neurologists. Of course, further studies will perform on subjects with pathological biomarkers of AD. Finally, partial volume correction (PVC) was not performed for the measurement of CBF, which confounds the evaluation of perfusion due to brain atrophy (Zhang et al., 2017; Chappell et al., 2021). Our results have shown the high differentiation performance for patients with AD, possibly owing to the additive discriminatory effect of cortical atrophy (Østergaard et al., 2013; Wierenga et al., 2014; Kisler et al., 2017; Ma et al., 2017), indicating that PVC may not necessary for the identification of AD. However, further research is warranted to use PVC with ASL to explore the CBF changes and diagnostic performance for NC subjects and patients with MCI because of the complex changes in atrophy and in perfusion with age and disease (Chen et al., 2011).

CONCLUSION

Our study showed patients with AD had apparent CBF decrease and ATT prolongation in ROIs using multi-delay ASL, supporting that there is a neurovascular impairment with the AD pathologic process. The combination of CBF and ATT with 7-delay ASL in the ten ROIs showed a higher diagnostic performance for MCI than CBF of 1-delay, when adding to sex, age, *APOE* ε4 carrier status, and education years, the diagnostic performance was further increased, presenting a potential imaging biomarker in early AD.

DATA AVAILABILITY STATEMENT

The raw data supporting the conclusions of this article will be made available by the authors, without undue reservation.

ETHICS STATEMENT

The studies involving human participants were reviewed and approved by the Research Ethics Committee of Beijing Tiantan Hospital, Capital Medical University. The patients/participants provided their written informed consent to participate in

this study. Written informed consent was obtained from the individual(s) for the publication of any potentially identifiable images or data included in this article.

AUTHOR CONTRIBUTIONS

MS wrote the original draft. Y-LW performed the statistical analyses and reviewed the manuscript. RL, JJ, and YaZ designed the study and reviewed the manuscript. WL, YuZ, and ZJ organized the database. MC and JX reviewed and finalized the manuscript. All authors contributed to manuscript revision, read, and approved the submitted version.

FUNDING

This study was supported by the National Key Research and Development Program of China (2021YFC2500103), the National Natural Science Foundation of China (82071187, 81870821, and 81471215), Beijing Youth Talent Team Support Program (2018000021223TD08), National Key Research and Development Program (2019YFC0120902), Beijing Natural Science Foundation grant (L182055), and Engineering and Physical Sciences Research Council United Kingdom (EP/P012361/1 and EP/P012361/2).

ACKNOWLEDGMENTS

The authors thank Zeshan Yao, Ph.D., engineer of AnImage (Beijing) Technology Co., Ltd., Juan Wei, from MR Research, GE Healthcare (Beijing, China), and Silun Wang and Huanhui Xiao, from YIWEI Medical Technology Co., Ltd. for providing technical guidance.

SUPPLEMENTARY MATERIAL

The Supplementary Material for this article can be found online at: https://www.frontiersin.org/articles/10.3389/fnins.2022.934471/full#supplementary-material

REFERENCES

Albert, M. S., DeKosky, S. T., Dickson, D., Dubois, B., Feldman, H. H., Fox, N. C., et al. (2011). The diagnosis of mild cognitive impairment due to Alzheimer's disease: recommendations from the National Institute on Aging-Alzheimer's Association workgroups on diagnostic guidelines for Alzheimer's disease. *Alzheimers Dement.* 7, 270–279. doi: 10.1016/j.jalz.2011.03.008

Alsop, D. C., Detre, J. A., Golay, X., Günther, M., Hendrikse, J., Hernandez-Garcia, L., et al. (2015). Recommended implementation of arterial spin-labeled perfusion MRI for clinical applications: a consensus of the ISMRM perfusion study group and the European consortium for ASL in dementia. *Magn. Reson. Med.* 73, 102–116. doi: 10.1002/mrm.25197

Alzheimer's Association (2018). 2018 Alzheimer's disease facts and figures. *Alzheimers Dement.* 14, 367–429. doi: 10.1016/j.jalz.2018.02.001

Asllani, I., Habeck, C., Scarmeas, N., Borogovac, A., Brown, T. R., and Stern, Y. (2008). Multivariate and univariate analysis of continuous arterial spin labeling perfusion MRI in Alzheimer's disease. *J. Cereb. Blood Flow Metab.* 28, 725–736. doi: 10.1038/sj.jcbfm.9600570

Bangen, K. J., Thomas, K. R., Sanchez, D. L., Edmonds, E. C., Weigand, A. J., Delano-Wood, L., et al. (2021). Entorhinal perfusion predicts future memory decline, neurodegeneration, and white matter hyperintensity progression in older adults. *J. Alzheimers Dis.* 81, 1711–1725. doi: 10.3233/JAD-201474

Bell, R. D., and Zlokovic, B. V. (2009). Neurovascular mechanisms and blood-brain barrier disorder in Alzheimer's disease. *Acta Neuropathol.* 118, 103–113. doi: 10.1007/s00401-009-0522-3

Binnewijzend, M. A. A., Kuijer, J. P. A., Benedictus, M. R., van der Flier, W. M., Wink, A. M., Wattjes, M. P., et al. (2013). Cerebral blood flow measured with 3D pseudocontinuous arterial spin-labeling MR imaging in Alzheimer disease and mild cognitive impairment: a marker for disease severity. *Radiology* 267, 221–230. doi: 10.1148/radiol.12120928

Chappell, M. A., McConnell, F. A. K., Golay, X., Günther, M., Hernandez-Tamames, J. A., van Osch, M. J., et al. (2021). Partial volume correction in arterial spin labeling perfusion MRI: a method to disentangle anatomy from physiology or an analysis step too far? *Neuroimage* 238:118236. doi: 10.1016/j.neuroimage.2021.118236

Chen, J. J., Rosas, H. D., and Salat, D. H. (2011). Age-associated reductions in cerebral blood flow are independent from regional atrophy. *Neuroimage* 55, 468–478. doi: 10.1016/j.neuroimage.2010.12.032

Dai, W., Lopez, O. L., Carmichael, O. T., Becker, J. T., Kuller, L. H., and Gach, H. M. (2009). Mild cognitive impairment and alzheimer disease: patterns of altered cerebral blood flow at MR imaging. *Radiology* 250, 856–866. doi: 10.1148/radiol.2503080751

De Vis, J. B., Peng, S. L., Chen, X., Li, Y., Liu, P., Sur, S., et al. (2018). Arterial-spin-labeling (ASL) perfusion MRI predicts cognitive function in elderly individuals: a 4-year longitudinal study. *J. Magn. Reson. Imaging* 48, 449–458. doi: 10.1002/jmri.25938

Dolui, S., Li, Z., Nasrallah, I. M., Detre, J. A., and Wolk, D. A. (2020). Arterial spin labeling versus 18F-FDG-PET to identify mild cognitive impairment. *Neuroimage Clin.* 25:102146. doi: 10.1016/j.nicl.2019.102146

Duan, W., Sehrawat, P., Balachandrasekaran, A., Bhumkar, A. B., Boraste, P. B., Becker, J. T., et al. (2020). Cerebral blood flow is associated with diagnostic class and cognitive decline in Alzheimer's disease. *J. Alzheimers Dis.* 76, 1103–1120. doi: 10.3233/JAD-200034

Duan, W., Zhou, G. D., Balachandrasekaran, A., Bhumkar, A. B., Boraste, P. B., Becker, J. T., et al. (2021). Cerebral blood flow predicts conversion of mild cognitive impairment into Alzheimer's disease and cognitive decline: an arterial spin labeling follow-up study. *J. Alzheimers Dis.* 82, 293–305. doi: 10.3233/JAD-210199

Dubois, B., Hampel, H., Feldman, H. H., Scheltens, P., Aisen, P., Andrieu, S., et al. (2016). Preclinical Alzheimer's disease: definition, natural history, and diagnostic criteria. *Alzheimers Dement.* 12, 292–323. doi: 10.1016/j.jalz.2016.02.002

Frisoni, G. B., Winblad, B., and O'Brien, J. T. (2011). Revised NIA-AA criteria for the diagnosis of Alzheimer's disease: a step forward but not yet ready for widespread clinical use. *Int. Psychogeriatr.* 23, 1191–1196. doi: 10.1017/S1041610211001220

Jack, C. R., Bennett, D. A., Blennow, K., Carrillo, M. C., Dunn, B., Haeberlein, S. B., et al. (2018). NIA-AA research framework: toward a biological definition of Alzheimer's disease. *Alzheimers Dement.* 14, 535–562. doi: 10.1016/j.jalz.2018.02.018

Jiang, W., Lin, F., Zhang, J., Zhan, T., Cao, P., and Wang, S. (2020). Deep-learning-based segmentation and localization of white matter hyperintensities on magnetic resonance images. *Interdiscip. Sci.* 12, 438–446. doi: 10.1007/s12539-020-00398-0

Kisler, K., Nelson, A. R., Montagne, A., and Zlokovic, B. V. (2017). Cerebral blood flow regulation and neurovascular dysfunction in Alzheimer disease. *Nat. Rev. Neurosci.* 18, 419–434. doi: 10.1038/nrn.2017.48

Leeuwis, A. E., Benedictus, M. R., Kuijer, J. P. A., Binnewijzend, M. A. A., Hooghiemstra, A. M., Verfaillie, S. C. J., et al. (2017). Lower cerebral blood flow is associated with impairment in multiple cognitive domains in Alzheimer's disease. *Alzheimers Dement.* 13, 531–540. doi: 10.1016/j.jalz.2016.08.013

Liu, Y., Zeng, X., Wang, Z., Zhang, N., Fan, D., and Yuan, H. (2015). Different post label delay cerebral blood flow measurements in patients with Alzheimer's disease using 3D arterial spin labeling. *Magn. Reson. Imaging* 33, 1019–1025. doi: 10.1016/j.mri.2015.05.001

Liu, Y., Zhu, X., Feinberg, D., Guenther, M., Gregori, J., Weiner, M. W., et al. (2012). Arterial spin labeling MRI study of age and gender effects on brain perfusion hemodynamics. *Magn. Reson. Med.* 68, 912–922. doi: 10.1002/mrm.23286

Love, S., and Miners, J. S. (2016). Cerebrovascular disease in ageing and Alzheimer's disease. *Acta Neuropathol.* 131, 645–658. doi: 10.1007/s00401-015-1522-0

Ma, H. R., Pan, P. L., Sheng, L. Q., Dai, Z. Y., Di Wang, G., Luo, R., et al. (2017). Aberrant pattern of regional cerebral blood flow in Alzheimer's disease: a voxel-wise meta-analysis of arterial spin labeling MR imaging studies. *Oncotarget* 8, 93196–93208. doi: 10.18632/oncotarget.21475

McDade, E., Kim, A., James, J., Sheu, L. K., Kuan, D. C.-H., Minhas, D., et al. (2014). Cerebral perfusion alterations and cerebral amyloid in autosomal dominant Alzheimer disease. *Neurology* 83, 710–717. doi: 10.1212/WNL.0000000000000721

McKhann, G. M., Knopman, D. S., Chertkow, H., Hyman, B. T., Jack, C. R., Kawas, C. H., et al. (2011). The diagnosis of dementia due to Alzheimer's disease: recommendations from the National Institute on Aging-Alzheimer's Association workgroups on diagnostic guidelines for Alzheimer's disease. *Alzheimers Dement.* 7, 263–269. doi: 10.1016/j.jalz.2011.03.005

Nelson, A. R., Sweeney, M. D., Sagare, A. P., and Zlokovic, B. V. (2016). Neurovascular dysfunction and neurodegeneration in dementia and Alzheimer's disease. *Biochim. Biophys. Acta* 1862, 887–900. doi: 10.1016/j.bbadis.2015.12.016

Østergaard, L., Aamand, R., Gutiérrez-Jiménez, E., Ho, Y.-C. L., Blicher, J. U., Madsen, S. M., et al. (2013). The capillary dysfunction hypothesis of Alzheimer's disease. *Neurobiol. Aging* 34, 1018–1031. doi: 10.1016/j.neurobiolaging.2012.09.011

Riederer, I., Bohn, K. P., Preibisch, C., Wiedemann, E., Zimmer, C., Alexopoulos, P., et al. (2018). Alzheimer disease and mild cognitive impairment: integrated pulsed arterial spin-labeling MRI and 18F-FDG PET. *Radiology* 288, 198–206. doi: 10.1148/radiol.2018170575

Rolls, E. T., Joliot, M., and Tzourio-Mazoyer, N. (2015). Implementation of a new parcellation of the orbitofrontal cortex in the automated anatomical labeling atlas. *Neuroimage* 122, 1–5. doi: 10.1016/j.neuroimage.2015.07.075

Sanchez, D. L., Thomas, K. R., Edmonds, E. C., Bondi, M. W., and Bangen, K. J. (2020). Regional hypoperfusion predicts decline in everyday functioning at three-year follow-up in older adults without dementia. *J. Alzheimers Dis.* 77, 1291–1304. doi: 10.3233/JAD-200490

Sierra-Marcos, A. (2017). Regional cerebral blood flow in mild cognitive impairment and Alzheimer's disease measured with arterial spin labeling magnetic resonance imaging. *Int. J. Alzheimers Dis.* 2017:5479597. doi: 10.1155/2017/5479597

Soman, S., Raghavan, S., Rajesh, P. G., Varma, R. P., Mohanan, N., Ramachandran, S. S., et al. (2021). Relationship between cerebral perfusion on arterial spin labeling (ASL) MRI with brain volumetry and cognitive performance in mild cognitive impairment and dementia due to alzheimer's disease. *Ann. Indian Acad. Neurol.* 24, 559–565. doi: 10.4103/aian.AIAN_848_20

Thomas, B., Sheelakumari, R., Kannath, S., Sarma, S., and Menon, R. N. (2019). Regional cerebral blood flow in the posterior cingulate and precuneus and the entorhinal cortical atrophy score differentiate mild cognitive impairment and dementia due to Alzheimer disease. *AJNR Am. J. Neuroradiol.* 40, 1658–1664. doi: 10.3174/ajnr.A6219

Thomas, K. R., Osuna, J. R., Weigand, A. J., Edmonds, E. C., Clark, A. L., Holmqvist, S., et al. (2021). Regional hyperperfusion in older adults with objectively-defined subtle cognitive decline. *J. Cereb. Blood Flow Metab.* 41, 1001–1012. doi: 10.1177/0271678X20935171

van der Thiel, M., Rodriguez, C., Giannakopoulos, P., Burke, M. X., Lebel, R. M., Gninenko, N., et al. (2018). Brain perfusion measurements using multidelay arterial spin-labeling are systematically biased by the number of delays. *AJNR Am. J. Neuroradiol.* 39, 1432–1438. doi: 10.3174/ajnr.A5717

Verberk, I. M. W., Slot, R. E., Verfaillie, S. C. J., Heijst, H., Prins, N. D., van Berckel, B. N. M., et al. (2018). Plasma amyloid as prescreener for the earliest alzheimer pathological changes. *Ann. Neurol.* 84, 648–658. doi: 10.1002/ana.25334

Wang, D. J. J., Alger, J. R., Qiao, J. X., Gunther, M., Pope, W. B., Saver, J. L., et al. (2013). Multi-delay multi-parametric arterial spin-labeled perfusion MRI in acute ischemic stroke – comparison with dynamic susceptibility contrast enhanced perfusion imaging. *Neuroimage Clin.* 3, 1–7. doi: 10.1016/j.nicl.2013.06.017

Wei, Y., Huang, N., Liu, Y., Zhang, X., Wang, S., and Tang, X. (2020). Hippocampal and amygdalar morphological abnormalities in Alzheimer's disease based on three chinese MRI datasets. *Curr. Alzheimer Res.* 17, 1221–1231. doi: 10.2174/1567205018666210218150223

Wierenga, C. E., Hays, C. C., and Zlatar, Z. Z. (2014). Cerebral blood flow measured by arterial spin labeling MRI as a preclinical marker of Alzheimer's disease. *J. Alzheimers Dis.* 42(Suppl. 4), S411–S419. doi: 10.3233/JAD-141467

Xekardaki, A., Rodriguez, C., Montandon, M.-L., Toma, S., Tombeur, E., Herrmann, F. R., et al. (2015). Arterial spin labeling may contribute to the prediction of cognitive deterioration in healthy elderly individuals. *Radiology* 274, 490–499. doi: 10.1148/radiol.14140680

Yan, L., Liu, C. Y., Wong, K.-P., Huang, S.-C., Mack, W. J., Jann, K., et al. (2018). Regional association of pCASL-MRI with FDG-PET and PiB-PET in people at risk for autosomal dominant Alzheimer's disease. *Neuroimage Clin.* 17, 751–760. doi: 10.1016/j.nicl.2017.12.003

Yoshiura, T., Hiwatashi, A., Yamashita, K., Ohyagi, Y., Monji, A., Takayama, Y., et al. (2009). Simultaneous measurement of arterial transit time, arterial blood volume, and cerebral blood flow using arterial spin-labeling in patients with Alzheimer disease. *AJNR Am. J. Neuroradiol.* 30, 1388–1393. doi: 10.3174/ajnr.A1562

Zhang, N., Gordon, M. L., and Goldberg, T. E. (2017). Cerebral blood flow measured by arterial spin labeling MRI at resting state in normal aging and Alzheimer's disease. *Neurosci. Biobehav. Rev.* 72, 168–175. doi: 10.1016/j.neubiorev.2016.11.023

Zhang, Q., Wang, Q., He, C., Fan, D., Zhu, Y., Zang, F., et al. (2021). Altered regional cerebral blood flow and brain function across the Alzheimer's disease spectrum: a potential biomarker. *Front. Aging Neurosci.* 13:630382. doi: 10.3389/fnagi.2021.630382

Zlokovic, B. V. (2011). Neurovascular pathways to neurodegeneration in Alzheimer's disease and other disorders. *Nat. Rev. Neurosci.* 12, 723–738. doi: 10.1038/nrn3114

Conflict of Interest: The authors declare that the research was conducted in the absence of any commercial or financial relationships that could be construed as a potential conflict of interest.

Publisher's Note: All claims expressed in this article are solely those of the authors and do not necessarily represent those of their affiliated organizations, or those of the publisher, the editors and the reviewers. Any product that may be evaluated in this article, or claim that may be made by its manufacturer, is not guaranteed or endorsed by the publisher.

Copyright © 2022 Sun, Wang, Li, Jiang, Zhang, Li, Zhang, Jia, Chappell and Xu. This is an open-access article distributed under the terms of the Creative Commons Attribution License (CC BY). The use, distribution or reproduction in other forums is permitted, provided the original author(s) and the copyright owner(s) are credited and that the original publication in this journal is cited, in accordance with accepted academic practice. No use, distribution or reproduction is permitted which does not comply with these terms.

frontiers | Frontiers in Neuroscience

TYPE Original Research
PUBLISHED 27 July 2022
DOI 10.3389/fnins.2022.966087

Check for updates

OPEN ACCESS

EDITED BY
Long-Biao Cui,
Fourth Military Medical University, China

REVIEWED BY
Yujun Gao,
Wuhan University, China
Xin Guo,
Wuhan University, China

*CORRESPONDENCE
Ren-Qiang Yu
yurenqiang@hospital.cqmu.edu.cn

†These authors have contributed equally to this work

SPECIALTY SECTION
This article was submitted to Brain Imaging Methods, a section of the journal Frontiers in Neuroscience

RECEIVED 10 June 2022
ACCEPTED 07 July 2022
PUBLISHED 27 July 2022

CITATION
Xiong Y, Chen R-S, Wang X-Y, Li X, Dai L-Q and Yu R-Q (2022) Cerebral blood flow in adolescents with drug-naive, first-episode major depressive disorder: An arterial spin labeling study based on voxel-level whole-brain analysis. *Front. Neurosci.* 16:966087. doi: 10.3389/fnins.2022.966087

COPYRIGHT
© 2022 Xiong, Chen, Wang, Li, Dai and Yu. This is an open-access article distributed under the terms of the Creative Commons Attribution License (CC BY). The use, distribution or reproduction in other forums is permitted, provided the original author(s) and the copyright owner(s) are credited and that the original publication in this journal is cited, in accordance with accepted academic practice. No use, distribution or reproduction is permitted which does not comply with these terms.

Cerebral blood flow in adolescents with drug-naive, first-episode major depressive disorder: An arterial spin labeling study based on voxel-level whole-brain analysis

Ying Xiong[1,2†], Rong-Sheng Chen[1†], Xing-Yu Wang[1], Xiao Li[3], Lin-Qi Dai[3] and Ren-Qiang Yu[1*]

[1]Department of Radiology, The First Affiliated Hospital of Chongqing Medical University, Chongqing, China, [2]Department of Hematology, Chongqing General Hospital, Chongqing, China, [3]Department of Psychiatry, The First Affiliated Hospital of Chongqing Medical University, Chongqing, China

Purpose: The major depressive disorder (MDD) can be a threat to the health of people all over the world. Although governments have developed and implemented evidence-based interventions and prevention programs to prevent MDD and maintain mental health in adolescents, the number of adolescents with this condition has been on the rise for the past 10 years.

Methods: A total of 60 adolescents were recruited, including 32 drug-naive adolescents with first-episode MDD and 28 healthy controls (HCs). Alterations in the intrinsic cerebral activity of the adolescents with MDD were explored using arterial spin labeling (ASL) while differences in the regional cerebral blood flow (rCBF) of the two groups were assessed based on voxel-based whole-brain analysis. Finally, correlations between the regional functional abnormalities and clinical variables were investigated for adolescents with MDD.

Results: Compared with HCs, MDD patients had a lower rCBF in the left triangular part of the inferior frontal gyrus (IFGtriang) but a higher one in the right Precental gyrus (PreCG). Negative correlations were also noted between the CBF in the left IFGtriang and the Hamilton depression scale (HAMD) scores of MDD patients.

Conclusion: Elucidating the neurobiological features of adolescent patients with MDD is important to adequately develop methods that can assist in early diagnosis, precaution and intervention.

KEYWORDS

major depressive disorder, adolescent, arterial spin labeling, regional cerebral blood flow, fMRI

Introduction

Major depressive disorder (MDD), a mental illness characterized by persistent low mood, is linked to significant morbidity and mortality. According to the World Health Organization (WHO), around 350 million people from around the world suffer from depression which largely contributes to illness and disability (Frankish et al., 2018). At the same time, for half of the people diagnosed with mental disorders, the first symptoms generally appear before the age of 14 (Kessler et al., 2007). The case for MDD is not different as its incidence largely increases after adolescence (Kessler et al., 2003). Indeed, while 10–20% of adolescents are estimated to have a mental health disorder (Olfson et al., 2014), the lifetime prevalence of MDD in adolescents exceeds 15% (Kessler et al., 2007). Furthermore, numerous studies have shown some degree of continuity between MDD in adolescents and that of adults (Kessler et al., 2007) since the risk of depression persisting into adulthood is two to four times higher (Pine et al., 1999). Although governments have developed and implemented evidence-based interventions and prevention programs to prevent MDD and maintain mental health in adolescents, between 34 and 75% of them experience a relapse within the first five years since the first depressive events (Kennard et al., 2006). Unfortunately, these cases tend to remain underdiagnosed and undertreated (Olfson et al., 2014).

Early (<30 years) depression and higher heritability (Lyons et al., 1998) as well as suicidal ideation associated with longer symptom duration (Korten et al., 2012) are strongly associated with later relapse (Birmaher et al., 2004).

At present, the pathogenesis of MDD remains unclear, with its clinical diagnosis being mainly based on symptoms (Gao et al., 2019; Yu et al., 2021). At the same time, due to self-reports and doctor bias, misdiagnosis and missed diagnosis may also occur. Nevertheless, with the brain being in a developing state during adolescence (Dennis et al., 2013; Luna et al., 2015), plasticity provides a means for applying additional diagnostic interventions. However, to date, the understanding of the neural basis of adolescent MDD remains limited.

Considering the breadth and severity of MDD in adolescents, in-depth research on its neural mechanism is crucial in order to provide evidence for the early diagnosis of depression, the development of interventions as well as the improvement of current treatments.

Functional neuroimaging provides a means for undertaking neurobiological studies of MDD. Early studies of brain functions in depressed patients mainly relied on the positron emission tomography (PET) and the single photon emission computed tomography (SPECT) to measure glucose metabolism and the baseline regional cerebral blood flow (rCBF) (Seminowicz et al., 2004; Smith and Cavanagh, 2005). However, both approaches are not free from significant disadvantages which include the use of radioactive materials, the risk of allergy, invasiveness, poor spatial resolution, limited scope of use, high price, and risk factors that limit their use in adolescents with depression (Ho et al., 2013; Chen et al., 2016). In contrast, blood oxygenation level dependence (BOLD) is not only non-radioactive but it is also easily accessible as well as reliable (Fox and Raichle, 2007; Greicius, 2008; Detre et al., 2009). However, since the measurement of BOLD signals relies on vascular factors and is sensitive to blood flow and blood volume, results may still be influenced by confounding factors (Wintermark et al., 2005). Furthermore, BOLD indirectly measures neuronal activation without focusing on cerebral perfusion and hence, measures of neural activity tend to be relative instead of absolute. As such, they cannot be well applied to the study of the neurophysiology of depression.

Emerging arterial spin labeling (ASL) perfusion magnetic resonance imaging (MRI) is a technique that applies magnetically labeled arterial blood water as an endogenous tracer to quantitatively assess rCBF (Ma et al., 2017; Zheng et al., 2019; Momosaka et al., 2020; Wang et al., 2022). This approach not only provides results which are consistent with PET and SPECT (Chen et al., 2011; Boscolo Galazzo et al., 2016; Tosun et al., 2016; Verclytte et al., 2016), but it also enables absolute quantification of rCBF (Detre et al., 2009; Bokkers et al., 2010), thus presenting ASL as a reliable physiological marker of neural activity (Akgoren et al., 1994; Hoge and Pike, 2001; Lauritzen, 2001). Assessing whether the rCBF pattern in high-risk groups for depression deviates significantly from the norm may be helpful for early diagnosis, intervention and prevention (Bonne and Krausz, 1997). In addition, in various neuropsychiatric disorders, perfusion patterns can act as objective biomarkers which help to track disease progression as well as developmental brain maturation (Brown et al., 2007; Borogovac and Asllani, 2012). In these contexts, ASL offers several advantages in terms of its safety, non-invasiveness, non-radioactivity, ease to obtain, reproducibility, its ability to quantitatively display perfusion abnormalities, its high spatial resolution and its good accuracy. Altogether, these features make ASL a powerful tool for the study of rCBF in patients with depression (Wang et al., 2011; Ho et al., 2013). In particular, it has the potential to be applied in the study of the neural basis and for the early diagnosis of depression.

Previous studies have mostly recruited patients with long-term diseases and those undergoing drug treatment (Duhameau et al., 2010; Vasic et al., 2015) as different antidepressants may have potentiating or weakening effects on rCBF (Nobler et al., 2002). This fact causes the research to be concentrated on adult patients (Vasic et al., 2015; Fu et al., 2017), thereby making it unsuitable for considering the early diagnosis and treatment of adolescent depression. Therefore, this study, involving first-episode untreated adolescents with major depressive disorder, may help in reducing confounding factors, in resolving inconsistencies in the existing literature, and eventually in

determining whether hyperactive perfusion or hypoperfusion is indeed responsible for adolescent MDD potential biomarkers.

Consequently, ASL was applied for testing the following hypotheses: (1) the rCBF values of the relevant brain regions in patients with MDD can change compared to the control group and (2) the changes in rCBF values are linked to the severity of the disease.

Materials and methods

Participant selection

This study recruited 40 adolescents between 12 and 17 years old and diagnosed with MDD from the inpatient clinics of the First Affiliated Hospital of Chongqing Medical University, China. Two experienced psychiatrists independently evaluated the presence or absence of diagnoses based on the Mini International Neuropsychiatric Interview for Children and Adolescents (MINI-KID). The validated and reliable Chinese version of the 17-item depression scale Hamilton depression scale-17 (HAMD-17) was then used to assess the severity of depression. The HAMD-17 instrument was selected on account of its extensive application in clinical practice and scientific research. On the day of MRI-based assessments, the patients obtained a total score of at least 17 on the HAMD-17 scale.

The exclusion criteria for the participants were as follows: being left-handed; drug misuse; intense physical diseases or any other somatic ones; a history of neurological disorders running in the family; head motion exceeding 3 mm in translation or 3° in rotation; the presence of any surgically-placed electronic or metal materials that could interfere with functional MRI (fMRI) assessment; the existence of other psychiatric disorders such as personality disorders or schizophrenia; the presence of abnormal cerebral structures after early MRI scanning. In the case of the healthy controls (HCs), the inclusion criteria were: aged 12–17 years; being from the Han Chinese population; no previous history of psychiatric diagnosis; no history of severe neurological (e.g., stroke, concussion) or medical conditions (e.g., chronic inflammatory or autoimmune diseases); no conditions affecting metabolism (e.g., hypertension, diabetes, or thyroid dysfunction). The same set of exclusion criteria was applied to both groups. Overall, 32 patients as well as 28 healthy participants were controlled for variations in factors such as educational status, age and gender, with the same exclusion standards as depressive patients.

Prior to participation in the current study, a written informed consent was signed by all participants. The study was also performed with the approval of the Medical Ethics Committee of the First Affiliated Hospital of Chongqing Medical University in accordance with the Helsinki's Declaration.

Image acquisition

Magnetic resonance images were acquired with a 3.0 Tesla GE Signa HDx system (General Electric Healthcare), housed in the department of Radiology of the First Affiliated Hospital of Chongqing Medical University.

After lying down for the scans, participants were required to remain quiet, close their eyes without thinking of anything in particular and to relax without moving. Throughout the scanning process, they were required to remain awake. Their hearing was also protected with earplugs while head movement was minimized with the help of a sponge. A standard eight-channel head coil was used with the MRI scanner. Structural abnormalities as well as intracranial lesions were excluded when acquiring 3D T1WI, T2WI, and T2 FLAIR sequences and the resting state perfusion imaging was performed using a 3D ASL with the following parameters: NEX 3, TE 9.8 ms, TR 4,639 ms, FOV 240 mm × 240 mm, slice thickness 4.0 mm, post label delay time 1,525 ms, 3D spiral k-space filling, points 512, arms 8, acquisition scan slices 40, acquisition time 4 min 29 s.

Image processing

Quality control of results was performed by one experienced radiologist who directly checked the data acquired on the MR scanner. In this case, the scanning process was repeated when motion artifacts were observed as a result of head movements. The dcm2nii software[1] was then used to convert digital imaging and communications in medicine (DICOM) images of CBF into neuroimaging informatics technology initiative (NIFTI) formats before running SPM12[2] in MATLAB 2013b. To normalize images, those of each participant were registered for a one-step registration method before subsequently checking the image quality. This was followed by image standardization and spatial smoothing with dpabi4.3[3] and SPM12, respectively. The full width at half-maximum (FWHM) of the Gaussian kernel was 8 mm with the removal of non-brain tissues.

Statistical analyses

All data were analyzed using SPSS22 (Chicago, IL, United States) software. Education level, gender, age, and rCBF were compared between groups using two-sample *t*-tests, with regression analysis also performed using years of education, gender and age as covariates. In this case, a False Discovery Rate (FDR) correction of 0.050, or an

1 https://neuroelf.net/wiki/doku.php?id=dcm2nii
2 https://www.fil.ion.ucl.ac.uk/spm/software/spm12/
3 http://rfmri.org/dpabi

TABLE 1 Demographic characteristics of healthy controls (HCs) and major depressive disorder (MDD) patients.

Demographic data	HCs ($n = 28$)	MDD ($n = 32$)	T (orx^2)	P-value
Gender (male/female)	28(4/24)	32(4/28)	0.010	0.922[a]
Age (years)	15.07 ± 3.90	14.31 ± 1.31	1.592	0.117[b]
Years of education (years)	9.75 ± 2.38	9.06 ± 1.63	1.320	0.192[b]
HAMD score	0.18 ± 0.48	25.22 ± 5.16		

HAMD, Hamilton depression scale. [a]The p-value for gender distribution was obtained by chi-square test. [b]The p-value were obtained by two sample t-tests.

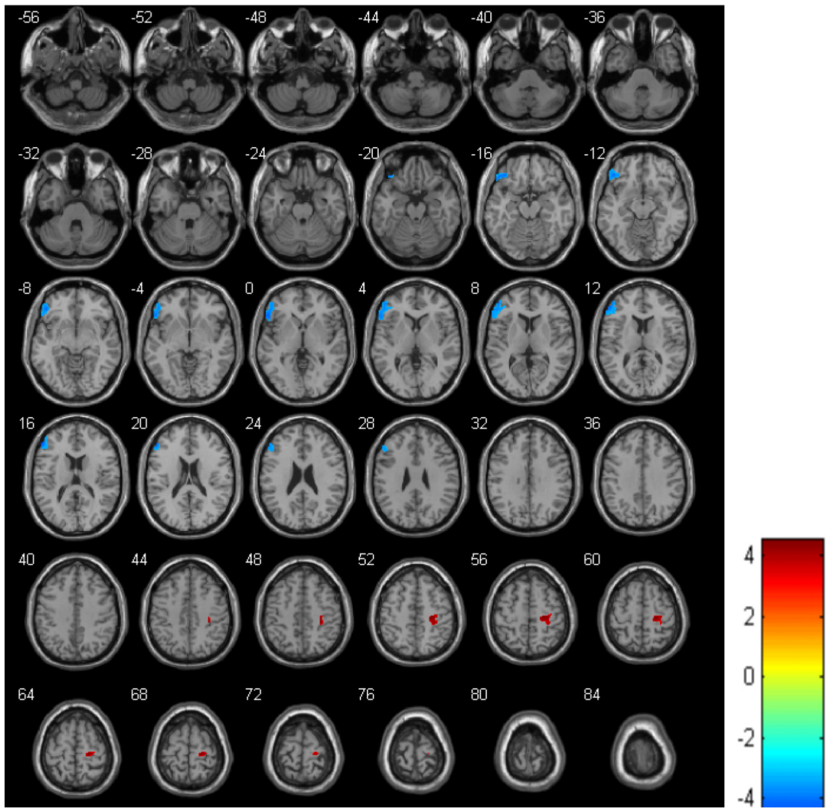

FIGURE 1
Differences in regional cerebral blood flow (rCBF) between healthy controls (HCs) and major depressive disorder (MDD) patients. The blue area represents a decrease in rCBF while the red one represents an increase in rCBF.

TABLE 2 Significant differences in regional cerebral blood flow (rCBF) values between healthy controls (HCs) and major depressive disorder (MDD) patients.

Cluster location	Peak (MNI)			Number of voxels	T-value
	X	Y	Z		
Left IFGtriang	−54	40	16	1178	4.2955
Right PreCG	22	−24	60	384	−4.5095

MNI, Montreal Neurological Institute; IFGtriang, triangular part of the inferior frontal gyrus; PreCG, Precental gyrus.

uncorrected p-value at 0.001 was selected as the threshold for statistical significance. The above steps were completed with SPM12. The CBF values of brain regions showing differences were extracted with dpabi4.3 before visualizing results in Xjview10. The relationship between rCBF values and HAMD scores were eventually determined based on Spearman correlational analysis, with p-values of <0.05 considered to be statistically significant.

Results

Demographic and clinical data

Table 1 summarizes the demographic characteristics of HCs and MDD patients. The MDD patients and the healthy control groups were not significantly different from each other in terms of education level, gender and age ($p > 0.05$).

Differences in regional cerebral blood flow between healthy controls and major depressive disorder patients

The analysis showed that, compared with the HCs, the MDD group displayed a decrease in rCBF in the left IFGtriang (cluster = 1178, and peak $t = 4.2955$), along with an increase in the right PreCG (cluster = 384, and peak $t = -4.5095$) (Figure 1 and Table 2). In this case, a p-value of <0.001 was selected as the cluster threshold.

Correlation between regional cerebral blood flow and Hamilton depression scale scores

Correlational analysis indicated a negative but significant relationship between HAMD scores and rCBF changes in the left IFGtriang when HCs and MDD patients were compared ($R^2 = 0.141$, $p = 0.034$) (Figure 2). However, for the right PreCG, similar comparisons between the two groups did not yield significant correlations between Hamilton depression scale (HAMD) scores and rCBF changes ($R^2 = 0.038$, $p = 0.286$).

Discussion

Voxel-based whole-brain analysis was performed based on arterial spin labeling imaging for calculating rCBF (Wang et al., 2022). Compared with the traditional fMRI data analysis, ASL provides quantitative and reproducible whole-brain measures that are closely related to neural activity for local cerebral blood flow. It also has low inter-subject variability while providing quantitative measures of cerebral blood flow which directly reflect neural activities as well as brain physiology (Haller et al., 2016).

The current study used ASL techniques for quantitatively investigating rCBF in patients diagnosed with MDD. The results confirmed the hypotheses that the rCBF values of the relevant brain regions in MDD patients could change compared to the control group, with this observation corroborating previously-reported findings (Cooper et al., 2020). This analysis revealed reduced rCBF in the right parahippocampus, thalamus, fusiform, and middle temporal gyrus as well as the left and right insula, for those with MDD. After comparing the rCBF in the current study, two abnormal brain regions, namely the left IFGtriang and the right PreCG were identified. Furthermore, subsequent correlational analyses indicated that depression severity (HAMD scores) in MDD was significantly correlated to altered CBF in the left IFGtriang. Overall, the results suggest that altered CBF in the left IFGtriang could represent a potential neural biomarker of vulnerability to MDD.

The influence of rCBF on the pathogenesis of MDD remains unclear but previous studies have shown that different genotypes could have some effects on cerebral blood flow metabolism during depression (Rao et al., 2007; Li et al., 2016). In recent years, numerous studies (Crookes et al., 2018; Nanayakkara et al., 2018) have consistently suggested that high-risk factors

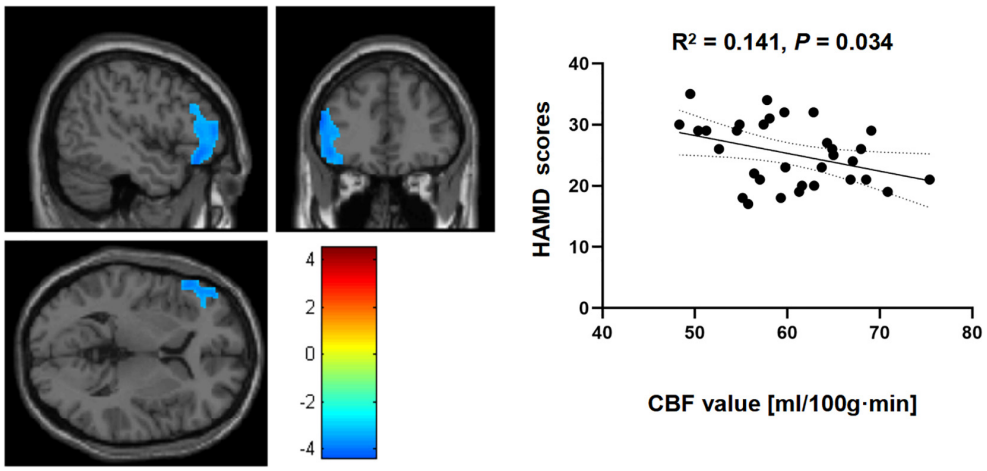

FIGURE 2
Correlational analyses between cerebral blood flow (CBF) in the left triangular part of the inferior frontal gyrus (IFGtriang) and Hamilton depression scale (HAMD) scores for the two groups.

for cerebrovascular diseases such as hypertension, diabetes, and atherosclerosis could also influence the occurrence of depression. It was further found that changes in CBF could be the result of changes in neurotransmitters such as dopamine, serotonin, catecholamines, and glutamate as well as gamma-aminobutyric acid (GABA) that play a role in regulating vascular responses (Dukart et al., 2018). Correlations between cerebral blood flow and local neural activity and metabolism are known as neurovascular coupling (Zhu et al., 2017; Chen et al., 2022). This feature depends on the integrity of the neurovascular unit as altered neuronal activity can lead to changes in blood flow.

Studies of the frontal lobe, involved in higher-order cognitive control and emotional processing, have, so far, yielded the most consistent findings in MDD (Zhang et al., 2018; Zhao et al., 2021). In particular, as an important part of the frontal lobe, the left IFGtriang plays a vital role in anhedonia and emotional activities (Hou et al., 2021) in patients with MDD as it is involved in controlling attention and regulating emotions.

The results finally showed that abnormal rCBF values were negatively correlated to the left IFGtriang and HAMD scores, and this could possibly be attributed to rumination and emotional processing in depressive patients.

Limitations

In addition to its small sample size, this study could not totally exclude physiological noises such as heart and respiratory rhythms in the resting state. Secondly, the age of the patients varied between 12 and 17 years and possible confounding variables regarding age differences could not be removed. Thirdly, the HAMD-17 is yet to be fully validated for rating the severity of depression in adolescent samples. Finally, some patients initially considered to have uni-polar depressions were subsequently diagnosed with bipolar ones in clinical practice.

Conclusion

This study, in comparing HCs and MDD patients, highlighted discrepancies in their corresponding rCBF values. In particular, compared with healthy participants, drug-naive adolescents with a first-episode of MDD had lower rCBF in the left IFGtriang and the right PreCG. Finally, abnormal rCBF values in the left IFGtriang were found to be negatively correlated with HAMD scores, hence suggesting that the left IFGtriang could be an area of interest for better understanding the neurobiology of MDD.

Data availability statement

The raw data supporting the conclusions of this article will be made available by the authors, without undue reservation.

Ethics statement

The studies involving human participants were reviewed and approved by the Medical Ethics Committee of the First Affiliated Hospital of Chongqing Medical University. Written informed consent to participate in this study was provided by the participants' legal guardian/next of kin. Written informed consent was obtained from the individual(s), and minor(s)' legal guardian/next of kin, for the publication of any potentially identifiable images or data included in this article.

Author contributions

YX: writing—original draft. R-SC: writing—original draft and data analyses. X-YW: scanning MRI. XL and L-QD: investigation. R-QY: conceptualization, checking the data, methodology, writing—review and editing, resources, supervision, project administration, and final approval. All authors contributed to the article and approved the submitted version.

Funding

The Foundation of The First Affiliated Hospital of Chongqing Medical University supported the present work financially (No. PYJJ2017-30).

Acknowledgments

We acknowledge all the participants and anonymous commentators for their criticisms and proposals. We also would like to thank all the reviewers who participated in the review and MJEditor (www.mjeditor.com) for its linguistic assistance during the preparation of this manuscript.

Conflict of interest

The authors declare that the research was conducted in the absence of any commercial or financial relationships that could be construed as a potential conflict of interest.

Publisher's note

All claims expressed in this article are solely those of the authors and do not necessarily represent those of their affiliated organizations, or those of the publisher, the editors and the reviewers. Any product that may be evaluated in this article, or claim that may be made by its manufacturer, is not guaranteed or endorsed by the publisher.

References

Akgoren, N., Fabricius, M., and Lauritzen, M. (1994). Importance of nitric oxide for local increases of blood flow in rat cerebellar cortex during electrical stimulation. *Proc. Natl. Acad. Sci. U.S.A.* 91, 5903–5907. doi: 10.1073/pnas.91.13.5903

Birmaher, B., Williamson, D. E., Dahl, R. E., Axelson, D. A., Kaufman, J., Dorn, L. D., et al. (2004). Clinical presentation and course of depression in youth: does onset in childhood differ from onset in adolescence? *J. Am. Acad. Child Adolesc. Psychiatry* 43, 63–70. doi: 10.1097/00004583-200401000-00015

Bokkers, R. P., Bremmer, J. P., van Berckel, B. N., Lammertsma, A. A., Hendrikse, J., Pluim, J. P., et al. (2010). Arterial spin labeling perfusion MRI at multiple delay times: a correlative study with H(2)(15)O positron emission tomography in patients with symptomatic carotid artery occlusion. *J. Cereb. Blood Flow Metab.* 30, 222–229. doi: 10.1038/jcbfm.2009.204

Bonne, O., and Krausz, Y. (1997). Pathophysiological significance of cerebral perfusion abnormalities in major depression-trait or state marker? *Eur. Neuropsychopharmacol.* 7, 225–233. doi: 10.1016/S0924-977X(97)00410-0

Borogovac, A., and Asllani, I. (2012). Arterial spin labeling (ASL) fMRI: advantages, theoretical constrains, and experimental challenges in neurosciences. *Int. J. Biomed. Imaging* 2012:818456. doi: 10.1155/2012/818456

Boscolo Galazzo, I., Mattoli, M. V., Pizzini, F. B., De Vita, E., Barnes, A., Duncan, J. S., et al. (2016). Cerebral metabolism and perfusion in MR-negative individuals with refractory focal epilepsy assessed by simultaneous acquisition of (18)F-FDG PET and arterial spin labeling. *Neuroimage Clin.* 11, 648–657. doi: 10.1016/j.nicl.2016.04.005

Brown, G. G., Clark, C., and Liu, T. T. (2007). Measurement of cerebral perfusion with arterial spin labeling: part 2. Applications. *J. Int. Neuropsychol. Soc.* 13, 526–538. doi: 10.1017/S1355617707070634

Chen, G., Bian, H., Jiang, D., Cui, M., Ji, S., Liu, M., et al. (2016). Pseudo-continuous arterial spin labeling imaging of cerebral blood perfusion asymmetry in drug-naive patients with first-episode major depression. *Biomed. Rep.* 5, 675–680. doi: 10.3892/br.2016.796

Chen, J., Xue, K., Yang, M., Wang, K., Xu, Y., Wen, B., et al. (2022). Altered coupling of cerebral blood flow and functional connectivity strength in first-episode schizophrenia patients with auditory verbal hallucinations. *Front. Neurosci.* 16:821078. doi: 10.3389/fnins.2022.821078

Chen, Y., Wolk, D. A., Reddin, J. S., Korczykowski, M., Martinez, P. M., Musiek, E. S., et al. (2011). Voxel-level comparison of arterial spin-labeled perfusion MRI and FDG-PET in Alzheimer disease. *Neurology* 77, 1977–1985. doi: 10.1212/WNL.0b013e31823a0ef7

Cooper, C. M., Chin Fatt, C. R., Liu, P., Grannemann, B. D., Carmody, T., Almeida, J. R. C., et al. (2020). Discovery and replication of cerebral blood flow differences in major depressive disorder. *Mol. Psychiatry* 25, 1500–1510. doi: 10.1038/s41380-019-0464-7

Crookes, D. M., Demmer, R. T., Keyes, K. M., Koenen, K. C., and Suglia, S. F. (2018). Depressive symptoms, antidepressant use, and hypertension in young adulthood. *Epidemiology* 29, 547–555. doi: 10.1097/EDE.0000000000000840

Dennis, E. L., Jahanshad, N., McMahon, K. L., de Zubicaray, G. I., Martin, N. G., Hickie, I. B., et al. (2013). Development of brain structural connectivity between ages 12 and 30: a 4-Tesla diffusion imaging study in 439 adolescents and adults. *Neuroimage* 64, 671–684. doi: 10.1016/j.neuroimage.2012.09.004

Detre, J. A., Wang, J., Wang, Z., and Rao, H. (2009). Arterial spin-labeled perfusion MRI in basic and clinical neuroscience. *Curr. Opin. Neurol.* 22, 348–355. doi: 10.1097/WCO.0b013e32832d9505

Duhameau, B., Ferre, J. C., Jannin, P., Gauvrit, J. Y., Verin, M., Millet, B., et al. (2010). Chronic and treatment-resistant depression: a study using arterial spin labeling perfusion MRI at 3Tesla. *Psychiatry Res.* 182, 111–116. doi: 10.1016/j.pscychresns.2010.01.009

Dukart, J., Holiga, S., Chatham, C., Hawkins, P., Forsyth, A., McMillan, R., et al. (2018). Cerebral blood flow predicts differential neurotransmitter activity. *Sci. Rep.* 8:4074. doi: 10.1038/s41598-018-22444-0

Fox, M. D., and Raichle, M. E. (2007). Spontaneous fluctuations in brain activity observed with functional magnetic resonance imaging. *Nat. Rev. Neurosci.* 8, 700–711. doi: 10.1038/nrn2201

Frankish, H., Boyce, N., and Horton, R. (2018). Mental health for all: a global goal. *Lancet* 392, 1493–1494. doi: 10.1016/S0140-6736(18)32271-2

Fu, C., Shi, D., Gao, Y., and Xu, J. (2017). Functional assessment of prefrontal lobes in patients with major depression disorder using a dual-mode technique of 3D-arterial spin labeling and (18)F-fluorodeoxyglucose positron emission tomography/computed tomography. *Exp. Ther. Med.* 14, 1058–1064. doi: 10.3892/etm.2017.4594

Gao, Y., Yao, Y., Liang, X., Tang, J., Ma, J., Qi, Y-q, et al. (2019). Changes in white matter and the effects of fluoxetine on such changes in the CUS rat model of depression. *Neurosci. Lett.* 694, 104–110. doi: 10.1016/j.neulet.2018.11.013

Greicius, M. (2008). Resting-state functional connectivity in neuropsychiatric disorders. *Curr. Opin. Neurol.* 21, 424–430. doi: 10.1097/WCO.0b013e328306f2c5

Haller, S., Zaharchuk, G., Thomas, D. L., Lovblad, K. O., Barkhof, F., and Golay, X. (2016). Arterial spin labeling perfusion of the brain: emerging clinical applications. *Radiology* 281, 337–356. doi: 10.1148/radiol.2016150789

Ho, T. C., Wu, J., Shin, D. D., Liu, T. T., Tapert, S. F., Yang, G., et al. (2013). Altered cerebral perfusion in executive, affective, and motor networks during adolescent depression. *J. Am. Acad. Child Adolesc. Psychiatry* 52, 1076–1091.e2. doi: 10.1016/j.jaac.2013.07.008

Hoge, R. D., and Pike, G. B. (2001). Oxidative metabolism and the detection of neuronal activation via imaging. *J. Chem. Neuroanat.* 22, 43–52. doi: 10.1016/S0891-0618(01)00114-4

Hou, Z., Liu, X., Jiang, W., Hou, Z., Yin, Y., Xie, C., et al. (2021). Effect of NEUROG3 polymorphism rs144643855 on regional spontaneous brain activity in major depressive disorder. *Behav. Brain Res.* 409:113310. doi: 10.1016/j.bbr.2021.113310

Kennard, B. D., Emslie, G. J., Mayes, T. L., and Hughes, J. L. (2006). Relapse and recurrence in pediatric depression. *Child Adolesc. Psychiatr. Clin. N. Am.* 15, 1057–1079, xi. doi: 10.1016/j.chc.2006.05.003

Kessler, R. C., Angermeyer, M., Anthony, J. C., Graaf, D. E., Demyttenaere, K., Gasquet, I., et al. (2007). Lifetime prevalence and age-of-onset distributions of mental disorders in the World Health Organization's World Mental Health Survey Initiative. *World Psychiatry* 6, 168–176.

Kessler, R. C., Berglund, P., Demler, O., Jin, R., Koretz, D., Merikangas, K. R., et al. (2003). National comorbidity survey R: the epidemiology of major depressive disorder: results from the National comorbidity survey replication (NCS-R). *JAMA* 289, 3095–3105. doi: 10.1001/jama.289.23.3095

Korten, N. C., Comijs, H. C., Lamers, F., and Penninx, B. W. (2012). Early and late onset depression in young and middle aged adults: differential symptomatology, characteristics and risk factors? *J. Affect. Disord.* 138, 259–267. doi: 10.1016/j.jad.2012.01.042

Lauritzen, M. (2001). Relationship of spikes, synaptic activity, and local changes of cerebral blood flow. *J. Cereb. Blood Flow Metab.* 21, 1367–1383. doi: 10.1097/00004647-200112000-00001

Li, X. B., Wang, J., Xu, A. D., Huang, J. M., Meng, L. Q., Huang, R. Y., et al. (2016). Apolipoprotein E polymorphisms increase the risk of post-stroke depression. *Neural Regen. Res.* 11, 1790–1796. doi: 10.4103/1673-5374.194748

Luna, B., Marek, S., Larsen, B., Tervo-Clemmens, B., and Chahal, R. (2015). An integrative model of the maturation of cognitive control. *Annu. Rev. Neurosci.* 38, 151–170. doi: 10.1146/annurev-neuro-071714-034054

Lyons, M. J., Eisen, S. A., Goldberg, J., True, W., Lin, N., Meyer, J. M., et al. (1998). A registry-based twin study of depression in men. *Arch. Gen. Psychiatry* 55, 468–472. doi: 10.1001/archpsyc.55.5.468

Ma, H., Wang, Z., Xu, K., Shao, Z., Yang, C., Xu, P., et al. (2017). Three-dimensional arterial spin labeling imaging and dynamic susceptibility contrast perfusion-weighted imaging value in diagnosing glioma grade prior to surgery. *Exp. Ther. Med.* 13, 2691–2698. doi: 10.3892/etm.2017.4370

Momosaka, D., Togao, O., Hiwatashi, A., Yamashita, K., Kikuchi, K., Tomiyama, H., et al. (2020). A voxel-based analysis of cerebral blood flow abnormalities in obsessive-compulsive disorder using pseudo-continuous arterial spin labeling MRI. *PLoS One* 15:e0236512. doi: 10.1371/journal.pone.0236512

Nanayakkara, N., Pease, A., Ranasinha, S., Wischer, N., Andrikopoulos, S., Speight, J., et al. (2018). Depression and diabetes distress in adults with type 2 diabetes: results from the Australian National Diabetes Audit (ANDA) 2016. *Sci. Rep.* 8:7846. doi: 10.1038/s41598-018-26138-5

Nobler, M. S., Olvet, K. R., and Sackeim, H. A. (2002). Effects of medications on cerebral blood flow in late-life depression. *Curr. Psychiatry Rep.* 4, 51–58. doi: 10.1007/s11920-002-0013-x

Olfson, M., Blanco, C., Wang, S., Laje, G., and Correll, C. U. (2014). National trends in the mental health care of children, adolescents, and adults by office-based physicians. *JAMA Psychiatry* 71, 81–90. doi: 10.1001/jamapsychiatry.2013.3074

Pine, D. S., Cohen, E., Cohen, P., and Brook, J. (1999). Adolescent depressive symptoms as predictors of adult depression: moodiness or mood disorder? *Am. J. Psychiatry* 156, 133–135. doi: 10.1176/ajp.156.1.133

Rao, H., Gillihan, S. J., Wang, J., Korczykowski, M., Sankoorikal, G. M., Kaercher, K. A., et al. (2007). Genetic variation in serotonin transporter alters resting brain function in healthy individuals. *Biol. Psychiatry* 62, 600–606. doi: 10.1016/j.biopsych.2006.11.028

Seminowicz, D. A., Mayberg, H. S., McIntosh, A. R., Goldapple, K., Kennedy, S., Segal, Z., et al. (2004). Limbic-frontal circuitry in major depression: a path modeling metanalysis. *Neuroimage* 22, 409–418. doi: 10.1016/j.neuroimage.2004.01.015

Smith, D. J., and Cavanagh, J. T. (2005). The use of single photon emission computed tomography in depressive disorders. *Nucl. Med. Commun.* 26, 197–203. doi: 10.1097/00006231-200503000-00004

Tosun, D., Schuff, N., Rabinovici, G. D., Ayakta, N., Miller, B. L., Jagust, W., et al. (2016). Diagnostic utility of ASL-MRI and FDG-PET in the behavioral variant of FTD and AD. *Ann. Clin. Transl. Neurol.* 3, 740–751. doi: 10.1002/acn3.330

Vasic, N., Wolf, N. D., Gron, G., Sosic-Vasic, Z., Connemann, B. J., Sambataro, F., et al. (2015). Baseline brain perfusion and brain structure in patients with major depression: a multimodal magnetic resonance imaging study. *J. Psychiatry Neurosci.* 40, 412–421. doi: 10.1503/jpn.140246

Verclytte, S., Lopes, R., Lenfant, P., Rollin, A., Semah, F., Leclerc, X., et al. (2016). Cerebral hypoperfusion and hypometabolism detected by arterial spin labeling MRI and FDG-PET in early-onset Alzheimer's disease. *J. Neuroimaging* 26, 207–212.

Wang, D. J., Chen, Y., Fernandez-Seara, M. A., and Detre, J. A. (2011). Potentials and challenges for arterial spin labeling in pharmacological magnetic resonance imaging. *J. Pharmacol. Exp. Ther.* 337, 359–366.

Wang, X. H., Liu, X. F., Ao, M., Wang, T., He, J., Gu, Y. W., et al. (2022). Cerebral perfusion patterns of anxiety state in patients with pulmonary nodules: a study of cerebral blood flow based on arterial spin labeling. *Front. Neurosci.* 16:912665. doi: 10.3389/fnins.2022.912665

Wintermark, M., Sesay, M., Barbier, E., Borbely, K., Dillon, W. P., Eastwood, J. D., et al. (2005). Comparative overview of brain perfusion imaging techniques. *Stroke* 36, e83–e99.

Yu, R., Tan, H., Peng, G., Du, L., Wang, P., Zhang, Z., et al. (2021). Anomalous functional connectivity within the default-mode network in treatment-naive patients possessing first-episode major depressive disorder. *Medicine (Baltimore)* 100:e26281. doi: 10.1097/MD.0000000000026281

Zhang, F. F., Peng, W., Sweeney, J. A., Jia, Z. Y., and Gong, Q. Y. (2018). Brain structure alterations in depression: psychoradiological evidence. *CNS Neurosci. Ther.* 24, 994–1003.

Zhao, S., Xia, Y., Huang, Y., Zou, H., Wang, X., Chen, Z., et al. (2021). The correlation between thyroid function, frontal gray matter, and executive function in patients with major depressive disorder. *Front. Endocrinol. (Lausanne)* 12:779693. doi: 10.3389/fendo.2021.779693

Zheng, W., Ren, S., Zhang, H., Liu, M., Zhang, Q., Chen, Z., et al. (2019). Spatial patterns of decreased cerebral blood flow and functional connectivity in multiple system atrophy (cerebellar-type): a combined arterial spin labeling perfusion and resting state functional magnetic resonance imaging study. *Front. Neurosci.* 13:777. doi: 10.3389/fnins.2019.00777

Zhu, J., Zhuo, C., Xu, L., Liu, F., Qin, W., and Yu, C. (2017). Altered coupling between resting-state cerebral blood flow and functional connectivity in schizophrenia. *Schizophr. Bull.* 43, 1363–1374.

frontiers | Frontiers in Neuroscience

TYPE Original Research
PUBLISHED 02 August 2022
DOI 10.3389/fnins.2022.961164

Check for updates

OPEN ACCESS

EDITED BY
Guolin Ma,
China-Japan Friendship Hospital, China

REVIEWED BY
Jiu Chen,
Nanjing Medical University, China
Wenbin Zhang,
Nanjing Brain Hospital Affiliated to Nanjing Medical University, China

*CORRESPONDENCE
Jun Xu
neurojun@126.com

†These authors have contributed equally to this work and share first authorship

SPECIALTY SECTION
This article was submitted to Brain Imaging Methods, a section of the journal Frontiers in Neuroscience

RECEIVED 04 June 2022
ACCEPTED 11 July 2022
PUBLISHED 02 August 2022

CITATION
Li W, Jiang J, Zou X, Zhang Y, Sun M, Jia Z, Li W and Xu J (2022) The characteristics of arterial spin labeling cerebral blood flow in patients with subjective cognitive decline: The Chinese imaging, biomarkers, and lifestyle study.
Front. Neurosci. 16:961164.
doi: 10.3389/fnins.2022.961164

COPYRIGHT
© 2022 Li, Jiang, Zou, Zhang, Sun, Jia, Li and Xu. This is an open-access article distributed under the terms of the Creative Commons Attribution License (CC BY). The use, distribution or reproduction in other forums is permitted, provided the original author(s) and the copyright owner(s) are credited and that the original publication in this journal is cited, in accordance with accepted academic practice. No use, distribution or reproduction is permitted which does not comply with these terms.

The characteristics of arterial spin labeling cerebral blood flow in patients with subjective cognitive decline: The Chinese imaging, biomarkers, and lifestyle study

Wenyi Li[1,2†], Jiwei Jiang[1,2†], Xinying Zou[1,2], Yuan Zhang[1,2], Mengfan Sun[1,2], Ziyan Jia[1,2], Wei Li[1,2] and Jun Xu[1,2*]

[1]Department of Neurology, Beijing Tiantan Hospital, Capital Medical University, Beijing, China, [2]China National Clinical Research Center for Neurological Diseases, Beijing, China

Objective: We aimed to characterize the potential risk factors and cerebral perfusion of patients with subjective cognitive decline (SCD).

Methods: This prospective study enrolled consecutive patients from the Chinese Imaging, Biomarkers, and Lifestyle (CIBL) Cohort of Alzheimer's disease between February 2021 and March 2022. Patients who met the SCD diagnostic criteria were categorized into the SCD group, while those without cognitive complaints or any concerns were assigned to the healthy control (HC) group. The demographic and clinical characteristics and cerebral blood flow (CBF) from pseudo-continuous arterial spin labeling (pCASL) in standard cognitive regions were compared between these two groups. A multivariate analysis was performed to identify independent factors associated with SCD.

Results: The frequency of family history of dementia in the SCD group was higher compared with the HC group (p = 0.016). The CBF of left hippocampus (p = 0.023), left parahippocampal gyrus (p = 0.004), left precuneus (p = 0.029), left middle temporal gyrus (p = 0.022), right parahippocampal gyrus (p = 0.018), and right precuneus (p = 0.024) in the SCD group were significantly increased than those in the HC group. The multivariate logistic regression analyses demonstrated that the family history of dementia [*OR* = 4.284 (1.096–16.747), p = 0.036] and the CBF of left parahippocampal gyrus [*OR* = 1.361 (1.006–1.840), p = 0.045] were independently associated with SCD.

Conclusion: This study demonstrated that the family history of dementia and the higher CBF within the left parahippocampal gyrus were independent risk factors associated with patients with SCD, which could help in the early identification of the SCD and in intervening during this optimal period.

KEYWORDS

subjective cognitive decline, dementia, cerebral blood flow, neuroimaging, parahippocampal gyrus

Introduction

With the global increase in the elderly population, Alzheimer's disease (AD), the leading cause of dementia in the elderly, has been the greatest challenge for global public health and social care. The Alzheimer's Disease International (ADI) predicted that the global population suffering from dementia would rise to 82 million in 2030 and exceed 152 million in 2050 (Patterson, 2018). However, having limited options for assessing the exact pathophysiology and early diagnosis of AD, the clinical experts are faced with great challenge in providing effective therapeutic strategies (Selkoe, 2021). Current drugs for AD mainly aim at the correction of neurotransmitter abnormalities, such as cholinesterase enzyme inhibitors (ChEIs) and *N*-methyl D-aspartate (NMDA) receptor antagonists, which can only provide symptomatic treatment to the disease to a certain extent but cannot reverse the disease progression (Joe and Ringman, 2019).

In 2018, the National Institute on Aging and Alzheimer's Association (NIA-AA) proposed the "ATN" research framework, including biomarkers of Aβ deposition, pathologic tau, and neurodegeneration, which emphasized the progression of AD as a continuum (Jack et al., 2018). Asymptomatic individuals with abnormal AD biomarkers should be considered as a stage of AD, called "preclinical AD," rather than a separate diagnosis. The Dominantly Inherited Alzheimer Network (DIAN) study has demonstrated that in the continuous progress, longitudinal Aβ begins to change first (starting 25 years before estimated symptom onset), followed by the declines in cortical metabolism and CSF p-tau$_{181}$ and tau (approximately 7–10 years later), then the cognitive decline and the hippocampal atrophy (approximately 20 years later) (McDade et al., 2018). In preclinical AD, individuals still retain sufficiently intact cognitive function that can be harnessed and directed toward either compensation or restitution of function (Rabin et al., 2017). Thus, the preclinical stage should be an important consideration for starting the interventions to prevent cognitive impairment before the onset of clinical symptoms.

Subjective cognitive decline (SCD) refers to the self-perception of cognitive decline and does not require confirmation by external observation (Jessen et al., 2014). SCD is a generalized heterogeneous concept that can be induced by many conditions other than AD (Jessen et al., 2020). Increasing evidence has demonstrated that SCD in the elderly is a risk factor for mild cognitive impairment (MCI) or dementia (van Harten et al., 2018; Jessen et al., 2020; Pike et al., 2021). Moreover, abnormalities in several AD-related biomarkers in cerebrospinal fluid or neuroimaging were also found in individuals with SCD (Slot et al., 2019; Jessen et al., 2020), which makes SCD the second stage of six numeric stages in the AD continuum. Thus, effective recognition of SCD may provide important clues for a preclinical stage closely related to dementia or AD. It has been widely accepted that modifying risk factors might prevent or delay up to 40% of dementias (Livingston et al., 2020), which highlights the feasibility and importance of early prevention. However, the implementation of the "ATN" framework has limitations due to the invasive of lumbar puncture and the expense of positron emission tomography (PET). The SCD that is being recognized clinically still needs to be paired with other feasible biomarkers for improving its diagnostic value.

In addition to Aβ deposition, recent evidence from neuroimaging cohort studies and animal models strongly suggests other underlying pathophysiological processes of AD, particularly neurovascular dysregulation (Iturria-Medina et al., 2016; Dounavi et al., 2021). Vascular dysfunction result in reduced clearance of Aβ by periarteriolar and impaired Aβ transporters across the blood-brain barrier, which can increase Aβ deposition. Aβ induces contraction of pericytes and vascular smooth muscle cells and then exacerbates hypoperfusion (Fisher et al., 2022). Duan et al. (2020) have proposed that CBF could be a neuroimaging marker to reflect the degree of cognitive impairment. Arterial spin labeling (ASL) is a non-invasive technique for quantifying cerebral perfusion that has been proven as a useful biomarker of the early stages of AD, which is consistent with the findings of PET (Hays et al., 2016). However, despite increasing studies of ASL on dementia, only a few on individuals with SCD are available, and the findings seem to be not in agreement. Hays et al. (2018) have demonstrated significant negative correlations between verbal memory and CBF within the posterior cingulate cortex, middle temporal

gyrus, hippocampus, fusiform gyrus, and inferior frontal gyrus in patients with SCD. Another observational study has revealed that compared with elderly controls, participants with SCD presented a significant decline in CBF values, mainly in the hippocampal and posterior cingulate cortex (Yang et al., 2021). Moreover, the outstanding relevance of classical risk factors for dementia may not be proven in SCD, which makes SCD difficult to be identified (Wen et al., 2021). The significant clinical and neuroimaging characteristics of SCD are yet to be identified. Therefore, our study aimed to explore risk factors of SCD, especially the perfusion characteristics, for providing new clues to early recognition and intervention of SCD.

Materials and methods

Ethics

The study was approved by the Institutional Review Board of Beijing Tiantan Hospital of Capital Medical University (KY-2021-028-01) before enrolling participants. All individuals involved in this study provided written informed consent for clinical and genetic analyses before enrollment.

Patient or participant selection

All data were analyzed from the Chinese Imaging, Biomarkers, and Lifestyle (CIBL) study of AD, an ongoing large-scale prospective cohort study majorly conducted in 2020 and focused on the risk factors, biomarkers, and neuroimaging in the Chinese population with cognitive impairment, which is registered at chictr.org.cn (ChiCTR2100049131). This study selected consecutive patients with SCD between February 2021 and March 2022. The inclusion criteria were as follows: (1) SCD that met the diagnostic framework proposed by the SCD Initiative Working Group in 2014 and 2020 (Jessen et al., 2014; Jessen et al., 2020); (2) self-experienced persistent decline in memory, rather than other domains of cognition, while healthy control (HC) volunteers with no cognitive complaints or any concerns (worries); (3) normal performance on standardized cognitive tests, adjusted for age, gender, and years of education; and (4) onset of SCD within the last 5 years. Patients were excluded from the study if they (1) were left-handed/ambidexter; (2) met the criteria for MCI or dementia; (3) had other central nervous system diseases that may cause cognitive impairment, such as stroke, Parkinson's disease, frontotemporal dementia, tumor, encephalitis, and epilepsy; (4) had a mental disorder history that met the Diagnostic and Statistical Manual of Mental Disorders-5 (DSM-5); (5) presented cognitive impairment due to traumatic brain injury; (6) had a history of drug abuse or toxic exposure; (7) had systemic diseases, such as thyroid dysfunction, syphilis, and HIV; and (8) had congenital mental developmental delay. Patients with SCD were categorized into the SCD group, while those who met HC volunteers were assigned to the control group.

Data collection

Information on sex, age of enrolled in the cohort, years of education, medical history, family history of dementia, and clinical symptoms were collected. DNA samples were extracted from whole blood samples. *Apolipoprotein E (APOE)* genotyping was performed based on two single nucleotide polymorphism (SNP) sites (rs429358 and rs7412) at WeGene Lab using a customized Illumina WeGene V3 Array by Illumina iScan System, which contains roughly 700,000 markers. All participants completed a comprehensive neuropsychological assessment to evaluate their global cognitive functions, such as Mini-mental State Examination (MMSE), the Montreal Cognitive Assessment (MoCA), the Hamilton Depression Rating Scale (HAMD), and the Hamilton Anxiety Rating Scale (HAMA). The SCD-questionnaire 9 (SCD-Q9) was performed to help diagnose and quantitatively assess the severity of SCD (Gifford et al., 2015; Hao et al., 2017). In this study, two trained neurologists or neuropsychologists performed the cognitive tests, respectively.

Magnetic resonance imaging acquisition and processing

Image acquisition was performed on a 3-T MR scanner (SIGNA Premier; GE Healthcare, Milwaukee, WI, United State) with a 48-channel head coil. High-resolution 3D T1 scans were performed using the Inversion Recovery Gradient Recalled Echo (IR-GRE) sequence with the following parameters: repetition time (TR) = 7.3 ms, echo time (TE) = 3.0 ms, inversion time (TI) = 450 ms; flip angle (FA) = 12 degrees, field of view (FOV) = 256 mm × 256 mm, acquisition matrix = 256 × 256, slice thickness = 1.0 mm, slice number = 176, and scan time = 4 min 56 s. ASL was performed using pseudo-continuous arterial spin labeling (pCASL) with a 3D readout (3D pCASL) sequence with the following parameters: axial acquisition, TR = 4,849 ms, TE = 10.6 ms, FOV = 220 mm × 220 mm, acquisition matrix = 512 × 512, slice thickness = 4 mm, slice number = 36, post-labeling delay = 2,025 ms, and scan time = 4 min 22 s.

Data processing was performed using CereFlow software (Anying Technology Beijing Co., Ltd.)[1] with the following steps: (1) calculation of CBF from the GE scanner's ASL's perfusion-weighted (PW) image and proton density (PD) image using

1 www.cereflow.cn

the standard simple compartment model with an assumption that the arterial transit time (ATT) is equivalent to post-label delay (PLD); (2) co-registration of the M0 image (GE ASL's PD image) with the anatomical T1w image, the calculated CBF image was also co-registered to T1w with the same transformation parameters; (3) normalization of T1w images to the Montreal Neurological Institute (MNI) template; (4) CBF image warped into the MNI space using the forward transformation matrix derived from T1w; and (5) extraction of the regional CBF by the automated anatomical labeling (AAL) atlas (Tzourio-Mazoyer et al., 2002). The brain areas that showed significant CBF differences between the two groups were further analyzed, including bilateral hippocampal, parahippocampal gyrus, precuneus, middle temporal gyrus, and posterior cingulate.

Statistical analysis

All statistical analyses were performed using SPSS 26.0 statistical software (SPSS Inc., Chicago, IL, United States). Categorical variables are presented as the total number (n) and percentage (%) per group, and the χ^2 or Fisher's exact test was used to assess statistical differences. The mean and standard deviations (SDs) were calculated for continuous variables with normal distribution, while the median and interquartile range (IQR) were used for continuous variables lacking a normal distribution. Subsequently, the t-test was used for normally distributed data. The Mann–Whitney U-test was used for data with no normal distribution. Risk factors ($p < 0.05$) were further analyzed using univariate and multivariate logistic regression. The p-values smaller than 0.05 were considered statistically significant.

Results

Baseline characteristics in both groups

The clinical variables and demographics are shown in Table 1. In the initial stage, a total of 349 participants underwent basic information collection and neuropsychological assessment, and then 61 patients were included in the final analysis (Figure 1). Of these, 31 patients (50.8%) were diagnosed with SCD and 30 patients (49.2%) were assigned to the control group. There was no significant difference between the two groups in gender, age, education, and the prevalence of hypertension and diabetes, except for a family history of dementia. The frequency of family history of dementia in the SCD group (45.2%) was significantly higher than that in the HC group (16.7%). Subsequently, we compared the scores of MMSE, MoCA, HAMD, and HAMA and found that there was no significant difference between the two groups in the neuropsychological assessments. Additionally, we found no significant difference in the frequency of *APOE* ε4 carriers between the two groups.

The absolute cerebral blood flow in both groups

The absolute CBF in various brain regions between the two groups is shown in Table 2. The CBF of the SCD group was generally higher than the HC group, and the differences in six brain regions, including the left hippocampus ($p = 0.023$), left parahippocampal gyrus ($p = 0.004$), right parahippocampal gyrus ($p = 0.018$), left precuneus ($p = 0.029$), right precuneus ($p = 0.024$), and left middle temporal gyrus ($p = 0.022$) were statistically significant. The comparison of the cerebral blood perfusion diagram in Figure 2 also conforms to the above statistics.

Univariate and multivariate logistic regression analyses

We assessed all risk factors with p values < 0.05 (Tables 1, 2) using a univariate and multivariate logistic regression model. The results of univariate logistic regression analyses were consistent with the T-test and the χ^2 test (Table 3), which showed that the family history of dementia and CBF in the above-mentioned brain regions were significantly increased in

TABLE 1 Demographic and neuropsychological assessments for participants.

Variables	HC ($n = 30$)	SCD ($n = 31$)	p-value
Age (years)	62.53 ± 7.71	60.94 ± 9.33	0.496
Gender (%, Male)	12 (40)	7 (22.6)	0.142
Education (years)	10.60 ± 4.70	12.68 ± 3.52	0.056
Hypertension (%)	13 (43.3)	7 (22.6)	0.084
Diabetes (%)	7 (23.3)	2 (6.5%)	0.081
Family history of dementia (%)	5 (16.7)	14 (45.2)	**0.016**
MMSE (scores)	29 (27.75–29)	29 (28–29)	0.703
MoCA (scores)	26 (23.75–28)	27 (26–28)	0.090
HAMD (scores)	4 (1–7)	6 (3–8)	0.171
HAMA (scores)	3 (0.75–5.5)	4 (1–6)	0.301
APOE genotype (%)			0.603
2/3	8 (26.7)	5 (16.1)	
3/3	17 (56.7)	20 (64.5)	
3/4	5 (16.7)	6 (19.4)	

MMSE, Mini-mental State Examination; MoCA, the Montreal Cognitive Assessment; HAMD, Hamilton Depression Rating Scale; HAMA, Hamilton Anxiety Rating Scale; HC, healthy control; SCD, subjective cognitive decline. The numbers in bold are statistically significant (p-value 0.05).

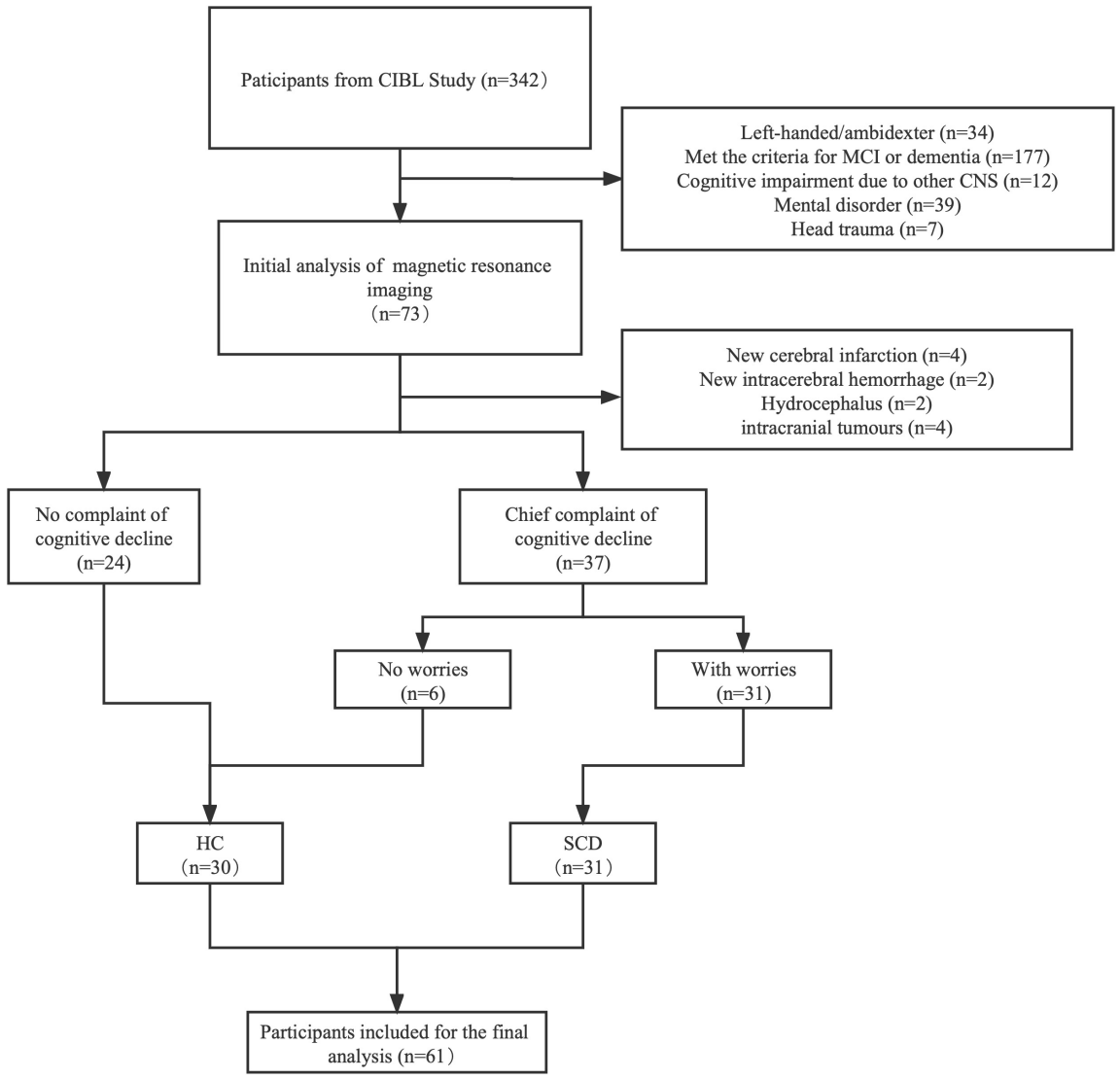

FIGURE 1
A flowchart of the inclusion and exclusion criteria. MRI, magnetic resonance imaging; MCI, mild cognition impairment; HC, healthy control; SCD, subjective cognition decline.

the SCD group compared with the HC group. According to the odds ratio (*OR*) value, the first five factors were selected for multivariate logistic regression analysis. The multivariate logistic regression analyses demonstrated that the family history of dementia [*OR* = 4.284 (1.096–16.747), $p = 0.036$] and the CBF of left parahippocampal gyrus [*OR* = 1.361 (1.006–1.840), $p = 0.045$] were independently associated with SCD (**Table 4**).

Discussion

Currently, there is no consensus on which clinical and neuroimaging characteristics of individuals lead to a higher risk of developing SCD, despite the increasing research evidence about the clinical and cerebral microstructural and blood flow alterations associated with SCD (Yang et al., 2021; Zhang et al., 2021). We speculate that the different findings may be related to the ethnic difference, different inclusion criteria, and factors analysis methods. This study demonstrated that the family history of dementia and the hyperperfusion alterations in the left parahippocampus were independent risk factors associated with patients with SCD, which could help in the early identification of the SCD and in intervening during this optimal period. The results of Wolfsgruber et al. (2022) are consistent with ours, which found that the first-degree family history of AD revealed higher SCD-plus scores than healthy controls. Another prospective cohort study has found that greater subjective memory impairment is associated with a first-degree family

TABLE 2 Differences in CBF of cognition-related brain regions between the two groups.

Brain regions	CBF (ml/100 g/min)		*p*-value
	HC ($n = 30$)	SCD ($n = 31$)	
Hippocampus_L	40.96 ± 8.20	45.98 ± 8.64	**0.023**
Hippocampus_R	40.79 ± 8.60	44.80 ± 8.03	0.065
Posterior cingulate_L	62.05 ± 11.08	69.05 ± 17.24	0.064
Posterior cingulate_R	52.99 ± 10.85	58.62 ± 14.83	0.097
Parahippocampal gyrus_L	37.60 ± 6.48	42.52 ± 6.15	**0.004**
Parahippocampal gyrus_R	39.54 ± 7.67	44.19 ± 7.32	**0.018**
Precuneus_L	50.62 ± 10.41	56.85 ± 11.33	**0.029**
Precuneus_R	50.66 ± 10.55	57.06 ± 11.08	**0.024**
Middle temporal gyrus_L	53.04 ± 9.46	59.30 ± 11.27	**0.022**
Middle temporal gyrus_R	48.74 ± 8.55	52.69 ± 9.28	0.089

CBF, cerebral blood flow; HC, healthy control; SCD, subjective cognitive decline. The numbers in bold are statistically significant (*p*-value 0.05).

history of AD in healthy older adults (Haussmann et al., 2018). As we all know, the uncontrollable and common risk factors of dementia include aging, a first-degree family history of dementia, carrying *APOE* ε4 allele, and being a female, especially after the age of 80 years; among these, the strongest risk factors are advanced age and *APOE* ε4 allele carrier (Scheltens et al., 2021). However, there were no significant differences of *APOE* ε4 allele and aging between patients with SCD and those elderly controls in this study. A previous study found that neither the family history of dementia nor *APOE* ε4 status was associated with SCD (Nicholas et al., 2017). The above-mentioned evidence suggested that SCD was highly heterogeneous, and the classical risk factors for AD and SCD might be mismatched (Wen et al., 2021). Therefore, it is not enough to use AD-related risk factors alone to evaluate and predict SCD.

One of the key points in our study is the measurement of CBF via ASL. ASL is an MRI perfusion technique that enables quantification of the CBF of cerebral regions without the need for contrast injection. Compared with the Aβ-PET or tau-PET, ASL is more widely used in clinical practice and research, and with ^{18F}FDG PET/CT, ASL is less expensive without ionizing radiation exposure (Dolui et al., 2020). Recently, ASL has been performed for patients with cognitive impairment, which is believed to closely match between components,

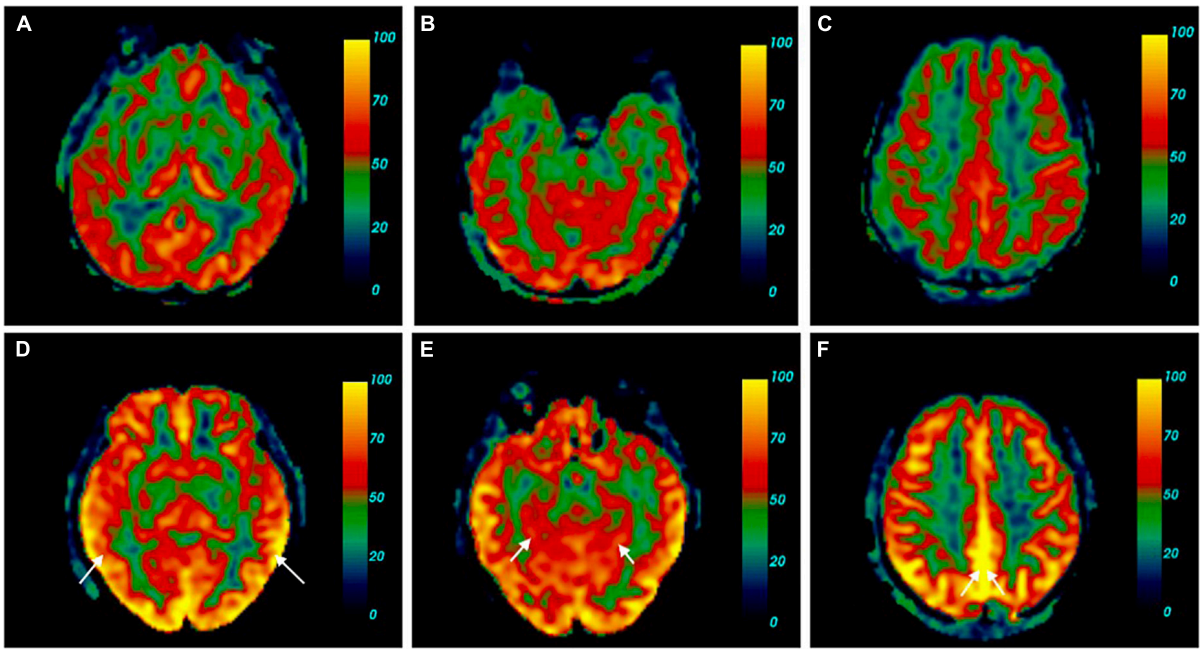

FIGURE 2
Cerebral perfusion map contrast of SCD and HC. **(A–C)** Were cerebral blood flow maps from one of the HC. **(D–F)** Belong to a participant with SCD [female, 60 years old, complaint of memory decline for 2 years, sister has a history of dementia, mini-mental state examination (MMSE) 30, the Montreal Cognitive Assessment (MoCA) 29, SCD-Q9 6, and *Apolipoprotein E (ApoE)* ε3/ε4]. Brain pseudo-continuous arterial spin labeling (pCASL) revealed the patient with SCD had increased cerebral perfusion, especially in the bilateral middle temporal gyrus **(A)**, the absolute CBF in the right bilateral middle temporal gyrus of the HC was 42.20 ml/100 g/min, the left was 37.49 ml/100 g/min. **(D)** The absolute CBF in the right bilateral middle temporal gyrus of the SCD was 67.69 ml/100 g/min, the left was 74.47 ml/100 g/min, parahippocampal gyrus **(B)**, the absolute CBF in the right parahippocampal gyrus of the HC was 27.59 ml/100 g/min, the left was 35.27 ml/100 g/min. **(E)** The absolute CBF in the right parahippocampal gyrus of the SCD was 50.99 ml/100 g/min, the left was 53.73 ml/100 g/min, precuneus **(C)**, the absolute CBF in the right precuneus of the HC was 39.44 ml/100 g/min, the left was 43.15 ml/100 g/min. **(F)** The absolute CBF in the right precuneus of the SCD was 71.42 ml/100 g/min, the left was 77.33 ml/100 g/min.

TABLE 3 Univariate logistic regression analyses of risk factors in patients with SCD.

Variables	B	SE	Wald	OR	95% CI	*p*-value
Family history of dementia	1.415	0.608	5.410	4.118	1.249–3.570	**0.020**
Hippocampus_L	0.074	0.034	4.736	1.076	1.007–1.150	**0.030**
Hippocampus_R	0.060	0.033	3.277	1.061	0.995–1.132	0.070
Posterior cingulate_L	0.035	0.019	3.226	1.035	0.997–1.075	0.072
Posterior cingulate_R	0.035	0.021	2.671	1.035	0.993–1.079	0.102
Parahippocampal gyrus_L	0.124	0.046	7.351	1.132	1.035–1.238	**0.007**
Parahippocampal gyrus_R	0.085	0.038	5.072	1.089	1.011–1.173	**0.024**
precuneus_L	0.054	0.025	4.441	1.055	1.004–1.109	**0.035**
precuneus_R	0.056	0.026	4.655	1.058	1.005–1.114	**0.031**
Middle temporal gyrus_L	0.060	0.027	4.771	1.061	1.006–1.120	**0.029**
Middle temporal gyrus_R	0.051	0.030	2.813	1.052	0.991–1.117	0.093

SE, standard error; OR, odds ratio; CI, confidence interval. The numbers in bold are statistically significant (*p*-value 0.05).

TABLE 4 Multivariate logistic regression analyses of risk factors in patients with SCD.

Factors	B	SE	Wald	OR	95% CI	*p*-value
Family history of dementia	1.455	0.696	4.375	4.284	1.096–16.747	**0.036**
Hippocampus_L	−0.105	0.084	1.551	0.901	1.006–1.840	0.213
Parahippocampal gyrus_L	0.308	0.154	4.002	1.361	1.006–1.840	**0.045**
Parahippocampal gyrus_R	0.006	0.103	0.003	1.006	0.822–1.230	0.956
precuneus_R	−0.018	0.068	0.074	0.982	0.860–1.121	0.786
Middle temporal gyrus_L	−0.040	0.069	0.345	0.961	0.840–1.099	0.557

SE, standard error; OR, odds ratio; CI, confidence interval. The numbers in bold are statistically significant (*p*-value 0.05).

regional and quantitative hypoperfusion and hypometabolism by ^{18F}FDG PET (Ho, 2018; Riederer et al., 2018). In 2015, the ISMRM Perfusion Study Group and the European ASL in Dementia Consortium released consensus guidelines that recommended the standardized implementation of 3D pseudo-continuous ASL (pCASL) with background suppression (Alsop et al., 2015). In a recent head-to-head comparison, the multiplanar and multi-delay pCASL on a GE Signa PET/MR have similar diagnostic accuracy in dementia to the ^{18F}FDG PET (Ceccarini et al., 2020). The evidence suggests significant diagnostic and application value of pCASL in the cognitive impairment disorders.

However, to the best of our knowledge, only a few pCASL studies of individuals with SCD are available, and the findings are inconsistent. Hays et al. (2018) demonstrated that patients with SCD displayed higher CBF in the posterior cingulate cortex, middle temporal gyrus, hippocampus, fusiform gyrus, and inferior frontal gyrus. Another study that investigated regional CBF in 162 Alzheimer's Disease Neuroimaging Initiative participants had shown that patients with SCD had increased hippocampal and inferior parietal CBF relative to HC participants (Thomas et al., 2021). The hyperperfusion within the classical cognitive areas may reflect early neurovascular dysregulation, whereby higher CBF is needed to maintain tissue metabolism and cognitive functioning and is also reflective of early cognitive inefficiencies that distinguish SCD from healthy elderly people (Østergaard et al., 2013). Our study revealed that increased CBF in the left parahippocampus was independent risk factor associated with SCD, which was rarely described before in SCD. Choo et al. (2019) have found that subjective memory complaints were associated with Aβ depositions, especially in the left parahippocampus (Choo et al., 2019). There is evidence suggesting that parahippocampus volume reduction and thinning might reflect the initial sign of olfactory impairment and lead to dysfunction in the connection of olfactory memory to the neocortex (Kubota et al., 2020). These findings indicate that the left parahippocampal gyrus may be one of the earliest involved areas of cognitive decline. However, a prospective cohort study displayed that patients with SCD showed a poor level of CBF in the right middle frontal gyrus compared with the HC subjects (Zhang et al., 2021). Participants with SCD plus demonstrated a significant decline in CBF values, mainly in the hippocampal head and posterior cingulate cortex (Yang et al., 2021). Moreover, the study from the Amsterdam Dementia Cohort found that reduced CBF was not associated with worse performance in patients with SCD (Leeuwis et al., 2017). We speculate these controversial results may be due to the use of different cohorts or inclusion criteria (SCD or SCD plus) and image processing methodologies.

Our study has several limitations. This was a single-center study, and included a relatively limited number of individuals. Thus, the findings may not be applicable to other settings due to the inherent selection bias.

Conclusion

This study found the family history of dementia and the hyperperfusion in the left parahippocampal gyrus were independently associated with SCD patients, which combined the risk factors of AD and evidence of vascular dysregulation for earlier identifying the SCD and interfering in this optimal period. Prospective multicenter studies are needed to evaluate the effectiveness of this finding and develop a reliable predictive model for SCD.

Data availability statement

The original contributions presented in this study are included in the article/supplementary material, further inquiries can be directed to the corresponding author.

Author contributions

WyL and JJ designed the study, analyzed the data, and drafted the manuscript. XZ, YZ, MS, ZJ, and WL edited and reviewed the manuscript. JX designed the study, revised the manuscript, and provided funding supports. All authors contributed to the article and approved the submitted version.

Funding

This study was supported by the National Key Research and Development Program of China (2021YFC2500103 and 2019YFC0120902), the National Natural Science Foundation of China (82071187, 81870821, and 81471215), the Beijing Youth Talent Team Support Program (2018000021223TD08), and the Beijing Natural Science Foundation Grant (L182055).

Acknowledgments

We gratefully thank Zeshan Yao for the imaging consultation.

Conflict of interest

The authors declare that the research was conducted in the absence of any commercial or financial relationships that could be construed as a potential conflict of interest.

Publisher's note

All claims expressed in this article are solely those of the authors and do not necessarily represent those of their affiliated organizations, or those of the publisher, the editors and the reviewers. Any product that may be evaluated in this article, or claim that may be made by its manufacturer, is not guaranteed or endorsed by the publisher.

References

Alsop, D. C., Detre, J. A., Golay, X., Günther, M., Hendrikse, J., Hernandez-Garcia, L., et al. (2015). Recommended implementation of arterial spin-labeled perfusion MRI for clinical applications: a consensus of the ISMRM perfusion study group and the European consortium for ASL in dementia. *Magn. Reson. Med.* 73, 102–116. doi: 10.1002/mrm.25197

Ceccarini, J., Bourgeois, S., Van Weehaeghe, D., Goffin, K., Vandenberghe, R., Vandenbulcke, M., et al. (2020). Direct prospective comparison of 18F-FDG PET and arterial spin labelling MR using simultaneous PET/MR in patients referred for diagnosis of dementia. *Eur. J. Nucl. Med. Mol. Imaging* 47, 2142–2154. doi: 10.1007/s00259-020-04694-1

Choo, I. H., Chong, A., Chung, J. Y., and Kim, H. (2019). Association of subjective memory complaints with the left parahippocampal amyloid burden in mild cognitive impairment. *J. Alzheimers Dis.* 72, 1261–1268. doi: 10.3233/JAD-190816

Dolui, S., Li, Z., Nasrallah, I. M., Detre, J. A., and Wolk, D. A. (2020). Arterial spin labeling versus 18F-FDG-PET to identify mild cognitive impairment. *Neuroimage Clin.* 25:102146. doi: 10.1016/j.nicl.2019.102146

Dounavi, M. E., Low, A., McKiernan, E. F., Mak, E., Muniz-Terrera, G., Ritchie, K., et al. (2021). Evidence of cerebral hemodynamic dysregulation in middle-aged APOE ε4 carriers: the PREVENT-Dementia study. *J. Cereb. Blood Flow Metab.* 41, 2844–2855. doi: 10.1177/0271678X211020863

Duan, W., Sehrawat, P., Balachandrasekaran, A., Bhumkar, A. B., Boraste, P. B., Becker, J. T., et al. (2020). Cerebral blood flow is associated with diagnostic class and cognitive decline in Alzheimer's disease. *J. Alzheimers Dis.* 76, 1103–1120. doi: 10.3233/JAD-200034

Fisher, R. A., Miners, J. S., and Love, S. (2022). Pathological changes within the cerebral vasculature in Alzheimer's disease: New perspectives. *Brain Pathol.* e13061. doi: 10.1111/bpa.13061 [Epub ahead of print].

Gifford, K. A., Liu, D., Romano, R. III, Jones, R. N., and Jefferson, A. L. (2015). Development of a subjective cognitive decline questionnaire using item response theory: a pilot study. *Alzheimers Dement. (Amst).* 1, 429–439. doi: 10.1016/j.dadm.2015.09.004

Hao, L., Wang, X., Zhang, L., Xing, Y., Guo, Q., Hu, X., et al. (2017). Prevalence, risk factors, and complaints screening tool exploration of subjective cognitive decline in a large cohort of the Chinese population. *J. Alzheimers Dis.* 60, 371–388. doi: 10.3233/JAD-170347

Haussmann, R., Ganske, S., Gruschwitz, A., Werner, A., Osterrath, A., Lange, J., et al. (2018). Family history of Alzheimer's disease and subjective memory performance. *Am. J. Alzheimers Dis. Other Dement.* 33, 458–462. doi: 10.1177/1533317518775033

Hays, C. C., Zlatar, Z. Z., and Wierenga, C. E. (2016). The utility of cerebral blood flow as a biomarker of preclinical Alzheimer's disease. *Cell Mol. Neurobiol.* 36, 167–179. doi: 10.1007/s10571-015-0261-z

Hays, C. C., Zlatar, Z. Z., Campbell, L., Meloy, M. J., and Wierenga, C. E. (2018). Subjective cognitive decline modifies the relationship between cerebral blood flow and memory function in cognitively normal older adults. *J. Int. Neuropsychol. Soc.* 24, 213–223. doi: 10.1017/S135561771700087X

Ho, M. L. (2018). Arterial spin labeling: clinical applications. *J. Neuroradiol.* 45, 276–289. doi: 10.1016/j.neurad.2018.06.003

Iturria-Medina, Y., Sotero, R. C., Toussaint, P. J., Mateos-Pérez, J. M., Evans, A. C., and Alzheimer's Disease Neuroimaging Initiative (2016). Early role of vascular dysregulation on late-onset Alzheimer's disease based on multifactorial data-driven analysis. *Nat. Commun.* 7:11934. doi: 10.1038/ncomms11934

Jack, C. R. Jr., Bennett, D. A., Blennow, K., Carrillo, M. C., Dunn, B., Haeberlein, S. B., et al. (2018). NIA-AA research framework: toward a biological definition of Alzheimer's disease. *Alzheimers Dement.* 14, 535–562. doi: 10.1016/j.jalz.2018.02.018

Jessen, F., Amariglio, R. E., Buckley, R. F., van der Flier, W. M., Han, Y., Molinuevo, J. L., et al. (2020). The characterisation of subjective cognitive decline. *Lancet Neurol.* 19, 271–278. doi: 10.1016/S1474-4422(19)30368-0

Jessen, F., Amariglio, R. E., van Boxtel, M., Breteler, M., Ceccaldi, M., Chételat, G., et al. (2014). A conceptual framework for research on subjective cognitive decline in preclinical Alzheimer's disease. *Alzheimers Dement.* 10, 844–852. doi: 10.1016/j.jalz.2014.01.001

Joe, E., and Ringman, J. M. (2019). Cognitive symptoms of Alzheimer's disease: clinical management and prevention. *BMJ* 367:l6217. doi: 10.1136/bmj.l6217

Kubota, S., Masaoka, Y., Sugiyama, H., Yoshida, M., Yoshikawa, A., Koiwa, N., et al. (2020). Hippocampus and Parahippocampus volume reduction associated with impaired olfactory abilities in subjects without evidence of cognitive decline. *Front. Hum. Neurosci.* 14:556519. doi: 10.3389/fnhum.2020.556519

Leeuwis, A. E., Benedictus, M. R., Kuijer, J., Binnewijzend, M., Hooghiemstra, A. M., Verfaillie, S., et al. (2017). Lower cerebral blood flow is associated with impairment in multiple cognitive domains in Alzheimer's disease. *Alzheimers Dement.* 13, 531–540. doi: 10.1016/j.jalz.2016.08.013

Livingston, G., Huntley, J., Sommerlad, A., Ames, D., Ballard, C., Banerjee, S., et al. (2020). Dementia prevention, intervention, and care: 2020 report of the Lancet Commission. *Lancet* 396, 413–446. doi: 10.1016/S0140-6736(20)30367-6

McDade, E., Wang, G., Gordon, B. A., Hassenstab, J., Benzinger, T., Buckles, V., et al. (2018). Longitudinal cognitive and biomarker changes in dominantly inherited Alzheimer disease. *Neurology* 91, e1295–e1306. doi: 10.1212/WNL.0000000000006277

Nicholas, C. R., Dowling, N. M., Racine, A. M., Clark, L. R., Berman, S. E., Koscik, R. L., et al. (2017). Longitudinal assessment of self- and informant-subjective cognitive complaints in a sample of healthy late-middle aged adults enriched with a family history of Alzheimer's disease. *J. Int. Neuropsychol. Soc.* 23, 617–626. doi: 10.1017/S1355617717000509

Østergaard, L., Aamand, R., Gutiérrez-Jiménez, E., Ho, Y. C., Blicher, J. U., Madsen, S. M., et al. (2013). The capillary dysfunction hypothesis of Alzheimer's disease. *Neurobiol. Aging* 34, 1018–1031. doi: 10.1016/j.neurobiolaging.2012.09.011

Patterson, C. (2018). *World Alzheimer Report 2018. The State of the art of Dementia Research: New Frontiers*. London: Alzheimer's Disease International.

Pike, K. E., Cavuoto, M. G., Li, L., Wright, B. J., and Kinsella, G. J. (2021). Subjective cognitive decline: Level of risk for future dementia and mild cognitive impairment, a meta-analysis of longitudinal studies. *Neuropsychol. Rev.* doi: 10.1007/s11065-021-09522-3 [Epub ahead of print].

Rabin, L. A., Smart, C. M., and Amariglio, R. E. (2017). Subjective cognitive decline in preclinical Alzheimer's disease. *Annu. Rev. Clin. Psychol.* 13, 369–396. doi: 10.1146/annurev-clinpsy-032816-045136

Riederer, I., Bohn, K. P., Preibisch, C., Wiedemann, E., Zimmer, C., Alexopoulos, P., et al. (2018). Alzheimer disease and mild cognitive impairment: integrated pulsed arterial spin-labeling MRI and 18F-FDG PET. *Radiology* 288, 198–206. doi: 10.1148/radiol.2018170575

Scheltens, P., De Strooper, B., Kivipelto, M., Holstege, H., Chételat, G., Teunissen, C. E., et al. (2021). Alzheimer's disease. *Lancet* 397, 1577–1590. doi: 10.1016/S0140-6736(20)32205-4

Selkoe, D. J. (2021). Treatments for Alzheimer's disease emerge. *Science* 373, 624–626. doi: 10.1126/science.abi6401

Slot, R., Sikkes, S., Berkhof, J., Brodaty, H., Buckley, R., Cavedo, E., et al. (2019). Subjective cognitive decline and rates of incident Alzheimer's disease and non-Alzheimer's disease dementia. *Alzheimers Dement.* 15, 465–476. doi: 10.1016/j.jalz.2018.10.003

Thomas, K. R., Osuna, J. R., Weigand, A. J., Edmonds, E. C., Clark, A. L., Holmqvist, S., et al. (2021). Regional hyperperfusion in older adults with objectively-defined subtle cognitive decline. *J. Cereb. Blood Flow Metab.* 41, 1001–1012. doi: 10.1177/0271678X20935171

Tzourio-Mazoyer, N., Landeau, B., Papathanassiou, D., Crivello, F., Etard, O., Delcroix, N., et al. (2002). Automated anatomical labeling of activations in SPM using a macroscopic anatomical parcellation of the MNI MRI single-subject brain. *NeuroImage* 15, 273–289. doi: 10.1006/nimg.2001.0978

van Harten, A. C., Mielke, M. M., Swenson-Dravis, D. M., Hagen, C. E., Edwards, K. K., Roberts, R. O., et al. (2018). Subjective cognitive decline and risk of MCI: the mayo clinic study of aging. *Neurology* 91, e300–e312. doi: 10.1212/WNL.0000000000005863

Wen, C., Hu, H., Ou, Y. N., Bi, Y. L., Ma, Y. H., Tan, L., et al. (2021). Risk factors for subjective cognitive decline: the CABLE study. *Transl. Psychiatry* 11:576. doi: 10.1038/s41398-021-01711-1

Wolfsgruber, S., Kleineidam, L., Weyrauch, A. S., Barkhoff, M., Röske, S., Peters, O., et al. (2022). relevance of subjective cognitive decline in older adults with a first-degree family history of Alzheimer's disease. *J. Alzheimers Dis.* 87, 545–555. doi: 10.3233/JAD-215416

Yang, Z., Rong, Y., Cao, Z., Wu, Y., Zhao, X., Xie, Q., et al. (2021). Microstructural and cerebral blood flow abnormalities in subjective cognitive decline plus: diffusional kurtosis imaging and three-dimensional arterial spin labeling study. *Front. Aging Neurosci.* 13:625843. doi: 10.3389/fnagi.2021.625843

Zhang, Q., Wang, Q., He, C., Fan, D., Zhu, Y., Zang, F., et al. (2021a). Altered regional cerebral blood flow and brain function across the Alzheimer's disease spectrum: a potential biomarker. *Front. Aging Neurosci.* 13:630382. doi: 10.3389/fnagi.2021.630382

Zhang, Y., Du, W., Yin, Y., Li, H., Liu, Z., Yang, Y., et al. (2021b). Impaired cerebral vascular and metabolic responses to parametric N-back tasks in subjective cognitive decline. *J. Cereb. Blood Flow Metab.* 41, 2743–2755. doi: 10.1177/0271678X211012153

frontiers | Frontiers in Neuroscience

TYPE Original Research
PUBLISHED 03 August 2022
DOI 10.3389/fnins.2022.961489

Check for updates

OPEN ACCESS

EDITED BY
Long-Biao Cui,
Fourth Military Medical University, China

REVIEWED BY
Huang Biao,
Guangdong Academy of Medical Sciences, China
Hong Yin,
Fourth People's Hospital of Xian, China

*CORRESPONDENCE
Guihua Jiang
jianggh@gd2h.org.cn

†These authors have contributed equally to this work and share first authorship

SPECIALTY SECTION
This article was submitted to Brain Imaging Methods, a section of the journal Frontiers in Neuroscience

RECEIVED 04 June 2022
ACCEPTED 07 July 2022
PUBLISHED 03 August 2022

CITATION
Fang J, Hua K, Chen F, Wan Z, Yin Y, Liu P, Wang T and Jiang G (2022) Altered cerebral blood flow patterns in ankylosing spondylitis: A three-dimensional pseudo-continuous arterial spin labeling study. *Front. Neurosci.* 16:961489. doi: 10.3389/fnins.2022.961489

COPYRIGHT
© 2022 Fang, Hua, Chen, Wan, Yin, Liu, Wang and Jiang. This is an open-access article distributed under the terms of the Creative Commons Attribution License (CC BY). The use, distribution or reproduction in other forums is permitted, provided the original author(s) and the copyright owner(s) are credited and that the original publication in this journal is cited, in accordance with accepted academic practice. No use, distribution or reproduction is permitted which does not comply with these terms.

Altered cerebral blood flow patterns in ankylosing spondylitis: A three-dimensional pseudo-continuous arterial spin labeling study

Jin Fang[1,2†], Kelei Hua[2†], Feng Chen[2†], Zhifang Wan[3], Yi Yin[2], Ping Liu[2], Tianyue Wang[2] and Guihua Jiang[1,2*]

[1]The Second School of Clinical Medicine, Southern Medical University, Guangzhou, China, [2]Department of Medical Imaging, Guangdong Second Provincial General Hospital, Guangzhou, China, [3]Department of Medical Image Center, Yuebei People's Hospital, Shaoguan, China

Objective: This study aimed to detect the cerebral blood flow (CBF) values changes in patients with ankylosing spondylitis (AS) and to evaluate the correlation between the CBF values and the specific clinical characteristics.

Materials and methods: Forty-eight patients with AS (43 male and 5 female) and 42 healthy controls (HCs) (38 male and 4 female) were recruited. Three-dimensional pseudo-continuous arterial spin labeling (3D-pCASL) was performed on a 3.0T magnetic resonance imaging (MRI). CBF values were obtained on the Philips post-processing workstation based on arterial spin labeling (ASL) data. The two-sample *t*-test was used to compare CBF differences. The correlation between CBF values and specific clinical characteristics of AS was evaluated.

Results: The AS group showed increased CBF values in the right precentral gyrus, the left inferior frontal gyrus, and the left temporal pole compared with HCs the AS group also showed decreased CBF values in the left precuneus and the left superior occipital gyrus compared with HCs. There were no significant correlations between the CBF values and the clinical characteristics including total back pain (TBP), erythrocyte sedimentation rate (ESR), and C-reactive protein (CRP).

Conclusion: Patients with AS displayed CBF changes compared with HCs using 3D-PCASL. These results may enhance our understanding of the neural substrates of AS and provide evidence of AS-related neurological impairment.

KEYWORDS

ankylosing spondylitis (AS), cerebral blood flow (CBF), arterial spin labeling (ASL), brain perfusion, magnetic resonance imaging (MRI)

Introduction

Ankylosing spondylitis (AS) is the major subtype of an interrelated group of rheumatic diseases named spondyloarthritis (SpA) that affects the axial skeleton and other joints and organs (Braun and Sieper, 2007). The global incidence of AS is about 0.9% and it mainly occurs in young patients with a male-to-female ratio of roughly 2 to 1 (Feldtkeller et al., 2003). The main clinical manifestation of AS is lower back pain in the early stage and motion limitation due to stiffness of the spine in the late stage. In terms of etiology, AS may be the result of the dual effects of environmental factors and genetic inheritance, the most important of which is HLA-B27 (Bowness, 2015), but the exact pathogenesis is still unknown.

Increasingly studies have found brain structural and functional changes in AS (Cidem et al., 2014; Hemington et al., 2016). From the brain structural perspective, the gray matter volume in the left putamen in patients with AS increased significantly and was positively correlated with the duration of AS and total back pain (TBP) scores, whereas it was not correlated with bath ankylosing spondylitis disease activity index (BASDAI) scores, C-reactive protein (CRP), or erythrocyte sedimentation rate (ESR) (Hua et al., 2020). From the brain functional perspective, A whole-network analysis revealed that AS patients exhibited less anticorrelated functional connectivity (FC) between the salience network and the default mode network, suggesting that cross-network FC is a metric of functional brain abnormality in AS (Hemington et al., 2016). Another FC and low-frequency fluctuations (ALFF) study found that the FCs of the left middle temporal gyrus and left precuneus of AS patients were closely related to BASDAI scores, ESR, and CRP. Additionally, the ALFF values of multiple brain areas were significantly changed in AS patients (Li et al., 2017).

Previous studies have also found a relationship between pain disorders and cerebral perfusion using the method of arterial spin labeling (ASL). In chronic knee pain, significant hypo-perfusion was found in the anterior medial prefrontal cortex, the angular gyrus, and the ventral anterior insular cortex, while hyper-perfusion was found in posterior default mode, thalamus, and sensory regions (Iwabuchi et al., 2020). Perfusion changes in different brain regions in patients with chronic pain provided valuable insights into the pathogenesis of AS since the brain perfusion difference can reflect the level of neural activity.

Therefore, in the present study, we used the three-dimensional pseudo-continuous ASL (3D-pCASL) method to detect the brain cerebral blood flow (CBF) differences between patients with AS and healthy controls (HCs). We also evaluated the correlation between CBF values and the clinical characteristics of AS. We hope our results will help to explore the underlying pathophysiology of AS.

Materials and methods

Subjects

A total of 52 patients with AS were recruited from the Guangdong Second Provincial General Hospital. 44 sex- and age-matched HCs were recruited through local advertisements. All participants were right-handed. The inclusion criteria for AS patients were as follows: (1) diagnosis of active AS according to the revised New York criteria; (2) non-steroidal anti-inflammatory drugs (NSAIDs) were only taken in stable doses for pain; (3) did not take biological agents during the study or at any other time; (4) no comorbidities, such as anxiety, presence of fibromyalgia, and depression and so on; and (5) the average TBP score of the week before the report was $\geq$3 (out of 10, 0 = no pain, 10 = the most severe pain imaginable). The inclusion criteria for HCs were as follows: (1) 16–55 years old; (2) no prior diagnosis of neurological disease or mental illness; (3) no malignant disease in the past 2 years; (4) no pregnancy or no breastfeeding; and (5) no other MRI contraindications.

Magnetic resonance imaging data acquisition

The image data were performed on a 3.0T MRI scanner (Ingenia; Philips, Best, Netherlands). In the resting-state perfusion imaging, the pCASL sequence was used for three-dimensional (3D) fast spin-echo acquisition and background suppression. The acquisition parameters were the following: echo time (TE) = 33 ms, repetition time (TR) = 4,155 ms, field of view (FOV) = 240 mm^2 × 240 mm^2, post-labeling delay (PLD) = 2,000 ms, in-plane voxel size = 3.75 × 3.75 × 6.00, in-plane matrix = 64 × 59, slice thickness/gap = 6.0/0 mm, 20 axial slices covering the whole brain, NSA = 1, and acquisition time = 4 min 51 s. In addition, a 3D T1-weighted brain volume imaging sequence covering the whole brain was used for structural data acquisition with: TR/TE = 7.8/3.6 ms, slice thickness/gap = 1.0/0 mm, flip angle = 8, NSA = 1, matrix = 256 × 256, FOV = 240 mm × 240 mm, 185 sagittal slices, and acquisition time = 5 min 56 s. Routine MRI images were evaluated by two experienced neuroradiologists to confirm that there were no brain structural abnormalities.

Cerebral blood flow processing

The pCASL images were analyzed on a Philips post-processing workstation. Quantification of CBF was calculated with the equation:

$$CBF = \frac{6000 \cdot \lambda \cdot (SI_{control} - SI_{label}) \cdot e^{PLD/T_{1,blood}}}{2 \cdot a \cdot T_{1,blood} \cdot SI_{PD} \cdot (1 - e^{-\tau/T_{1,blood}}} \quad (1)$$

where T1 of blood ($T_{1,\ blood}$) was assumed to be 1,650 ms at 3.0T, labeling efficiency (α) 0.85, partition coefficient (λ) 0.9, PLD 2,000 ms, and labeling duration (τ) 1,800 ms. SI_{PD} is the signal intensity of a proton density weighted image, $SI_{control}$ is the time-averaged signal intensities in the control label images, and SI_{label} is the time-averaged signal intensities in the label images. The CBF maps were normalized to the standard space of the Montreal Neurological Institute (MNI) using the Statistical Parametric Mapping (SPM12)[1] software: (1) Co-registration of the individual CBF brain map and the individual 3D T1-weighted structural image to obtain the individual T1' brain map. (2) In the standard space, the T1 brain maps of all individuals are nonlinearly normalized to T1 templates. (3) All the CBF images are normalized to MNI space by using the normalization parameters estimated in step 2, and resampled to the voxel size of 2 mm × 2 mm × 2 mm. (4) The CBF value of each voxel was transformed by *z* transformation: (single voxel CBF – mean CBF of the whole brain)/standard deviation of the whole brain CBF. (5) The CBF maps were smoothed using a Gaussian smoothing kernel with a full width at half maximum of 6 mm.

Statistical analysis

SPSS for Windows version 22.0 (SPSS Inc., Chicago, IL, United States) was used for statistical analysis. Independent-sample *t*-tests were used to compare age, TBP, ESR, and CRP. Gender differences between the two groups were compared using the $\mathcal{X}^2$ test. All tests were the two-tailed test, $p < 0.05$ was considered to be statistically significant.

In order to compare the CBF maps, the CBF maps between the AS group and the HCs group, a voxel-based comparison was made, using the *t*-test of the two samples, and the individual's age and sex were used as nuisance covariates. The voxel-level correction of family-wise error (FWE) for multiple comparisons was used in all group comparisons.

Save the clusters that show significant group differences on the CBF maps between the two groups as a binary mask to extract CBF values. We then calculated the partial correlation analysis between these CBF values and TBP, ESR, and CRP. We used gender and age as covariates. Multiple comparisons were performed using the Bonferroni correction.

Results

Demographic information

Demographic information and clinical characteristics of all recruited participants are shown in Table 1. Two HCs and Four patients with AS were excluded from further analyses because of image artifacts. Finally, 48 AS patients and 42 HCs were included. There were no significant differences in age and sex between the two groups.

Differences in cerebral blood flow values between two groups

Compared with the HCs group, the AS group showed increased CBF values (Table 2 and Figure 1) in the right precentral gyrus, the left inferior frontal gyrus, and the left Temporal Pole, and showed decreased CBF values in the left precuneus and the superior occipital gyrus (Table 2 and Figure 2).

Correlation analysis

Partial correlation analysis showed that there were no significant correlations between the right precentral gyrus, the left inferior frontal gyrus, the left Temporal Pole, the left precuneus, the superior occipital gyrus, and the TBP, ESR, and CRP (Table 3).

Discussion

In this study, we explored the CBF changes in AS patients and the relationship between the altered CBF and the clinical characteristics including TBP, ESR, and CRP. We found increased CBF values in the right precentral gyrus, the left inferior frontal gyrus and the left temporal pole in AS patients compared with the HCs. In addition, our findings showed that AS patients exhibited decreased CBF values in the left precuneus and the superior occipital gyrus compared with HCs. There were no significant correlations between CBF values changes in the right precentral gyrus, the left inferior frontal gyrus, the left

TABLE 1 Demographic and clinical data comparisons.

Characteristics	AS	HC	Statistics	*P*-value
Case	48	42	N/A	N/A
Gender (M/F)	43/5	38/4	$\chi^2 = 0.020^a$	0.888
Age (years old)	25.9 ± 6.4	28.1 ± 3.7	$T = 8.460^b$	0.052
TBP	6.0 ± 1.4	N/A	N/A	N/A
ESR	14.3 ± 7.7	N/A	N/A	N/A
CRP	11.7 ± 9.1	N/A	N/A	N/A

Means and standard deviations (SD) are listed in the table.
AS, ankylosing spondylitis; HC, healthy control; M, male; F, female; TBP, total back pain; ESR, erythrocyte sedimentation rate; CRP, C-reactive protein; N/A, not applicable.
[a] χ^2-test.
[b] Two-sample *t*-test.

1 http://www.fil.ion.ucl.Ac.uk/spm

TABLE 2 The areas of significantly different CBF values between the AS patients and the HCs (voxel-level correction of FWE).

Brain regions	Brodman area	Montreal neurological institute coordinates			Peak *t*-value	Cluster size (voxel numbers)
		X	Y	Z		
CBF values: AS > HCs						
R precentral gyrus	48	58	4	8	6.37	32
L inferior frontal gyrus	47	−32	38	−18	5.69	19
L inferior frontal gyrus	48	−46	12	4	5.61	9
L temporal pole	36	−28	14	−40	5.51	13
CBF values: AS < HCs						
L precuneus	23	−6	−62	18	5.81	59
R superior occipital gyrus	18	24	−94	32	5.44	8

CBF, cerebral blood flow; AS, ankylosing spondylitis; HC, healthy control; FWE, family-wise error; L (R), left (right) hemisphere.

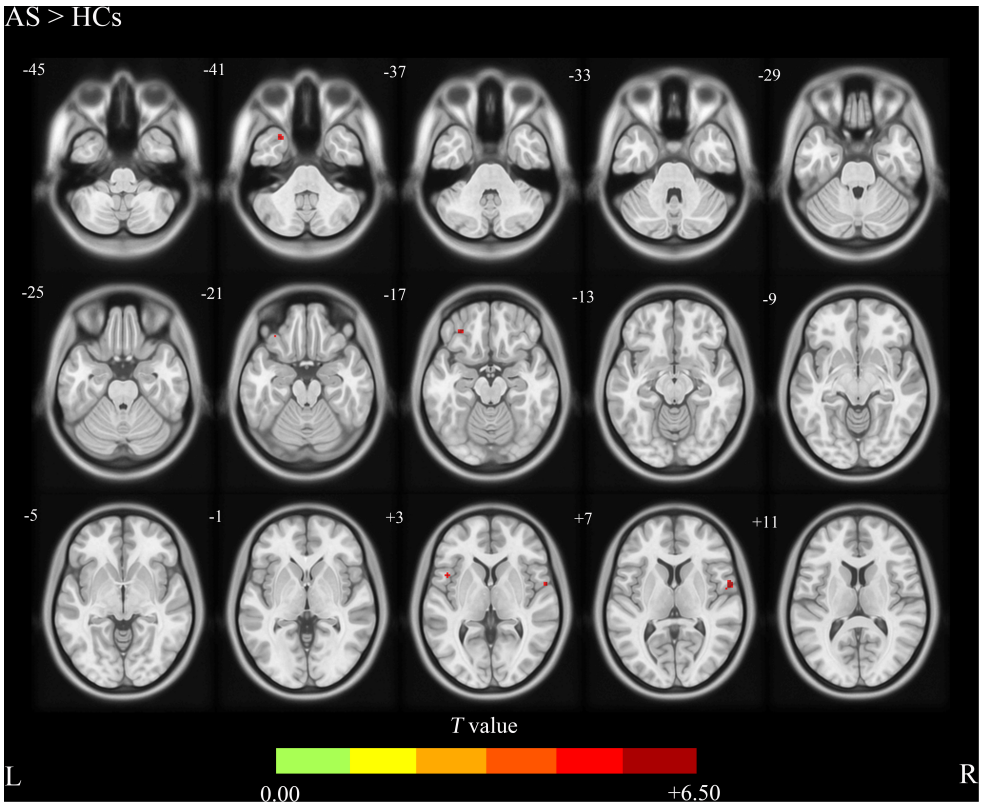

FIGURE 1
Ankylosing spondylitis patients showed significantly increased CBF clusters than HCs (voxel-level correction of FWE). AS, ankylosing spondylitis; HCs, healthy controls; CBF, cerebral blood flow; L (R), left (right) hemisphere; The color bar indicates the T value from the two-sample *t*-test.

Temporal Pole, the left precuneus, the superior occipital gyrus, and the TBP, ESR, and CRP.

To the best of our knowledge, this study is the first to investigate the CBF changes in AS using ASL. We found that AS patients exhibited significantly increased CBF values in the right precentral gyrus, the left inferior frontal gyrus, and the left temporal pole compared with the HCs. These altered CBF values in the brain regions described above may reflect the possible characteristics of neurological changes of AS. The precentral gyrus, also known as the primary motor cortex, is a very important structure involved in executing voluntary motor movements (Banker and Tadi, 2021). A previous functional MRI (fMRI) study found significantly lower ALFF in the right precentral gyrus (Li et al., 2017) and we found increased CBF in the same brain region. Lesions of the precentral gyrus can result in paralysis of the corresponding limbs or trunk

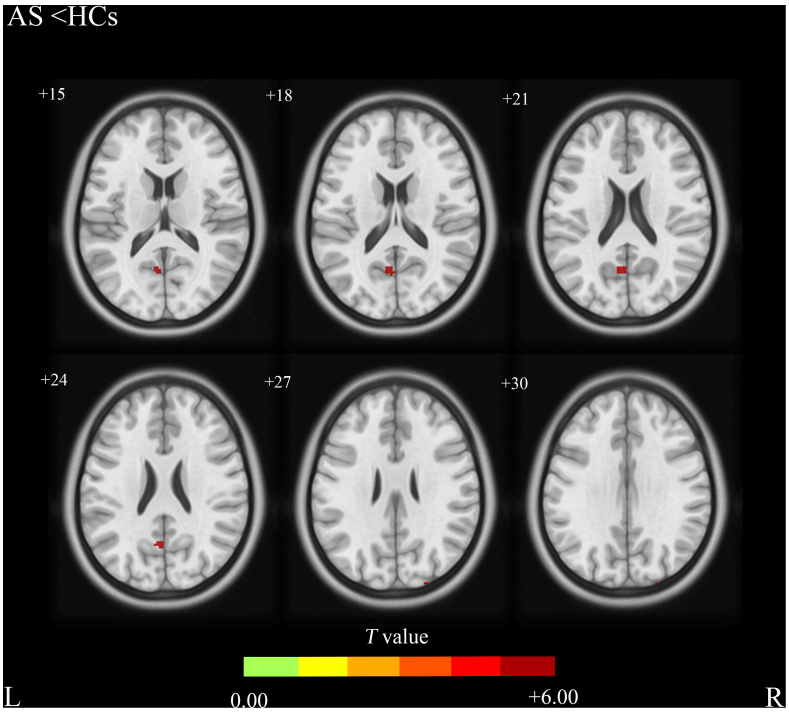

FIGURE 2
Ankylosing spondylitis patients showed significantly decreased CBF clusters than HCs (voxel-level correction of FWE). AS, ankylosing spondylitis; HCs, healthy controls; CBF, cerebral blood flow; L (R), left (right) hemisphere; The color bar indicates the T value from the two-sample *t*-test.

(Pikula et al., 2011). The increased CBF values in the precentral gyrus may be a compensatory mechanism for voluntary motor movement limitation in AS patients. This compensatory mechanism has also been reported in other motor restriction disorders (Sabatini et al., 2000; Mallol et al., 2007). The inferior frontal gyrus is limited above by the inferior frontal sulcus and below by the external border of the hemisphere in the front, and by the Sylvian fissure behind (Wagner et al., 2013). The inferior frontal gyrus is responsible for the motor component of speech in the dominant hemisphere, which involves related functions of the lips, tongue, larynx, and pharynx coordinated to produce phonation (Hartwigsen et al., 2019). Interestingly, we found the CBF values increased in the left frontal gyrus because it seems that there is no relationship between the function of this brain area and AS. There is growing interest regarding the role of the inferior frontal gyrus during a particular form of executive control referred to as response inhibition (Paulus et al., 2002; Picton et al., 2007; Prodoehl et al., 2008; Hampshire et al., 2010). As pain is one of the main symptoms of AS patients, the voluntary motor movement pattern may be influenced by the region of the inferior frontal lobe. The temporal pole is a complex anatomical region with several distinct areas in the anterior part of the temporal lobe, each part of which has specific cytoarchitectural organization and connectivity patterns, and it has been associated with many different functions (Dupont, 2002; Herlin et al., 2021). The increased CBF values in the left temporal pole of AS patients may be associated with the socio-emotional function of the temporal pole, because chronic pain, activity limitation, and even kyphosis in the late stage of the disease may cause some psychological problems (Martindale et al., 2006; Brionez et al., 2009; Yurdakul et al., 2017).

In this study, we also found significantly decreased CBF values in the left precuneus and the superior occipital gyrus

TABLE 3 Analysis of partial correlation between abnormal CBF values and clinical information.

		TBP	ESR	CRP
CBF values of the R precentral gyrus	*r*	0.161	−0.022	−0.016
	p	0.285	0.887	0.918
CBF values of the L inferior frontal gyrus	*r*	−0.034	0.201	0.281
	p	0.822	0.180	0.059
CBF values of the L inferior frontal gyrus	*r*	0.004	0.262	0.088
	p	0.981	0.079	0.559
CBF values of the L temporal pole	*r*	0.055	0.127	0.222
	p	0.717	0.399	0.138
CBF values of the L precuneus	*r*	−0.033	−0.223	−0.038
	p	0.825	0.137	0.800
CBF values of the R superior occipital gyrus	*r*	−0.259	0.121	−0.093
	p	0.082	0.422	0.537

CBF, cerebral blood flow; TBP, total back pain; ESR, erythrocyte sedimentation rate; CRP, C-reactive protein; L (R), left (right) hemisphere.

in AS patients compared with HCs. The precuneus is a brain region involved in a variety of complex functions and it is a functional core of the default-mode network (DMN) (Utevsky et al., 2014). Previous fMRI studies have proved that DMN is involved in the integration of autobiographical, self-monitoring, and social cognitive functions (Spreng et al., 2009). In addition, DMN may also participate in the central processing of fatigue or pain-related signals. Investigators have identified some brain alterations in DMN regions in migraine (Liu et al., 2015), fibromyalgia (Pujol et al., 2014), and knee osteoarthritis (Pujol et al., 2017). The decreased CBF values of the precuneus exhibited in our study may suggest the impairment of DMN which is common in chronic pain-related diseases and is consistent with the previous study (Amiri et al., 2021). The superior occipital gyrus is continuous along the superomedial margin of the hemisphere with the cuneus and is involved in many complex functions of the human body. The decreased CBF value in the superior occipital gyrus may reflect a neurological function decrease in this area, but the pathophysiology is still unclear and further studies are needed.

At last, we evaluated the correlation between the altered CBF values and clinical characteristics of AS including TBP, ESR, and CRP. It showed that there were no significant correlations between the CBF values and the TBP, ESR, and CRP. These results were in part consistent with previous studies (Li et al., 2017; Hua et al., 2020), indicating that those CBF value changes may represent a general basic brain functional transformation of AS.

There were several limitations in this study. First, in this cross-sectional study, we found the CBF values changed in several brain regions in AS patients, but the directionality of the relationship between AS and altered CBF values remains unclear, future longitudinal studies are needed to resolve this question. Second, because of the cross-sectional group data, we were unable to observe dynamic CBF values change over the developmental course of AS. Third, the sample of this study was small and the gender bias was large. Thus, the gender differences in brain CBF patterns may influence the results. Future studies should address these issues through longitudinal assessment of a large and gender-balanced sample of AS patients.

Conclusion

Our preliminary study explored CBF values change in AS patients compared with HCs using 3D-PCASL. Some of the increased and decreased CBF values in different brain regions are consistent with previous fMRI studies. These results may enhance our understanding of the neural substrates of AS and provide evidence of AS-related neurological impairment. Hence, further investigation of the pathophysiology of the regions with altered CBF values is warranted.

Data availability statement

The original contributions presented in this study are included in the article/supplementary material, further inquiries can be directed to the corresponding author/s.

Ethics statement

The studies involving human participants were reviewed and approved by Ethics Committee of Guangdong Second Provincial General Hospital. Written informed consent to participate in this study was provided by the participants' legal guardian/next of kin. Written informed consent was obtained from the individual(s), and minor(s)' legal guardian/next of kin, for the publication of any potentially identifiable images or data included in this article.

Author contributions

GJ designed the experiment. JF carried out the experiment and wrote the manuscript. JF, KH, and FC collected and sorted out the data. YY, ZW, PL, and TW helped with data management and processing. All authors contributed to the article and approved the submitted version.

Funding

This study was funded by grants from the National Natural Science Foundation of China (Grant Nos. U1903120, 81771807, and 81901729) and the Science and Technology Planning Project of Guangzhou (Grant No. 202002030234).

Conflict of interest

The authors declare that the research was conducted in the absence of any commercial or financial relationships that could be construed as a potential conflict of interest.

Publisher's note

All claims expressed in this article are solely those of the authors and do not necessarily represent those of their affiliated organizations, or those of the publisher, the editors and the reviewers. Any product that may be evaluated in this article, or claim that may be made by its manufacturer, is not guaranteed or endorsed by the publisher.

References

Amiri, P., Kazeminasab, S., Nejadghaderi, S. A., Mohammadinasab, R., Pourfathi, H., Araj-Khodaei, M., et al. (2021). Migraine: a review on its history, global epidemiology, risk factors, and comorbidities. *Front. Neurol.* 12:800605. doi: 10.3389/FNEUR.2021.800605

Banker, L., and Tadi, P. (2021). *Neuroanatomy, Precentral Gyrus. StatPearls*. Available online at: https://www.ncbi.nlm.nih.gov/books/NBK544218/ (accessed June 3, 2022).

Bowness, P. (2015). HLA-B27. *Annu. Rev. Immunol.* 33, 29–48. doi: 10.1146/ANNUREV-IMMUNOL-032414-112110

Braun, J., and Sieper, J. (2007). Ankylosing spondylitis. *Lancet (Lond. Engl.)* 369, 1379–1390. doi: 10.1016/S0140-6736(07)60635-7

Brionez, T. F., Assassi, S., Reveille, J. D., Learch, T. J., Diekman, L., Ward, M. M., et al. (2009). Psychological correlates of self-reported functional limitation in patients with Ankylosing spondylitis. *Arthritis Res. Ther.* 11:R182. doi: 10.1186/AR2874

Cidem, M., Sahin, Z., Aydin, T., and Aysal, F. (2014). Somatosensory evoked potential findings in ankylosing spondylitis. *Eurasian J. Med.* 46, 42–46. doi: 10.5152/EAJM.2013.100

Dupont, S. (2002). Investigating temporal pole function by functional imaging. *Epileptic Disord.* 4(Suppl. 1), S17–S22.

Feldtkeller, E., Khan, M. A., Van Der Heijde, D., Van Der Linden, S., and Braun, J. (2003). Age at disease onset and diagnosis delay in HLA-B27 negative vs. positive patients with ankylosing spondylitis. *Rheumatol. Int.* 23, 61–66. doi: 10.1007/S00296-002-0237-4

Hampshire, A., Chamberlain, S. R., Monti, M. M., Duncan, J., and Owen, A. M. (2010). The role of the right inferior frontal gyrus: inhibition and attentional control. *Neuroimage* 50:1313. doi: 10.1016/J.NEUROIMAGE.2009.12.109

Hartwigsen, G., Neef, N. E., Camilleri, J. A., Margulies, D. S., and Eickhoff, S. B. (2019). Functional segregation of the right inferior frontal gyrus: evidence from coactivation-based parcellation. *Cereb. Cortex* 29, 1532–1546. doi: 10.1093/CERCOR/BHY049

Hemington, K. S., Wu, Q., Kucyi, A., Inman, R. D., and Davis, K. D. (2016). Abnormal cross-network functional connectivity in chronic pain and its association with clinical symptoms. *Brain Struct. Funct.* 221, 4203–4219. doi: 10.1007/S00429-015-1161-1

Herlin, B., Navarro, V., and Dupont, S. (2021). The temporal pole: from anatomy to function—A literature appraisal. *J. Chem. Neuroanat.* 113:101925. doi: 10.1016/J.JCHEMNEU.2021.101925

Hua, K., Wang, P., Lan, Z., Li, M., Zhao, W., Wang, T., et al. (2020). Increased left putamen volume correlates with pain in Ankylosing spondylitis patients. *Front. Neurol.* 11:1616. doi: 10.3389/FNEUR.2020.607646/BIBTEX

Iwabuchi, S. J., Xing, Y., Cottam, W. J., Drabek, M. M., Tadjibaev, A., Fernandes, G. S., et al. (2020). Brain perfusion patterns are altered in chronic knee pain: a spatial covariance analysis of arterial spin labelling MRI. *Pain* 161, 1255–1263. doi: 10.1097/J.PAIN.0000000000001829

Li, C., Wei, X., Zou, Q., Zhang, Y., Yin, X., Zhao, J., et al. (2017). Cerebral functional deficits in patients with Ankylosing spondylitis- an fMRI study. *Brain Imaging Behav.* 11, 936–942. doi: 10.1007/S11682-016-9565-Y

Liu, J., Zhao, L., Lei, F., Zhang, Y., Yuan, K., Gong, Q., et al. (2015). Disrupted resting-state functional connectivity and its changing trend in migraine suffers. *Hum. Brain Mapp.* 36, 1892–1907. doi: 10.1002/HBM.22744

Mallol, R., Barrós-Loscertales, A., López, M., Belloch, V., Parcet, M. A., and Ávila, C. (2007). Compensatory cortical mechanisms in Parkinson's disease evidenced with fMRI during the performance of pre-learned sequential movements. *Brain Res.* 1147, 265–271. doi: 10.1016/J.BRAINRES.2007.02.046

Martindale, J., Smith, J., Sutton, C. J., Grennan, D., Goodacre, L., and Goodacre, J. A. (2006). Disease and psychological status in ankylosing spondylitis. *Rheumatology (Oxford)* 45, 1288–1293. doi: 10.1093/RHEUMATOLOGY/KEL115

Paulus, M. P., Hozack, N., Frank, L., and Brown, G. G. (2002). Error rate and outcome predictability affect neural activation in prefrontal cortex and anterior cingulate during decision-making. *Neuroimage* 15, 836–846. doi: 10.1006/nimg.2001.1031

Picton, T. W., Stuss, D. T., Alexander, M. P., Shallice, T., Binns, M. A., and Gillingham, S. (2007). Effects of focal frontal lesions on response inhibition. *Cereb. Cortex* 17, 826–838. doi: 10.1093/CERCOR/BHK031

Pikula, A., Stefanidou, M., Romero, J. R., and Kase, C. S. (2011). Pure motor upper limb weakness and infarction in the precentral gyrus: mechanisms of stroke. *J. Vasc. Interv. Neurol.* 4, 10–13.

Prodoehl, J., Yu, H., Little, D. M., Abraham, I., and Vaillancourt, D. E. (2008). Region of interest template for the human basal ganglia: comparing EPI and standardized space approaches. *Neuroimage* 39, 956–965. doi: 10.1016/J.NEUROIMAGE.2007.09.027

Pujol, J., Macià, D., Garcia-Fontanals, A., Blanco-Hinojo, L., López-Solà, M., Garcia-Blanco, S., et al. (2014). The contribution of sensory system functional connectivity reduction to clinical pain in fibromyalgia. *Pain* 155, 1492–1503. doi: 10.1016/J.PAIN.2014.04.028

Pujol, J., Martínez-Vilavella, G., Llorente-Onaindia, J., Harrison, B. J., López-Solà, M., López-Ruiz, M., et al. (2017). Brain imaging of pain sensitization in patients with knee osteoarthritis. *Pain* 158, 1831–1838. doi: 10.1097/J.PAIN.0000000000000985

Sabatini, U., Boulanouar, K., Fabre, N., Martin, F., Carel, C., Colonnese, C., et al. (2000). Cortical motor reorganization in akinetic patients with Parkinson's disease. A functional MRI study. *Brain* 123, 394–403. doi: 10.1093/BRAIN/123.2.394

Spreng, R. N., Mar, R. A., and Kim, A. S. N. (2009). The common neural basis of autobiographical memory, prospection, navigation, theory of mind, and the default mode: a quantitative meta-analysis. *J. Cogn. Neurosci.* 21, 489–510. doi: 10.1162/JOCN.2008.21029

Utevsky, A. V., Smith, D. V., and Huettel, S. A. (2014). Precuneus is a functional core of the default-mode network. *J. Neurosci.* 34, 932–940. doi: 10.1523/JNEUROSCI.4227-13.2014

Wagner, M., Jurcoane, A., and Hattingen, E. (2013). The U sign: tenth landmark to the central region on brain surface reformatted MR imaging. *AJNR Am. J. Neuroradiol.* 34, 323–326. doi: 10.3174/AJNR.A3205

Yurdakul, F., Garip, Y., Koçak, R. U., Almaz, E., Uçkun, A., and Bodur, H. (2017). FRI0439 Psychiatric disorders associated with ankylosing spondylitis. *Ann. Rheum. Dis.* 76, 652–653. doi: 10.1136/ANNRHEUMDIS-2017-EULAR.2629

frontiers | Frontiers in Neuroscience

TYPE Original Research
PUBLISHED 05 August 2022
DOI 10.3389/fnins.2022.974651

Check for updates

OPEN ACCESS

EDITED BY
Guolin Ma,
China-Japan Friendship Hospital, China

REVIEWED BY
Qingling Huang,
Nanjing Brain Hospital Affiliated to Nanjing Medical University, China
Guangbin Wang,
Shandong Provincial Hospital, China

*CORRESPONDENCE
Chunmei Li
bee9020@126.com
Min Chen
cjr.chenmin@vip.163.com

SPECIALTY SECTION
This article was submitted to Brain Imaging Methods, a section of the journal Frontiers in Neuroscience

RECEIVED 21 June 2022
ACCEPTED 18 July 2022
PUBLISHED 05 August 2022

CITATION
Wang X, Wang D, Li X, Wang W, Gao P, Lou B, Pfeuffer J, Zhang X, Zhu J, Li C and Chen M (2022) A diagnostic index based on pseudo-continuous arterial spin labeling and T1-mapping improves efficacy in discriminating Alzheimer's disease from normal cognition.
Front. Neurosci. 16:974651.
doi: 10.3389/fnins.2022.974651

COPYRIGHT
© 2022 Wang, Wang, Li, Wang, Gao, Lou, Pfeuffer, Zhang, Zhu, Li and Chen. This is an open-access article distributed under the terms of the Creative Commons Attribution License (CC BY). The use, distribution or reproduction in other forums is permitted, provided the original author(s) and the copyright owner(s) are credited and that the original publication in this journal is cited, in accordance with accepted academic practice. No use, distribution or reproduction is permitted which does not comply with these terms.

A diagnostic index based on pseudo-continuous arterial spin labeling and T1-mapping improves efficacy in discriminating Alzheimer's disease from normal cognition

Xiaonan Wang[1,2], Di Wang[1,2], Xinyang Li[1,2], Wenqi Wang[3], Ping Gao[4], Baohui Lou[1], Josef Pfeuffer[5], Xianchang Zhang[6], Jinxia Zhu[6], Chunmei Li[1,2]* and Min Chen[1,2]*

[1]Department of Radiology, National Center of Gerontology, Beijing Hospital, Institute of Geriatric Medicine, Chinese Academy of Medical Sciences, Beijing, China, [2]Graduate School of Peking Union Medical College, Chinese Academy of Medical Sciences, Beijing, China, [3]Department of Radiology, Children's Hospital, Zhejiang University School of Medicine, Hangzhou, China, [4]Department of Neurology, National Center of Gerontology, Beijing Hospital, Institute of Geriatric Medicine, Chinese Academy of Medical Sciences, Beijing, China, [5]MR Application Development, Siemens Healthcare GmbH, Erlangen, Germany, [6]MR Collaboration, Siemens Healthineers Ltd., Beijing, China

Background: Pseudo-continuous arterial spin labeling (pCASL) is widely used to quantify cerebral blood flow (CBF) abnormalities in patients with Alzheimer's disease (AD). T1-mapping techniques assess microstructural characteristics in various pathologic changes, but their application in AD remains in the exploratory stage. We hypothesized that combining quantitative CBF and T1 values would generate diagnostic results with higher accuracy than using either method alone in discriminating AD patients from cognitively normal control (NC) subjects.

Materials and methods: A total of 45 patients diagnosed with AD and 33 NC subjects were enrolled, and cognitive assessment was performed for each participant according to the Chinese version of the Mini-Mental State Examination (MMSE). T1-weighted magnetization-prepared 2 rapid acquisition gradient echo (MP2RAGE) and pCASL sequence were scanned on a 3T MR scanner. A brain morphometric analysis was integrated into prototype sequence, providing tissue classification and morphometric segmentation results. Quantitative CBF and T1 values of each brain region were automatically generated inline after data acquisition. Independent samples *t*-test was used to compare regional CBF and T1 values controlled by false discovery rate correction (corrected $p < 0.01$). The model with combined CBF and T1 values was compared with the individual index by performing receiver operating characteristic curves analysis. The associations between the MMSE score and CBF and T1 values of the brain were investigated using partial correlations.

Results: Cerebral blood flow of the right caudate nucleus (RCc) and left hippocampus (LHc) was significantly lower in the AD group compared with the NC group, while the T1 values of the right caudate nucleus (RCt) and left hippocampus (LHt) increased in the AD group. Prediction accuracies of 73.1, 77.2, 75.9, and 81.3% were achieved for each of the above parameters, respectively. In distinguishing patients from controls using the corresponding optimized cut-off values, most combinations of parameters were elevated (area under curve = 0.775–0.894). The highest area under curve value was 0.944, by combining RCc, LHc, RCt, and LHt.

Conclusion: In this preliminary study, the combined model based on pCASL and T1-mapping improved the diagnostic performance of discriminating AD and NC groups. T1-mapping may become a competitive technique for quantitatively measuring pathologic changes in the brain.

KEYWORDS

Alzheimer's disease, cerebral blood flow, T1-mapping, magnetic resonance imaging, arterial spin labeling

Introduction

Alzheimer's disease (AD) is a neurodegenerative disease with insidious onset and progressive development. Its main clinical manifestations include memory loss (Jagust et al., 2001), cognitive impairment, and behavioral abnormalities. With the rapidly aging population, degenerative diseases of the central nervous system have become the third most common diseases affecting human survival after cardiovascular and cerebrovascular diseases and cancer (Erkkinen et al., 2018). The number of people with AD-based dementia worldwide is expected to reach 113.4 million by 2050, and the increasing incidence has created a challenging scenario for global public health care systems (Knopman et al., 2021). Despite decades of research, the exact pathogenesis of AD remains to be elucidated. In addition to classical hypotheses, including β-amyloid peptide aggregation leading to neuroplaque formation (Arnold et al., 1991; Montine et al., 2012) and abnormal phosphorylation of tau proteins causing neurogenic fiber tangles (Gallardo and Holtzman, 2019; Dujardin et al., 2020) and early synaptic loss (Rice et al., 2019), multiple risk factors for cerebrovascular disease are closely associated with the development of AD (Cortes-Canteli and Iadecola, 2020). Therefore, discovering non-invasive, objective, quantitative, and reproducible imaging methods that indirectly reflect the pathologic changes of AD pathogenesis will clarify the pathologic process of AD and detect disease progression.

Perfusion abnormality is an integral part of assessing the pathophysiology of AD. Single-photon emission computed tomography (SPECT) and positron emission tomography-computed tomography (PETCT) indirectly reflect blood perfusion through brain glucose metabolism. However, nuclear medicine methods are invasive and involve intravenous radioactive tracer administration, limiting clinical applications. With the development of magnetic resonance imaging (MRI)-based neuroradiology, arterial spin labeling (ASL) is increasingly used as a non-invasive, inexpensive, easily accessible, and reproducible alternative for perfusion measurement (Verfaillie et al., 2015). ASL can quantitatively measure relative cerebral blood flow (CBF) in different brain regions using magnetically labeled water protons in arterial blood as a contrast agent instead of injecting exogenous contrast agents (Chandra et al., 2019). The accuracy of cerebral perfusion maps in AD patients is similar to that of SPECT, whereas ASL is more sensitive to areas with reduced cerebral perfusion (Kaneta et al., 2017). Therefore, this technique may be an alternative to invasive imaging and has the potential to serve as a biomarker in the early diagnosis of preclinical dementia (Xekardaki et al., 2015). Three kinds of ASL techniques are commonly used according to the labeling strategy: continuous ASL, pulsed ASL, and pseudo-continuous ASL (pCASL). Among them, pCASL 3D imaging can be acquired in multiple segments in a short period of time, overcoming magnetic sensitivity and distortion artifacts, and provides good image quality without the need for high-level hardware support (Soman et al., 2021). In this study, we used 3D pCASL to obtain CBF in different brain regions.

Abbreviations: AD, Alzheimer's disease; ASL, arterial spin labeling; AUC, area under the curve; CBF, cerebral blood flow; FDR, false discovery rate; LHc, CBF in the left hippocampus; LHt, T1 values in the left hippocampus; MMSE, Mini-Mental State Examination; MP2RAGE, magnetization-prepared 2 rapid acquisition gradient echo images; MRI, magnetic resonance imaging; pCASL, pseudo-continuous ASL; RCc, CBF in the right caudate nucleus; RCt, T1 values in the right caudate nucleus.

Quantitative MRI parameters can reveal not only macroscopic changes in brain tissue but also microstructural changes in the biochemical environment. Among them, longitudinal relaxation time (T1) is the characteristic time governing the relaxation of longitudinal magnetization toward thermal equilibrium after excitation by an RF pulse, and different biological tissues have specific T1 values due to differences in their cellular and interstitial components. Previous studies have shown that an altered T1 value is associated with increased β-amyloid load in the brain of AD patients (House et al., 2008). Experiments based on animal models of AD have also confirmed such tissue alterations (Forster et al., 2013). Previous study found that T1 in the hippocampus, thalamus and right caudate nucleus increased significantly with disease progression in AD patients bilaterally (Su et al., 2016). Therefore, we introduced the T1 values to enhance diagnostic confidence.

We hypothesized that combining CBF and T1 values would yield diagnostic results with greater accuracy than using separate methods in differentiating patients with AD from subjects with normal cognition. To test this hypothesis, we aimed to assess the efficacy of CBF, T1 values, and their combination in discriminating between AD and normal control (NC) cohorts.

Materials and methods

Participants

From September 2020 to October 2021, we prospectively recruited patients with AD and cognitively NC subjects from Beijing Hospital. This study was approved by the Ethics Committee of Beijing Hospital (batch no. 2018BJYYEC-147-02 and 2021BJYYEC-123-01), and all participants signed an informed consent form before the examination.

Criteria for inclusion in the AD group were as follows: (1) The neurologists or psychiatrists diagnosed the patients according to the National Institute of Neurological and Communicative Disorders and Stroke/Alzheimer's Disease and Related Disorders Association(NINCDS-ADRDA) criteria (McKhann et al., 1984). (2) MRI was completed within 48 h after the clinical diagnosis of AD. (3) Right handedness.

Normal control subjects were recruited from 20 community social centers in four districts and were included in this study based on the following criteria: (1) age and gender matching that of the AD group; (2) Chinese version of the MMSE score $\geq$ 27; and (3) Right handedness.

Exclusion criteria for the AD were as follows: (1) diagnosis of central nervous system tumor (n = 1), stroke (n = 2), and hydrocephalus (n = 1) on routine head MRI examination; (2) dementia of vascular origin with a score of $\geq$4 on the Harkinski Ischemic Index Scale (n = 2); (3) thyroid dysfunction, depression, drug addiction, substance abuse, or other diseases that cause abnormal cognitive function; (4) other reasons that prevented head MRI examination or cooperation with completion of the neuropsychologic scale, Claustrophobia diseases (n = 1); and (5) motion and metal artifacts (n = 3). Finally, 45 patients with AD and 33 NC individuals were eligible for this study.

MRI protocol

Clinical information collection and neuropsychologic scale scoring were completed at the Department of Neurology, Beijing Hospital. MRI examinations were performed within 60 min of clinical information collection.

All MR examinations were performed on a 3T MR system (MAGNETOM Prisma, Siemens Healthcare, Erlangen, Germany) with a 64-channel head coil. pCASL was performed using a prototype 3D gradient and spin-echo (GRASE) sequence with the following parameters: TR/TE = 4350/20.9 ms, FOV = 220 mm × 220 mm, matrix = 64 × 64 (interpolated to 128 × 128), bolus duration = 1,800 ms, 16 label timesTI = 800–3800 ms (Δ = 200 ms), and acquisition time = 4 min 55 s including a M0 calibration volume. Regional CBF maps were automatically generated inline after data acquisition (Buxton et al., 1998; Alsop et al., 2015). For quantification, the following parameters were used: blood/tissue water partition coefficient lambda = 0.9 mL/g, labeling efficiency alpha = 60% (four background suppression pulses accounted for), T1_blood = 1650 ms and T1_tissue = 1330 ms. T1 mapping was obtained using a prototype T1 magnetization prepared 2 rapid acquisition gradient echoes (MP2RAGE) sequence with the following parameters: TR/TE = 5000/3.59 ms, TI = 700/2500 ms, FA = 4°/5°, FOV = 230 mm × 216 mm, matrix = 320 × 240, and acquisition time = 3 min. MP2RAGE sequence produced simultaneously three contrast images (INV1, INV2, UNI) and a quantitative T1-mapping (Marques et al., 2010).

TABLE 1 Demographic and clinical data.

	AD group	NC group	p
Number	45	33	–
Age (years)	73.51 ± 7.51	70.51 ± 7.88	0.092
Gender (female %)	64.44	63.64	0.941
BMI	22.59 ± 2.70	23.49 ± 2.57	0.142
Educational years	10.82 ± 3.41	10.70 ± 3.50	0.874
MMSE	18.38 ± 3.07	27.12 ± 1.34	<0.001

AD, Alzheimer's disease; BMI, body mass index; MMSE, Chinese versions Mini-mental State Examination; NC, normal control.

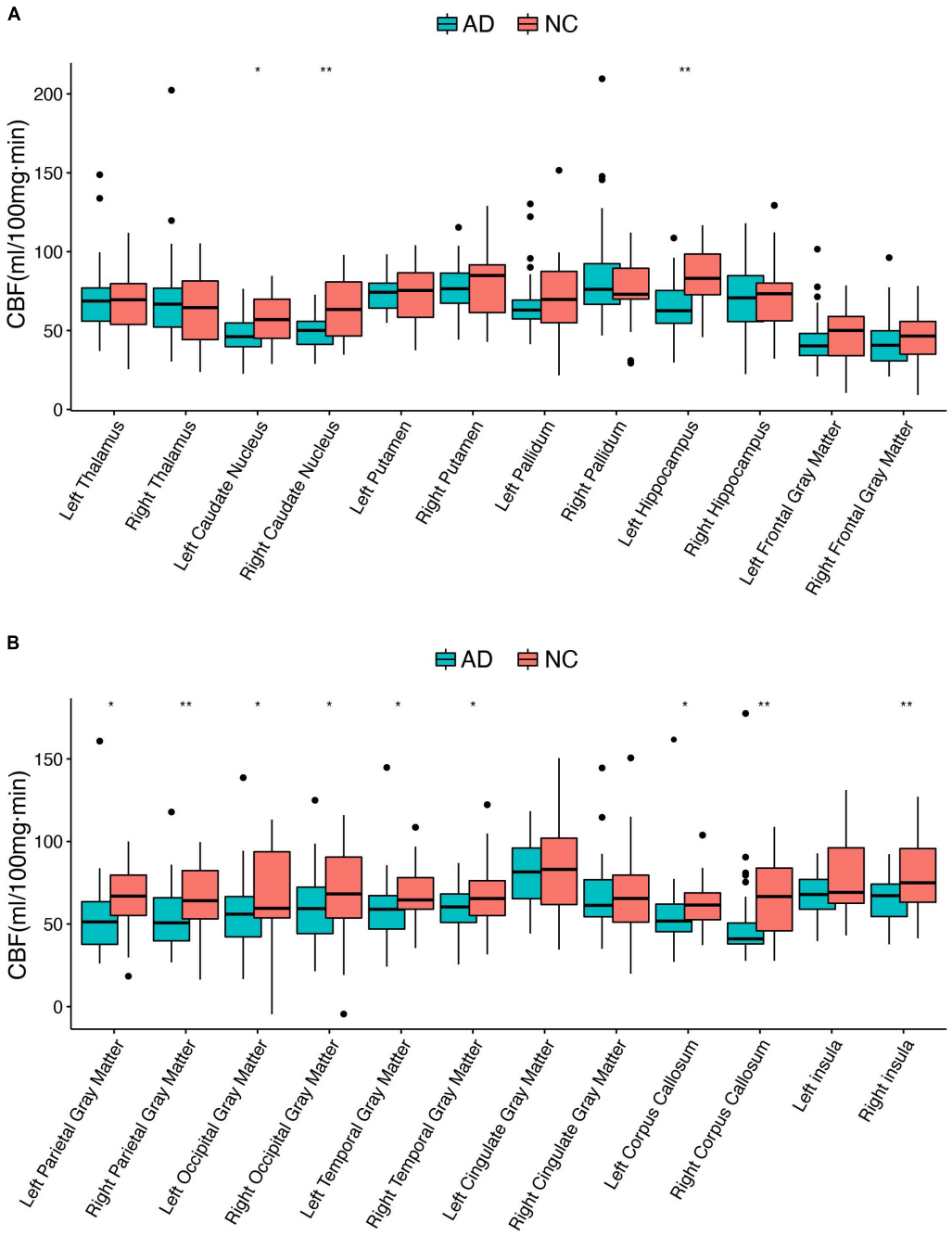

FIGURE 1
Differential cerebral blood flow between AD and NC individuals in 24 brain regions. AD, Alzheimer's disease; CBF, cerebral blood flow; NC, normal controls; *corrected $p < 0.05$; **corrected $p < 0.01$. **(A,B)** Boxplots of the CBF in different brain regions.

Image processing

A brain morphometry analysis was integrated into the prototype MP2RAGE sequence, providing tissue classification and morphometric segmentation results (Schmitter et al., 2014; Boto et al., 2017). In short, MP2RAGE-UNI image was used to segment the brain into 48 areas, among them. After registering the perfusion-weighted images to the MP2RAGE-UNI images, the obtained 48 brain area masks were used to extract CBF and T1 values for regional comparison between the AD and NC groups. Previous studies have shown that decreased CBF and elevated T1 values in patients with AD occur in specific brain regions (Wolk and Detre, 2012; Wang et al., 2013; Chandra et al., 2019). Therefore, we selected the bilateral thalamus, caudate

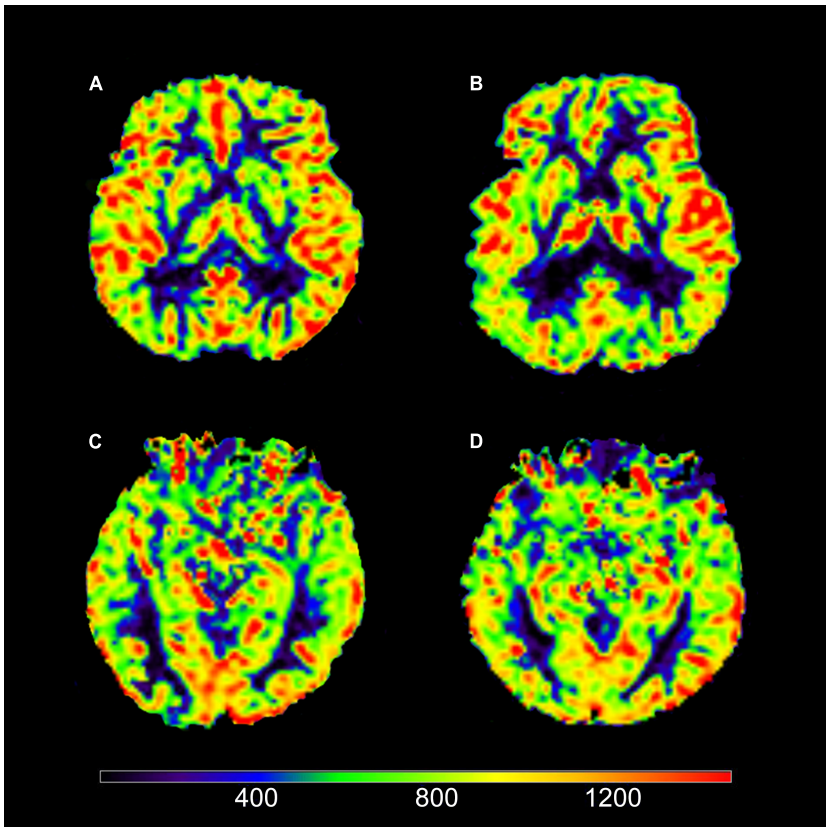

FIGURE 2
Axial view of cerebral blood flow (CBF). **(A)** Image of a typical AD patient (female; 67 years old). **(B)** Image of a NC subject (male; 73 years old). **(C)** Image of a typical AD patient (female; 64 years old). **(D)** Image of a NC subject (female; 64 years old). It could be intuitively shown that **(A)** views had decreased CBF in right caudate nucleus (RCc) compared to **(B)** views; **(C)** views had decreased CBF in left hippocampus (LHc) compared to **(D)** views.

nucleus, putamen, pallidum, hippocampus, frontal gray matter, parietal gray matter, occipital gray matter, temporal gray matter, cingulate gray matter, corpus callosum white matter, and insula as regions of interest to reduce the overfitting problem caused by irrelevant brain regions.

Statistical analysis

All data were analyzed using SPSS (version 24.0),[1] MedCalc 19.0, and MATLAB (MathWorks, Natick, MA, United States). The Kolmogorov–Smirnov and Levene tests were used to assess the normality and variance of CBF and T1 values. Data conforming to a normal distribution are expressed as $\bar{x} \pm s$, and non-conformities are denoted by M (Q1, Q3). Normally distributed data with homogeneous variances were compared between AD and NC groups using independent samples *t*-tests, and those with non-homogeneous variances used corrected *t*-tests. The non-parametric Mann–Whitney U test was used for those that were not normally distributed. The gender difference between the two groups was tested by chi-square. Logistic regression analysis was used to identify brain regions associated with AD diagnosis and establish a combined model. The diagnostic efficacy of each brain region and the combined model for AD were assessed using receiver operating characteristic (ROC) curves, and differences among non-homogeneous variances the areas under the curve (AUCs) were compared using the DeLong method. The correlation between MMSE scores was analyzed using partial correlation analysis, and the level of significance was set at $P < 0.05$. Multiple comparisons were controlled using false discovery rate (FDR) correction (corrected $p < 0.01$).

1 http://www.spss.com

Results

Demographics of the 78 participants are shown in **Table 1**. The differential CBF in different brain regions between AD and NC individuals is shown in **Figure 1**. There were five brain

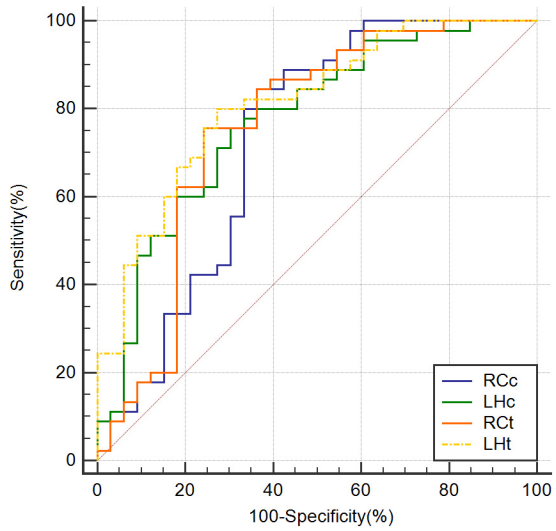

FIGURE 3
Receiver operating characteristic curves based on CBF of RCc, CBF of LHc, T1 value of RCt, and T1 value of LHt, respectively. CBF, cerebral blood flow; LHc, left hippocampus; LHt, left hippocampus; ROC, receiver operating characteristic; RCc, right caudate nucleus; RCt, right caudate nucleus.

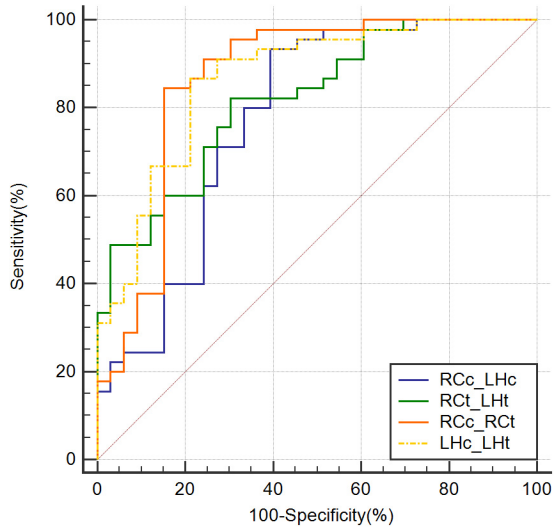

FIGURE 4
Receiver operating characteristic curves combining two parameters. CBF, cerebral blood flow; LHc_LHt, CBF of left hippocampus and T1 value of left hippocampus; RCc_LHc, CBF of right caudate nucleus and CBF of left hippocampus; RCc_RCt, CBF of right caudate nucleus and and T1 value of right caudate nucleus; RCt_LHt, T1 value of right caudate nucleus and T1 value of left hippocampus; ROC, receiver operating characteristic.

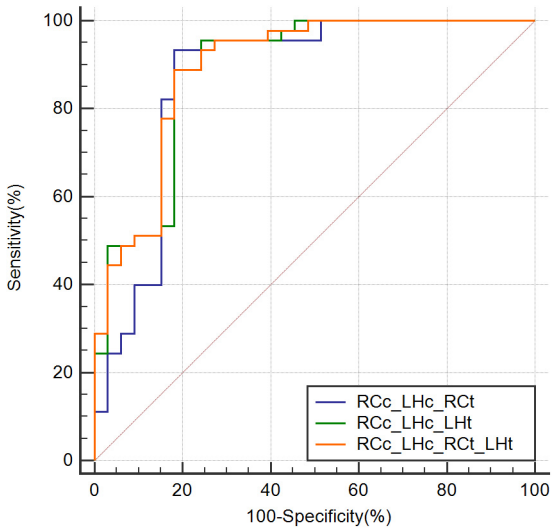

FIGURE 5
Receiver operating characteristic curves combining three or more parameters. CBF, cerebral blood flow; RCc_LHc_LHt, CBF of right caudate nucleus and, CBF of left hippocampus, and T1 value of left hippocampus; RCc_LHc_RCt, CBF of right caudate nucleus and, CBF of left hippocampus, and T1 value of right caudate nucleus; RCc_LHc_RCt_LHt, CBF of right caudate nucleus and, CBF of left hippocampus, T1 value of right caudate nucleus, and T1 value of left hippocampus; ROC, receiver operating characteristic.

regions with significantly lower CBF values in patients with AD compared with the NC subjects, including the right caudate nucleus, left hippocampus, right parietal gray matter, right corpus callosum, and right insula. Comparing the T1 values of the above five brain regions using the same method, the right caudate nucleus, left hippocampus, right parietal gray matter, and right insula were also significantly different (corrected $p < 0.01$). The T1 value of the right corpus callosum was higher in the NC group, but the difference was not statistically significant (corrected $p = 0.375$).

According to logistic regression analysis, the right caudate nucleus (odds ratio [OR] 0.959, $p < 0.05$) and left hippocampus (OR 0.960, $p < 0.05$) were the two relevant brain regions for perfusion abnormalities in AD, CBF of the right caudate nucleus (RCc) and left hippocampus (LHc) were show in Figure 2. Then, a multiple combined model was established corresponding to the T1 values.

The highest AUC value was 0.894 (sensitivity = 0.889, specificity = 0.818), obtained by combining CBF in the right caudate nucleus (RCc), CBF in the left hippocampus (LHc), T1 value in the right caudate nucleus (RCt), and T1 value in the left hippocampus (LHt) (Figures 3–5 and Table 2). On DeLong inspection, there was no significant difference in the diagnostic efficacy between the four single-parameter diagnostic models. The combined model had different degrees of increased diagnostic efficacy compared with the single-parameter model. RCc compared with RCc_LHc_RCt_LHt ($p = 0.001$); LHc compared with RCc_LHc_RCt_LHt ($p = 0.006$); RCt compared

TABLE 2 Receiver operating characteristic (ROC) curves of various parameter combinations.

	Cut-off	Sensitivity	Specificity	Youden index	AUC	
					Mean	95% CI
RCc	59.902	0.844	0.636	0.480	0.731	0.609–0.854
LHc	76.808	0.756	0.697	0.453	0.772	0.666–0.879
RCt	1191.832	0.756	0.758	0.513	0.759	0.641–0.0877
LHt	1320.708	0.800	0.727	0.527	0.813	0.718–0.908
RCc_LHc	0.457(RCc = 63.394, LHc = 77.987)	0.933	0.606	0.539	0.775	0.664–0.886
RCt_LHt	0.557(RCt = 1309.103, LHt = 1301.550)	0.822	0.697	0.519	0.820	0.729–0.910
RCc_RCt	0.556(RCc = 60.295, RCt = 1191.832)	0.844	0.849	0.693	0.865	0.772–0.957
LHc_LHt	0.491(LHc = 85.468, LHt = 1311.493)	0.867	0.788	0.655	0.866	0.784–0.948
RCc_LHc_RCt	0.424(RCc = 65.090, LHc = 83.520, RCt = 1191.682)	0.933	0.812	0.752	0.871	0.770–0.962
RCc_LHc_LHt	0.329(RCc = 65.090, LHc = 83.520, LHt = 1281.999)	0.956	0.758	0.713	0.887	0.809–0.965
RCc_LHc_RCt_LHt	0.452(RCc = 47.451; LHc = 83.771; RCt = 979.333; LHt = 1260.170)	0.889	0.818	0.707	0.894	0.819–0.968

AUC, area under the curve; CBF, cerebral blood flow; LHc, CBF of left hippocampus; LHt, T1 value of left hippocampus; RCC, CBF of right caudate nucleus; RCt, T1 value of right caudate nucleus.

with RCc_LHc_RCt_LHt ($p = 0.023$); and LHt compared with RCc_LHc_RCt_LHt ($p = 0.066$).

In the entire cohort of the AD and NC groups, excluding the interference of sex, age, years of education, and body mass index (BMI), RCc, LHc, RCt, and LHt were statistically significantly correlated with MMSE scores through partial correlation analysis, and the correlation cofficient of LHc is higher ($r = 0.572$, $p < 0.01$) (Table 3).

Discussion

This study investigated the diagnostic value of multi-modality quantitative MRI parameters. To the best of our knowledge, this is the first demonstration of the diagnostic power of CBF combined with T1-mapping. Group comparison found lower CBF values and higher T1 values in several brain areas in patients with AD compared with the NC group. Further ROC analysis demonstrated that a combined model based on both quantitative parameters achieved better diagnostic performance than either single parameter.

The present cohort included 45 AD and 33 NC subjects and compared CBF in 24 brain regions. Apart from the right thalamus and right pallidum, the mean perfusion values were reduced in the remaining 22 brain regions of patients with AD.

TABLE 3 Clinically observed severity measurements.

		RCc	LHc	RCt	LHt
MMSE	r	0.469	0.578	−0.236	−0.456
	p	<0.001	<0.001	0.043	<0.001

LHc, CBF in left hippocampus; LHt, T1 value in left hippocampus; MMSE, Chinese versions Mini-mental State Examination; RCc, CBF in right caudate nucleus; RCt, T1 value in right caudate nucleus.

According to previous AD neuroimaging studies, the pattern of reduced CBF in patients with AD is primarily concentrated in the hippocampus, basal nuclei clusters, and cognitive correlation cortical gray matter. Our study identified five brain regions (right caudate nucleus, left hippocampus, right parietal gray matter, right corpus callosum, and right insula) with significant differences when corrected by multiple comparisons (FDR correction, $p < 0.01$), consistent with findings from previous studies (Wolk and Detre, 2012; Wang et al., 2013; Wang, 2016; Camargo et al., 2021; Duan et al., 2021). These regions are closely associated with the development of AD. The caudate nucleus is a gray matter mass embedded in the medulla, buried deep in the base of the brain, responsible for the fine-tuning and coordination of movements (Valera-Bermejo et al., 2021). The hippocampus is a memory and cognitive center and is related to the occurrence and progression of AD (Dautricourt et al., 2021). The association between the corpus callosum and insula in AD is unclear, and some theories remain controversial and contradictory (Kamal et al., 2021; Giacomucci et al., 2022). However, the mean CBF values in the right thalamus and pallidum were elevated in the AD group, but these differences were not significant ($p > 0.05$). This result is similar to the previous finding of increased CBF in the basal nucleus cluster in the pre-AD period (Hays et al., 2018). Although the brain regions found in the Hays et al. study are not consistent with previous studies, the authors suggest that the reason for this change is suggestive of neurodegeneration leading to CBF dysregulation and the existence of a neural compensatory mechanism for cognitive decline in some brain regions.

T1-mapping has been used to study many central nervous system disorders such as epilepsy (Massire et al., 2021), multiple sclerosis (Massire et al., 2021; Thaler et al., 2021) and depression (Li et al., 2019). However, the findings of AD research are

controversial (Tang et al., 2018). Su et al. found that T1 values in patients with AD at baseline were reduced in temporal and parietal lobes, which is contrary to our results. Interestingly, in the original study, as the disease worsened, T1 values increased significantly in the right caudate, bilateral hippocampus, and other regions instead of decreasing, indirectly complementing our findings (Su et al., 2016). An earlier classical low-magnetic field MRI-based study showed an overall trend in T1 values that was consistent with our results, but they did not precisely stage the brain (Besson et al., 1989). The application of high field strength in our study increased the image signal-to-noise ratio, making the image segmentation more detailed and study results more reliable. Pelkmans et al. reported that myelin determines the conduction of neuronal signals along axonal connections in brain networks, and loss of myelin integrity might result in cognitive decline in AD. Changes in T1 values can reflect myelin content, and myelin is generally associated with increased T1 values (Pelkmans et al., 2019). Future research should further investigate the predicted value of T1-mapping.

In our study, T1 values in the right caudate nucleus and left hippocampus demonstrated good diagnostic performance (AUC = 0.759 and 0.813, respectively). We also combined CBF and T1 values, which improved the diagnostic efficacy compared with that of each single parameter. The highest achievable AUC of 0.894 (sensitivity = 0.889, specificity = 0.818) was obtained using a combination of four parameters. The combination of CBF and T1 values also improved the diagnostic rate (AUC = 0.775–0.865). Our multiparametric MRI measurements improved the results for AD discrimination from NC. Furthermore, several previous studies determined cutoff values in a relatively subjective manner (e.g., less than twice the standard deviation of the control group mean) (Raji et al., 2010). In this study, we used the Jorden index, which together reflects sensitivity and specificity, as a scientific measure to derive the optimal cutoff value for our local cohort.

Like previous studies (Duan et al., 2021; Giacomucci et al., 2022), in our cohort, the severity of neuropsychologic impairment was strongly associated with brain scan measurements. A previous study confirmed that gender, age, education level, and BMI affected cognitive decline (Nebel et al., 2018); therefore, we performed a partial correlation analysis to exclude multiple confounding factors. RCc, LHc, and LHt were found to be powerful predictors of the clinically observed severity measurements.

There are several limitations of this study. First and most importantly, multiple stages of progressive diseases such as subjective cognitive decline and mild cognitive impairment, were not included. Second, we only performed cross-sectional diagnosis in all patients; future longitudinal analysis is needed. Long-term clinical follow-up may improve the diagnostic accuracy for AD. Third, the superiority of temporal lobe diagnosis was not demonstrated in our cohort (Alexopoulos et al., 2012). The temporal lobe, especially the medial temporal lobe, is associated with memory consolidation. This discrepancy may be due to the small amount of data we had and possibly to the fact that the pCASL scanning technique still needs to be refined. Future large-scale clinical studies to validate the diagnostic accuracy and robustness of the CBF and T1 values are imperative.

Conclusion

In conclusion, combining the pCASL and T1-mapping methods is superior to using a single measure in discriminating AD and NC cohorts. T1-mapping is a competitive technique that provides quantitative measurements of pathologic changes in the brain. A "one-stop-shop" study of multimodal parameters in the future is essential for diagnosing and monitoring AD.

Data availability statement

The datasets presented in this study can be found in online repositories. The names of the repository/repositories and accession number(s) can be found in the article/supplementary material.

Ethics statement

The studies involving human participants were reviewed and approved by the Ethics Committee of Beijing Hospital. The patients/participants provided their written informed consent to participate in this study. Written informed consent was obtained from the individual(s) for the publication of any potentially identifiable images or data included in this article.

Author contributions

XW, CL, and MC designed the work. XW, DW, and XL collected and integrated the data. XW, WW, PG, and BL analyzed the data and prepared the manuscript. JP, XZ, and JZ edited and revised the manuscript. All authors contributed to the article and approved the final manuscript.

Funding

This study was supported by the National Natural Science Foundation of China (grant number: 81771826).

Acknowledgments

We would like to thank Editage (www.editage.cn) for English language editing.

Conflict of interest

XZ and JZ were employed by MR collaboration, Siemens Healthineers Ltd., and JP was employed by MR Application Development, Siemens Healthcare GmbH.

The remaining authors declare that the research was conducted in the absence of any commercial or financial relationships that could be construed as a potential conflict of interest.

The reviewer GW declared a past co-authorship with one of the authors JZ to the handling editor.

Publisher's note

All claims expressed in this article are solely those of the authors and do not necessarily represent those of their affiliated organizations, or those of the publisher, the editors and the reviewers. Any product that may be evaluated in this article, or claim that may be made by its manufacturer, is not guaranteed or endorsed by the publisher.

References

Alexopoulos, P., Sorg, C., Förschler, A., Grimmer, T., Skokou, M., Wohlschläger, A., et al. (2012). Perfusion abnormalities in mild cognitive impairment and mild dementia in Alzheimer's disease measured by pulsed arterial spin labeling MRI. *Eur. Arch. Psychiatry Clin. Neurosci.* 262, 69–77. doi: 10.1007/s00406-011-0226-2

Alsop, D. C., Detre, J. A., Golay, X., Günther, M., Hendrikse, J., Hernandez-Garcia, L., et al. (2015). Recommended implementation of arterial spin-labeled perfusion MRI for clinical applications: A consensus of the ISMRM perfusion study group and the European consortium for ASL in dementia. *Magn. Reson. Med.* 73, 102–116. doi: 10.1002/mrm.25197

Arnold, S. E., Hyman, B. T., Flory, J., Damasio, A. R., and Van Hoesen, G. W. (1991). The topographical and neuroanatomical distribution of neurofibrillary tangles and neuritic plaques in the cerebral cortex of patients with Alzheimer's disease. *Cereb. Cortex* 1, 103–116. doi: 10.1093/cercor/1.1.103

Besson, J. A., Crawford, J. R., Parker, D. M., and Smith, F. W. (1989). Magnetic resonance imaging in Alzheimer's disease, multi-infarct dementia, alcoholic dementia and Korsakoff's psychosis. *Acta Psychiatr. Scand.* 80, 451–458. doi: 10.1111/j.1600-0447.1989.tb03005.x

Boto, J., Gkinis, G., Roche, A., Kober, T., Maréchal, B., Ortiz, N., et al. (2017). Evaluating anorexia-related brain atrophy using MP2RAGE-based morphometry. *Eur. Radiol.* 27, 5064–5072. doi: 10.1007/s00330-017-4914-9

Buxton, R. B., Frank, L. R., Wong, E. C., Siewert, B., Warach, S., and Edelman, R. R. (1998). A general kinetic model for quantitative perfusion imaging with arterial spin labeling. *Magn. Reson. Med.* 40, 383–396. doi: 10.1002/mrm.28422

Camargo, A., Wang, Z., and Alzheimer's Disease Neuroimaging Initiative (2021). Longitudinal cerebral blood flow changes in normal aging and the Alzheimer's disease continuum identified by arterial spin labeling MRI. *J. Alzheimers. Dis.* 81, 1727–1735. doi: 10.3233/JAD-210116

Chandra, A., Dervenoulas, G., Politis, M., and Alzheimer's Disease Neuroimaging Initiative (2019). Magnetic resonance imaging in Alzheimer's disease and mild cognitive impairment. *J. Neurol.* 266, 1293–1302. doi: 10.1007/s00415-018-9016-3

Cortes-Canteli, M., and Iadecola, C. (2020). Alzheimer's disease and Vascular Aging: JACC Focus Seminar. *J. Am. Coll. Cardiol.* 75, 942–951. doi: 10.1016/j.jacc.2019.10.062

Dautricourt, S., de Flores, R., Landeau, B., Poisnel, G., Vanhoutte, M., Delcroix, N., et al. (2021). Longitudinal changes in hippocampal network connectivity in Alzheimer's disease. *Ann. Neurol.* 90, 391–406. doi: 10.1002/ana.26168

Duan, W., Zhou, G. D., Balachandrasekaran, A., Bhumkar, A. B., Boraste, P. B., Becker, J. T., et al. (2021). Cerebral Blood Flow Predicts Conversion of Mild Cognitive Impairment into Alzheimer's Disease and Cognitive Decline: An Arterial Spin Labeling Follow-up Study. *J. Alzheimers Dis.* 82, 293–305. doi: 10.3233/JAD-210199

Dujardin, S., Commins, C., Lathuiliere, A., Beerepoot, P., Fernandes, A. R., Kamath, T. V., et al. (2020). Tau molecular diversity contributes to clinical heterogeneity in Alzheimer's disease. *Nat. Med.* 26, 1256–1263. doi: 10.1038/s41591-020-0938-9

Erkkinen, M. G., Kim, M. O., and Geschwind, M. D. (2018). Clinical Neurology and Epidemiology of the Major Neurodegenerative Diseases. *Cold Spring Harb. Perspect. Biol.* 10:a033118. doi: 10.1101/cshperspect.a033118

Forster, D., Davies, K., and Williams, S. (2013). Magnetic resonance spectroscopy in vivo of neurochemicals in a transgenic model of Alzheimer's disease: a longitudinal study of metabolites, relaxation time, and behavioral analysis in TASTPM and wild-type mice. *Magn. Reson. Med.* 69, 944–955. doi: 10.1002/mrm.24349

Gallardo, G., and Holtzman, D. M. (2019). Amyloid-β and tau at the crossroads of Alzheimer's disease. *Adv. Exp. Med. Biol.* 1184, 187–203. doi: 10.1007/978-981-32-9358-8_16

Giacomucci, G., Galdo, G., Polito, C., Berti, V., Padiglioni, S., Mazzeo, S., et al. (2022). Unravelling neural correlates of empathy deficits in subjective cognitive decline, mild cognitive impairment and Alzheimer's Disease. *Behav. Brain Res.* 428:113893. doi: 10.1016/j.bbr.2022.113893

Hays, C. C., Zlatar, Z. Z., Campbell, L., Meloy, M. J., and Wierenga, C. E. (2018). Subjective Cognitive Decline Modifies the Relationship Between Cerebral Blood Flow and Memory Function in Cognitively Normal Older Adults. *J. Int. Neuropsychol. Soc.* 24, 213–223. doi: 10.1017/S135561771700087X

House, M. J., St Pierre, T. G., and McLean, C. (2008). 1.4T study of proton magnetic relaxation rates, iron concentrations, and plaque burden in Alzheimer's disease and control postmortem brain tissue. *Magn. Reson. Med.* 60, 41–52. doi: 10.1002/mrm.21586

Jagust, W., Thisted, R., Devous, M. D., Van Heertum, R., Mayberg, H., Jobst, K., et al. (2001). SPECT perfusion imaging in the diagnosis of Alzheimer's disease: A clinical-pathologic study. *Neurology* 56, 950–956. doi: 10.1212/wnl.56.7.950

Kamal, S., Park, I., Kim, Y. J., Kim, Y. J., and Lee, U. (2021). Alteration of the corpus callosum in patients with Alzheimer's disease: Deep learning-based assessment. *PLoS One* 16:e0259051. doi: 10.1371/journal.pone.0259051

Kaneta, T., Katsuse, O., Hirano, T., Ogawa, M., Yoshida, K., Odawara, T., et al. (2017). Head-to-Head visual comparison between brain perfusion SPECT and arterial spin-labeling MRI with different postlabeling delays in alzheimer disease. *AJNR Am. J. Neuroradiol.* 38, 1562–1568. doi: 10.3174/ajnr.A5238

Knopman, D. S., Amieva, H., Petersen, R. C., Chételat, G., Holtzman, D. M., Hyman, B. T., et al. (2021). Alzheimer disease. *Nat. Rev. Dis. Primers* 7:33. doi: 10.1038/s41572-021-00269-y

Li, Y., Wang, C., Teng, C., Jiao, K., Song, X., Tan, Y., et al. (2019). Hippocampus-driving progressive structural alterations in medication-naïve major depressive disorder. *J. Affect. Disord.* 256, 148–155. doi: 10.1016/j.jad.2019.05.053

Marques, J. P., Kober, T., Krueger, G., van der Zwaag, W., Van de Moortele, P. F., and Gruetter, R. (2010). MP2RAGE, a self bias-field corrected sequence for improved segmentation and T1-mapping at high field. *Neuroimage* 49, 1271–1281. doi: 10.1016/j.neuroimage.2009.10.002

Massire, A., Seiler, C., Troalen, T., Girard, O. M., Lehmann, P., Brun, G., et al. (2021). T1-Based synthetic magnetic resonance contrasts improve multiple

sclerosis and focal epilepsy imaging at 7 T. *Invest. Radiol.* 56, 127–133. doi: 10.1097/RLI.0000000000000718

McKhann, G., Drachman, D., Folstein, M., Katzman, R., Price, D., and Stadlan, E. M. (1984). Clinical diagnosis of alzheimer's disease: report of the NINCDS-ADRDA work group under the auspices of department of health and human services task force on alzheimer's disease. *Neurology* 34, 939–944. doi: 10.1212/wnl.34.7.939

Montine, T. J., Phelps, C. H., Beach, T. G., Bigio, E. H., Cairns, N. J., Dickson, D. W., et al. (2012). National Institute on Aging-Alzheimer's Association guidelines for the neuropathologic assessment of Alzheimer's disease: a practical approach. *Acta Neuropathol.* 123, 1–11. doi: 10.1007/s00401-011-0910-3

Nebel, R. A., Aggarwal, N. T., Barnes, L. L., Gallagher, A., Goldstein, J. M., Kantarci, K., et al. (2018). Understanding the impact of sex and gender in Alzheimer's disease: a call to action. *Alzheimers Dement.* 14, 1171–1183. doi: 10.1016/j.jalz.2018.04.008

Pelkmans, W., Dicks, E., Barkhof, F., Vrenken, H., Scheltens, P., van der Flier, W. M., et al. (2019). Gray matter T1-w/T2-w ratios are higher in Alzheimer's disease. *Hum. Brain Mapp.* 40, 3900–3909. doi: 10.1002/hbm.24638

Raji, C. A., Lee, C., Lopez, O. L., Tsay, J., Boardman, J. F., Schwartz, E. D., et al. (2010). Initial experience in using continuous arterial spin-labeled MR imaging for early detection of Alzheimer disease. *AJNR Am. J. Neuroradiol.* 31, 847–855. doi: 10.3174/ajnr.A1955

Rice, H. C., de Malmazet, D., Schreurs, A., Frere, S., Van Molle, I., Volkov, A. N., et al. (2019). Secreted amyloid-β precursor protein functions as a GABABR1a ligand to modulate synaptic transmission'. *Science* 363:eaao4827. doi: 10.1126/science.aao4827

Schmitter, D., Roche, A., Maréchal, B., Ribes, D., Abdulkadir, A., Bach-Cuadra, M., et al. (2014). An evaluation of volume-based morphometry for prediction of mild cognitive impairment and Alzheimer's disease. *Neuroimage Clin.* 7, 7–17. doi: 10.1016/j.nicl.2014.11.001

Soman, S., Raghavan, S., Rajesh, P. G., Varma, R. P., Mohanan, N., Ramachandran, S. S., et al. (2021). Relationship between cerebral perfusion on arterial spin labeling (ASL) MRI with brain volumetry and cognitive performance in mild cognitive impairment and dementia due to Alzheimer's disease. *Ann. Indian Acad. Neurol.* 24, 559–565. doi: 10.4103/aian.AIAN_848_20

Su, L., Blamire, A. M., Watson, R., He, J., Aribisala, B., and O'Brien, J. T. (2016). Cortical and subcortical changes in alzheimer's disease: a longitudinal and quantitative MRI Study. *Curr Alzheimer Res.* 13, 534–544. doi: 10.2174/1567205013666151116141416

Tang, X., Cai, F., Ding, D. X., Zhang, L. L., Cai, X. Y., and Fang, Q. (2018). Magnetic resonance imaging relaxation time in Alzheimer's disease. *Brain Res. Bull.* 140, 176–189. doi: 10.1016/j.brainresbull.2018.05.004

Thaler, C., Hartramph, I., Stellmann, J. P., Heesen, C., Bester, M., Fiehler, J., et al. (2021). T1 relaxation times in the cortex and Thalamus Are associated with working memory and information processing speed in patients with multiple sclerosis. *Front. Neurol.* 12:789812. doi: 10.3389/fneur.2021.789812

Valera-Bermejo, J. M., De Marco, M., and Venneri, A. (2021). Altered interplay among large-scale brain functional networks modulates multi-domain anosognosia in early Alzheimer's disease. *Front. Aging Neurosci.* 13:781465. doi: 10.3389/fnagi.2021.781465

Verfaillie, S. C., Adriaanse, S. M., Binnewijzend, M. A., Benedictus, M. R., Ossenkoppele, R., Wattjes, M. P., et al. (2015). Cerebral perfusion and glucose metabolism in Alzheimer's disease and frontotemporal dementia: Two sides of the same coin? *Eur. Radiol.* 25, 3050–3059. doi: 10.1007/s00330-015-3696-1

Wang, Z. (2016). "Longitudinal CBF changes predict disease conversion/revision in AD and MCI," in *Proceedings of the 22nd Annual Meeting of the Organization for Human Brain Mapping*, Geneva.

Wang, Z., Das, S. R., Xie, S. X., Arnold, S. E., Detre, J. A., Wolk, D. A., et al. (2013). Arterial spin labeled MRI in prodromal Alzheimer's disease: amulti-site study. *Neuroimage Clin.* 2, 630–636. doi: 10.1016/j.nicl.2013.04.014

Wolk, D. A., and Detre, J. A. (2012). Arterial spin labeling MRI: An emerging biomarker for Alzheimer's disease and other neurodegenerative conditions. *Curr. Opin. Neurol.* 25, 421–428. doi: 10.1097/WCO.0b013e328354ff0a

Xekardaki, A., Rodriguez, C., Montandon, M. L., Toma, S., Tombeur, E., Herrmann, F. R., et al. (2015). Arterial spin labeling may contribute to the prediction of cognitive deterioration in healthy elderly individuals. *Radiology* 274, 490–499. doi: 10.1148/radiol.14140680

frontiers | Frontiers in Neuroscience

TYPE Original Research
PUBLISHED 05 August 2022
DOI 10.3389/fnins.2022.944246

Check for updates

OPEN ACCESS

EDITED BY
Danny J. J. Wang,
University of Southern California,
United States

REVIEWED BY
Peiyu Huang,
Zhejiang University, China
Xiaowei Ma,
Central South University, China

*CORRESPONDENCE
Fugeng Sheng
fugeng_sheng@163.com
Cong Han
hc82225@126.com
Jianming Cai
beili12345@sina.cn

†These authors have contributed equally to this work

SPECIALTY SECTION
This article was submitted to Brain Imaging Methods, a section of the journal Frontiers in Neuroscience

RECEIVED 15 May 2022
ACCEPTED 05 July 2022
PUBLISHED 05 August 2022

CITATION
Zhang H, Lu M, Liu S, Liu D, Shen X, Sheng F, Han C and Cai J (2022) The value of 3D pseudo-continuousarterial spin labeling perfusion imaging in moyamoya disease—Comparison with dynamic susceptibility contrast perfusion imaging.
Front. Neurosci. 16:944246.
doi: 10.3389/fnins.2022.944246

COPYRIGHT
© 2022 Zhang, Lu, Liu, Liu, Shen, Sheng, Han and Cai. This is an open-access article distributed under the terms of the Creative Commons Attribution License (CC BY). The use, distribution or reproduction in other forums is permitted, provided the original author(s) and the copyright owner(s) are credited and that the original publication in this journal is cited, in accordance with accepted academic practice. No use, distribution or reproduction is permitted which does not comply with these terms.

The value of 3D pseudo-continuousarterial spin labeling perfusion imaging in moyamoya disease—Comparison with dynamic susceptibility contrast perfusion imaging

Hongtao Zhang[1†], Mingming Lu[2†], Shitong Liu[1†], Dongqing Liu[1], Xuxuan Shen[3], Fugeng Sheng[1*], Cong Han[3*] and Jianming Cai[1*]

[1]Department of Radiology, The Fifth Medical Center of Chinese People's Liberation Army (PLA) General Hospital, Beijing, China, [2]Department of Radiology, Pingjin Hospital, Characteristic Medical Center of Chinese People's Armed Police Force, Tianjin, China, [3]Department of Neurosurgery, The First Medical Center of Chinese People's Liberation Army (PLA) General Hospital, Beijing, China

Background and purpose: 3D pseudo-continuous arterial spin labeling (3D pCASL) is commonly used to measure arterial cerebral blood flow (CBF). The aim of this study was to assess the clinical feasibility and accuracy of 3D pCASL in comparison with dynamic susceptibility contrast (DSC) perfusion imaging in moyamoya disease (MMD).

Materials and methods: A total of 174 MMD patients underwent 3D pCASL and DSC-MRI for evaluating cerebral blood perfusion. 3D-pCASL with two single post-labeling delay (PLD) times (1,500 and 2,500 ms) was used to measure CBF. The values of DSC-CBF and ASL-CBF were calculated for major arterial territories including the anterior, middle, and posterior cerebral arteries as well as the areas based on the Alberta Stroke Program Early CT Score (ASPECTS) template. The correlation between DSC-CBF and ASL-CBF was analyzed. The consistency and accuracy between the two methods in assessing the cerebral ischemic state before and after surgery were analyzed.

Results: The correlation between ASL (2,500 ms) and DSC-MRI was slightly better than the correlation between ASL (1,500 ms) and DSC-MRI in major vascular territories before revascularization. Significant correlations were observed between ASL (2,500 ms) and DSC-MRI and between ASL (1,500 ms) and DSC-MRI in major vascular territories after revascularization. For 44 surgically treated patients, the scores of ASPECTS for CBF on the operated side were significantly different before and after revascularization ($p < 0.05$) and showed good consistency on all the examination methods. A comparison of the scores of ASPECTS of the three parameters before and

after revascularization showed that there was no statistical difference between them ($p > 0.05$).

Conclusion: Compared to DSC-MRI, 3D pCASL can assess the cerebral blood perfusion in MMD before and after revascularization effectively. 3D pCASL showed the feasibility and clinical utility value in patients with MMD.

KEYWORDS

magnetic resonance imaging, arterial spin labeling, dynamic susceptibility contrast enhanced perfusion, moyamoya disease, cerebral blood flow

Introduction

Moyamoya disease (MMD) is a chronic cerebrovascular disease characterized by gradual intimal thickening and progressive narrowing or occlusion at the junction of the bilateral internal carotid artery and the common origin of the middle cerebral artery and the anterior cerebral artery and is associated with compensatory expansion and stenosis of perforating arteries in the Circle of Willis (Qiao et al., 2017; Bang et al., 2020). The cerebral hemodynamics of patients with MMD is very complex. Therefore, for patients with MMD, an accurate assessment of cerebral hemodynamics is very important for the selection of treatment and evaluation of efficacy (Ishii et al., 2014, 2017).

Dynamic susceptibility contrast (DSC) perfusion imaging is an magnetic resonance imaging (MRI) technique that allows multiparameter assessment of cerebral hemodynamics. Compared with PET, the standard examination method of cerebral perfusion, MRI has no radioactivity and has better clinical availability, so DSC is widely used in the evaluation of cerebrovascular diseases (Wintermark et al., 2005; Zhang et al., 2018). The main disadvantages of DSC-MRI are the need for injection of contrast and semi-quantitative assessment of the parameters.

In the last decade, the use of arterial spin labeling (ASL) to quantify cerebral perfusion (in units of ml/100 g/min) has become increasingly popular (Haller et al., 2016; Kohno et al., 2016; Havsteen et al., 2018; Shao et al., 2018; Hu et al., 2019), as ASL is a non-invasive and reproducible examination that does not apply to contrast agents. In the classic application of 3D pseudo-continuous arterial spin labeling (3D pCASL), a single PLD is used. The PLD represents the time between the blood labeling by radiofrequency pulses, usually at the carotid artery level, and the time when 3D data acquisition begins with the imaging volume. In the study by Alsop et al. (2015) and Nery et al. (2018), a PLD of 2,000 ms was recommended for neonates, 1,500 ms for children, and 1,800 ms for adults. However, there is no clear recommendation for PLD in MMD patients. The purpose of our study was to observe the collateral circulation in the brain of patients with MMD, so two delay times were adopted, which were 1,500 and 2,500 ms.

The aim of this research was to study the correlation between dynamic susceptibility contrast-cerebral blood flow (DSC-CBF) and ASL-CBF using two single PLDs of 1,500 and 2,500 ms in patients with MMD. The results of the scores of ASPECTS of DSC-CBF and ASL-CBF were compared before and after revascularization to assess the value of changes in cerebral blood flow (CBF) in MMD for ASL.

Materials and methods

Patients

This was a prospective study and this study was approved by our Institutional Review Board. Informed consent was obtained from all patients. Between October 2020 and September 2021, 174 patients with angiographically confirmed MMD were included in the study. All patients underwent DSC and ASL examination before surgery. A total of 44 of these patients underwent encephaloduroarteriosynangiosis (EDAS) and DSC and ASL examinations were performed 3–4 months after surgery. The inclusion criteria were as follows: (1) patients diagnosed with MMD by digital subtraction angiography (DSA) according to the current diagnostic criteria and who underwent revascularization surgery for evaluation; (2) patients with preoperative and postoperative MRI data (patients who underwent DSC-MRI, 3D pCASL, and T1WI 3D-MPRAGE before and after surgery). The exclusion criteria were as follows: (1) secondary moyamoya phenomenon caused by other well-diagnosed diseases; (2) brain tumors; (3) intracranial aneurysms, and; (4) contradiction to MR examination.

Magnetic resonance imaging protocols

MR imaging examinations were performed with a 3.0-T system (MAGNETOM SKYRA, Siemens Healthcare) with

a 20-channel head coil. The scan sequences included DSC-MRI, ASL-MRI, and T1WI 3D MPRAGE. T1WI 3D-MPRAGE and 3D pCASL were scanned together and DSC-MRI was done the next day.

DSC-MRI, the axial brain MR imaging parameters were as follows: repetition time (TR)/echo time (TE) = 1,360/30 ms, slice thickness = 5 mm, intersection gap = 1.5 mm, field of view (FOV) = 230 × 230 mm^2, matrix size = 144 × 144, number of excitation (NEX) = 1. A gadolinium contrast agent of gadolinium-diethylenetriaminepentaacetic acid (Gd-DTPA) was injected intravenously at a rate of 4∼4.5 ml/s (20 ml) using a power injector at the sixth acquisition, followed by a 30-ml saline flush. The DSC-MRI original images obtained were processed by a post-processing workstation (Syngo *Via* 20, Simens) and analyzed using brain MRI perfusion software. Four parameters [relative cerebral blood volume (CBV), relative CBF, relative mean transit time (MTT), and time to peak (TTP)] were automatically obtained.

The ASL scan used a pCASL pulse sequence with background suppressed 3D Gradient and Spin Echo (GRASE) readout labeling pulse duration = 1,500 ms, PLD = 1,500 and 2,500 ms, no flow crushing gradient, FOV = 224 × 224 mm^2, matrix size = 64 × 64, TE/TR = 36.76/4,000 ms, thirty-two 4-mm slices acquired for covering the whole brain.

For structural imaging, T1-weighted sagittal images were acquired with a 3D MPRAGE sequence. The parameters were as follows: 192 slices at 1 mm slice thickness, voxel size = 1 × 1 × 1 mm^3, TR/TE = 2,000/2.26 ms, and the scan time of 4 min and 40 s.

Image analysis

The CBF value was automatically measured by software as follows: (1) ASL image data were processed using CereFlow software and were used to automatically calculate the value of CBF. The DSC-MRI images acquired were analyzed using the MR Neuro-Perfusion software (Syngo *Via* 20, Simens), automatically generating relative CBV, relative CBF, relative MTT, and TTP, with (2) co-registration with the high-resolution sagittal anatomical T1WI image and (3) standardization of T1WI anatomical images to the Montreal Neurological Institute (MNI) template. (4) The CBF image warped into MNI space using the forward transformation matrix derived from T1WI and regional CBF was extracted by applying the ASPECTS and vascular territory atlases, as was applied in the previous study by Wang and his colleagues (Tatu et al., 1998; Wang et al., 2013).

The quantitative parameters of DSC and ASL for major arterial territories of anterior cerebral artery (ACA), middle cerebral artery (MCA), posterior cerebral artery (PCA), and cerebellar hemispheres were measured in the bilateral cerebral hemispheres in all 174 patients with MMD. CBF was measured in the region of interests (ROIs) of DSC and ASL parameter maps. The values of the ratio of CBF of the supply territories of ACA, MCA, and PCA to ipsilateral cerebellar hemispheres were calculated ($CBF_{relative}$ = $CBF_{vascularterritories}$/$CBF_{cerebellarhemispheres}$). For 44 surgically treated patients, CBF values of the supply territories of ACA, MCA, PCA, and cerebellar hemispheres before and after revascularization were measured on the surgical site. The values of the ratio of CBF of the supply territories of ACA, MCA, and PCA to ipsilateral cerebellar hemispheres were calculated ($CBF_{relative}$ = $CBF_{vascularterritories}$/$CBF_{cerebellarhemispheres}$). The values of the difference between the postoperative ratios of CBF and preoperative ratios of CBF were calculated (CBF_{minus} = postoperative $CBF_{relative}$-preoperative $CBF_{relative}$). Finally, the correlations between DSC-$CBF_{relative}$ and ASL-$CBF_{relative}$ and between DSC-CBF_{minus} and ASL-CBF_{minus} were analyzed.

Evaluation of cerebral ischemic state: The assessment of the ischemic status of ASPECTS areas involved a quantitative assessment of ASL-CBF. The CBF values of ASPECTS areas less than 30 ml/100 g/min were defined as ischemic states. The assessment of the ischemic status of ASPECTS areas involved a qualitative assessment of DSC-CBF. The diagnostic criteria for ischemia were the presence of a decreased signal on the DSC-CBF images and the increased signal on the TTP images compared to the normal cerebral vascular area. DSC-CBF was independently evaluated by two experienced neuroradiologists and used to assess the presence of ischemia on ASPECTS areas. The final decisions were reached by consensus. The areas of ASPECTS standards assessment include 10 areas of MCA-related blood supply area. The normal ASPECTS area (without ischemia) scored 1 point, and the ischemic area scored 0 points. All ASPECTS areas without ischemic change scored 10 points, and all ASPECTS areas with ischemic change scored 0 points. The consistency and change between DSC and ASL in assessing preoperative and postoperative scores of ASPECTS were also analyzed.

Statistical analysis

The statistical analysis was performed using SPSS (version 22.0, IBM). All reported *p*-values were two-sided and were considered statistically significant at values of less than 0.05. According to the results of the normality test, the correlations between DSC-CBF and ASL-CBF were counted using Spearman's correlation analysis. The consistency between ASL-CBF (PLD = 1,500 and 2,500 ms) and DSC-CBF in assessing preoperative and postoperative ASPECTS scores was examined by calculating the intra-class correlation coefficient (ICC). A one-way ANOVA was used for assessing preoperative and postoperative ASPECTS scores of ASL-CBF (PLD = 1,500 and 2,500 ms) and DSC-CBF. Improvement of ASPECTS scores of postoperative and preoperative ischemic state was examined by *t*-test.

TABLE 1 The clinical and imaging characteristics of the patients with moyamoya disease (MMD).

Characteristics		All 174 MMD patients	44 Surgical patients
Age (years)		41.1 ± 11.1	39.5 ± 10.6
Male/Female (*n*)		89/85	22/22
Hemorrhagic stroke (*n*)		16 (9.2%)	3 (6.8%)
Ischemic stroke (*n*)	Frontal lobe	121 (69.5%)	31 (70.5%)
	Parietal lobe	58 (33.3%)	16 (36.4%)
	Occipital lobe	25 (14.4%)	6 (13.6%)
	Temporal lobe	23 (13.2%)	5 (11.4%)
	Basal ganglia	42 (24.1%)	4 (9.1%)

(n) is the number of patients. Other data are mean values ± standard deviations.

Results

Demographic and clinical information

A total of 174 patients with MMD underwent simultaneous preoperative DSC and ASL (PLD = 1,500 and 2,500 ms). The mean age of patients was 41.1 years (range: 14–66 years, 89 men). Forty-four of these patients underwent EDAS on one side. The mean age of surgical patients was 39.5 years (range: 15–60 years, 22 men) (see Table 1). All postoperative patients also underwent simultaneous preoperative DSC and ASL and followed by MRI examination 3–4 months after revascularization. CBF was measured in major arterial territories of ACA, MCA, and PCA in the bilateral cerebral hemispheres in all 174 patients, as well as in the corresponding cerebellar hemispheres. CBF values of all ASPECTS areas in the cerebral hemispheres before and after revascularization were measured.

Quantitative cerebral artery territory analysis

In 174 patients with MMD, the values of the ratio of CBF of the supply territories of ACA, MCA, and PCA to ipsilateral cerebellar hemispheres were calculated before revascularization. The correlations between DSC-$CBF_{relative}$ and ASL-$CBF_{relative}$ (1,500 ms) were statistically significant except for the correlations on the blood supply areas of ACA (right) and MCA (right). The correlations between DSC-$CBF_{relative}$ and ASL-$CBF_{relative}$ (2,500 ms) were statistically significant except for the correlation on the blood supply areas of PCA (right) (see Table 2).

For 44 patients with MMD who underwent unilateral surgery, the values of the difference between the postoperative ratios of CBF and preoperative ratios of CBF were calculated on the supply territories of ACA, MCA, and PCA. All correlations between DSC-CBF_{minus} and ASL-CBF_{minus} (1,500 ms) and between DSC-CBF_{minus} and ASL-CBF_{minus} (2,500 ms) were statistically significant (see Table 3 and Figure 1).

TABLE 2 The correlation between dynamic susceptibility contrast-cerebral blood flow (DSC-CBF) and arterial spin labeling (ASL)-CBF before revascularization.

Vascular territories	ASL-$CBF_{relative}$	DSC-$CBF_{relative}$	r	*P*-values
ACA (left)	1,500 ms	DSC	0.221	0.003
ACA (left)	2,500 ms	DSC	0.438	0.000
ACA (right)	1,500 ms	DSC	0.044	0.567
ACA (right)	2,500 ms	DSC	0.23	0.002
MCA (left)	1,500 ms	DSC	0.325	0.000
MCA (left)	2,500 ms	DSC	0.225	0.003
MCA (right)	1,500 ms	DSC	0.112	0.141
MCA (right)	2,500 ms	DSC	0.264	0.000
PCA (left)	1,500 ms	DSC	0.268	0.000
PCA (left)	2,500 ms	DSC	0.212	0.005
PCA (right)	1,500 ms	DSC	0.245	0.001
PCA (right)	2,500 ms	DSC	0.076	0.319

TABLE 3 The correlation between dynamic susceptibility contrast-cerebral blood flow (DSC-CBF) and arterial spin labeling (ASL)-CBF after revascularization.

Vascular territories	ASL-CBF_{minus}	DSC-CBF_{minus}	r	*P*-values
ACA (surgical side)	1,500 ms	DSC	0.306	0.044
ACA (surgical side)	2,500 ms	DSC	0.366	0.014
MCA (surgical side)	1,500 ms	DSC	0.517	0.000
MCA (surgical side)	2,500 ms	DSC	0.409	0.006
PCA (surgical side)	1,500 ms	DSC	0.424	0.004
PCA (surgical side)	2,500 ms	DSC	0.400	0.007

Quantitative alberta stroke program early CT score areas analysis

The consistency of ASL-CBF (1,500 ms), ASL-CBF (2,500 ms), and DSC-CBF in assessing ASPECTS area ischemia scores before and after revascularization was good for calculating the ICC. The result of the ICC of ASL-CBF (1,500 ms), ASL-CBF (2,500 ms), and DSC-CBF in assessing ASPECTS area ischemia scores before revascularization was 0.7696 (0.6200–0.8666) and the result of the ICC of ASL-CBF (1,500 ms), ASL-CBF (2,500 ms), and DSC-CBF after revascularization was 0.8335 (0.7255–0.9036). The differences in the preoperative ASPECTS area ischemia scores of ASL-CBF

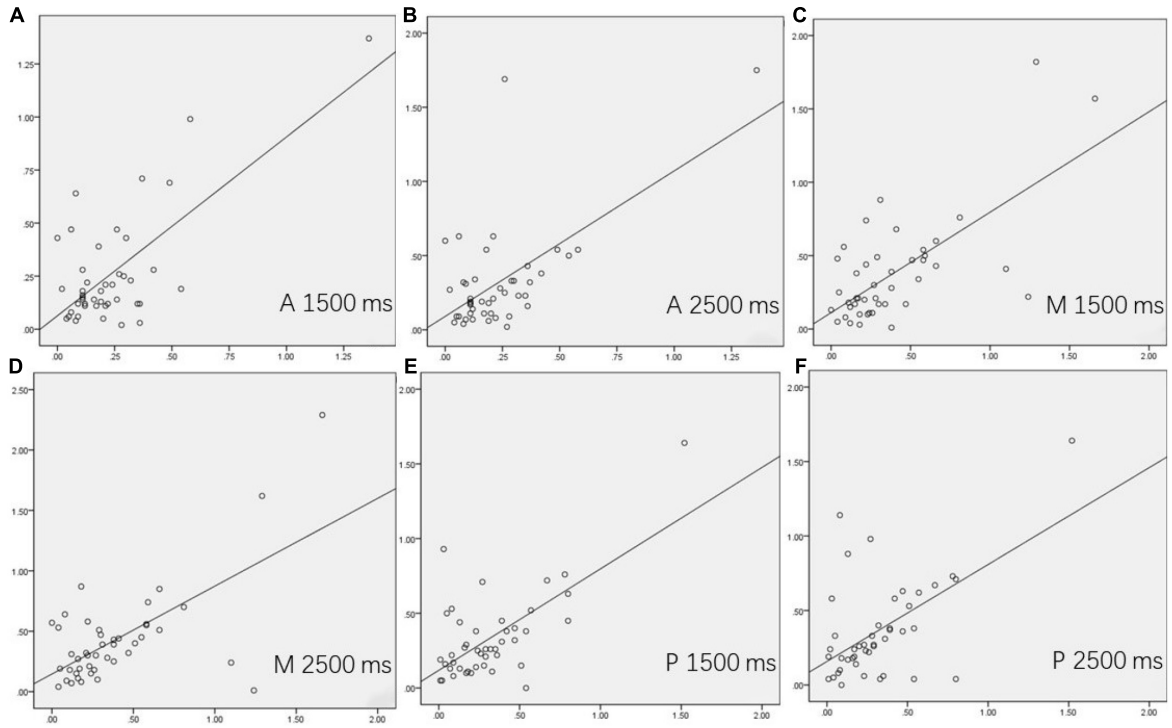

FIGURE 1
The correlations between dynamic susceptibility contrast-cerebral blood flow (DSC-CBF)$_{minus}$ and arterial spin labeling (ASL)-CBF$_{minus}$ (1,500 ms) and between DSC-CBF$_{minus}$ and ASL-CBF$_{minus}$ (2,500 ms) in 44 surgical patients. **(A–F)** showed the correlation of the supply territories of ACA, MCA, and PCA between DSC-CBF$_{minus}$ and ASL-CBF$_{minus}$ (1,500 ms) and between DSC-CBF$_{minus}$ and ASL-CBF$_{minus}$ (2,500 ms) on the surgical side.

(1,500 ms), ASL-CBF (2,500 ms), and DSC-CBF were not statistically significant ($F = 2.523$, $p = 0.084$), and the differences of the postoperative ASPECTS area ischemia scores were not also statistically significant ($F = 2.146$, $p = 0.121$). The postoperative ASPECTS area ischemia scores were higher than the preoperative scores using all three methods and the differences were statistically significant ($p < 0.05$) (see **Table 4** and **Figure 2**). This indicated that cerebral ischemia was improved after revascularization.

Discussion

In this study, we analyzed the correlation between DSC-CBF$_{relative}$ and ASL-CBF$_{relative}$ (1,500 ms) and between DSC-CBF$_{relative}$ and ASL-CBF$_{relative}$ (2,500 ms) of the main arterial supply areas in 174 patients with MMD before surgery. The results showed that there was no significant correlation between DSC-CBF$_{relative}$ and ASL-CBF$_{relative}$ (1,500 ms) in only two blood supply areas of all the main arterial supply areas. There was no significant correlation between DSC-CBF$_{relative}$ and ASL-CBF$_{relative}$ (2,500 ms) on only one blood supply area of all the main arterial supply areas. Analysis of preoperative data showed that the correlation between DSC-CBF$_{relative}$ and ASL-CBF$_{relative}$ (2,500 ms) was slightly better than the correlation between DSC-CBF$_{relative}$ and ASL-CBF$_{relative}$ (1,500 ms) in major vascular territories. For forty-four patients with MMD after unilateral surgery, the correlation between DSC-CBF$_{minus}$ and ASL-CBF$_{minus}$ (1,500 ms) and between DSC-CBF$_{minus}$ and ASL-CBF$_{minus}$ (2,500 ms) of the main arterial supply areas on the surgical side was analyzed. The results showed that the correlation of all data on the blood supply areas of ACA, MCA, and PCA was statistically significant. Previous studies in healthy subjects showed a good correlation between CBF measured using the gold standard ^{15}O-PET and ASL-CBF (Ye et al., 2000; Wang et al., 2014). The results of this study also showed a clear correlation between DSC-CBF and ASL-CBF. Recent studies showed that PLD is usually chosen between 1,500 and 2,000 ms in the clinical use of pCASL, which can better show true cerebral perfusion (Qiu et al., 2012; Wang et al., 2012; Han et al., 2017; Tong et al., 2020). In this study, however, we chose two PLDs, 1,500 and 2,500 ms. CBF in patients with MMD is very complicated, and we found that the delay time of 2,500 ms was better correlated with DSC and can more accurately assess CBF and collateral circulation in patients with MMD.

MMD is a cerebrovascular disease with progressive stenosis and occlusion of the distal internal carotid artery and the proximal middle cerebral artery with massive collateral circulation. Its cerebral hemodynamics is very complex, but the correct assessment of cerebral perfusion is an important

TABLE 4 Comparison Alberta Stroke Program Early CT Score (ASPECTS) area ischemia scores before and after revascularization.

CBF	Before revascularization	After revascularization	*t*	*P*-values
ASL-CBF (1,500 ms)	5.1 ± 3.3	7.9 ± 2.2	−3.052	0.003
ASL-CBF (2,500 ms)	4.8 ± 3.3	7.5 ± 2.3	−4.415	0.000
DSC-CBF	5.2 ± 2.1	8.5 ± 2.4	−4.122	0.000

factor in the choice of treatment and prognosis of patients with MMD. DSC cerebral perfusion technique is very common in the clinical application of MMD, and it can provide four parameters; the importance of its value has been fully affirmed in clinical practice. The combination of DSC-CBF with rMTT and TTP can accurately identify the areas of abnormal cerebral hypoperfusion in patients with MMD before operation and evaluate the changes in cerebral perfusion after the operation (Hirai et al., 2017). The disadvantages of DSC are traumatic examination, the need for injection of contrast, and semiquantitative measurements. ASL cerebral perfusion techniques are increasingly used in clinical practice because the advantages are that it does not require the injection of contrast agents, can be repeated, and can be completely quantified. The importance of ASL has been well validated in the study of ischemic brain diseases, and reduced CBF can cause irreversible damage to brain tissue, thereby increasing the risk of stroke (Noguchi et al., 2013; Soman et al., 2020).

For patients with MMD, accurate assessment of cerebral perfusion before and after surgery is very important to evaluate the therapeutic effect and prognosis. In this study, cerebral perfusion was assessed through preoperative and postoperative ASPECTS area ischemia scores. The consistency of preoperative and postoperative ASPECTS area ischemia scores of the assessment of DSC-CBF, ASL-CBF (PLD = 1,500 ms), and ASL-CBF (PLD = 2,500 ms) was good. In addition, the difference of preoperative ASPECTS area ischemia scores between DSC-CBF, ASL-CBF (PLD = 1,500 ms), and ASL-CBF (PLD = 2,500 ms) and the difference of postoperative ASPECTS area ischemia scores between DSC-CBF, ASL-CBF (PLD = 1,500 ms), and ASL-CBF (PLD = 2,500 ms) were not statistically significant ($p > 0.05$). The differences between preoperative and postoperative ASPECTS area ischemia scores using these three methods of DSC-CBF, ASL-CBF (PLD = 1,500 ms), and ASL-CBF (PLD = 2,500 ms) were statistically significant, and the postoperative scores were all greater than the preoperative scores. This suggests that ASL and DSC had consistent results in assessing preoperative and postoperative hypoperfusion areas of ASPECTS areas in patients with MMD and that both can accurately assess changes in postoperative CBF. Therefore, ASL was an imaging method that can replace DSC to evaluate cerebral perfusion changes before and after surgery in patients with MMD.

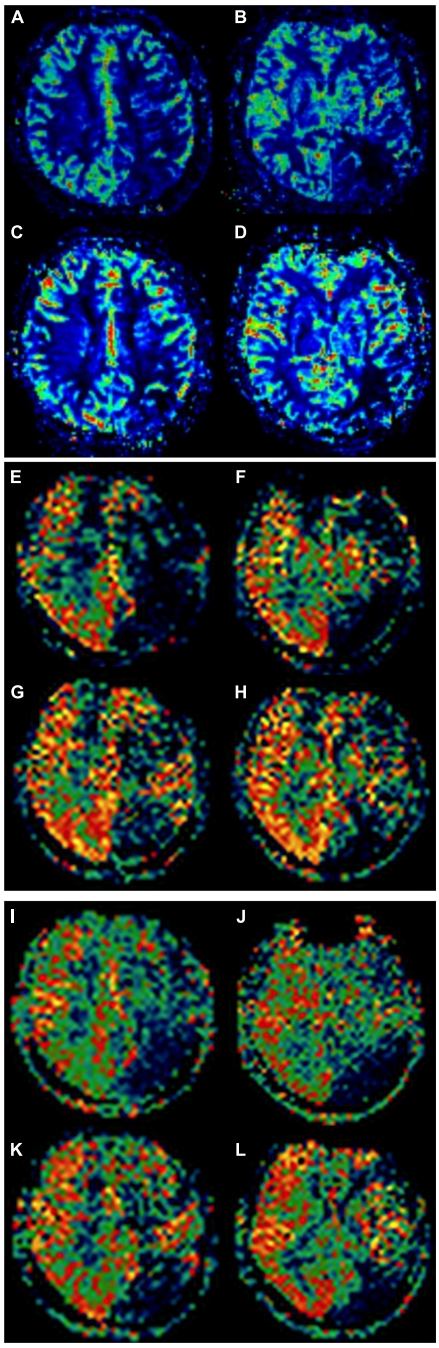

FIGURE 2
A 51-year-old female patient with moyamoya disease (MMD) underwent encephaloduroarteriosynangiosis (EDAS) on the left side. Alberta Stroke Program Early CT Score (ASPECTS) area ischemia scores of dynamic susceptibility contrast-cerebral blood flow (DSC-CBF) before revascularization were 5 points **(A,B)**. ASPECTS area ischemia scores after revascularization were 8 points **(C,D)**. ASPECTS area ischemia scores of arterial spin labeling (ASL)-CBF (1,500 ms) before revascularization were 5 points **(E,F)**. ASPECTS area ischemia scores after revascularization were 9 points **(G,H)**. ASPECTS area ischemia scores of ASL-CBF (2,500 ms) before revascularization was 4 points **(I,J)**. ASPECTS area ischemia scores after revascularization were 8 points **(K,L)**.

This study has several limitations. First, 3D pCASL with two single PLD times and only one parameter of CBF was compared with DSC-CBF. A subsequent comparative analysis of multi-delay ASL and DSC will be performed. Second, this study used the ratio of ASL-CBF and DSC-CBF to the CBF of the ipsilateral cerebellar hemisphere for correlation analysis, without direct use of ASL-CBF quantitative parameter values. Finally, for patients with MMD, ASL (PLD = 2,500 ms) can more accurately show cerebral blood perfusion, and further study with larger samples is needed.

Conclusion

In this study, there was a significant correlation between ASL-CBF and DSC-CBF in patients with MMD. Both ASL-CBF and DSC-CBF can evaluate cerebral perfusion before and after surgery. ASL, as a cerebral perfusion examination method without a contrast agent, can replace DSC as an imaging method for the evaluation of cerebral perfusion in patients with MMD.

Data availability statement

The raw data supporting the conclusions of this article will be made available by the authors, without undue reservation.

Ethics statement

This study has been approved by the appropriate Ethics Committee of the Chinese PLA General Hospital. Written informed consent to participate in this study was provided by the participants' legal guardian/next of kin. Written informed consent was obtained from the individual(s), and minor(s)' legal guardian/next of kin, for the publication of any potentially identifiable images or data included in this article.

Author contributions

HZ drafted the manuscript. JC and CH conceived and designed the study. ML and FS analyzed the data. SL, DL, and XS were responsible for the collection of data and image analysis. All authors contributed to the article and approved the submitted version.

Acknowledgments

We thank Yao for his technical support for this article.

Conflict of interest

The authors declare that the research was conducted in the absence of any commercial or financial relationships that could be construed as a potential conflict of interest.

Publisher's note

All claims expressed in this article are solely those of the authors and do not necessarily represent those of their affiliated organizations, or those of the publisher, the editors and the reviewers. Any product that may be evaluated in this article, or claim that may be made by its manufacturer, is not guaranteed or endorsed by the publisher.

Supplementary material

The Supplementary Material for this article can be found online at: https://www.frontiersin.org/articles/10.3389/fnins.2022.944246/full#supplementary-material

SUPPLEMENTARY IMAGE 1
Correlative scatter plots of the supply territories of ACA-left between $DSC\text{-}CBF_{relative}$ and $ASL\text{-}CBF_{relative}$ (1500 ms) before revascularization.

SUPPLEMENTARY IMAGE 2
Correlative scatter plots of the supply territories of ACA-left between $DSC\text{-}CBF_{relative}$ and $ASL\text{-}CBF_{relative}$ (2500 ms) before revascularization.

SUPPLEMENTARY IMAGE 3
Correlative scatter plots of the supply territories of ACA-right between $DSC\text{-}CBF_{relative}$ and $ASL\text{-}CBF_{relative}$ (1500 ms) before revascularization.

SUPPLEMENTARY IMAGE 4
Correlative scatter plots of the supply territories of ACA- right between $DSC\text{-}CBF_{relative}$ and $ASL\text{-}CBF_{relative}$ (2500 ms) before revascularization.

SUPPLEMENTARY IMAGE 5
Correlative scatter plots of the supply territories of MCA-left between $DSC\text{-}CBF_{relative}$ and $ASL\text{-}CBF_{relative}$ (1500 ms) before revascularization.

SUPPLEMENTARY IMAGE 6
Correlative scatter plots of the supply territories of MCA-left between $DSC\text{-}CBF_{relative}$ and $ASL\text{-}CBF_{relative}$ (2500 ms) before revascularization.

SUPPLEMENTARY IMAGE 7
Correlative scatter plots of the supply territories of MCA-right between $DSC\text{-}CBF_{relative}$ and $ASL\text{-}CBF_{relative}$ (1500 ms) before revascularization.

SUPPLEMENTARY IMAGE 8
Correlative scatter plots of the supply territories of MCA-right between $DSC\text{-}CBF_{relative}$ and $ASL\text{-}CBF_{relative}$ (2500 ms) before revascularization.

SUPPLEMENTARY IMAGE 9
Correlative scatter plots of the supply territories of PCA-left between $DSC\text{-}CBF_{relative}$ and $ASL\text{-}CBF_{relative}$ (1500 ms) before revascularization.

SUPPLEMENTARY IMAGE 10
Correlative scatter plots of the supply territories of PCA-left between $DSC\text{-}CBF_{relative}$ and $ASL\text{-}CBF_{relative}$ (2500 ms) before revascularization.

SUPPLEMENTARY IMAGE 11
Correlative scatter plots of the supply territories of PCA-right between $DSC\text{-}CBF_{relative}$ and $ASL\text{-}CBF_{relative}$ (1500 ms) before revascularization.

SUPPLEMENTARY IMAGE 12
Correlative scatter plots of the supply territories of PCA-right between $DSC\text{-}CBF_{relative}$ and $ASL\text{-}CBF_{relative}$ (2500 ms) before revascularization.

References

Alsop, D. C., Detre, J. A., Golay, X., Günther, M., Hendrikse, J., Hernandez-Garcia, L., et al. (2015). Recommended implementation of arterial spinlabeled perfusion MRI for clinical applications: a consensus of the ISMRM perfusion study group and the European consortium for ASL in dementia. *Magn. Reson. Med.* 73, 102–116. doi: 10.1002/mrm.25197

Bang, O. Y., Chung, J. W., Kim, D. H., Won, H. H., Yeon, J. Y., Ki, C. S., et al. (2020). Moyamoya disease and spectrums of RNF213 vasculopathy. *Transl. Stroke Res.* 11, 580–589. doi: 10.1007/s12975-019-00743-6

Haller, S., Zaharchuk, G., Thomas, D. L., Lovblad, K. O., Barkhof, F., and Golay, X. (2016). Arterial spin labeling perfusion of the brain: emerging clinical applications. *Radiology* 281, 337–356. doi: 10.1148/radiol.2016150789

Han, P. K., Choi, S. H., and Park, S. H. (2017). Investigation of control scans in pseudo-continuous arterial spin labeling (pCASL): strategies for improving sensitivity and reliability of pCASL. *Magn. Reson. Med.* 78, 917–929. doi: 10.1002/mrm.26474

Havsteen, I., Nybing, J., Christensen, H., and Christensen, A. F. (2018). Arterial spin labeling: a technical overview. *Acta Radiol.* 59, 1232–1238. doi: 10.1177/0284185117752552

Hirai, S., Inaji, M., Tanaka, Y., Hara, S., Nariai, T., and Maehara, T. (2017). Correlation between clinical presentations and hemodynamic parameters measured by dynamic susceptibility contrast magnetic resonance imaging in adult patients with Moyamoya disease. *J Stroke Cerebrovasc. Dis.* 26, 2814–2820. doi: 10.1016/j.jstrokecerebrovasdis.2017.06.057

Hu, H. H., Rusin, J. A., Peng, R., Shao, X., Smith, M., Krishnamurthy, R., et al. (2019). Multi-phase 3D arterial spin labeling brain MRI in assessing cerebral blood perfusion and arterial transit times in children at 3T. *Clin. Imaging.* 53, 210–220. doi: 10.1016/j.clinimag.2018.11.001

Ishii, Y., Nariai, T., Tanaka, Y., Mukawa, M., Inaji, M., Maehara, T., et al. (2014). Practical clinical use of dynamic susceptibility contrast magnetic resonance imaging for the surgical treatment of Moyamoya disease. *Neurosurgery* 74, 302–309. doi: 10.1227/NEU.0000000000000266

Ishii, Y., Tanaka, Y., Momose, T., Yamashina, M., Sato, A., Wakabayashi, S., et al. (2017). Chronologic evaluation of cerebral hemodynamics by dynamic susceptibility contrast magnetic resonance imaging after indirect bypass surgery for Moyamoya disease. *World Neurosurg.* 108, 427–435. doi: 10.1016/j.wneu.2017.09.001

Kohno, N., Okada, K., Yamagata, S., Takayoshi, H., and Yamaguchi, S. (2016). Distinctive patterns of three-dimensional arterial spin-labeled perfusion magnetic resonance imaging in subtypes of acute ischemic stroke. *J. Stroke Cerebrovasc. Dis.* 25, 1807–1812. doi: 10.1016/j.jstrokecerebrovasdis.2016.03.035

Nery, F., Gordon, I., and Thomas, D. L. (2018). Non-invasive renal perfusion imaging using arterial spin labeling MRI: challenges and opportunities. *Diagnostics* 8:2. doi: 10.3390/diagnostics8010002

Noguchi, T., Kawashima, M., Nishihara, M., Hirai, T., Matsushima, T., and Irie, H. (2013). Arterial spin-labeling MR imaging in Moyamoya disease compared with clinical assessments and other MR imaging findings. *Eur. J. Radiol.* 82, e840–e847. doi: 10.1016/j.ejrad.2013.08.040

Qiao, P. G., Han, C., Zuo, Z. W., Wang, Y. T., Pfeuffer, J., Duan, L., et al. (2017). Clinical assessment of cerebral hemodynamics in Moyamoya disease via multiple inversion time arterial spin labeling and dynamic susceptibility contrast-magnetic resonance imaging: a comparative study. *J. Neuroradiol.* 44, 273–280. doi: 10.1016/j.neurad.2016.12.006

Qiu, D., Straka, M., Zun, Z., Bammer, R., Moseley, M. E., and Zaharchuk, G. (2012). CBF measurements using multidelay pseudo continuous and velocity-selective arterial spin labeling in patients with long arterial transit delays: comparison with xenon CT CBF. *J. Magn. Reson. Imaging.* 36, 110–119. doi: 10.1002/jmri.23613

Shao, X., Liu, D., Martin, T., Chanlaw, T., Devaskar, S. U., Janzen, C., et al. (2018). Measuring human placental blood flow with multidelay 3D GRASE pseudocontinuous arterial spin labeling at 3T. *J. Magn. Reson. Imaging* 47, 1667–1676. doi: 10.1002/jmri.25893

Soman, S., Dai, W., Dong, L., Hitchner, E., Lee, K., Baughman, B. D., et al. (2020). Identifying cardiovascular risk factors that impact cerebrovascular reactivity: an ASL MRI study. *J. Magn. Reson. Imaging.* 51, 734–747. doi: 10.1002/jmri.26862

Tatu, L., Moulin, T., Bogousslavsky, J., and Duvernoy, H. (1998). Arterial territories of the human brain: cerebral hemispheres. *Neurology* 50, 1699–1708. doi: 10.1212/wnl.50.6.1699

Tong, Y., Jezzard, P., Okell, T. W., and Clarke, W. T. (2020). Improving PCASL at ultra-high field using a VERSE-guided parallel transmission strategy. *Magn. Reson. Med.* 84, 777–786. doi: 10.1002/mrm.28173

Wang, D. J., Alger, J. R., Qiao, J. X., Gunther, M., Pope, W. B., Saver, J. L., et al. (2013). Multi-delaymulti-parametric arterial spin-labeled perfusion MRI in acute ischemic stroke-Comparison with dynamic susceptibility contrast enhanced perfusion imaging. *Neuroimage Clin.* 3, 1–7. doi: 10.1016/j.nicl.2013.06.017

Wang, D. J., Alger, J. R., Qiao, J. X., Hao, Q., Hou, S., Fiaz, R., et al. (2012). The value of arterial spin labeled perfusion imaging in acute ischemic stroke: comparison with dynamic susceptibility contrast-enhanced MRI. *Stroke* 43, 1018–1024. doi: 10.1161/STROKEAHA.111.631929

Wang, R., Yu, S., Alger, J. R., Zuo, Z., Chen, J., Wang, R., et al. (2014). Multi-delay arterial spin labeling perfusion MRI in moyamoya disease–comparison with CT perfusion imaging. *Eur. Radiol.* 24, 1135–1144. doi: 10.1007/s00330-014-3098-9

Wintermark, M., Sesay, M., Barbier, E., Borbély, K., Dillon, W. P., Eastwood, J. D., et al. (2005). Comparative overview of brain perfusion imaging techniques. *Stroke* 36, e83–e99. doi: 10.1161/01.STR.0000177884.72657.8b

Ye, F. Q., Berman, K. F., Ellmore, T., Esposito, G., van Horn, J. D., Yang, Y., et al. (2000). H(2)(15)O PET validation of steady-state arterial spin tagging cerebral blood flow measurements in humans. *Magn. Reson. Med.* 44, 450–456. doi: 10.1002/1522-2594(200009)44:3<450::aid-mrm16<3.0.co;2-0

Zhang, J., Xia, C., Liu, Y., Qian, W., Peng, W., Liu, K., et al. (2018). Comparative study of MR mTI-ASL and DSC-PWI in evaluating cerebral hemodynamics of patients with Moyamoya disease. *Medicine* 97:e12768. doi: 10.1097/MD.0000000000012768

frontiers | Frontiers in Neuroscience

TYPE Original Research
PUBLISHED 13 September 2022
DOI 10.3389/fnins.2022.977145

Check for updates

OPEN ACCESS

EDITED BY
Zhengjia Dai,
Sun Yat-sen University, China

REVIEWED BY
Zhiqiang Zhang,
Nanjing University School of Medicine, China
Akira Matsushima,
Shinshu University, Japan
Xiaochun Wang,
First Hospital of Shanxi Medical University, China

*CORRESPONDENCE
Guolin Ma
maguolin1007@qq.com
Linwei Zhang
zhanglw999@hotmail.com

SPECIALTY SECTION
This article was submitted to Brain Imaging Methods, a section of the journal Frontiers in Neuroscience

RECEIVED 24 June 2022
ACCEPTED 24 August 2022
PUBLISHED 13 September 2022

CITATION
Liu B, Yang A, Gao W, Chen Y, Wang Y, Liu X, Lv K, Zhang L and Ma G (2022) Altered cerebral blood flow in patients with spinocerebellar degeneration. *Front. Neurosci.* 16:977145. doi: 10.3389/fnins.2022.977145

COPYRIGHT
© 2022 Liu, Yang, Gao, Chen, Wang, Liu, Lv, Zhang and Ma. This is an open-access article distributed under the terms of the Creative Commons Attribution License (CC BY). The use, distribution or reproduction in other forums is permitted, provided the original author(s) and the copyright owner(s) are credited and that the original publication in this journal is cited, in accordance with accepted academic practice. No use, distribution or reproduction is permitted which does not comply with these terms.

Altered cerebral blood flow in patients with spinocerebellar degeneration

Bing Liu[1,2], Aocai Yang[1,2], Wenwen Gao[1,3], Yue Chen[1,3], Yige Wang[1,2], Xiuxiu Liu[1,3], Kuan Lv[1,3], Linwei Zhang[4]* and Guolin Ma[1,2]*

[1]Department of Radiology, China-Japan Friendship Hospital, Beijing, China, [2]Graduate School of Peking Union Medical College, Chinese Academy of Medical Sciences and Peking Union Medical College, Beijing, China, [3]Department of Radiology, Peking University China-Japan Friendship School of Clinical Medicine, Beijing, China, [4]Department of Neurology, China-Japan Friendship Hospital, Beijing, China

Objectives: Spinocerebellar degeneration (SCD) comprises a multitude of disorders with sporadic and hereditary forms, including spinocerebellar ataxia (SCA). Except for progressive cerebellar ataxia and structural atrophy, hemodynamic changes have also been observed in SCD. This study aimed to explore the whole-brain patterns of altered cerebral blood flow (CBF) and its correlations with disease severity and psychological abnormalities in SCD *via* arterial spin labeling (ASL).

Methods: Thirty SCD patients and 30 age- and sex-matched healthy controls (HC) were prospectively recruited and underwent ASL examination on a 3.0T MR scanner. The Scale for Assessment and Rating of Ataxia (SARA) and the International Cooperative Ataxia Rating Scale (ICARS) scores were used to evaluate the disease severity in SCD patients. Additionally, the status of anxiety, depression and sleep among all patients were, respectively, evaluated by the Self-Rating Anxiety Scale (SAS), Self-Rating Depression Scale (SDS) and Self-Rating Scale of Sleep (SRSS). We compared the whole-brain CBF value between SCD group and HC group at the voxel level. Then, the correlation analyses between CBF and disease severity, and psychological abnormalities were performed on SCD group.

Results: Compared with HC, SCD patients demonstrated decreased CBF value in two clusters (FWE corrected $P < 0.05$), covering bilateral dentate and fastigial nuclei, bilateral cerebellar lobules I-IV, V and IX, left lobule VI, right lobule VIIIb, lobules IX and X of the vermis in the cerebellar Cluster 1 and the dorsal part of raphe nucleus in the midbrain Cluster 2. The CBF of cerebellar Cluster 1 was negatively correlated with SARA scores (Spearman's rho = −0.374, $P = 0.042$) and SDS standard scores (Spearman's rho = −0.388, $P = 0.034$), respectively. And, the CBF of midbrain Cluster 2 also had negative correlations with SARA scores (Spearman's rho = −0.370, $P = 0.044$) and ICARS scores (Pearson $r = -0.464$, $P = 0.010$).

Conclusion: The SCD-related whole-brain CBF changes mainly involved in the cerebellum and the midbrain of brainstem, which are partially overlapped

with the related function cerebellar areas of hand, foot and tongue movement. Decreased CBF was related to disease severity and depression status in SCD. Therefore, CBF may be a promising neuroimaging biomarker to reflect the severity of SCD and suggest mental changes.

KEYWORDS

spinocerebellar degeneration, spinocerebellar ataxia, cerebral blood flow, arterial spin labeling, cerebellum

Introduction

Spinocerebellar degeneration (SCD) comprises a group of rare neurodegenerative diseases, including sporadic SCD [e.g., multiple system atrophy (MSA) cerebellar type] and hereditary SCD (e.g., autosomal dominant or recessive cerebellar ataxias). Neuropathological studies in SCD have revealed neuronal cell loss in the cerebellum, brainstem and spinal cord, occasionally in the basal ganglia and cerebral cortex (Yamada et al., 2016; Iwabuchi et al., 2022). Generally the cerebellum is most severely involved, with progressive cerebellar ataxia and atrophy as the main characteristics of SCD, but patients may also appear truncal and limb ataxias, dysarthria, dysphagia, pyramidal and extrapyramidal signs, oculomotor deficits (nystagmus, hypermetria/hypometria of saccades), and autonomic disorders (Kawai et al., 2009). In addition, patients with SCD may have a higher prevalence of non-motor psychological symptoms such as depression, anxiety and sleep disorders which lead to the strong negative impact on their quality of life (Pedroso et al., 2011; Silva et al., 2015; Mastammanavar et al., 2020). Therefore, particular attention should also be paid to the mental health of SCD patients. Except for brain structural alterations affected by local pathology, these clinical manifestations and psychological impairments are likely to be associated with brain functional changes as well because the brain activity measured by hemodynamics or metabolism can reflect the underlying neuronal events. One of the important indicators for hemodynamic change reflection and cerebral perfusion evaluation is the cerebral blood flow (CBF) value. Cerebellar hemodynamic changes such as hypoperfusion have been detected in SCD patients with decreased CBF measured by positron emission tomography (PET) or single-photon emission computed tomography (SPECT) (Kondo et al., 1993; Gilman et al., 1995; De Michele et al., 1998; Honjo et al., 2004), indicating the reduction in neuronal activity. Although PET has been regarded as the gold standard for CBF measurement, ionizing radiation and contrast injection during PET/SPECT become the bottleneck of its extensive application in clinical routine.

Nowadays, as a completely non-invasive and non-radiative magnetic resonance imaging (MRI) technique with magnetically labeled blood water rather than exogenous contrast agents serving as the flow tracer, arterial spin labeling (ASL) imaging (Detre et al., 1992) has increasingly become the proxy measure for blood flow to provide MR-based CBF quantification. Currently, pseudo-continuous ASL (PCASL) (Dai et al., 2008) is the first choice for clinical application (Alsop et al., 2015) due to its higher signal-to-noise ratio (SNR). Demonstrating good correlation and agreement with PET and SPECT (Detre and Alsop, 1999; Ikawa et al., 2018), ASL MRI has already been used for evaluating the aberrant cerebral perfusion in neurodegenerative diseases such as Parkinson's disease (PD) and MSA (Lin et al., 2017; Erro et al., 2020; Ivanidze et al., 2020), but rarely in SCD. A Previous study retrospectively estimated CBF values in 4 cerebellar regions of 16 patients with SCD and demonstrated lower cerebellar CBF (Ikawa et al., 2018). Another study (Xing et al., 2014) had applied ASL on one specific subtype of SCD, namely spinocerebellar ataxia (SCA) type 3 (SCA3), and found decreased regional CBF (rCBF) in the pons, cerebellar dentate nucleus and cerebellar cortex of the onset SCA3 group. However, these studies only analyzed CBF values that were extracted from the predefined regions of interest (ROIs), without considering the whole brain. Given that SCD contains various subtypes and each subtype might have its own representative brain regions, the selection of ROIs becomes difficult in patients with SCD and the results of perfusion pattern would be influenced by the chosen ROIs. To our knowledge, the commonality of CBF alteration explored at the whole-brain level and the associations between hemodynamics and clinical measures (especially psychological scales) in SCD remain largely unknown.

As a data-driven method, voxel-based whole-brain analysis can investigate the spatial specificity of CBF changes without being limited to specific brain regions, which may be more appropriate in the comprehensive comparison between patients with SCD and the healthy controls. Besides, given the importance of visualization in neuroimaging, CBF results should be displayed appropriately, especially in the infratentorial space. To figure this out, our study applied a high-resolution spatially unbiased atlas template of the cerebellum and brainstem spatially unbiased infratentorial template (SUIT) (Diedrichsen, 2006) to better characterize

cerebellar CBF alterations in SCD patients. Therefore, this study aimed to investigate the whole-brain pattern of altered CBF at the voxel level in patients with SCD by using the three-dimensional (3D) PCASL. Normalized CBF was used for narrowing the inter-subject difference. And we further explored the associations between CBF changes and clinical measures (especially the disease severity and psychological abnormalities) of SCD in brain regions with altered hemodynamics through regional analysis.

Materials and methods

Subjects

This study was approved by the Ethics Committee of China-Japan Friendship Hospital. All subjects had obtained written informed consent.

From June 2021 to November 2021, 30 SCD patients (20 males and 10 females; mean age, 45.6 ± 12.8 years; age range, 25–67 years; median disease duration, 6 years) and 30 age- and sex-matched healthy controls (HC) (18 males and 12 females; mean age, 45.6 ± 14.9 years; age range, 24–68 years) were prospectively recruited into this study at the China-Japan Friendship Hospital. Twenty six of the 30 SCD patients were diagnosed as hereditary SCD, including 23 SCA patients (SCA1, n = 1; SCA2, n = 2; and SCA3, n = 20) and 3 autosomal recessive cerebellar ataxias (ARCA) patients (*ANO10*-ARCA, n = 1; *SPG7*-ARCA, n = 1; *NPC1*-ARCA, n = 1). And the other 4 patients were diagnosed with sporadic MSA cerebellar type (MSA-C). The inclusion criteria for patients were: (1) diagnosed as SCD by trained neurologists according to the neurological manifestations, genetic tests, family history, and routine brain MRI findings, thereinto, the hereditary SCD and its specific subtypes (SCA or ARCA) should be proven by genetic testing and the sporadic MSA-C (probable or possible) should be diagnosed by the second consensus statement of 2008 (Gilman et al., 2008); (2) age ≥ 18 years; (3) right-handed. The exclusion criteria for patients were as follows: (1) with contraindications to MRI examination; (2) having the history of other neurological diseases, such as brain trauma, strokes and tumors; (3) artifacts in MRI images. Recruitment of HC from the local communities was based on the following inclusion criteria: (1) without the history of any neuropsychiatric disorders; (2) age ≥ 18 years; (3) right-handed. The exclusion criteria for HC were the same as that for SCD patients.

Clinical characteristics

Demographic information collection and neurological evaluation were performed on the MRI scanning day, before the MR data acquisition. The Scale for Assessment and Rating of Ataxia (SARA) (Schmitz-Hübsch et al., 2006) and the International Cooperative Ataxia Rating Scale (ICARS) (Trouillas et al., 1997) scores were used to quantify neurological manifestations and reflect the disease severity in SCD patients. In addition, we evaluate the status of depression, anxiety and sleep among all patients according to the Self-Rating Anxiety Scale (SAS) (Zung, 1971), Self-Rating Depression Scale (SDS) (Zung, 1972) and Self-Rating Scale of Sleep (SRSS) (Li, 2012) to reflect psychological impairments in SCD group. For SAS and SDS, we used the standard score rather than the total score for anxiety and depression status assessment. Only when the standard SAS score ≥ 50 or the standard SDS score ≥ 53 could patients themselves be considered in anxious or depressed status, respectively.

Magnetic resonance imaging data acquisition

MRI scans of all subjects were performed on a 3.0T MR scanner (General Electric, Discovery MR750, Milwaukee, WI, United States) with an 8-channel head coil. Acquisition parameters for resting-state 3D PCASL were: slice thickness = 4 mm, repetition time (TR) = 4,817 ms, echo time (TE) = 14.6 ms, flip angle = 111°, post label delay = 1,525 ms, spiral in readout of 12 arms with 1,024 sample points, field of view (FOV) = 240 mm × 240 mm, voxel size = 1.875 mm × 1.875 mm, number of excitations (NEX) = 3, matrix = 128 × 128. The total acquisition time for the resting state ASL scan was 6 min 54 s. Earplugs and paddings were provided to all subjects for noise reduction, and foam paddings were given to restrict head motion. During the resting-state ASL scans, all subjects were asked to keep their eyes closed without falling asleep, relax and think nothing special.

Reconstruction and post processing of cerebral blood flow

Briefly, the PCASL difference images were calculated after the subtraction of the label images from the control images. The CBF maps were subsequently derived from the ASL difference images with Functool perfusion software in GE (General Electric Healthcare). The detailed calculation procedures have been described in a previous study (Xu et al., 2010).

CBF image processing and further voxel-based analysis were handled in a MATLAB-based software, Statistical Parametric Mapping 8 (SPM8).[1] First, the CBF images of all subjects were

1 https://www.fil.ion.ucl.ac.uk/spm/software/

non-linearly coregistered to a PET-perfusion template of SPM8 and spatially warped into the Montreal Neurological Institute (MNI) space, meanwhile the voxel size was resampled into 2 mm × 2 mm × 2 mm. After the spatial standardization, the CBF value of each voxel across the whole brain was normalized by the mean division method (Aslan and Lu, 2010). And a Gaussian kernel of 8 mm × 8 mm × 8 mm full-width at half maximum (FWHM) was applied for the spatial smooth to improve the whole-brain statistical analysis.

Each cluster with significant group differences compared in the voxelwise whole-brain manner would be regarded as the ROI in the following regional CBF analyses. A binary mask of the cluster ROI was firstly generated by the xjView toolbox (Version 10.0)[2] and then loaded into Data Processing and Analysis of Brain Imaging (DPABI, Version 5.1) (Yan et al., 2016) toolbox to calculate the normalized CBF values within that mask. For each subject, the mean normalized CBF of each significant cluster was extracted and used for ROI-based regional analyses.

Statistical analysis

Whole-brain analyses of cerebral blood flow

Voxel-based intergroup differences in normalized CBF values of whole-brain were analyzed using independent two-sample *t*-test in SPM8. Age and sex were induced as the nuisance variables in statistical model. Correction of multiple comparisons was executed using the family-wise error (FWE) method with a corrected voxel-level threshold of $P < 0.05$ and cluster size > 10 voxels.

Regional analyses of cerebral blood flow

ROI-based intergroup comparisons were analyzed by two-sample *t*-test in the SPSS software (Version 26.0, IBM Corp., Armonk, NY, United States). For SCD group, the ROI-based Pearson or Spearman correlation analyses were performed between normalized CBF values and clinical features (including disease duration, SARA scores, ICARS scores, SDS standard scores, SAS standard scores and SRSS scores). Significant threshold was set at $P < 0.05$.

Other statistical analyses

Other statistical analyses were also performed in the SPSS software, with graphs drawn in GraphPad Prism 9 (GraphPad Software, San Diego, CA, United States). The normality of data distribution was evaluated by the Shapiro-Wilk normality test. As for demographic comparisons between SCD patients and HCs, student's *t*-test was used for age and Pearson Chi-square ($\chi 2$) test was used for sex. Significant threshold was set at $P < 0.05$.

Visualization

Significant clusters of the whole-brain voxel-wise CBF analysis were visualized using MRIcron.[3] And clusters that located at the cerebellum were overlaid onto the coronal SUIT (Diedrichsen et al., 2009) to better display the involvement of the cerebellar lobules as well as the deep cerebellar nuclei. Specifically, the cerebellar-located clusters were also projected to the surface-based cerebellar flatmap (Diedrichsen and Zotow, 2015) using SUIT toolbox (Version 3.4)[4] implemented in SPM. The outline of surface-based clusters was further overlaid onto flatmaps for the anatomical orientation of cerebellar lobules I-X (both hemispheric and vermal) and the cerebellar movement orientation (Diedrichsen and Zotow, 2015), respectively.

Results

Demographic information and clinical characteristics

Demographic information and clinical characteristics of all SCD patients and healthy controls (HCs) are summarized in **Table 1**, with normal data shown in mean ± standard deviation (SD) and non-normal data shown in median (quartile). No significant group differences were found in age ($P = 0.993$) or sex ($P = 0.592$) between SCD group and HC group. In patients with SCD, disease duration ranged from 0 to 36 years with a median of 6 years. Total SARA scores of SCD group ranged between 1 and 36 with a median of 13, while total ICARS scores ranged from 0 to 88 with a mean of 41.0 ($SD = 22.0$). For three self-rating scales, the range of SAS standard scores was 25–71 with a mean of 47.8 ($SD = 12.0$); the range of SDS standard scores was also 25–71 with a median of 53, and that of SRSS scores was 12–43 with a mean of 25.7 ($SD = 8.1$). In addition, 15 of 30 SCD patients' SAS standard scores were 50 or more. And the percentage of patients with SDS standard score ≥ 53 was 50% as well. We also collected data for the presence of additional neurological manifestations (e.g., truncal and limb ataxias: 96.7%, pyramidal and extrapyramidal signs: 46.7%, oculomotor deficits: 86.7%, dysarthria: 86.7%, dysphagia: 46.7%, and autonomic disorders: 13.3%).

2 https://www.alivelearn.net/xjview

3 https://www.nitrc.org/projects/mricron/

4 https://www.diedrichsenlab.org/imaging/suit_flatmap.htm

TABLE 1 The demographical information and clinical characteristics of SCD group and HC group.

	SCD group (n = 30)	HC group (n = 30)	p-value
Age (years)	45.6 ± 12.8	45.6 ± 14.9	0.993[a]
Sex (M/F)	20/10	18/12	0.592[b]
Disease duration (years)	6.0 (3.0–10.0)[c]	N/A	N/A
SARA score	13.0 (10.0–20.5)[c]	N/A	N/A
ICARS score	41.0 ± 22.0	N/A	N/A
SAS standard score	47.8 ± 12.0	N/A	N/A
SDS standard score	53.0 (39.5–63.8)[c]	N/A	N/A
SRSS score	25.7 ± 8.1	N/A	N/A
Truncal and limb ataxias (n)	29 (96.7%)	N/A	N/A
Pyramidal and extrapyramidal signs (n)	14 (46.7%)	N/A	N/A
Oculomotor deficits (n)	26 (86.7%)	N/A	N/A
Dysarthria (n)	26 (86.7%)	N/A	N/A
Dysphagia (n)	14 (46.7%)	N/A	N/A
Autonomic disorders (n)	4 (13.3%)	N/A	N/A

[a]Two-sample student's t-test; [b]Pearson chi-squared test; [c]Non-normal data is shown as Median (Q1–Q3). Q1, first quartile; Q3, third quartile. M, male; F, female; SCD, spinocerebellar degeneration; SARA, scale for assessment and rating of ataxia (0 = no ataxia, 40 = most severe ataxia); ICARS, international cooperative ataxia rating scale (0 = no ataxia, 100 = most severe ataxia); SAS, self-rating anxiety scale; SDS, self-rating depression scale; SRSS, self-rating scale of sleep; N/A, not applicable.

Group differences in normalized cerebral blood flow

Whole-brain voxel-based analyses

In the whole-brain voxel-based analyses, the CBF group differences between the SCD patients and the HCs are shown in Table 2. For HC > SCD comparison, voxels that survived after the FWE correction at a voxel-level threshold of $P < 0.05$ and cluster size > 10 are mainly gathered in two clusters, namely Cluster 1 and Cluster 2. Cluster 1 was located at the cerebellum, with the vermis and bilateral cerebellar hemispheres involved, including AAL3 brain regions such as bilateral Cerebellum_4_5, Cerebellum_9 and Cerebellum_3, left Cerebellum_6, right Cerebellum_8, Vermis_4_5, Vermis_3, Vermis_10, Vermis_9 and Vermis_1_2. Other anatomy structures involved in Cluster 1 but not in AAL3 were culmen, dentate nuclei, cerebellar tonsil, fastigial nuclei, nodule, and declive. While Cluster 2 was found in the midbrain of brainstem with one meaningful AAL3-specific brain label Raphe_D, known as the dorsal part of raphe nucleus. For HC < SCD contrast, however, no brain regions or even voxels showed significantly increased CBF in SCD patients compared to HCs after FWE correction.

Figures 1, 2 show the detailed visualization for Cluster 1 and Cluster 2. In Figure 1A, the cerebellar-located Cluster 1, overlaid onto the SUIT template, shows its cover of bilateral dentate and fastigial nuclei, bilateral cerebellar lobules I-IV, V and IX, left lobule VI and right lobule VIIIb. While in Figure 1B, the smaller Cluster 2 is located on the midbrain of brainstem; and the AAL3 brain region Raphe_D is overlaid onto Cluster 2, showing its position in the midbrain. As the vermis has not been well demonstrated in the coronal slice view in Figure 1A, we further plotted the t-values of Cluster 1 to the SUIT flatmap, and generated a flat t-map displayed in Figure 2A. The outline of surface-based Cluster 1 is overlaid onto the anatomical orientation of cerebellar lobules I-X (both hemispheric and vermal) as well as the cerebellar movement orientation (Diedrichsen and Zotow, 2015) to form Figures 2B,C, respectively. According to Figure 2B, Cluster 1 also covers lobules IX and X of the vermis besides cerebellar hemispheric regions. And Figure 2C indicates the motor involvement of the foot (bilateral), hand (bilateral, more severe in right) and tongue.

Regional analyses

In the regional analyses based on the ROIs of significant clusters, results about intergroup comparison of normalized CBF values in Cluster 1 and Cluster 2 are shown in Figure 3 and Table 3. Compared to HC group (Cluster 1: 1.833 ± 0.141; Cluster 2: 1.823 ± 0.137), the normalized CBF values of Cluster 1 (1.493 ± 0.218) and Cluster 2 (1.542 ± 0.211) were both significantly decreased in SCD group with $P < 0.0001$.

Correlations between cerebral blood flow and clinical characteristics

The ROI-based correlations between normalized CBF values and the clinical-relevant demographic characteristics (disease duration), clinical severity (SARA and ICARS scores) or psychological scales (SDS, SAS and SRSS) were analyzed in both Cluster 1 and Cluster 2, with significant correlations depicted graphically in Figure 4. The normalized CBF value of SCD patients in Cluster 1 showed a negative correlation with SARA scores (Spearman's rho = –0.374, P = 0.042; Figure 4A) and standard SDS scores (Spearman's rho = –0.388, P = 0.034; Figure 4B), respectively. Although in Cluster 1 the normalized CBF was negatively correlated with ICARS scores (Pearson r = –0.226, P = 0.229), standard SAS scores (Pearson r = –0.245, P = 0.191) and SRSS scores (Pearson r = –0.149, P = 0.431), these correlations were not significant. For Cluster 2, the normalized CBF was significantly negatively correlated with both SARA scores (Spearman's rho = –0.370, P = 0.044; Figure 4C) and ICARS scores (Pearson r = –0.464, P = 0.010; Figure 4D),

TABLE 2 Brain regions with voxel-based significant group differences in normalized CBF.

Contrast	Cluster	Total voxels	*t*-value	Height threshold $T = 4.973$ [voxel level, $P < 0.05$ (FWE), k = 0, cluster size > 10]		Peak MNI coordinate (mm)		
				Brain region	No. of significant voxels	x	y	z
HC > SCD	Cluster 1	1,329	6.920	Culmen	585	10	-46	-18
				Vermis_4_5*	173			
				Cerebellum_4_5_L*	160			
				Dentate nuclei	143			
				Cerebellum_4_5_R*	123			
				Cerebellum_9_R*	103			
				Cerebellar tonsil	81			
				Fastigial nuclei	75			
				Nodule	73			
				Vermis_3*	67			
				Declive	53			
				Cerebellum_9_L*	49			
				Vermis_10*	40			
				Cerebellum_3_R*	36			
				Cerebellum_3_L*	27			
				Vermis_9*	24			
				Vermis_1_2*	24			
				Cerebellum_6_L*	21			
				Cerebellum_8_R*	16			
HC > SCD	Cluster 2	95	6.192	Midbrain	67	2	-26	-4
				Raphe_D*	11			

*Brain labels defined in AAL3. The Arabic numerals in the AAL3 brain labels indicated the lobule number of the cerebellar hemisphere or vermis. For example, the anatomical description for Cerebellum_4_5_L was the lobule IV, V of the left cerebellar hemisphere.

without showing any correlation with those three psychological scales (standard SAS scores: Pearson $r = -0.138$, $P = 0.467$; standard SDS scores: Spearman's rho = −0.174, $P = 0.358$; SRSS scores: Pearson $r = -0.339$, $P = 0.067$). For both two clusters, the negative correlations between normalized CBF and disease duration of SCD patients were statistically insignificant (Cluster 1: Spearman's rho = −0.218, $P = 0.248$; Cluster 2: Spearman's rho = −0.287, $P = 0.124$).

Discussion

In this study, we detected a whole-brain pattern of CBF alterations and assessed the relationships between CBF and clinical characteristics in patients with SCD using the non-invasive PCASL imaging technique. Our main findings are that: (1) compared with healthy controls, SCD patients showed hypoperfusion mainly in two clusters, with the involvement of several cerebellar lobules, cerebellar nuclei (dentate and fastigial) and part of the midbrain; (2) decreased CBF was associated with increased disease severity in both cerebellar and midbrain clusters; (3) mental disorder in terms of depression status was correlated with CBF in the cerebellar cluster.

The whole-brain voxel-based analysis demonstrated decreased normalized CBF, which approximately reflected the decline of brain neuronal activity and was predominantly distributed in the cerebellar Cluster 1 (bilateral dentate and fastigial nuclei, bilateral cerebellar lobules I-IV, V and IX, left lobule VI, right lobule VIIIb and lobules IX and X of the vermis) and in the midbrain Cluster 2 (dorsal part of raphe nucleus). Although we did not detect any hemodynamic changes in the cerebral regions, the hypoperfusion areas in our study are consistent with neuropathological findings that neuronal cell losses of SCD often happened in the cerebellar cortex (Purkinje cells), spinal cord and brainstem nuclei but occasionally associated with degeneration of the basal ganglia and cerebral cortex (Yamada et al., 2016). In addition, our MR-based CBF decline in patients with SCD is also coinciding with previous reports using PET and SPECT (Sun et al., 1994; De Michele et al., 1998; Sidtis et al., 2010; Braga-Neto et al., 2012, 2016). A previous ROI-based retrospective ASL MRI study also showed significantly reduced mean normalized

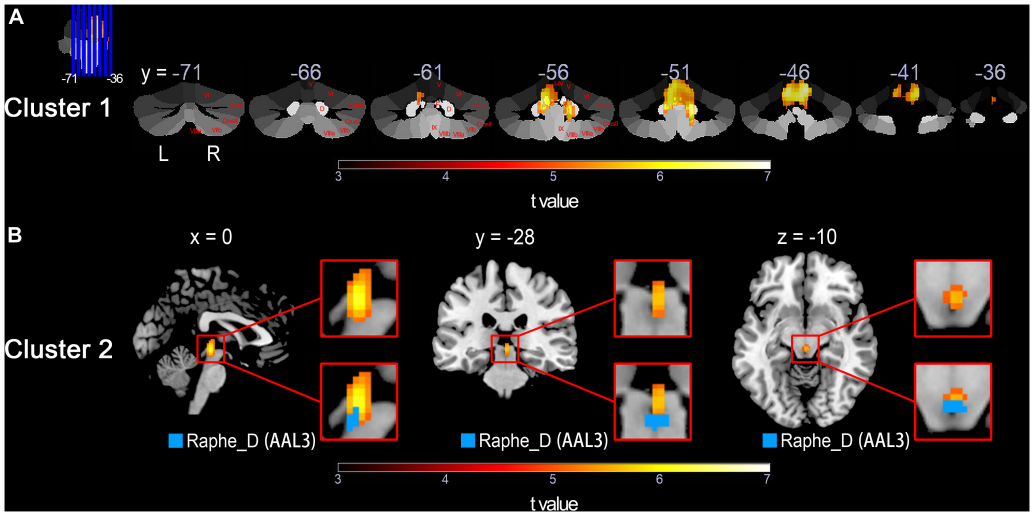

FIGURE 1
Detailed visualization for voxel-based HC > SCD comparison across groups using normalized CBF values performed by the two-sample *t*-test with a threshold of $P < 0.05$ (FWE corrected) and cluster size of 10 voxels. The warm color represents voxels with significantly decreased CBF in the SCD group compared with the HC group. Results of the HC < SCD comparison are not shown because no significant voxel was detected under the same FWE correction threshold and cluster size. **(A)** Cluster 1 shown in yellow/red, overlaid onto the cerebellar atlas (Diedrichsen et al., 2009) in coronal slices. Cerebellar lobules and nucleus are marked in red on the right cerebellum. **(B)** Top row: magnified Cluster 2 shown in yellow/red; Bottom row: Cluster 2 with AAL3 brain region mapped on. HC, healthy control; SCD, spinocerebellar degeneration; CBF, cerebral blood flow; FWE, family-wise error; Roman numerals I-X, number of cerebellar hemisphere lobules (Schmahmann et al., 1999); D, dentate nucleus; F, fastigial nucleus; Raphe_D, dorsal raphe nucleus (Rolls et al., 2020); L, left; R, right; x,y,z, space coordinates.

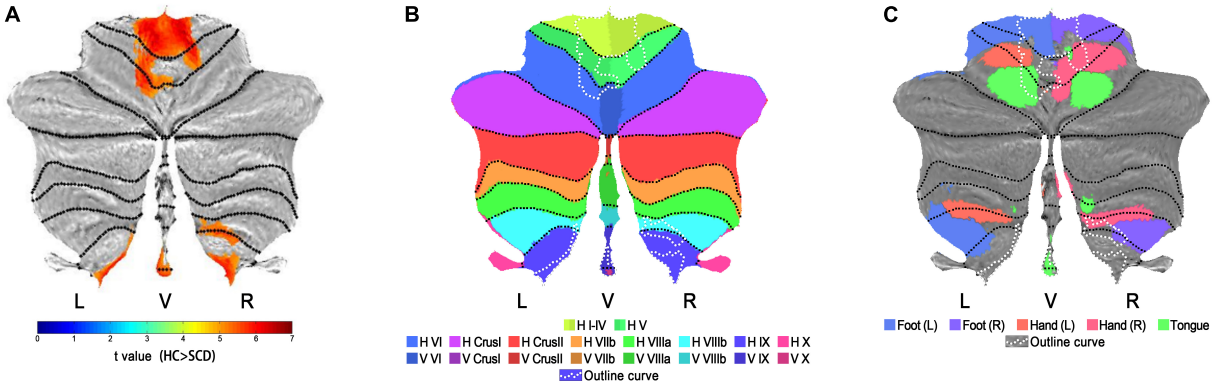

FIGURE 2
Visualization on flatmaps for cerebellar-located Cluster 1. **(A)** The t-map of Normalized CBF group results (HC > SCD) projected to the cerebellar SUIT flatmap. Regions displayed in warm colors represent the significant CBF decrease in SCD patients. **(B)** Outline curves of results in flatmap **(A)** shown in white dotted lines are overlaid onto the flatmap of anatomical distributions for cerebellar lobules I-X. Note that for lobule VI-X, two hemispheric and one vermal compartment (displayed in slightly different colors) are defined. **(C)** Outline curves of results in flatmap **(A)** shown in white dotted lines are overlaid onto the flatmap of the sensorimotor topography for activation related to hand, foot and tongue movement activations. HC, healthy control; SCD, spinocerebellar degeneration; L, left; R, right; V, vermis; H, hemisphere; Roman numerals I-X, number of cerebellar lobules (Schmahmann et al., 1999).

CBF in cerebellar cortices and crus in SCD (Ikawa et al., 2018). Furthermore, in patients with SCD subtypes, lower regional CBF (rCBF) values were detected by ASL in the ROIs of cerebellar cortex, cerebellar dentate nucleus, and pons in SCA3 (Xing et al., 2014) and by SPECT in the cerebellum and brainstem in MSA-C (Kimura et al., 2011). Compared to these studies that extracted and calculated CBF within their size-fixed or roughly hand-drawn single-slice ROIs, our data-driven voxel-level method could obtain the similar but more precise results and demonstrate the involved brain regions with more detail at the lobular level.

In cerebellar Cluster 1, affected cerebellar lobules I-IV and V belong to the anterior cerebellum which is thought to be important for motor control, whereas lobules VI, VIIIb and

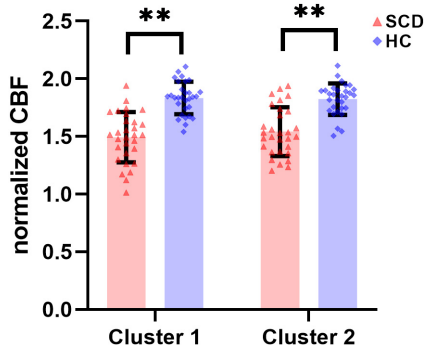

FIGURE 3
There were statistically significant differences in normalized CBF of ROI-based Cluster 1 and Cluster 2 between the SCD group and the HC group. SCD, spinocerebellar degeneration. ** indicates $P < 0.0001$.

TABLE 3 Results about ROI-based intergroup differences in CBF.

Regions	Normalized CBF		*T*-value	*p*-value
	SCD group	HC group		
Cluster 1	1.493 ± 0.218	1.833 ± 0.141	−7.179	<0.0001
Cluster 2	1.542 ± 0.211	1.823 ± 0.137	−6.127	<0.0001

IX belong to the posterior cerebellum which is more involved in cognitive processing (Stoodley and Schmahmann, 2018). Moreover, the posterior cerebellum (lobules VIIIb, IX and X) was found to be the primary cerebellar targets of SCA 10 and the affected regions would expand to the anterior cerebellum in later stages (Hernandez-Castillo et al., 2019). Thus, hypoperfusion in these cerebellar regions may contribute to the clinical motor symptoms in SCD and its subtypes. Interestingly, after overlying our cerebellar results onto the cerebellar movement orientation flatmap (Diedrichsen and Zotow, 2015) generated by using task-based data from $N = 100$ participants scanned in the Human Connectome Project (Van Essen et al., 2013) to figure out the activation impairments related to the simple movements, we found a lot of overlap in the foot (bilateral), hand (bilateral, more severe in right) and tongue movement areas. The overlap indicates that the decreased CBF in these common regions may represent the drop of neuronal activity which could contribute to clinical motor symptoms in our SCD patients such as limb ataxias, dysarthria and dysphagia. Among those five simple movements, the involvement of bilateral feet seems most severe. And the non-symmetrically involvement of hand may result from the right handedness.

Apart from cerebellar lobules, the dentate and fastigial nuclei in Cluster 1 also demonstrated decreased CBF. The dentate nuclei (DN) of the cerebellum, which could project output to non-motor areas of the prefrontal and posterior parietal cortex (Bostan et al., 2013), are characteristic sites of neurodegeneration in several SCD subtypes such as SCA3 and Friedreich's ataxia (Scherzed et al., 2012; Harding et al., 2016; Koeppen, 2018). The lower CBF in DN has also been detected using ASL in both onset and non-onset SCA3 patients (Xing et al., 2014). Together with DN, the fastigial nucleus (FN) is one of the ultimate integration stations and outputs of the spinocerebellum serving as a classical subcortical motor coordinator, holding a key position in the axial, proximal and ocular motor control by projecting to the medial descending systems and eye movement-related nuclei, and has also been implicated in the regulation of emotional activities (Zhang et al., 2016). Previous research on patients with SCA with saccadic intrusions (SCASI) also pointed out that FN played a critical role in eye movement, especially in programming sequences of saccades (King et al., 2011). It is worth noting that 86.7 percent of our SCD patients exist oculomotor deficits. And to the best of our knowledge, this is the first time that hypoperfusion has been identified in FN in patients with SCD. Thus, we speculate that the CBF decline in FN may contribute to motor symptoms especially the oculomotor deficits in SCD.

Similar to prior findings that identified decreased CBF in the brainstem (Sun et al., 1994; De Michele et al., 1998; Watanabe et al., 2005; Sidtis et al., 2010; Xing et al., 2014), our finding of Cluster 2 is situated in the midbrain of brainstem with the dorsal part of raphe nuclei involved in CBF decline. The raphe nuclei (RN), whose main neuronal components are serotonergic neurons, are distributed near the midline of the brainstem and the serotonergic projections participate in the regulation of motor, somatosensory and limbic systems and have been associated with sleep, depression and anxiety behavior (Hornung, 2003). Pathoanatomical studies suggested that marked neuronal loss in RN was observed in SCD, and damage to RN might contribute to the slowing of horizontal saccades (Rüb et al., 2003; Hellenbroich et al., 2006; Hoche et al., 2011). In addition, FN in Cluster 1 also receives serotonergic projections arising from the medullary/pontine reticular formation and RN (Bishop et al., 1988), which may indicates that hemodynamic damage of RN may affect the perfusion status in FN and the SCD-related eye movement function. According to a previous study, the baseline activity of raphe neurons increases in phase with swallowing (Ribeiro-do-Valle, 1997). And in this study, 46.7 percent of SCD patients suffered from dysphagia which may be associated with the decrease neuronal activity reflected by hypoperfusion in RN.

In terms of clinical characteristics, we found that SARA and ICARS scores were both significantly negatively correlated with the normalized CBF in Cluster 2. But in Cluster 1, only the SARA scores but not the ICARS scores significantly negatively correlated with the normalized CBF. The possible reason behind this might be the slight difference between ICARS and SARA. A previous study that compared ICARS scores with SARA scores among patients with SCD suggested that SARA was

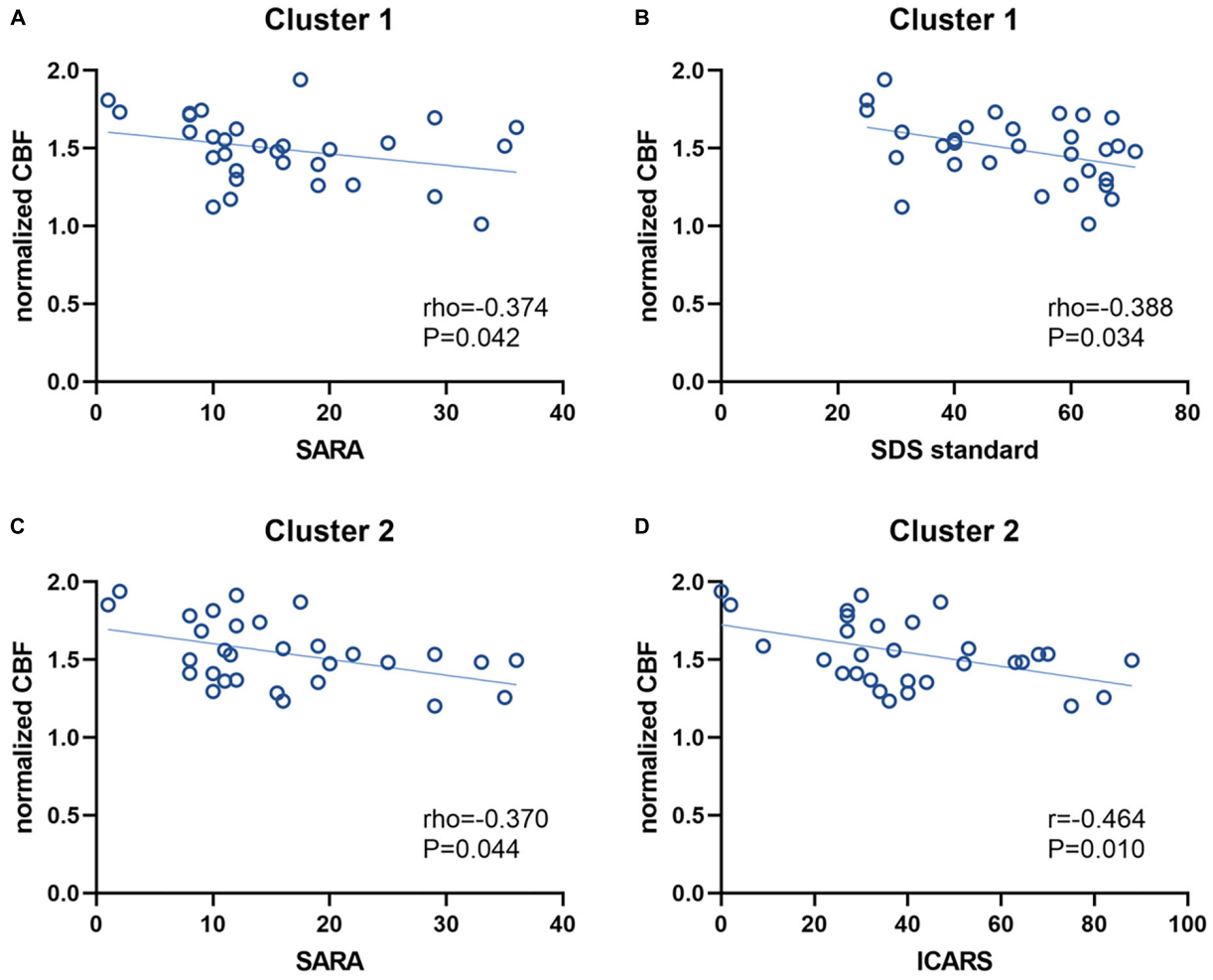

FIGURE 4
Correlations between the normalized CBF values and clinical characteristics. The normalized CBF of Cluster 1 had a negative correlation with SARA scores **(A)** and SDS standard scores **(B)**, respectively. For Cluster 2, the normalized CBF was also negatively correlated with SARA scores **(C)** and ICARS scores **(D)**, respectively. CBF, cerebral blood flow; SARA, scale for assessment and rating of ataxia; SDS, self-rating depression scale; ICARS, international cooperative ataxia rating scale.

superior to ICARS in terms of practicability, reliability, and scale structure through assessing ataxia by the two scales at the same time, and might be more objective as the use of vague expressions reduced in SARA compared to that in ICARS (Yabe et al., 2008). Given that the significant relationship between increased SARA scores and decreased CBF in both Cluster 1 and Cluster 2, the MR-based CBF alteration detected by PCASL in the cerebellum and midbrain is likely to be the reflection of SCD disease severity. However, in this study, no significant correlations were found between disease duration and the normalized CBF (neither in Cluster 1 nor in Cluster 2), which is similar to another SCD study (Ikawa et al., 2018) where the correlation between disease duration and cerebellar CBF was insignificant as well no matter measured by ASL or SPECT. In addition, CBF of the cerebellum showed no correlation to the duration of the illness even if using PET in 23 patients with SCD (Sakai et al., 1989). One explanation for the insignificant relationship between decreased cerebellar/midbrain CBF and increased disease duration may be that the total number of SCD patients is relatively small (no more than 30 in those studies mentioned as well as ours), which may reduce the statistical efficiency. Another possible interpretation is that the progression speed of disease varies from subtype to subtype, which means patients who have the same disease duration might be in different disease stage. However, several studies regarded cerebellar CBF value as an imaging biomarker for the early stage of SCA3/SCD as the decline of CBF could appear in non-onset patients or even before apparent structural atrophy or disease onset (Sakai et al., 1989; Xing et al., 2014). Therefore, the present finding might indicate that the hypoperfusion in either cerebellum or midbrain would not continue to develop with the prolongation of SCD course.

As for non-motor psychological symptoms, a previous study summarized that 17–26 percent of SCA patients suffered from depression (Lo et al., 2016). Though depressive symptoms worsen with disease progression, the relationships between neurodegeneration, disease severity, motor disability and depression are complex (Schmitz-Hübsch et al., 2010; Klockgether et al., 2019). We further assessed the correlation between CBF and depressive status in this study. Although the affected lobules IX of the vermis of Cluster 1 was thought to be involved in emotional processing (Schraa-Tam et al., 2012) and interruption in brainstem raphe of Cluster 2 was highly prevalent in patients with depression associated with certain neurodegenerative diseases (Mijajlovic et al., 2014), SDS standard scores only significantly negatively correlated with the normalized CBF in the cerebellar Cluster 1 rather than the midbrain Cluster 2. Given that patients with depression displayed lower rCBF in cerebellum and thalamus in a PET investigation (Liotti et al., 2002), our finding may suggest the possible contribution of cerebellar hypoperfusion to emotional changes of depressive status in SCD. Except for depression, anxiety and impaired sleep quality are also present in vast majority of SCD patients (Pedroso et al., 2011; Silva et al., 2015; Yuan et al., 2019; Mastammanavar et al., 2020). However, no significant correlations were found between CBF and the rest psychological scales (SAS and SPSS) in either Cluster 1 or Cluster 2. Thus, whether hypoperfusion of cerebellum and midbrain is related to anxiety and sleep disorders still needs further verification. Overall, the decline of cerebellar CBF value in SCD patients could give clues to some mental health problems, and psychiatric interventions for those with lower CBF should be prioritized.

This study has a few limitations. First, the sample size of our study is relatively small, which might have reduced the statistical power in altered CBF assessment and correlation analyses. Further investigations in larger SCD cohort with subtype analyses are required to confirm the CBF changes and clinical correlates. Second, as a pilot study, we did not separate the gray and white matter during whole-brain analysis, and did not take the gray matter volume changes into consideration, further studies should analyze the cortical and subcortical CBF alterations with the control of the regional gray matter volume. Third, some of our patients received medications (such as coenzyme Q_{10}, vitamin E and mecobalamin) to treat their ataxia symptoms, but the influence of drugs was often ignored in neuroimaging studies of patients with SCD because of the poor drug efficacy and the irregular medication. It is still not yet clear to what extent the finding and its interpretation can be influenced by medication, which need more rigorous research to explore. Finally, we only employed a single MRI modality to measure CBF with the cross-section study design to reveal the CBF alteration, follow-up longitudinal and multimodal studies might help in the future to differentiate perfusion signature of SCD from presymptomatic to late disease stages of the disease and monitor CBF changes with the disease progression.

Conclusion

In conclusion, through the non-invasive ASL-MRI method, we investigate the altered whole-brain normalized CBF in SCD patients. We found decreased CBF in multiple cerebellar lobules and deep cerebellar nuclei as well as the midbrain of brainstem, and hypoperfusion in these regions was correlated with disease severity and depression scores, which may indicate deficits in motor and emotional conditions. MRI-based CBF value may be a promising neuroimaging biomarker to reflect the severity of neurodegeneration at the whole-brain level *in vivo*, and suggesting mental changes.

Data availability statement

The original contributions presented in this study are included in the article/supplementary material, further inquiries can be directed to the corresponding author/s.

Ethics statement

The studies involving human participants were reviewed and approved by the Ethics Committee of China-Japan Friendship Hospital. The patients/participants provided their written informed consent to participate in this study.

Author contributions

BL and AY collected, processed, analyzed and interpreted data and images, wrote, and drafted the manuscript. WG and YC performed the MRI scanning and checked the image quality. YW, XL, and KL searched and managed the literature. LZ undertook neurological diagnosis and the acquisition of neuropsychology data. GM and LZ designed the study and critically revised the manuscript. All authors contributed to the article and have approved the final submitted manuscript.

Funding

This work was supported by the National Natural Science Foundation of China (NSFC) (Grant no. 81971585),

the National Key Research and Development Program of China (Grant nos. 2020YFC2003903 and 2020YFC2007301), the Guangzhou Science and Technology Plan Project (Grant no. 202103010001), the Beijing Municipal Science and Technology Project (Grant no. Z211100003521009), and the Wu Jieping Medical Foundation (Grant no. 320.6750.19089-57).

Acknowledgments

We gratefully thank for the support and assistance from Lizhi Xie Ph.D. of GE Healthcare China Research Team and all participants who were involved in this study as well as everyone who offered help.

Conflict of interest

The authors declare that the research was conducted in the absence of any commercial or financial relationships that could be construed as a potential conflict of interest.

Publisher's note

All claims expressed in this article are solely those of the authors and do not necessarily represent those of their affiliated organizations, or those of the publisher, the editors and the reviewers. Any product that may be evaluated in this article, or claim that may be made by its manufacturer, is not guaranteed or endorsed by the publisher.

References

Alsop, D. C., Detre, J. A., Golay, X., Günther, M., Hendrikse, J., Hernandez-Garcia, L., et al. (2015). Recommended implementation of arterial spin-labeled perfusion MRI for clinical applications: A consensus of the ISMRM perfusion study group and the European consortium for ASL in dementia. *Magn. Reson. Med.* 73, 102–116. doi: 10.1002/mrm.25197

Aslan, S., and Lu, H. (2010). On the sensitivity of ASL MRI in detecting regional differences in cerebral blood flow. *Magn. Reson. Imaging* 28, 928–935. doi: 10.1016/j.mri.2010.03.037

Bishop, G. A., Ho, R. H., and King, J. S. (1988). A temporal analysis of the origin and distribution of serotoninergic afferents in the cerebellum of pouch young opossums. *Anat. Embryol. (Berl)* 179, 33–48. doi: 10.1007/bf00305098

Bostan, A. C., Dum, R. P., and Strick, P. L. (2013). Cerebellar networks with the cerebral cortex and basal ganglia. *Trends Cogn. Sci.* 17, 241–254. doi: 10.1016/j.tics.2013.03.003

Braga-Neto, P., Dutra, L. A., Pedroso, J. L., Felício, A. C., Alessi, H., Santos-Galduroz, R. F., et al. (2012). Cognitive deficits in Machado-Joseph disease correlate with hypoperfusion of visual system areas. *Cerebellum* 11, 1037–1044. doi: 10.1007/s12311-012-0354-x

Braga-Neto, P., Pedroso, J. L., Gadelha, A., Laureano, M. R., de Souza Noto, C., Garrido, G. J., et al. (2016). Psychosis in Machado-Joseph disease: Clinical correlates, pathophysiological discussion, and functional brain imaging. Expanding the cerebellar cognitive affective syndrome. *Cerebellum* 15, 483–490. doi: 10.1007/s12311-015-0716-2

Dai, W., Garcia, D., de Bazelaire, C., and Alsop, D. C. (2008). Continuous flow-driven inversion for arterial spin labeling using pulsed radio frequency and gradient fields. *Magn. Reson. Med.* 60, 1488–1497. doi: 10.1002/mrm.21790

De Michele, G., Mainenti, P. P., Soricelli, A., Di Salle, F., Salvatore, E., Longobardi, M. R., et al. (1998). Cerebral blood flow in spinocerebellar degenerations: A single photon emission tomography study in 28 patients. *J. Neurol.* 245, 603–608. doi: 10.1007/s004150050253

Detre, J. A., and Alsop, D. C. (1999). Perfusion magnetic resonance imaging with continuous arterial spin labeling: Methods and clinical applications in the central nervous system. *Eur. J. Radiol.* 30, 115–124. doi: 10.1016/s0720-048x(99)00050-9

Detre, J. A., Leigh, J. S., Williams, D. S., and Koretsky, A. P. (1992). Perfusion imaging. *Magn. Reson. Med.* 23, 37–45. doi: 10.1002/mrm.1910230106

Diedrichsen, J. (2006). A spatially unbiased atlas template of the human cerebellum. *Neuroimage* 33, 127–138. doi: 10.1016/j.neuroimage.2006.05.056

Diedrichsen, J., Balsters, J. H., Flavell, J., Cussans, E., and Ramnani, N. (2009). A probabilistic MR atlas of the human cerebellum. *Neuroimage* 46, 39–46. doi: 10.1016/j.neuroimage.2009.01.045

Diedrichsen, J., and Zotow, E. (2015). Surface-based display of volume-averaged cerebellar imaging data. *PLoS One* 10:e0133402. doi: 10.1371/journal.pone.0133402

Erro, R., Ponticorvo, S., Manara, R., Barone, P., Picillo, M., Scannapieco, S., et al. (2020). Subcortical atrophy and perfusion patterns in Parkinson disease and multiple system atrophy. *Parkinsonism Relat. Disord.* 72, 49–55. doi: 10.1016/j.parkreldis.2020.02.009

Gilman, S., St Laurent, R. T., Koeppe, R. A., Junck, L., Kluin, K. J., and Lohman, M. (1995). A comparison of cerebral blood flow and glucose metabolism in olivopontocerebellar atrophy using PET. *Neurology* 45, 1345–1352. doi: 10.1212/wnl.45.7.1345

Gilman, S., Wenning, G. K., Low, P. A., Brooks, D. J., Mathias, C. J., Trojanowski, J. Q., et al. (2008). Second consensus statement on the diagnosis of multiple system atrophy. *Neurology* 71, 670–676. doi: 10.1212/01.wnl.0000324625.00404.15

Harding, I. H., Raniga, P., Delatycki, M. B., Stagnitti, M. R., Corben, L. A., Storey, E., et al. (2016). Tissue atrophy and elevated iron concentration in the extrapyramidal motor system in Friedreich ataxia: The IMAGE-FRDA study. *J. Neurol. Neurosurg. Psychiatry* 87, 1261–1263. doi: 10.1136/jnnp-2015-312665

Hellenbroich, Y., Gierga, K., Reusche, E., Schwinger, E., Deller, T., de Vos, R. A., et al. (2006). Spinocerebellar ataxia type 4 (SCA4): Initial pathoanatomical study reveals widespread cerebellar and brainstem degeneration. *J. Neural. Transm. (Vienna)* 113, 829–843. doi: 10.1007/s00702-005-0362-9

Hernandez-Castillo, C. R., Diaz, R., Vaca-Palomares, I., Torres, D. L., Chirino, A., Campos-Romo, A., et al. (2019). Extensive cerebellar and thalamic degeneration in spinocerebellar ataxia type 10. *Parkinsonism Relat. Disord.* 66, 182–188. doi: 10.1016/j.parkreldis.2019.08.011

Hoche, F., Balikó, L., den Dunnen, W., Steinecker, K., Bartos, L., Sáfrány, E., et al. (2011). Spinocerebellar ataxia type 2 (SCA2): Identification of early brain degeneration in one monozygous twin in the initial disease stage. *Cerebellum* 10, 245–253. doi: 10.1007/s12311-010-0239-9

Honjo, K., Ohshita, T., Kawakami, H., Naka, H., Imon, Y., Maruyama, H., et al. (2004). Quantitative assessment of cerebral blood flow in genetically confirmed spinocerebellar ataxia type 6. *Arch. Neurol.* 61, 933–937. doi: 10.1001/archneur.61.6.933

Hornung, J. P. (2003). The human raphe nuclei and the serotonergic system. *J. Chem. Neuroanat.* 26, 331–343. doi: 10.1016/j.jchemneu.2003.10.002

Ikawa, M., Kimura, H., Kitazaki, Y., Sugimoto, K., Matsunaga, A., Hayashi, K., et al. (2018). Arterial spin labeling MR imaging for the clinical detection of cerebellar hypoperfusion in patients with spinocerebellar degeneration. *J. Neurol. Sci.* 394, 58–62. doi: 10.1016/j.jns.2018.09.007

Ivanidze, J., Skafida, M., Pandya, S., Patel, D., Osborne, J. R., Raj, A., et al. (2020). Molecular imaging of striatal dopaminergic neuronal loss and the neurovascular unit in Parkinson disease. *Front. Neurosci.* 14:528809. doi: 10.3389/fnins.2020.528809

Iwabuchi, K., Koyano, S., and Yagishita, S. (2022). Simple and clear differentiation of spinocerebellar degenerations: Overview of macroscopic and

low-power view findings. *Neuropathology* doi: 10.1111/neup.12823 [Epub ahead of print].

Kawai, Y., Suenaga, M., Watanabe, H., and Sobue, G. (2009). Cognitive impairment in spinocerebellar degeneration. *Eur. Neurol.* 61, 257–268. doi: 10.1159/000206850

Kimura, N., Kumamoto, T., Masuda, T., Nomura, Y., Hanaoka, T., Hazama, Y., et al. (2011). Evaluation of the effects of thyrotropin releasing hormone (TRH) therapy on regional cerebral blood flow in the cerebellar variant of multiple system atrophy using 3DSRT. *J. Neuroimaging* 21, 132–137. doi: 10.1111/j.1552-6569.2009.00411.x

King, S. A., Schneider, R. M., Serra, A., and Leigh, R. J. (2011). Critical role of cerebellar fastigial nucleus in programming sequences of saccades. *Ann. N. Y. Acad. Sci.* 1233, 155–161. doi: 10.1111/j.1749-6632.2011.06119.x

Klockgether, T., Mariotti, C., and Paulson, H. L. (2019). Spinocerebellar ataxia. *Nat. Rev. Dis. Primers* 5:24. doi: 10.1038/s41572-019-0074-3

Koeppen, A. H. (2018). The neuropathology of spinocerebellar ataxia type 3/Machado-Joseph disease. *Adv. Exp. Med. Biol.* 1049, 233–241. doi: 10.1007/978-3-319-71779-1_11

Kondo, S., Tanaka, M., Sun, X., Sakai, Y., and Hirai, S. (1993). [Study of patients with spinocerebellar degeneration using positron emission tomography]. *Rinsho Shinkeigaku* 33, 1039–1046.

Li, J. M. (2012). Seff-rating scale of sleep (SRSS). *China J. Health Psychol.* 20:1851.

Lin, W. C., Chen, P. C., Huang, C. C., Tsai, N. W., Chen, H. L., Wang, H. C., et al. (2017). Autonomic function impairment and brain perfusion deficit in Parkinson's disease. *Front. Neurol.* 8:246. doi: 10.3389/fneur.2017.00246

Liotti, M., Mayberg, H. S., McGinnis, S., Brannan, S. L., and Jerabek, P. (2002). Unmasking disease-specific cerebral blood flow abnormalities: Mood challenge in patients with remitted unipolar depression. *Am. J. Psychiatry* 159, 1830–1840. doi: 10.1176/appi.ajp.159.11.1830

Lo, R. Y., Figueroa, K. P., Pulst, S. M., Perlman, S., Wilmot, G., Gomez, C., et al. (2016). Depression and clinical progression in spinocerebellar ataxias. *Parkinsonism Relat. Disord.* 22, 87–92. doi: 10.1016/j.parkreldis.2015.11.021

Mastammanavar, V. S., Kamble, N., Yadav, R., M, N., Jain, S., Kumar, K., et al. (2020). Non-motor symptoms in patients with autosomal dominant spinocerebellar ataxia. *Acta Neurol. Scand.* 142, 368–376. doi: 10.1111/ane.13318

Mijajlovic, M. D., Tsivgoulis, G., and Sternic, N. (2014). Transcranial brain parenchymal sonography in neurodegenerative and psychiatric diseases. *J. Ultrasound Med.* 33, 2061–2068. doi: 10.7863/ultra.33.12.2061

Pedroso, J. L., Braga-Neto, P., Felício, A. C., Dutra, L. A., Santos, W. A., do Prado, G. F., et al. (2011). Sleep disorders in Machado-Joseph disease: Frequency, discriminative thresholds, predictive values, and correlation with ataxia-related motor and non-motor features. *Cerebellum* 10, 291–295. doi: 10.1007/s12311-011-0252-7

Ribeiro-do-Valle, L. E. (1997). Serotonergic neurons in the caudal raphe nuclei discharge in association with activity of masticatory muscles. *Braz. J. Med. Biol. Res.* 30, 79–83. doi: 10.1590/s0100-879x1997000100013

Rolls, E. T., Huang, C. C., Lin, C. P., Feng, J., and Joliot, M. (2020). Automated anatomical labelling atlas 3. *Neuroimage* 206:116189. doi: 10.1016/j.neuroimage.2019.116189

Rüb, U., Brunt, E. R., Gierga, K., Schultz, C., Paulson, H., de Vos, R. A., et al. (2003). The nucleus raphe interpositus in spinocerebellar ataxia type 3 (Machado-Joseph disease). *J. Chem. Neuroanat.* 25, 115–127. doi: 10.1016/s0891-0618(02)00099-6

Sakai, Y., Shouji, M., Ishihara, T., Morimatsu, M., and Hirai, S. (1989). [Analysis of cerebellar functions in spinocerebellar degeneration using positron emission tomography (PET)]. *Rinsho Shinkeigaku* 29, 284–289.

Scherzed, W., Brunt, E. R., Heinsen, H., de Vos, R. A., Seidel, K., Bürk, K., et al. (2012). Pathoanatomy of cerebellar degeneration in spinocerebellar ataxia type 2 (SCA2) and type 3 (SCA3). *Cerebellum* 11, 749–760. doi: 10.1007/s12311-011-0340-8

Schmahmann, J. D., Doyon, J., McDonald, D., Holmes, C., Lavoie, K., Hurwitz, A. S., et al. (1999). Three-dimensional MRI atlas of the human cerebellum in proportional stereotaxic space. *Neuroimage* 10(3 Pt 1), 233–260. doi: 10.1006/nimg.1999.0459

Schmitz-Hübsch, T., Coudert, M., Giunti, P., Globas, C., Baliko, L., Fancellu, R., et al. (2010). Self-rated health status in spinocerebellar ataxia–results from a European multicenter study. *Mov. Disord.* 25, 587–595. doi: 10.1002/mds.22740

Schmitz-Hübsch, T., du Montcel, S. T., Baliko, L., Berciano, J., Boesch, S., Depondt, C., et al. (2006). Scale for the assessment and rating of ataxia: Development of a new clinical scale. *Neurology* 66, 1717–1720. doi: 10.1212/01.wnl.0000219042.60538.92

Schraa-Tam, C. K., Rietdijk, W. J., Verbeke, W. J., Dietvorst, R. C., van den Berg, W. E., Bagozzi, R. P., et al. (2012). fMRI activities in the emotional cerebellum: A preference for negative stimuli and goal-directed behavior. *Cerebellum* 11, 233–245. doi: 10.1007/s12311-011-0301-2

Sidtis, J. J., Strother, S. C., Groshong, A., Rottenberg, D. A., and Gomez, C. (2010). Longitudinal cerebral blood flow changes during speech in hereditary ataxia. *Brain Lang.* 114, 43–51. doi: 10.1016/j.bandl.2010.03.007

Silva, U. C., Marques, W. Jr., Lourenço, C. M., Hallak, J. E., and Osório, F. L. (2015). Psychiatric disorders, spinocerebellar ataxia type 3 and CAG expansion. *J. Neurol.* 262, 1777–1779. doi: 10.1007/s00415-015-7807-3

Stoodley, C. J., and Schmahmann, J. D. (2018). Functional topography of the human cerebellum. *Handb. Clin. Neurol.* 154, 59–70. doi: 10.1016/b978-0-444-63956-1.00004-7

Sun, X., Tanaka, M., Kondo, S., Hirai, S., and Ishihara, T. (1994). Reduced cerebellar blood flow and oxygen metabolism in spinocerebellar degeneration: A combined PET and MRI study. *J. Neurol.* 241, 295–300. doi: 10.1007/bf00868436

Trouillas, P., Takayanagi, T., Hallett, M., Currier, R. D., Subramony, S. H., Wessel, K., et al. (1997). International cooperative ataxia rating scale for pharmacological assessment of the cerebellar syndrome. The ataxia neuropharmacology committee of the world federation of neurology. *J. Neurol. Sci.* 145, 205–211. doi: 10.1016/s0022-510x(96)00231-6

Van Essen, D. C., Smith, S. M., Barch, D. M., Behrens, T. E., Yacoub, E., and Ugurbil, K. (2013). The WU-Minn human connectome project: An overview. *Neuroimage* 80, 62–79. doi: 10.1016/j.neuroimage.2013.05.041

Watanabe, H., Sugihara, H., Horiuchi, M., and Takahashi, Y. (2005). [Analysis of brain images in patients with spinocerebellar degeneration; Using statistical parametric mapping (SPM) and easy Z score imaging system (eZIS)]. *Kaku Igaku* 42, 107–113.

Xing, W., Wang, X. Y., Liao, X. X., Liao, W. H., and Shen, L. (2014). Spin labeling artery method perfusion MRI study of SPG4 and SCA3/MJD. *Magn. Reson. Imaging* 32, 1330–1334. doi: 10.1016/j.mri.2014.08.022

Xu, G., Rowley, H. A., Wu, G., Alsop, D. C., Shankaranarayanan, A., Dowling, M., et al. (2010). Reliability and precision of pseudo-continuous arterial spin labeling perfusion MRI on 3.0 T and comparison with 15O-water PET in elderly subjects at risk for Alzheimer's disease. *NMR Biomed.* 23, 286–293. doi: 10.1002/nbm.1462

Yabe, I., Matsushima, M., Soma, H., Basri, R., and Sasaki, H. (2008). Usefulness of the scale for assessment and rating of ataxia (SARA). *J. Neurol. Sci.* 266, 164–166. doi: 10.1016/j.jns.2007.09.021

Yamada, M., Toyoshima, Y., Makifuchi, T., Kakita, A., and Takahashi, H. (2016). Spinocerebellar degeneration: Discrepancies between clinical and pathological diagnoses. *Neuropathology* 36, 405–410. doi: 10.1111/neup.12278

Yan, C. G., Wang, X. D., Zuo, X. N., and Zang, Y. F. (2016). DPABI: Data processing & analysis for (Resting-State) brain imaging. *Neuroinformatics* 14, 339–351. doi: 10.1007/s12021-016-9299-4

Yuan, X., Ou, R., Hou, Y., Chen, X., Cao, B., Hu, X., et al. (2019). Extra-cerebellar signs and non-motor features in Chinese patients with spinocerebellar ataxia type 3. *Front. Neurol.* 10:110. doi: 10.3389/fneur.2019.00110

Zhang, X. Y., Wang, J. J., and Zhu, J. N. (2016). Cerebellar fastigial nucleus: From anatomic construction to physiological functions. *Cerebellum Ataxias* 3:9. doi: 10.1186/s40673-016-0047-1

Zung, W. W. (1971). A rating instrument for anxiety disorders. *Psychosomatics* 12, 371–379. doi: 10.1016/s0033-3182(71)71479-0

Zung, W. W. (1972). The depression status inventory: An adjunct to the self-rating depression scale. *J. Clin. Psychol.* 28, 539–543. doi: 10.1002/1097-4679(197210)28:4<539::aid-jclp2270280427<3.0.co;2-s

frontiers | Frontiers in Neuroscience

TYPE Original Research
PUBLISHED 29 November 2022
DOI 10.3389/fnins.2022.987248

Check for updates

OPEN ACCESS

EDITED BY
Danny J. J. Wang,
University of Southern California,
United States

REVIEWED BY
Lubin Wang,
Institute of Basic Medical Sciences,
China
Benedictor Alexander Nguchu,
University of Science and Technology
of China, China

*CORRESPONDENCE
Hao Xu
xuhao@fmmu.edu.cn
Baojuan Li
libjuan@163.com
Jian Liu
liu-jian@fmmu.edu.cn

†These authors have contributed
equally to this work

SPECIALTY SECTION
This article was submitted to
Brain Imaging Methods,
a section of the journal
Frontiers in Neuroscience

RECEIVED 06 July 2022
ACCEPTED 07 November 2022
PUBLISHED 29 November 2022

CITATION
Wei L, Zhang Y, Zhai W, Wang H,
Zhang J, Jin H, Feng J, Qin Q, Xu H,
Li B and Liu J (2022) Attenuated
effective connectivity of large-scale
brain networks in children with autism
spectrum disorders.
Front. Neurosci. 16:987248.
doi: 10.3389/fnins.2022.987248

COPYRIGHT
© 2022 Wei, Zhang, Zhai, Wang,
Zhang, Jin, Feng, Qin, Xu, Li and Liu.
This is an open-access article
distributed under the terms of the
Creative Commons Attribution License
(CC BY). The use, distribution or
reproduction in other forums is
permitted, provided the original
author(s) and the copyright owner(s)
are credited and that the original
publication in this journal is cited, in
accordance with accepted academic
practice. No use, distribution or
reproduction is permitted which does
not comply with these terms.

Attenuated effective connectivity of large-scale brain networks in children with autism spectrum disorders

Lei Wei[1†], Yao Zhang[2†], Wensheng Zhai[3†], Huaning Wang[4], Junchao Zhang[1], Haojie Jin[1], Jianfei Feng[1], Qin Qin[1], Hao Xu[1*], Baojuan Li[3*] and Jian Liu[1*]

[1]Network Center, Air Force Medical University, Xi'an, China, [2]Military Medical Center, Xijing Hospital, Air Force Medical University, Xi'an, China, [3]School of Biomedical Engineering, Air Force Medical University, Xi'an, China, [4]Department of Psychiatry, Xijing Hospital, Air Force Medical University, Xi'an, China

Introduction: Understanding the neurological basis of autism spectrum disorder (ASD) is important for the diagnosis and treatment of this mental disorder. Emerging evidence has suggested aberrant functional connectivity of large-scale brain networks in individuals with ASD. However, whether the effective connectivity which measures the causal interactions of these networks is also impaired in these patients remains unclear.

Objects: The main purpose of this study was to investigate the effective connectivity of large-scale brain networks in patients with ASD during resting state.

Materials and methods: The subjects were 42 autistic children and 127 age-matched normal children from the ABIDE II dataset. We investigated effective connectivity of 7 large-scale brain networks including visual network (VN), default mode network (DMN), cerebellum, sensorimotor network (SMN), auditory network (AN), salience network (SN), frontoparietal network (FPN), with spectral dynamic causality model (spDCM). Parametric empirical Bayesian (PEB) was used to perform second-level group analysis and furnished group commonalities and differences in effective connectivity. Furthermore, we analyzed the correlation between the strength of effective connectivity and patients' clinical characteristics.

Results: For both groups, SMN acted like a hub network which demonstrated dense effective connectivity with other large-scale brain network. We also observed significant causal interactions within the "triple networks" system, including DMN, SN and FPN. Compared with healthy controls, children with ASD showed decreased effective connectivity among some large-scale brain networks. These brain networks included VN, DMN, cerebellum, SMN, and FPN. In addition, we also found significant negative correlation between the strength of the effective connectivity from right angular gyrus (ANG_R) of DMN to left precentral gyrus (PreCG_L) of SMN and

ADOS-G or ADOS-2 module 4 stereotyped behaviors and restricted interest total (ADOS_G_STEREO_BEHAV) scores.

Conclusion: Our research provides new evidence for the pathogenesis of children with ASD from the perspective of effective connections within and between large-scale brain networks. The attenuated effective connectivity of brain networks may be a clinical neurobiological feature of ASD. Changes in effective connectivity of brain network in children with ASD may provide useful information for the diagnosis and treatment of the disease.

KEYWORDS

autism spectrum disorder, brain network, dynamic causal modelling, effective connectivity, parametric empirical bayesian

Introduction

Since its first clinical description in the 1940s, autism spectrum disorder (ASD) has gone from a rare childhood-onset disorder to a pervasive, lifelong developmental disorder. As a neurodevelopmental deficit, the disorder is clinically characterized by impairments in social interaction, communication disorders, restricted interests, stereotyped and repetitive behavioral patterns, and in most patients, developmental delay (Belmonte et al., 2004). A data statistics in 2012 in the United States shows that the incidence rate of ASD is very high, with an average of 1 in 68 children suffering from ASD, and the prevalence rate of boys is 4.5 times that of girls (Christensen et al., 2016). Children with ASD may need long-term or even lifelong care. Therefore, ASD treatment incurs higher medical and educational costs, which is a huge financial burden for most families and society. However, the underlying pathophysiological and neurological basis of ASD remains unclear, and effective diagnosis and treatment of ASD is elusive (Courchesne et al., 2011).

Researchers are attempting to understand the neurological basis of ASD by identifying biomarkers associated with core defects (Mohammad-Rezazadeh et al., 2016). One of the most commonly used methods is functional magnetic resonance imaging (fMRI). A growing number of imaging studies involving different groups of children, adolescents, and adults have shown that ASD is a disorder of abnormal brain connections. These abnormal connections exist not only in separate brain networks, such as visual network (VN), default mode network (DMN), auditory network (AN), salience network (SN), and frontoparietal network (FPN), but also between different brain networks (Bi et al., 2018; Chen et al., 2021). In studies concerning VN, survey such as that conducted by Lombardo et al. (2019) found reduced functional connectivity between DMN and VN in patients with ASD from 12 to 48 months of age, and eye-tracking procedures revealed low connectivity between DMN and occipito-temporal cortex (OTC). In contract, another study found increased connectivity of language areas with posterior cingulate cortex (PCC) and visual areas in adolescents with ASD (Gao et al., 2019). About DMN, One study by Lynch et al. (2013) found that children with ASD exhibited high connectivity of the posterior cingulate and retrosplenial cortices, yet their precuneus showed localized hypo-connectivity with the visual cortex, basal ganglia, and posteromedial cortex. Besides, in a study of patients with ASD from Autism Brain Imaging Data Exchange I (ABIDE I), it was found that connectivity of the precuneus, posterior cingulate gyrus and the medial prefrontal gyrus was decreased in DMN (Yao et al., 2016). Similarly, Funakoshi et al. (2016) found reduced functional connectivity in the bilateral inferior parietal lobule and posterior cingulate cortex of DMN in children with ASD. In studies of the cerebellum, one study found reduced gray matter in the inferior cerebellar vermis (lobule IX), left lobule VIIIB, and right Crux I in patients with ASD (Stoodley, 2014). In another study, functional connectivity between the right cerebellar region and the supratentorial regulatory language areas was absent in adolescents with ASD (Verly et al., 2014). Conversely, a new study demonstrated that adolescents with ASD had cerebro-cerebellar functional overconnectivity (Khan et al., 2015). In an analysis of AN (Linke et al., 2018), the interhemispheric connectivity of the left and right auditory combined ROI decreased, and the connectivity between auditory cortical areas and the thalamus increased in the adolescents with ASD. In a study investigating SN, Zenghui et al. (2019) reported that adolescents with ASD had higher functional connectivity between the right dorsolateral prefrontal cortex and the left superior frontal gyrus, the middle frontal gyrus and the anterior cingulate cortex. About FPN, it was found that patients with ASD had greater activation in the right middle frontal gyrus and anterior cingulate cortex and less activation in the bilateral middle frontal, left inferior frontal gyrus, right inferior parietal lobule, and precuneus (May and Kana, 2020). In addition, data from several studies suggest that connections between different brain networks were both

increased and decreased in patients with ASD. Compared with the control group, the connectivity between VN and sensorimotor network (SMN) and between the posterior part of the cerebellum and the occipital and parietal cortices was enhanced, while the connectivity between VN and AN, between the lateral cerebellum and the pre-frontal and other relevant cortical regions was reduced (Wang et al., 2019; Chen et al., 2021). Another study found that adolescents with ASD had varying increases or decreases in functional connectivity in eight brain networks, including DMN, VN, AN and so on (Bi et al., 2018). In conclusion, these studies show that the connections between the brain and cerebellum, between VN and SMN, and those related to AN in autistic patients show higher functional connectivity compared with the control group (Khan et al., 2015; Linke et al., 2018; Chen et al., 2021). However, the connection between VN and AN presents lower functional connectivity (Wang et al., 2019). In addition, the functional connection between DMN and VN, as well as the functional connection related to FPN, both increases and decreases (Lynch et al., 2013; Gao et al., 2019; Lombardo et al., 2019; May and Kana, 2020). These abnormal connections may be related to the special clinical symptoms of patients with ASD, such as social interaction disorder, communication disorder, limited interest and repetitive behavior patterns.

Functional connectivity in the brain is defined as the correlation of spontaneous functional activity between different brain regions (Harikumar et al., 2021), and refers to the time-dependence of neural activity signals in spatially disconnected brain regions (Chiang et al., 2016). It has been widely used to assess the functional interactions between different brain regions. It has also been widely used by researchers in previous studies on ASD. However, functional connectivity cannot portray the directional information of connections between brain regions (Friston et al., 2003). Effective connectivity has been defined as the effect of neurological activity in one brain region on another brain region. Unlike functional connectivity, effective connectivity can estimate the direction of information transfer of neural activity (Rajabioun et al., 2020), which helps to understand the brain mechanisms behind neural activity. Dynamic causal modelling (DCM) (Friston et al., 2003) is a common approach to effective connectivity. Li et al. (2011) proposed a stochastic DCM model. By introducing noise as the input signal of the model, the effective connectivity parameters under noise interference were estimated, thus allowing the DCM to be used for resting-state fMRI analysis. To solve the problem of DCM model instability in the time domain inversion, Friston et al. (2014) proposed the spectral dynamic causal modelling (spDCM) method, which can effectively reduce the complexity of model estimation by transferring the model to the frequency domain for inversion through frequency domain approximation. In addition, the stability and accuracy of spDCM model estimation are improved compared with stochastic DCM (Razi et al., 2015). Subsequently, to address some problems in the DCM process, such as local maxima in Bayesian model comparisons, Friston et al. (2016) proposed a Bayesian model reduction from the classical random effects model to a parametric empirical Bayesian (PEB) model using only the full model. By using the posterior density of the full model, the reduced model can be inverted by Bayesian methods.

In this study, we investigated the effective connectivity between different regions of each brain network in children with ASD. We used the public dataset KKI, which is part of the Autism Brain Imaging Data Exchange II (ABIDE II), which was created with the support of the National Institute of Mental Health and provides better phenotypic characteristics (Di Martino et al., 2017). In addition, ABIDE II includes a series of psychiatric variables, which can help us understand the neural correlates of psychopathology. Through spDCM, we investigated the effective connectivity of 7 large-scale brain networks in 42 children with ASD and 127 age-matched healthy controls. First, the regions of different brain networks were identified by spatially independent component analysis (McKeown and Sejnowski, 1998). Then, the effective connectivity of the regions of 7 large-scale brain networks were characterized using spDCM and Bayesian model reduction to find the directional and causal relationships of neural activity between regions. In addition, we analyzed the correlation between the effective connectivity between regions and some clinical indicators in children.

Materials and methods

Participants

We used the KKI dataset in this study. The KKI dataset collected from 211 children aged 8 to 13 years, including 56 children with ASD and 155 children in the typical controls (TC) group. Participants were enlisted as part of an ongoing study at the Kennedy Krieger Institute's Center for Neurodevelopmental and Imaging Research. Informed consents were provided by the children's parents or guardians, and consents were provided by children. They had a Wechsler Intelligence Scale for Children-IV (WISC-IV) (Wechsler, 2003) or WISC-V (Wechsler, 2014) full scale IQ greater than 80. Children were excluded if they had a definite neurological disease, severe chronic illness, severe visual impairment, alcohol or drug dependence, conditions that prohibit or make it difficult to obtain MRI, and were at developmental level 3 or higher on the Physical Development Scale (Carskadon and Acebo, 1993). The diagnosis of ASD was confirmed using the Autism Diagnostic Interview-Revised (ADI-R) (Lord et al., 1994) or the Autism Diagnostic Observation Schedule-2nd edition (ADOS-2) (Lord et al., 2012) module 3. The WISC-IV or WISC-V were used

to assess intelligence. The Edinburgh Handedness Inventory (Oldfield, 1971) was used to determine handiness.

Data acquisition

Scans were performed at the F.M. Kirby Research Center for Functional Brain Imaging using one of two Philips 3T scanners with an 8- or 32-channel phased-array head coil. Resting-state fMRI scans were collected before or after the structural scans. During resting-state scans, children were asked to relax and focus on a crosshair while remaining as still as possible. The scanning parameters of Resting-state fMRI scans were: repetition time = 2,500 ms, echo time = 30 ms, field of view = 256 mm x 256 mm, matrix = 96 × 96, flip angle = 75°, number of slices = 47, slice thickness = 3 mm, inter-slice gap = 0 mm. The scanning parameters of structural scans were: repetition time = 8.0 ms, echo time = 3.7 ms, field of view = 256 mm × 256 mm, matrix = 256 × 256, flip angle = 8°, slice thickness = 1 mm.

Preprocessing

The preprocessing of data analysis is shown in **Figure 1**. Data processing was performed with the GRETNA toolbox (v2.0.0) (Wang et al., 2015) based on SPM12. In general, functional preprocessing included the following four steps. (1) Slice Timing: corrected the difference in acquisition time between slices in each volume; (2) Realignment: used rigid body transformation to correct for head motion; (3) Normalization: transformed brain of each subject into a standardized space defined by the Montreal Neurological Institute (MNI); (4) Spatially Smoothing: spatially smoothed data using a Gaussian filter with a full width at half maximum (FWHM) of 6 mm.

Some children were excluded from analysis after preprocessing due to poor normalization and excessive head motion. In addition, four children were excluded because the subsequent spDCM process did not converge. Therefore, a total of 14 children with ASD and 28 TC children were excluded, and the final sample included 42 children with ASD and 127 TC children. The demographic and clinical data of the subjects of each dataset are shown in **Table 1**.

Group independent component analysis

The preprocessed data were subjected to independent component analysis (ICA) using the Group ICA of fMRI Toolbox (GIFT) software package.[1] The GIFT software first estimated and decomposed each subject's fMRI image into 33 spatially independent components. Then performed back reconstruction on each subject to obtain the corresponding ICA map. According to the mean image of the spatially independent components of all the subjects, all the independent components are sorted by the ICA independent component template (Smith et al., 2009), and each brain network that matches the template was selected as the independent component of brain network. There are 7 selected brain networks, including VN, DMN, cerebellum, SMN, AN, SN, and FPN.

Selection of regions of interest

Next, the corresponding regions of interest (ROI) in each of the identified brain networks were selected. Frist defined the ROI as a sphere with a radius of 6 mm, and used xjView[2] to determine the coordinates of the center of each sphere. Then 24 ROIs corresponding to 7 brain networks were selected using the AAL standard brain template provided by the Montreal Neurological Institute (MNI). The peak value of each ROI was used as the coordinate of this ROI. The coordinates of different brain networks are shown in **Table 2**. The name of each ROI was represented by the corresponding abbreviation of the brain area in the AAL template.

Dynamic causal modeling and statistical analysis

To investigate the effective connectivity in brain networks, we used spDCM embedded in the SPM12. For each subject, a complete connectivity model is created that allows bidirectional connections between any two ROIs. The model did not include any external input because our analysis was based on resting-state fMRI data. The full connectivity model's parameters are then estimated using spDCM. More free parameters will be generated as more ROIs are used to build fully connected models. We employ Bayesian model reduction (Friston et al., 2016). The classical stochastic effect model was first transformed into a parameter empirical Bayesian PEB model, and then Bayesian inversion of the reduced model was performed using the complete model's posterior density.

Furthermore, to investigate the correlations between the effective connection and clinical data, we measured Pearson's correlation coefficient between the effective connectivity and clinical data such as ADOS generic or ADOS-2 module 4 total (ADOS_G_TOTAL), ADOS-G or ADOS-2 module 4 communication total (ADOS_G_COMM), ADOS-G or ADOS-2 module 4 reciprocal social interaction

1 https://trendscenter.org/software/gift/

2 http://www.alivelearn.net/xjview/

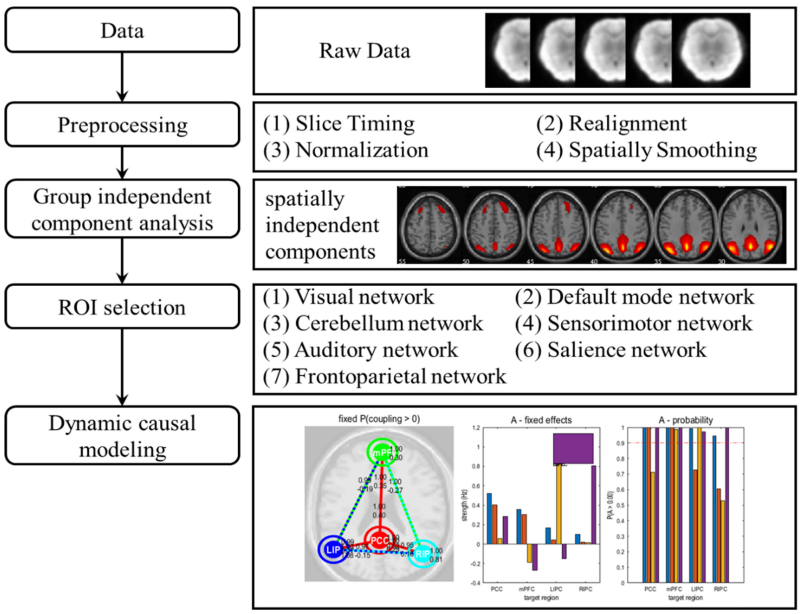

FIGURE 1
The data analysis pipeline. After data acquisition and preprocessing, the data were divided into 7 different brain networks through group independent component analysis. For each brain network, selected the corresponding regions of interest. Finally, dynamic causal modelling of all brain networks was carried out.

TABLE 1 Demographic and clinical data of the subjects.

	ASD ($N = 42$)	TC ($N = 127$)	p-value
Sex (Male/Female)	29/13	75/52	0.2485
Age	10.48 ± 1.41	10.36 ± 1.14	0.5846
ADOS_G_TOTAL	13.72 ± 3.18	–	–
ADOS_G_COMM	3.44 ± 1.07	–	–
ADOS_G_SOCIAL	7.67 ± 2.19	–	–
ADOS_G_STEREO_BEHAV	2.61 ± 1.38	–	–

total (ADOS_G_SOCIAL), and ADOS-G or ADOS-2 module 4 stereotyped behaviors and restricted interest total (ADOS_G_STEREO_BEHAV).

Results

Selected brain networks

The 24 ROIs corresponding to the 7 brain networks selected according to the ICA independent component template are shown in Figure 2. Different brain networks are marked with different colors to indicate their locations in the brain. The ROIs within each brain network are connected by lines. The 7 brain networks are evenly distributed in the brain, including the cerebellum.

The common parts of the effective connectivity between the two groups

The common parts of the effective connectivity between the two groups of 24 ROIs are shown in Figure 3. Each colored circle in the figure indicates that there is an effective connection between the brain regions of the corresponding row and column. The size of the colored circle corresponds to the size of the effective connectivity value, and the direction is from the brain region of the corresponding column to the brain region of the corresponding row. Blank indicates that there is no effective connection between the brain regions of the row and column. There was a total of 62 common effective connections between the 24 ROIs of the two groups. Among them, 60 effective connections were excitatory connections, and 2 connections were inhibitory connections, i.e., from VN_SPG_L to SN_TPOsup_L and from DMN_ANG_R to SN_TPOsup_L. The effective connectivity with the largest excitatory connection value was from SMN_PCUN_L to itself. It can be seen that the common effective connectivity is distributed in these 7 brain networks.

The different parts of the effective connectivity between the two groups

The different parts of the effective connectivity between the two groups of 24 ROIs are shown in Figure 4. Consistent

TABLE 2 The coordinates of different brain networks.

Brain networks	ROI	Abbreviation	Coordinate
VN	Calcarine fissure and surrounding cortex	CAL_L	−6 −76 10
	Inferior occipital gyrus	IOG_R	28 −94 −4
	Middle occipital gyrus	MOG_L	−28 −94 −4
	Superior parietal gyrus	SPG_L	−20 −72 54
	Superior parietal gyrus	SPG_R	20 −74 54
DMN	Precuneus	PCUN_L	2 −76 40
	Inferior parietal, but supramarginal and angular gyri	IPL_L	−32 −72 42
	Angular gyrus	ANG_R	36 −70 42
	Superior frontal gyrus, medial	SFGmed_L	0 58 10
Cerebellum	Pons	Pons	0 −42 −42
SMN	Postcentral gyrus	PoCG_R	58 −6 28
	Precentral gyrus	PreCG_L	−56 −8 30
	Precuneus	PCUN_L	−2 −48 76
AN	Superior temporal gyrus	STG_R	62 −22 16
	Supramarginal gyrus	SMG_L	−60 −22 16
SN	Middle frontal gyrus	MFG_L	−30 56 16
	Middle frontal gyrus	MFG_R	32 56 16
	Anterior cingulate and paracingulate gyri	ACG_L	0 30 28
	Superior temporal gyrus	STG	54 14 -4
	Temporal pole: superior temporal gyrus	TPOsup_L	−50 14 −6
FPN	Middle frontal gyrus	MFG_R	44 18 50
	Inferior parietal, but supramarginal and angular gyri	IPL_R	44 -56 56
	Middle frontal gyrus	MFG_L	−44 22 46
	Superior parietal gyrus	SPG_L	−32 −74 52

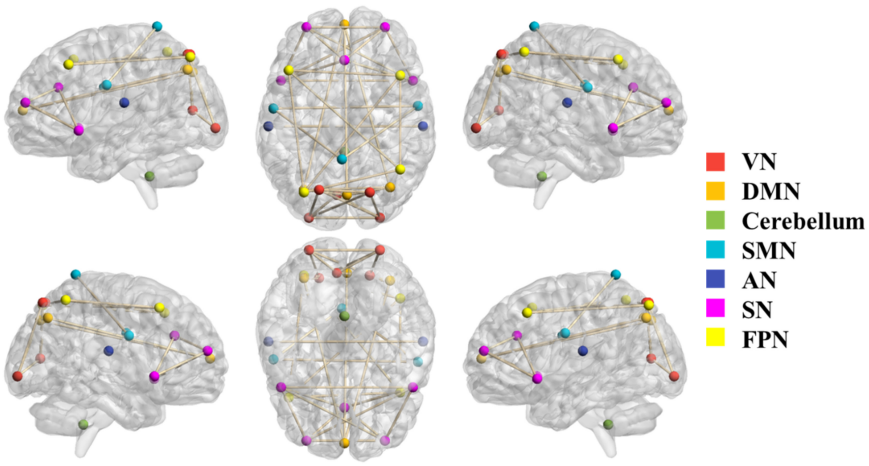

FIGURE 2
The selected 24 ROIs correspond to 7 brain networks. The color of the node represents the brain network to which the node belongs. The ROIs of each brain network are connected by lines.

with Figure 3, each colored circle in the figure indicates that there is an effective connection between the brain regions of the corresponding rows and columns. The size of the colored circle corresponds to the size of the effective connectivity value, and the direction is from the brain region of the corresponding column to the brain region of the corresponding row. There were 11 different effective connections between the 24 ROIs of the two groups, and these 11 effective connections were all excitatory connections. The specific effective connectivity are shown in Table 3. It can be seen that the difference of effective

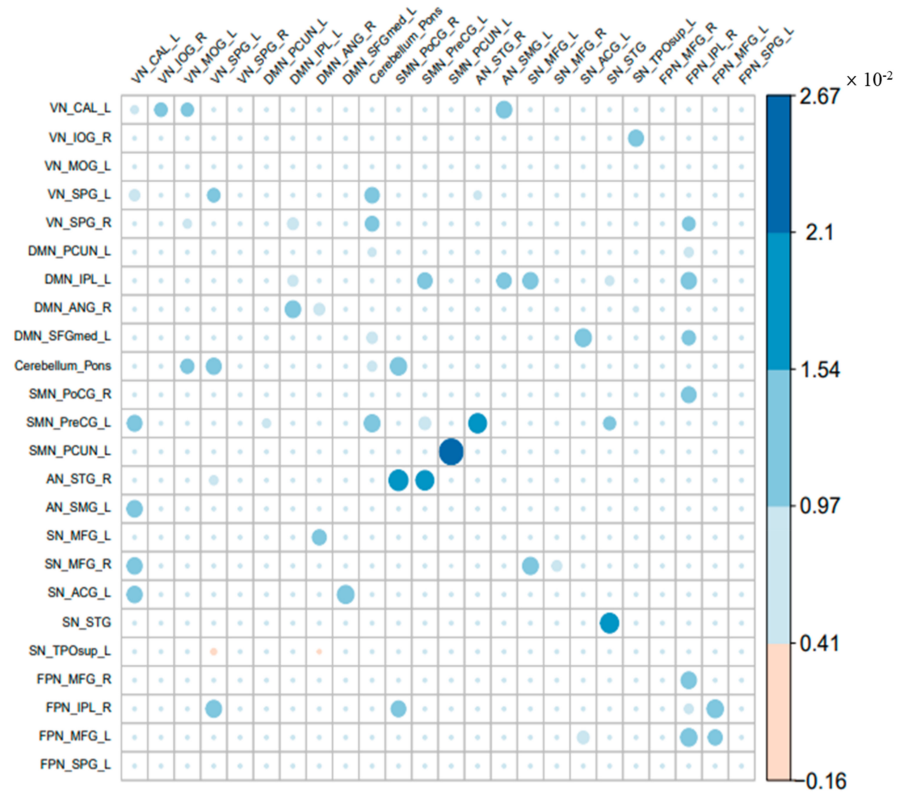

FIGURE 3
The common part of the effective connectivity between the two groups. The size of the circle indicates the size of the effective connectivity value.

connectivity was reflected in VN, cerebellum, DMN, SMN, and FPN, among which there were many excitatory connections between VN and FPN.

Correlation

We analyzed the correlation between the clinical data of the patient group and the common parts of the effective connectivity between the two groups. And the correlation coefficient with significance level less than 0.05 was selected. A total of 17 effective connections was significantly correlated with clinical data. In addition, we analyzed the correlation between the clinical data of the patient group and the different parts of the effective connectivity between the two groups. And the correlation coefficient with significance level less than 0.05 was selected. We found a significant correlation between only one effective connection and one clinical data. We found an effective connectivity (from DMN_ANG_R to SMN_PreCG_L) and ADOS_G_STEREO_BEHAV had significant negative correlation. Figure 5 shows the details of relationships between the effective connectivity and ADOS_G_STEREO_BEHAV. From left to right are scatter plot, box plot and probability density plot separately.

Discussion

In this study, we used spDCM method to compare the differences of effective connectivity between 24 ROIs corresponding to 7 large-scale brain networks between autistic children and matched healthy controls from the ABIDE II dataset. Three findings emerged from our analysis. First, for both groups, SMN is similar to a central network, which is closely and effectively connected to other brain networks. In addition, we also observed important causal interactions in the "triple network" system, including DMN, SN and FPN. Second, we found that children with ASD were characterized by attenuated effective connectivity among large-scale brain networks. Third, we observed significant correlation between the strength of the effective connectivity from ANG_R of DMN to PreCG_L of SMN and the ADOS_G_STEREO_BEHAV scores.

With the help of spDCM, we studied effective connectivity among large-scale brain networks in children with ASD. In both subject groups, we found that there were 62 significant effective connections in total, of which 60 were excitatory connections and 2 were inhibitory connections. Among these connections, the majority were related to the SMN. Our results are in line

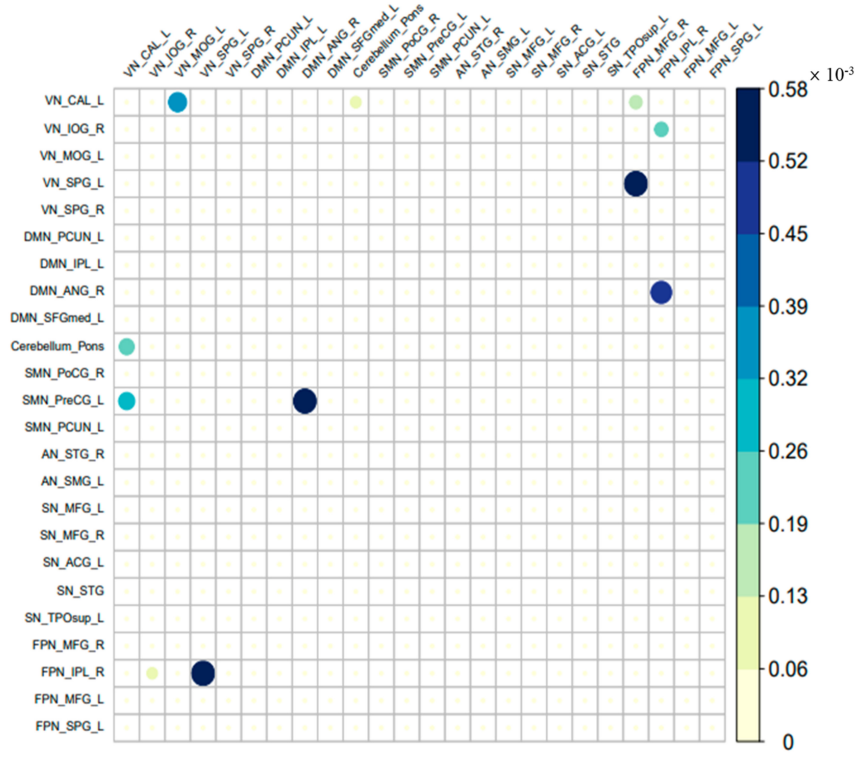

FIGURE 4
The different part of the effective connectivity between the two groups. The size of the circle indicates the size of the effective connectivity value.

TABLE 3 The different parts of the effective connectivity between the two groups.

Number	Effective connectivity direction
1	VN_CAL_L - > Cerebellum_Pons
2	VN_CAL_L - > SMN_PreCG_L
3	VN_IOG_R - > FPN_IPL_R
4	VN_MOG_L - > VN_CAL_L
5	VN_SPG_L - > FPN_IPL_R
6	DMN_ANG_R - > SMN_PreCG_L
7	Cerebellum_Pons - > VN_CAL_L
8	FPN_MFG_R - > VN_CAL_L
9	FPN_MFG_R - > VN_SPG_L
10	FPN_IPL_R - > VN_IOG_R
11	FPN_IPL_R - > DMN_ANG_R

with previous studies of traditional functional connectivity (Du et al., 2021; Lepping et al., 2022). Furthermore, our studies extended previous finding by providing the directionality of the influences among these networks. In the connection within the DMN network, Yao et al. (2016) found that the connection between the precuneus, posterior cingulate gyrus and the medial prefrontal gyrus was reduced in DMN of children with ASD. Funakoshi et al. (2016) found that the functional connections of bilateral inferior parietal lobule and posterior cingulate cortex of DMN in children with ASD were reduced. We found that in DMN internal connections, effective connectivity involved IPL_L and ANG_R. They were from IPL_L to itself, from ANG_R to itself and from IPL_L to ANG_R, respectively. All three connections were excitatory connections. In the connection between different networks, Lombardo et al. (2019) found that the functional connection between DMN and VN in children with ASD was reduced. We further demonstrated in the current study, that the influences were mainly coming from the excitatory connection from IPL_L of DMN to SPG_R of VN. Chen et al. (2021) found hyperconnectivity between VN and SMN in children with ASD. We found that the effective connection between VN and SMN was from CAL_L of VN to PreCG_L of SMN.

In compared with healthy controls, we found attenuated effective connectivity in children with ASD. There were 11 effective connections, and these 11 effective connections were all excitatory connections. First, we found that the effective connection between the triple networks of ASD patients changed. This was consistent with previous studies that the dysfunction of one core network may affect the other two networks (Menon, 2011). Second, in the connection related to VN, we found that compared with normal children, the effective

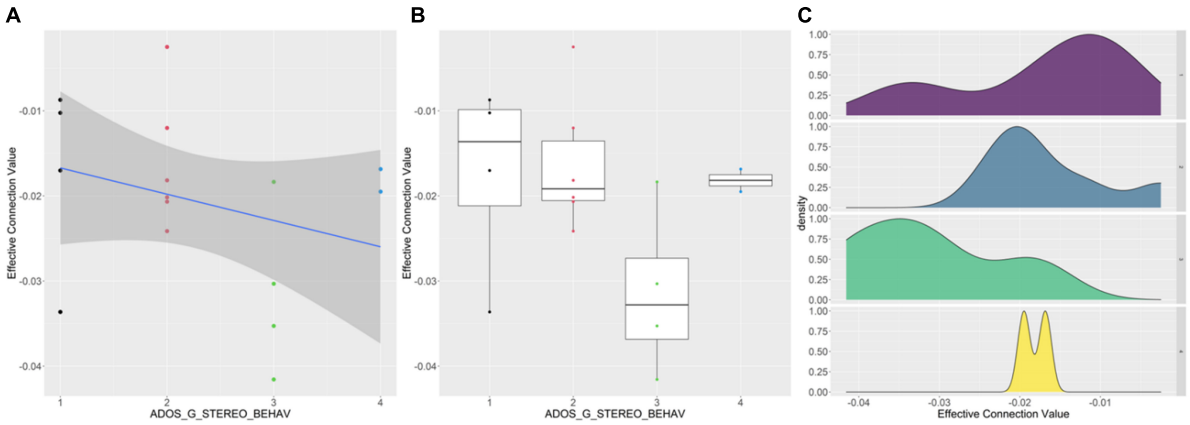

FIGURE 5
Correlations between effective connectivity values (from DMN_ANG_R to SMN_PreCG_L) and ADOS_G_STEREO_BEHAV. **(A)** The effective values and ADOS_G_STEREO_BEHAV has significant negative correlation. **(B)** The overall trend of ADOS_G_STEREO_BEHAV decreases as the effective connection value decreases. **(C)** For different ADOS_G_STEREO_BEHAV, the probability density distributions of the effective connection values are significantly different.

connectivity from MOG_L to CAL_L reduced in children with ASD. Keehn et al. (2021) found that the functional connection between the primary visual and extrastriate cortices within VM of ASD children increased. In addition, we found that the effective connectivity from CAL_L of VN to PreCG_L of SMN reduced in children with ASD. This was consistent with the results of Du et al. (2021). Their study showed that the functional connection between VN and SMN reduced in patients with ASD. And our results showed that part of VN had an excitatory effect on the part of SMN. Compared with normal children, children with ASD had 5 reduced effective connections between VN and FPN, namely, from IOG_R of VN to IPL_R of FPN, form SPG_L of VN to IPL_R of FPN, from MFG_R of FPN to CAL_L of VN, from MFG_R of FPN to SPG_L of VN, and from IPL_R of FPN to IOG_R of VN. This was consistent with previous studies. Yerys et al. (2019) found that there was a weak functional connection between FPN and the ventral attention subnetwork in patients with ASD. Third, in the connection related to DMN, we found that the connection between DMN and other brain networks was abnormal, in which the effective connectivity from ANG_R of DMN to PreCG_L of SMN reduced, and the effective connectivity from IPL_R of FPN to ANG_R of DMN reduced. This was consistent with previous functional connectivity studies. Previous studies have found underconnectivity and overconnectivity of DMN functional connections in children with ASD (Lynch et al., 2013; Yao et al., 2016).

In the study of the related mechanisms of brain regions, past studies have shown that visual impairment at birth or in early childhood can lead to psychological and emotional disorders (Wrzesinska et al., 2017). Our study further suggested that children with ASD may be associated with impaired vision. In connection with cerebellum, we found that the effective connectivity from CAL_L of VN to the pons of cerebellum reduced in children with ASD, and the effective connectivity of the opposite direction also reduced. These studies have shown that the effective connectivity between VN and cerebellum in children with ASD is abnormal. Anatomical and clinical studies have shown that the cerebellum is very important in motor learning and coordination and it supports cognitive, language and executive functions (Becker and Stoodley, 2013). Many clinical studies and animal model studies have shown that cerebellar dysfunction plays an important role in ASD (Tsai, 2016). So cerebellum may be related to the pathogenesis of ASD. Differences in DMN functional connectivity seem to be related to a wide range of social, communication, defects, and delays (Harikumar et al., 2021). The results of effective connection obtained in this paper prove this from another aspect. FPN was related to cognitive control processes, including behavioral response inhibition and working memory. And studies have proved that there are problems in VN of patients with ASD, so the abnormal connection between VN and FPN may be related to the pathogenesis of ASD.

In the study on effective connectivity of ASD, Rajabioun et al. (2020) found that in the resting state, the effective connectivity between active areas of children with ASD reduced, which was consistent with the results of reduced effective connectivity of children with ASD in this paper. In addition, we found that the effective connection from ANG_R of DMN to PreCG_L of SMN and ADOS_G_STEREO_BEHAV score had significant negative correlation. Rolls et al. (2020) found that the effective connectivity from the middle temporal

gyrus to precuneus was negatively correlated with the total, communication and social scores of ASD. It can be speculated that the effective connectivity between brain regions of ASD patients is related to some clinical scores of ASD. The lower the effective connectivity, the higher the score of autistic children, and the more serious the ASD.

Limitations

Our research has several limitations. First of all, we studied the effective connectivity in the resting state, we can study the effective connection in the task state and compare the differences in the future. Secondly, the age of the subjects we selected is between 8 and 13 years old, we can select subjects of other ages in the next study. Finally, the differences between patients before and after drug treatment should be considered in order to comprehensively understand the mechanism of ASD.

Conclusion

In this study, different from the conventional functional connection, we use effective connectivity to study the relationship between different brain regions in children with ASD. The subjects were 42 autistic children and 127 age-matched normal children from the public data set KKI. The results showed that compared with normal children, the effective connectivity between different brain regions in ASD children were reduced. Our research provides new evidence for the pathogenesis of autistic children from the perspective of effective connections within and between large-scale brain networks. The decrease of effective connectivity of brain network may be a clinical neurobiological feature of ASD. The changes of effective connectivity of brain network in children with ASD may provide useful information for the diagnosis and treatment of the disease.

Data availability statement

The original contributions presented in this study are included in the article/supplementary material, further inquiries can be directed to the corresponding authors.

Ethics statement

The studies involving human participants were reviewed and approved by the Johns Hopkins Medical Institutional Review Board. Written informed consent to participate in this study was provided by the participants' legal guardian/next of kin.

Author contributions

BL, JL, and HX designed the study and provided important suggestions. LW, YZ, WZ, HW, JZ, HJ, JF, and QQ collected and collated the research data. LW, YZ, and WZ conducted data analysis and helped explain the results. LW, YZ, BL, and JL drafted the manuscript. All authors thoroughly reviewed and approved the manuscript for publication.

Funding

This research was supported by the National Natural Science Foundation of China (61976248 and 81974215).

Conflict of interest

The authors declare that the research was conducted in the absence of any commercial or financial relationships that could be construed as a potential conflict of interest.

Publisher's note

All claims expressed in this article are solely those of the authors and do not necessarily represent those of their affiliated organizations, or those of the publisher, the editors and the reviewers. Any product that may be evaluated in this article, or claim that may be made by its manufacturer, is not guaranteed or endorsed by the publisher.

References

Becker, E. B., and Stoodley, C. J. (2013). Autism spectrum disorder and the cerebellum. *Int. Rev. Neurobiol.* 113, 1–34. doi: 10.1016/B978-0-12-418700-9.00001-0

Belmonte, M. K., Allen, G., Beckel-Mitchener, A., Boulanger, L. M., Carper, R. A., and Webb, S. J. (2004). Autism and abnormal development of brain connectivity. *J. Neurosci.* 24, 9228–9231. doi: 10.1523/JNEUROSCI.3340-04.2004

Bi, X. A., Zhao, J., Xu, Q., Sun, Q., and Wang, Z. (2018). Abnormal functional connectivity of resting state network detection based on linear ICA analysis in autism spectrum disorder. *Front. Physiol.* 9:475. doi: 10.3389/fphys.2018.00475

Carskadon, M. A., and Acebo, C. (1993). A self-administered rating scale for pubertal development. *J. Adolesc. Health* 14, 190–195. doi: 10.1016/1054-139x(93)90004-9

Chen, B., Linke, A., Olson, L., Ibarra, C., Reynolds, S., Müller, R. A., et al. (2021). Greater functional connectivity between sensory networks is related to symptom severity in toddlers with autism spectrum disorder. *J. Child Psychol. Psychiatry* 62, 160–170. doi: 10.1111/jcpp.13268

Chiang, S., Cassese, A., Guindani, M., Vannucci, M., Yeh, H. J., Haneef, Z., et al. (2016). Time-dependence of graph theory metrics in functional connectivity analysis. *Neuroimage* 125, 601–615. doi: 10.1016/j.neuroimage.2015.10.070

Christensen, D. L., Baio, J., Braun, K. V., Bilder, D., Charles, J., Constantino, J. N., et al. (2016). Prevalence and characteristics of autism spectrum disorder among children aged 8 Years - autism and developmental disabilities monitoring network, 11 Sites, United States, 2012. *Mmwr. Surveillance Summaries* 65, 1–23.

Courchesne, E., Mouton, P. R., Calhoun, M. E., Semendeferi, K., Ahrens-Barbeau, C., Hallet, M. J., et al. (2011). Neuron number and size in prefrontal cortex of children with autism. *JAMA* 306, 2001–2010. doi: 10.1001/jama.2011.1638

Di Martino, A., O'Connor, D., Chen, B., Alaerts, K., Anderson, J. S., Assaf, M., et al. (2017). Enhancing studies of the connectome in autism using the autism brain imaging data exchange II. *Sci. Data* 4:170010. doi: 10.1038/sdata.2017.10

Du, Y., Fu, Z., Xing, Y., Lin, D., Pearlson, G., Kochunov, P., et al. (2021). Evidence of shared and distinct functional and structural brain signatures in schizophrenia and autism spectrum disorder. *Commun. Biol.* 4:1073. doi: 10.1038/s42003-021-02592-2

Friston, K. J., Harrison, L., and Penny, W. (2003). Dynamic causal modelling. *Neuroimage* 19, 1273–1302. doi: 10.1016/s1053-8119(03)00202-7

Friston, K. J., Kahan, J., Biswal, B., and Razi, A. (2014). A DCM for resting state fMRI. *Neuroimage* 94, 396–407. doi: 10.1016/j.neuroimage.2013.12.009

Friston, K. J., Litvak, V., Oswal, A., Razi, A., Stephan, K. E., van Wijk, B. C. M., et al. (2016). Bayesian model reduction and empirical Bayes for group (DCM) studies. *Neuroimage* 128, 413–431. doi: 10.1016/j.neuroimage.2015.11.015

Funakoshi, Y., Harada, M., Otsuka, H., Mori, K., Ito, H., and Iwanaga, T. (2016). Default mode network abnormalities in children with autism spectrum disorder detected by resting-state functional magnetic resonance imaging. *J. Med. Invest.* 63, 204–208. doi: 10.2152/jmi.63.204

Gao, Y., Linke, A., Jao Keehn, R. J., Punyamurthula, S., Jahedi, A., Gates, K., et al. (2019). The language network in autism: Atypical functional connectivity with default mode and visual regions. *Autism Res.* 12, 1344–1355. doi: 10.1002/aur.2171

Harikumar, A., Evans, D. W., Dougherty, C. C., Carpenter, K. L. H., and Michael, A. M. (2021). A review of the default mode network in autism spectrum disorders and attention deficit hyperactivity disorder. *Brain Connect.* 11, 253–263. doi: 10.1089/brain.2020.0865

Keehn, R. J. J., Pueschel, E. B., Gao, Y. F. F., Jahedi, A., Alemu, K., Carper, R., et al. (2021). Underconnectivity between visual and salience networks and links with sensory abnormalities in autism spectrum disorders. *J. Am. Acad. Child Adolesc. Psychiatry* 60, 274–285. doi: 10.1016/j.jaac.2020.02.007

Khan, A. J., Nair, A., Keown, C. L., Datko, M. C., Lincoln, A. J., and Müller, R. A. (2015). Cerebro-cerebellar resting-state functional connectivity in children and adolescents with autism spectrum disorder. *Biol. Psychiatry* 78, 625–634. doi: 10.1016/j.biopsych.2015.03.024

Lepping, R. J., McKinney, W. S., Magnon, G. C., Keedy, S. K., Wang, Z., Coombes, S. A., et al. (2022). Visuomotor brain network activation and functional connectivity among individuals with autism spectrum disorder. *Hum. Brain Mapp.* 43, 844–859. doi: 10.1002/hbm.25692

Li, B., Daunizeau, J., Stephan, K. E., Penny, W., Hu, D., and Friston, K. (2011). Generalised filtering and stochastic DCM for fMRI. *Neuroimage* 58, 442–457. doi: 10.1016/j.neuroimage.2011.01.085

Linke, A. C., Jao Keehn, R. J., Pueschel, E. B., Fishman, I., and Müller, R. A. (2018). Children with ASD show links between aberrant sound processing, social symptoms, and atypical auditory interhemispheric and thalamocortical functional connectivity. *Dev. Cogn. Neurosci.* 29, 117–126. doi: 10.1016/j.dcn.2017.01.007

Lombardo, M. V., Eyler, L., Moore, A., Datko, M., Carter Barnes, C., Cha, D., et al. (2019). Default mode-visual network hypoconnectivity in an autism subtype with pronounced social visual engagement difficulties. *eLife* 8:e47427. doi: 10.7554/eLife.47427

Lord, C., Rutter, M., and Le Couteur, A. (1994). Autism Diagnostic Interview-Revised: A revised version of a diagnostic interview for caregivers of individuals with possible pervasive developmental disorders. *J. Autism Dev. Disord.* 24, 659–685. doi: 10.1007/bf02172145

Lord, C., Rutter, M., Dilavore, P., Risi, S., Gotham, K., and Bishop, S. (2012). *Autism diagnostic observation schedule: ADOS-2*. Los Angeles, CA: Western Psychological Services.

Lynch, C. J., Uddin, L. Q., Supekar, K., Khouzam, A., Phillips, J., and Menon, V. (2013). Default mode network in childhood autism: Posteromedial cortex heterogeneity and relationship with social deficits. *Biol. Psychiatry* 74, 212–219. doi: 10.1016/j.biopsych.2012.12.013

May, K. E., and Kana, R. K. (2020). Frontoparietal Network in Executive Functioning in Autism Spectrum Disorder. *Autism Res.* 13, 1762–1777. doi: 10.1002/aur.2403

McKeown, M. J., and Sejnowski, T. J. (1998). Independent component analysis of fMRI data: Examining the assumptions. *Hum. Brain Mapp.* 6, 368–372.

Menon, V. (2011). Large-scale brain networks and psychopathology: A unifying triple network model. *Trends Cogn. Sci.* 15, 483–506. doi: 10.1016/j.tics.2011.08.003

Mohammad-Rezazadeh, I., Frohlich, J., Loo, S. K., and Jeste, S. S. (2016). Brain connectivity in autism spectrum disorder. *Curr. Opin. Neurol.* 29, 137–147. doi: 10.1097/WCO.0000000000000301

Oldfield, R. C. (1971). The assessment and analysis of handedness: The Edinburgh inventory. *Neuropsychologia* 9, 97–113. doi: 10.1016/0028-3932(71)90067-4

Rajabioun, M., Nasrabadi, A. M., Shamsollahi, M. B., and Coben, R. (2020). Effective brain connectivity estimation between active brain regions in autism using the dual Kalman-based method. *Biomed. Eng.* 65, 23–32. doi: 10.1515/bmt-2019-0062

Razi, A., Kahan, J., Rees, G., and Friston, K. J. (2015). Construct validation of a DCM for resting state fMRI. *Neuroimage* 106, 1–14. doi: 10.1016/j.neuroimage.2014.11.027

Rolls, E. T., Zhou, Y. Y., Cheng, W., Gilson, M., Deco, G., and Feng, J. F. (2020). Effective connectivity in autism. *Autism Res.* 13, 32–44. doi: 10.1002/aur.2235

Smith, S. M., Fox, P. T., Miller, K. L., Glahn, D. C., Fox, P. M., Mackay, C. E., et al. (2009). Correspondence of the brain's functional architecture during activation and rest. *Proc. Natl. Acad. Sci. U.S.A.* 106, 13040–13045. doi: 10.1073/pnas.0905267106

Stoodley, C. J. (2014). Distinct regions of the cerebellum show gray matter decreases in autism, ADHD, and developmental dyslexia. *Front. Syst. Neurosci.* 8:92. doi: 10.3389/fnsys.2014.00092

Tsai, P. T. (2016). Autism and cerebellar dysfunction: Evidence from animal models. *Semin. Fetal Neonatal Med.* 21, 349–355. doi: 10.1016/j.siny.2016.04.009

Verly, M., Verhoeven, J., Zink, I., Mantini, D., Peeters, R., Deprez, S., et al. (2014). Altered functional connectivity of the language network in ASD: Role of classical language areas and cerebellum. *Neuroimage Clin.* 4, 374–382. doi: 10.1016/j.nicl.2014.01.008

Wang, J., Wang, X., Xia, M., Liao, X., Evans, A., and He, Y. (2015). GRETNA: A graph theoretical network analysis toolbox for imaging connectomics. *Front. Hum. Neurosci.* 9:386. doi: 10.3389/fnhum.2015.00386

Wang, Z., Wang, Y., Sweeney, J. A., Gong, Q., Lui, S., and Mosconi, M. W. (2019). Resting-state brain network dysfunctions associated with visuomotor impairments in autism spectrum disorder. *Front. Integr. Neurosci.* 13:17. doi: 10.3389/fnint.2019.00017

Wechsler, D. (2003). *Wechsler intelligence scale for children-WISC-IV*. New York, NY: Psychological Corporation.

Wechsler, D. (2014). *Wechsler intelligence scale for children-fifth edition (WISC-V)*. New York, NY: Psychological Corporation.

Wrzesinska, M., Kapias, J., Nowakowska-Domagala, K., and Kocur, J. (2017). Visual impairment and traits of autism in children. *Psychiatr. Pol.* 51, 349–358. doi: 10.12740/PP/OnlineFirst/61352

Yao, Z., Hu, B., Xie, Y., Zheng, F., Liu, G., Chen, X., et al. (2016). Resting-state time-varying analysis reveals aberrant variations of functional connectivity in autism. *Front. Hum. Neurosci.* 10:463. doi: 10.3389/fnhum.2016.00463

Yerys, B. E., Tunc, B., Satterthwaite, T. D., Antezana, L., Mosner, M. G., Bertollo, J. R., et al. (2019). Functional connectivity of frontoparietal and salience/ventral attention networks have independent associations with co-occurring attention-deficit/hyperactivity disorder symptoms in children with autism. *Biol. Psychiatry Cogn. Neurosci. Neuroimaging* 4, 343–351. doi: 10.1016/j.bpsc.2018.12.012

Zenghui, M., Qingjiu, C., Chaogan, Y., Ting, M., Bin, L., Jingran, L., et al. (2019). Functional connectivity characteristics of executive control network in patients with high-functioning autism aged 6 - 18 years. *Chin. Ment. Health J.* 33, 401–405.

Frontiers in Neuroscience

Provides a holistic understanding of brain function from genes to behavior

Part of the most cited neuroscience journal series which explores the brain - from the new eras of causation and anatomical neurosciences to neuroeconomics and neuroenergetics.

Discover the latest Research Topics

See more →

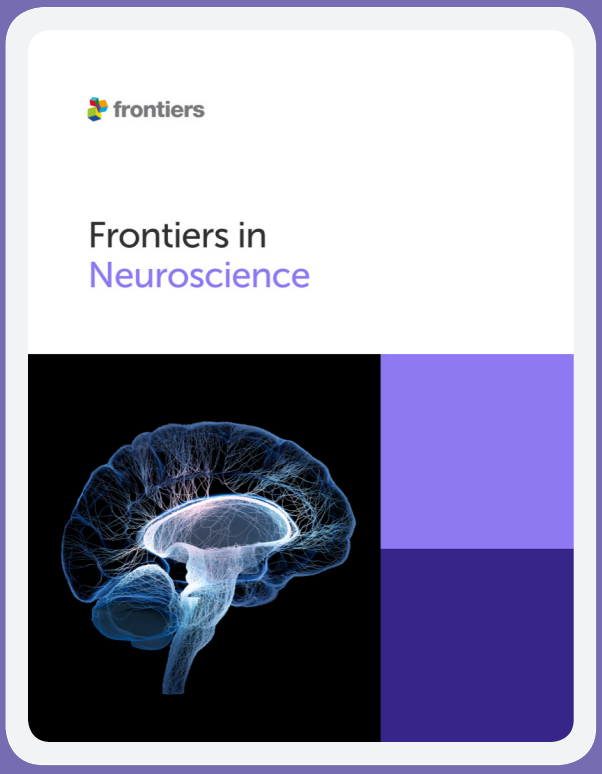

Frontiers

Avenue du Tribunal-Fédéral 34
1005 Lausanne, Switzerland
frontiersin.org

Contact us

+41 (0)21 510 17 00
frontiersin.org/about/contact